The Dissertation Committee for Andrea Keidel
certifies that this is the approved version of the following dissertation:

Exploiting high precision single particle diffusion measurements to probe cellular functions *in vitro* and *in vivo*

Committee:

Ernst-Ludwig Florin, Supervisor

George Shubeita

Vernita Gordon

Manfred Fink

Jeanne Stachowiak

Exploiting high precision single particle diffusion measurements to probe cellular functions *in vitro* and *in vivo*

by

Andrea Keidel, M.A.

DISSERTATION

Presented to the Faculty of the Graduate School of

The University of Texas at Austin

in Partial Fulfillment

of the Requirements

for the Degree of

DOCTOR OF PHILOSOPHY

THE UNIVERSITY OF TEXAS AT AUSTIN

May 2014

Dedicated to my family.

Acknowledgments

First, I want to thank Dr. Florin for the support I received during my stay in Austin. I am grateful for his guidance, advice and showing me ways to work around problems arising during this research. Discussions with him provided necessary understanding of the experiment and how to proceed with research.

I would also like to express my gratitude towards my committee members for taking the time to read my dissertation and helpful feedback. Thanks go also out to Dr. Fink and the University of Wuerzburg, Germany for making my initial stay at the University of Texas at Austin possible by an exchange program.

To work with Dr. Florin's biophysics group was an outstanding experience and I want to thank all current and previous lab members for their support throughout the years. It is usually the former lab members, from whom you initially learn the most like Katie, Katja, Vasilli, Pinyu, Martin, and Rongxin. I am especially grateful for the help and support I received from Tobias Bartsch on the membrane fusion project and the many LabView programs he wrote for data acquisition. I also want to thank Chieze Ibeneche, who first introduced me to the yeast project. Her help and support continued long after she had left the lab. The helpful discussions and input of our collaborators on the yeast project Dr. Brunner and his student Maria as well as Dr. Hoenger and his student Minghua are greatly appreciated.

I am very thankful for help, support and distractions by everyone in the CNLD and the physics department, especially Tony, Chih-Hung, Frank, Dave, BJ, Orrin, and Rafael , who made my stay in Austin a great experience. In this context I also would like to thank everyone who received parts of this dissertation for proofreading. I also want to thank Olga, Rachael, and Marybeth for keeping the CNLD organized and always running well.

I also want to extend my gratitude to the Japan Karate Association of Austin, which is a good place to meet nice people and get a fresh look on your research. It is a especially refreshing place to go when the experiments are not working well. Thank you to all the previous people teaching and training there.

Finally I want to say thank you to my parents and family. Without their encouragement, support and guidance through the years, this would have been impossible.

Exploiting high precision single particle diffusion measurements to probe cellular functions *in vitro* and *in vivo*

Publication No. ____________________

Andrea Keidel, Ph.D.
The University of Texas at Austin, 2014

Supervisor: Ernst-Ludwig Florin

Diffusion plays an important role for many processes at the microscopic level in cells. In this dissertation we present two model systems in which we monitor diffusion with high precision single particle tracking to gain insight into cellular functions. First we present an *in vitro* membrane fusion assay, in which fusion intermediates are described by the thermal motion of a membrane coated tracer particle. In the second part the diffusive motion of endogenous lipid droplets in the model organism *Schizosaccharomyces pombe* is utilized to probe the cytoplasmic behavior in response to glucose starvation.

In the first part of this dissertation we present a novel membrane fusion assay that uses solid supported membranes on silica beads and on coverslips. The fusion of the lipid bilayers is induced by bringing an optically trapped bead in contact with the coverslip surface while observing the bead's thermal motion with microsecond temporal and nanometer spatial resolution using a three-dimensional position detector. The probability of fusion is controlled by the membrane tension on the particle. The progression of fusion is monitored by changes in the three-dimensional position histograms of the bead and in its rate of diffusion. We were able to observe all fusion intermediates including transient fusion, formation of a stalk, hemifusion and the completion of a fusion pore. Fusion intermediates are characterized by axial but not lateral confinement of the motion of the bead and independently by the change of its rate of diffusion due to the additional drag from the stalk-like connection between the two membranes. We provide an estimate of the cross-sectional area of fusion intermediates using a theory that describes the viscous drag on a cylinder diffusing in a two-dimensional fluid near a solid substrate. From changes in the axial fluctuations maximal transition times between intermediate states are estimated. Lower bounds of energy barriers between states are estimated form the depth of the energy landscapes for each state. The detailed information provided by this assay makes it ideally suited for studies of early events in pure lipid bilayers fusion or fusion assisted by fusogenic molecules.

In the seconcd part we utilize the Brownian motion of endogenous lipid granules in *Schizosaccharomyces pombe* to probe the changes in the cytoplasm due to glucose starvation. The fission yeast cells are observed with DIC microscopy. To measure granule's trajectory with high spatial precision we integrate the DIC images to transform the typical DIC shadow-cast contrast into a single peak, whose center can be determined with sub-nanometer precision. Image integration also lead to a new method, which allows axial DIC single particle tracking with $5nm$ precision from a single image. The axial position is used to implement a feedback loop, which is able to follow granules in three-dimensions within the cell for longer than 30 minutes. The ability to increase the observation time of exponentially growing cells leads to a more accurate calculation of the mean square displacement on long time scales, and the possibility to image the stable structures within a cell or the time evolution of transient ones. Additionally we further our understanding of cell freezing induced by glucose starvation. Although actin seems to form filamentous structures in frozen cells, we discount actin for being the cause of cell freezing. Additionally we show that cell freezing is independent from the initial glucose concentration in the range of $1g/L$ to $20g/L$ glucose. Cells can recover form the frozen state by the addition of glucose. We characterize the cell's recovery over the first few minutes, in which a significant increase in the mobility occurs. The increased motion can be observed in the measured alpha value and the standard deviation of the position fluctuations. The frozen state itself is characterized in more detail by microrheology experiments. The application of force by optical traps leads to a classification of cells into three states: free, tethered, and immobile. The frequency behavior of the storage and loss modulus of granules belonging to these three categories has been evaluated by passive microrheology. The storage modulus increased by a factor of 340 from exponential growth, $G'_0 = 0.26Pa$, to the frozen state, $G'_0 = 89Pa$, and the loss

modulus by a factor of 280, from $G''_0 = 0.25Pa$ to $G''_0 = 71Pa$. The exponent of the power law behavior decreases with decreasing alpha, from $\beta_{free} = 0.61$ to $\beta_{im} = 0.13$ indicating a transition from a more fluid-like cytoplasm to a more solid-like one during starvation. The values for the modulus as well as the exponent in exponential growth are similar to the ones in *Dictyostelium* cells [218]. Tethered cells have a comparable storage modulus to fibrin and collagen networks and frozen cells are comparable to cross-linked actin networks [200].

Table of Contents

List of Tables

List of Figures

Part I

Direct observation of intermediate states in model membrane fusion by photonic force microscopy

Chapter 1

Introduction

1.1 Introduction to membrane fusion

Membrane fusion is essential for many biological processes. Cell-to-cell fusion [39] is important for fertilization [171] and in carcinogenesis [55]. Furthermore, fusion is a necessary step in the life cycle of many viruses [181, 107, 215, 82]. Inside the cell, membrane fusion is crucial for exocytosis [137, 138], protein trafficking [216], neurotransmitter release [174, 175], mitochondrial remodeling [91] and resealing of the plasma membrane [136]. Despite membrane fusion's significance, its physical basis remains poorly understood: the exact sequence of events along the fusion pathway, the importance of the lipid composition of the membranes and the contribution of fusion proteins within the membranes is still not completely clear.

The nature of membrane fusion varies vastly amongst different biological systems. Yeast vacuoles take minutes to fuse [217] and have a contact area approximately 10,000 larger than the one of synaptic vesicles which fuse in milliseconds [174]. The large number of different fusion proteins and peptides is adding to the diversity of fusion processes. For example in synaptic vesicle fusion proteins recruit the specific vesicles to their target location and aid in

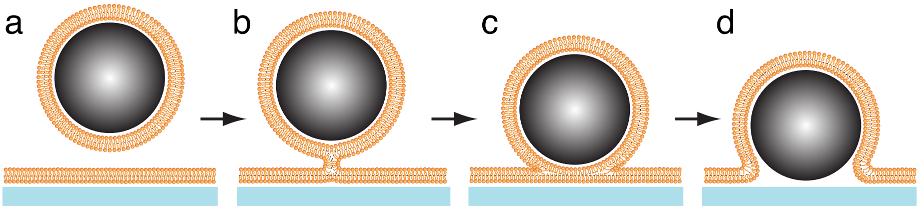

Figure 1.1: Model of the fusion process of a vesicle on a target membrane. a) In order for fusion to occur, the two opposing lipid bilayers must be brought into close contact. b) After the first initial contact, a stalk-like connection is formed. This can be a transient process. c) Subsequently following is hemifusion, a second fusion intermediate, which is formed by radial expansion of the stalk. d) A hole opens in the hemifusion diaphragm, and expands into a fusion pore to complete fusion.

achieving membrane contact. Achieving close contact by SNAREs is necessary for the initiation of membrane fusion, not the actual evolution of fusion, which is thought to be driven by the lipid bilayers [120, 123, 235]. Despite the large variety of fusion processes, the common factor among all of them is the involvement of the lipid membrane. This elementary process occurs on the nanoscale, below the resolution of light microscopy, and has transient intermediates. Intermediate states, like hemifusion, are found in both biological systems [64, 234, 139, 42, 8, 126, 227, 71, 89] and in model membranes [156, 36, 40, 122, 43] which emphasizes the significance of the lipid membrane and its composition for membrane fusion. In order to fully understand how proteins drive the lipids through the fusion process, the fusion mechanism and intermediates of model membranes and the underlying physics need to be understood down to the nanoscale. Figure 1.1 summarizes the generally accepted, essential steps in the fusion pathway [41]. In the most common pathway a stalk forms between two bilayers (stalk-hypothesis) following initial contact (Figure 1.1b). The stalk, an hourglass shaped connection of the proximal membrane leaflets, radially expands into a hemifusion diaphragm (Figure 1.1c). Then, the distal-monolayers make contact, and the connecting area increases. Finally, in the hemifusion diaphragm a hole is created which enlarges into a fusion pore and completes fusion (Figure 1.1d).

In order for the membrane to fulfill its functions in the cell, it needs long-term mechanical stability. This stability arises from the hydrophobic effect, which drives the self-assembly into bilayers and is responsible for maintaining its integrity. Fusion on the other hand requires dramatic local changes in the membrane structure and hole formation. Spatial rearrangements and the formation of holes require an energy input, which needs to be significantly larger than the thermal energy to preserve long-term stability. To preserve long-term stability of the membrane, the energy barrier of spatial rearrangement and hole formation needs to be significantly larger than the thermal energy. This, though, is a simplified picture: due to different intermediates along the membrane fusion pathway, there are actually multiple energy barriers. First, the water between the two opposing bilayers needs to be removed so that the membranes can make an initial contact. This process is thought to be energy demanding [135]. Subsequent to initial contact, every structural change in the lipid arrangement, transitioning from one fusion intermediate to the next, requires an input of energy. The energy barrier between the individual intermediates can be calculated using elastic continuum models [132, 194, 118, 133, 115] or field theory [105, 104, 121]. The resulting energy barriers depend highly on the membrane curvature, the lipid composition, and the actual fusion pathway. If the applied energy is not sufficient to cross all energy barriers, fusion can be arrested in one of the intermediates, most commonly in the hemifused state [156, 122]. It is important to measure these energy barriers in order to further our understanding of the role of fusion proteins. This, for example, will allow a direct comparison between the energy a fusion protein like a SNARE can exert [68] and the energy necessary to overcome the individual energy barriers.

Experimentally, energy barriers between fusion intermediates can be overcome in protein-free bilayers by freezing and thawing [92], electrostatic interaction [122], dehydration [231], poly(ethylene glycol) [119], UV-light pulses [85], femtosecond laser pulses [73] or mechanical force [163, 129, 1, 34, 223, 225, 116]. The initiation of fusion can be achieved by any of those methods, but none of them can can be used to observe the dynamics of the fusion process at the single vesicle level with high temporal and spatial resolution. Furthermore, they do not allow the instantaneous measurement of additional parameters like the height of the individual energy barriers.

1.2 Lipids and membranes

Next section 1.2.1 gives a brief introduction to the basic component of membranes the lipids, their self-assembly and formed structures. Subsequently, section 1.2.2 details the biologically most relevant structure, the lipid bilayer, is described in more detail. Finally, section 1.2.3. discusses the difference between biological membranes of cells and a pure lipid model membrane.

1.2.1 Lipids and self-assembly

Lipids, the main component of model membranes and a major component of biological membranes, are amphiphilic molecules which commonly consist of a hydrophilic head-group and one or two hydrophobic hydrocarbon chains. Frequently, lipids have a polar head-group and a non-polar tail, but there is nonetheless a huge variety of head-groups and chains which construct different lipids. Some categories of lipids are fatty acids, glycerolipids, glycerophospholipids, sphingolipids, sterol lipids, prenol lipids, saccharolipids, and polyketides. Two common head-groups in membranes are ethanolamine and chlorine, which build the two groups of phospholipids, phosphatidylethanolamine (PE) and phosphatidylchlorine (PC). Model membranes are typically built from these phospholipids, sometimes with the addition of cholesterol. The hydrocarbon tails can be either saturated, which means there are no double bonds in the hydrocarbon chain, or unsaturated, with at least one double bond in the chain. The degree of saturation influences their physical properties like the phase transition temperature. Structures made of lipids are fluid-like above their phase-transition temperature, which means that the lipid molecules can diffuse almost freely within the formation, comparable to a two-dimensional fluid. The temperature at which the system starts to transition into the crystalline phase is highly determined by their lipids degree of saturation. Additionally, the double bond introduces a kink in the chain, so that efficient spatial packing is increasingly difficult. Besides acting as a structural component in cell membranes, other biological functions of lipids include storing energy [151] and signaling [210]. Figure 1.2 shows the structure of lipids found in biological membranes, which are also commonly used in model membranes. The lipid mainly used in this dissertation, DOPC, has two unsaturated hydrocarbon chains, with a chain length of eighteen carbon bonds. Because of its two unsaturated chains, it has a very low phase transition temperature of $T_c = -20°C$.

Due to the lipid's amphiphilic nature, they self-assemble if dispersed in an aqueous solution. Lipids arrange in such a way that the hydrophilic head-groups point to the outside, and inside is a core filled with fatty acid tails and held together by weak, long-range van der Waals interactions and an opposing strong, short-range, hard-core repulsion. These two interactions are assumed to determine the typical features of the interior of the bilayer, which has a constant, uniform, liquid-like density [185]. Self-assembly only occurs, if the energy of the system can be decreased by forming aggregates. The thermodynamics of the self-assembly of micelles can be described as followed [204, 96].

In equilibrium, it is required that the chemical potential of all identical

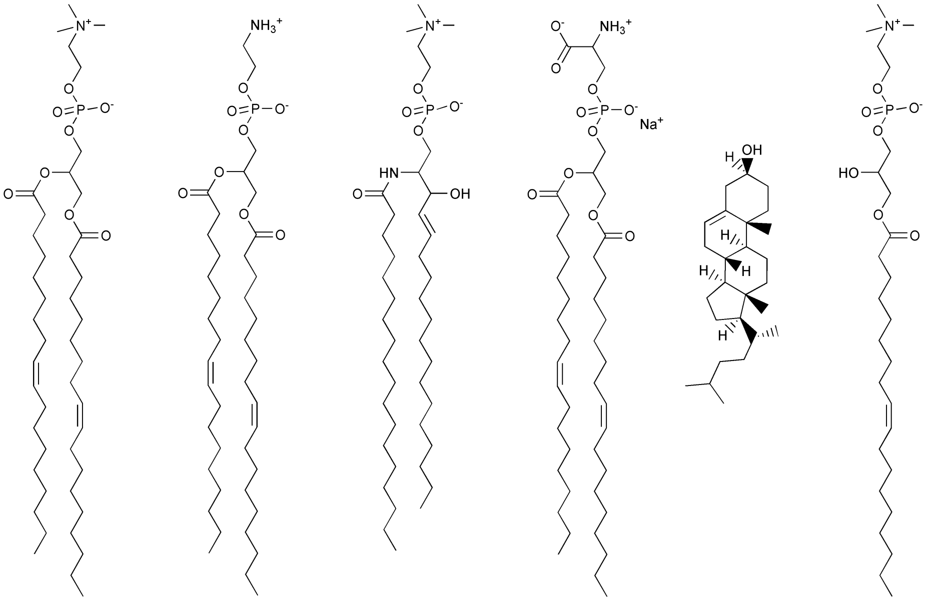

Figure 1.2: Structure of lipids found in biological membranes and commonly used in model membranes. From left to right: Dioleoylphosphatidylcholine (DOPC), dioleoylphosphatidylethanolamine (DOPE), sphingomyelin (SM), dioleoylphosphatidylserine (DOPS), cholesterol (CH) and lysophosphatidyl choline (LPC). Reprinted with permission from [134]

molecules in different aggregates is equal. This can be expressed as

$$\mu = \mu_N = \mu_N^0 + \frac{kT}{N} \cdot \log \frac{X_N}{N} = const \tag{1.1}$$

$$N = 1, 2, 3, \ldots, \tag{1.2}$$

with μ_N being the mean chemical potential of a molecule in an aggregate of aggregation number N, μ_N^0 the standard part of the chemical potential in aggregates of aggregation number N, and X_N the concentration of molecules in the individual aggregates. To get more information about the aggregated dispersion, the form and magnitude of μ_N^0 as a function of N need to be specified. Aggregates will only form if there is a difference between the cohesive energies of the aggregated and dispersed states. For self-assembly $\mu_N^0 < \mu_1^0$ needs to be fulfilled for some values of N. The functional variation of μ_N^0 with N determines many physical properties of the aggregates, like average size and polydiversity. For micelles of radius R, N is proportional to the volume $\frac{4}{3}\pi R^3$ and the number of surface molecules is proportional to the surface area $4\pi R^2$. This results in

$$\mu_N^0 = \mu_\infty^0 + \frac{\alpha kT}{N^{1/3}}, \tag{1.3}$$

where $-\alpha kT$ is the monomer-monomer bond energy in the aggregate relative to isolated monomers in solution. From this the critical micelle concentration can be calculated to be

$$(X_1)_{crit} \approx e^{-\frac{\mu_1^0 - \mu_N^0}{kT}}. \tag{1.4}$$

This defines the concentration at which the further addition of lipids results in the formation of more aggregates, whereas the monomer concentration remains approximately unchanged.

The packing parameter $\frac{v}{a_0 l_c}$ highly influences the structure lipids form by self-assembly, where v is the chain volume, a_0 the head group area, and l_c the chain length of the lipid. Figure 1.3 shows a summary of lipids of different packing parameters and the structures they tend to form. Cone shaped lipids, $\frac{v}{a_0 l_c} < \frac{1}{3}$, form micelles. If $\frac{1}{3} < \frac{v}{a_0 l_c} < \frac{1}{2}$, the lipid has a truncated cone shape and forms cylindrical micelles. Bilayer lipids like DOPC also have a truncated cone shape, but their head group area is smaller in comparison to the chain volume, $\frac{1}{2} < \frac{v}{a_0 l_c} < 1$. They form flexible bilayers and vesicles. If $\frac{v}{a_0 l_c} \approx 1$ the lipids are cylindrical and form planar bilayers. Inverted truncated cone shaped lipids, $\frac{v}{a_0 l_c} > 1$, can form inverted micelles, the hexagonal phase.

1.2.2 Lipid bilayers as Model Membranes

To be a good model, model membrane should exhibit as many features as possible of a biological membrane but should still be simple enough that the physical properties can be described by a small set of parameters. Simplifying biological membranes to its crucial components, allows us to gain insight into the underlying mechanisms of phenomena like membrane fusion, phase separation and diffusional behavior of lipids. Model membranes are usually made from a lipid bilayer and can vary in size, composition and architecture. Some examples are giant unilamellar vesicles (GUVs), supported lipid bilayers

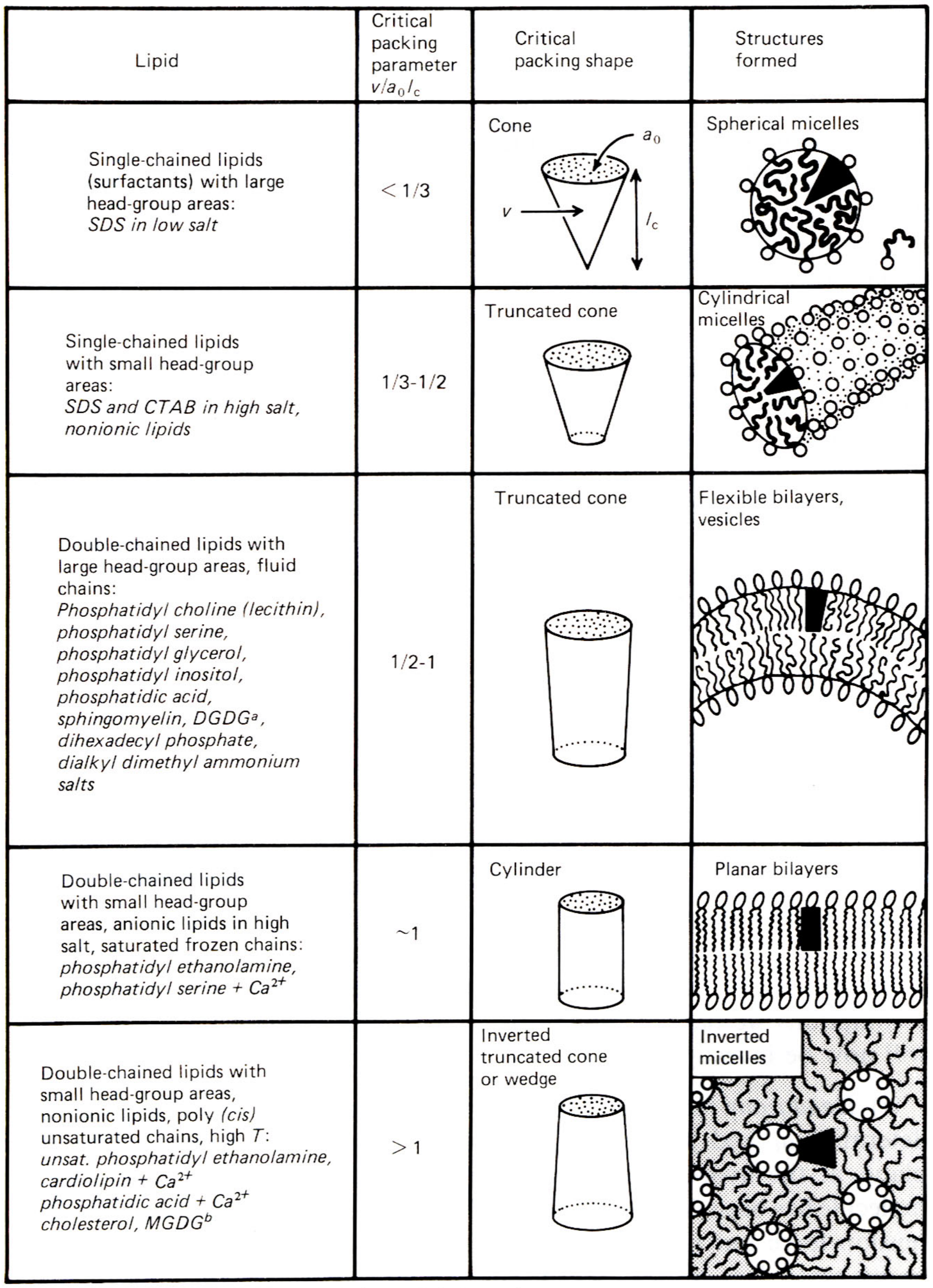

Lipid	Critical packing parameter $v/a_0 l_c$	Critical packing shape	Structures formed
Single-chained lipids (surfactants) with large head-group areas: *SDS in low salt*	$< 1/3$	Cone a_0 v l_c	Spherical micelles
Single-chained lipids with small head-group areas: *SDS and CTAB in high salt, nonionic lipids*	1/3-1/2	Truncated cone	Cylindrical micelles
Double-chained lipids with large head-group areas, fluid chains: *Phosphatidyl choline (lecithin), phosphatidyl serine, phosphatidyl glycerol, phosphatidyl inositol, phosphatidic acid, sphingomyelin, DGDG*[a]*, dihexadecyl phosphate, dialkyl dimethyl ammonium salts*	1/2-1	Truncated cone	Flexible bilayers, vesicles
Double-chained lipids with small head-group areas, anionic lipids in high salt, saturated frozen chains: *phosphatidyl ethanolamine, phosphatidyl serine +* Ca^{2+}	~1	Cylinder	Planar bilayers
Double-chained lipids with small head-group areas, nonionic lipids, poly *(cis)* unsaturated chains, high *T*: *unsat. phosphatidyl ethanolamine, cardiolipin +* Ca^{2+} *phosphatidic acid +* Ca^{2+} *cholesterol, MGDG*[b]	> 1	Inverted truncated cone or wedge	**Inverted micelles**

[a] DGDG, digalactosyl diglyceride, diglucosyl diglyceride.

[b] MGDG, monogalactosyl diglyceride, monoglucosyl diglyceride.

Figure 1.3: Packing shapes of lipids and formed structures [96].

[81], and tethered vesicles, which can either be purely lipidic or incorporate proteins [33].

Model membranes are extensively used to study phase separation in membranes and the nature of lipid rafts. GUVs that contain lipids with a high and a low melting temperature as well as cholesterol, exhibit coexisting liquid phases on the micron scale [90]. Additionally, in asymmetric membranes, as they occur in cells, domains can be found in a single leaflet only or even be suppressed by the interleaflet interaction with the other leaflet depending on its composition [48]. Studying phase behavior in model membranes builds a good foundation for understanding lipid rafts in model systems and cells [196, 56, 195, 125, 192].

In the field of membrane fusion model membranes are also important and are reviewed in [134]. Fusion processes in living cells are complex and involve many different proteins, but model membranes with several components are used to study the fundamental mechanics of membrane fusion [41, 32]. Lipid and content mixing of vesicles is studied using fluorescence video microscopy [36, 87, 156, 122] often also with Foerster Resonance Energy Transfer (FRET) [208] or Total Internal Reflection Fluorescence (TIRF) [95, 189]. Once the mechanics of pure lipid bilayer fusion is sufficiently known, the effect of fusogenic molecules [80, 4, 205] and fusion proteins like Soluble N-ethylmaleimide-sensitive factor Attachment protein REceptor (SNAREs) [35, 54, 86] can be systematically examined.

1.2.3 Biological Membranes

Plasma membranes are the most common cellular structure in animals and plants. A main function of the cell membrane is to separate the the cellular content from the external environment. Accordingly, the membrane is selectively permeable to ions and organic molecules like nutrients and waste products but also needs to maintain a difference in the chemical composition between the inside and outside of the cell. Cell membranes are involved in many other cellular functions such as motility, food entrapment and transport, energy transduction, immunological recognition, nerve conduction, and biosynthesis. Besides surrounding the cell as its entirety, membranes enclose many organelles such as the endoplasmatic reticulum, the Golgi apparatus, mitochondria and the nucleus to name a few. The composition of the membrane can depend highly on the cell type and its function.

Biological membranes are much more complex than most model membranes. They consist of phospholipids and glycolipids with various head groups, numbers of chains, chain lengths, degrees of saturation, and steroids. Many of the phospholipids and glycolipids are double-chained with 16 to 18 carbons per chain and one of them is unsaturated. As mentioned before, the unsaturation leads to a lower melting temperature and therefore ensures that the cell membrane will be in the fluid state at physiological temperatures which facilitates bending and spatial rearrangement. Biological membranes can contain more than 50 different proteins, which can be either integral or peripheral membrane proteins and their percentage of mass ranges between 25 and 75 %

[5].

1.3 Fusion Models

The fusion process can be studied in many ways, some of which are presented in this section. The continuum approach of the elastic model calculates the energy barriers for a postulated fusion pathway by approximating the membrane as elastic sheets, which are bent into different conformations along the fusion pathway. The energy barriers are computed by calculating the bending energy of the fusion intermediates. The elastic model is based on a minimal number of assumptions about the detailed structure of the system. The assumptions typically involve the elastic moduli of the lipid bilayer, stretching and tilting of the hydrocarbon chains and the modulus of the gaussian curvature. The elastic model can calculate the energy barriers for fusion provided the fusion pathway is assumed by the model. The fusion pathway, as it is commonly pictured, is shown in Figure 1.4. Before fusion, the bilayers are in close contact and a point-like protrusion in one layer initiates the fusion process. The formation of a stalk is the first intermediate step. The stalk then expands into a hemifusion diaphragm. Fusion completes when a fusion pore is formed.

Another continuum model uses a self-consistent field theory of the lipid bilayer and the solution to calculate an energy landscape. Necessary assumptions of the model are the self-consistent field parameters of the interaction between the lipid molecules themselves and with water molecules, need to be

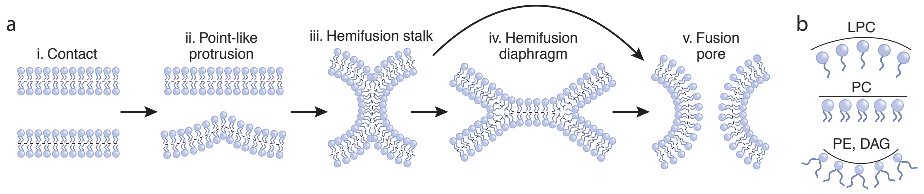

Figure 1.4: Fusion pathway as commonly agreed upon. a) Fusion is preceded by pre-fusion contact. A point-like protrusion is facilitating membrane contact and subsequently stalk formation. Stalk expansion leads to formation of a hemifusion diaphragm. Hole formation in the hemifusion diaphragm or the stalk initiates the formation of a fusion pore. b) Demonstration of spontaneous curvature of cone-shaped, inverted cone-shaped and cylindrical shaped lipids. Reprinted with permission [41].

known.

Computer simulations can have the advantage that the fusion pathway is not an input parameter, but a result of the given interactions between the atoms and molecules. Since there are no prior constraints on the fusion pathway, alternative fusion intermediates are observed, some of which break the axial symmetry. As long as the results strongly depend on the features of the specific computational model - parameters, limitations of simulation times and number of molecules - the results need to be taken with care [41].

1.3.1 Continuum Approach: Elastic Model

To form a connection between two membranes, the membranes' proximal monolayers must be strongly bent into an hourglass-shaped stalk, Figure 1.5A). The mathematical implementation of the elastic model, also called the stalk model, is based on the calculation of the elastic energy of the curved monolayers. The first mathematical analysis was performed in 1983 by Kozlov and Markin [113, 132]. The model was further developed by implementing additional features such as hydrophobic voids [194], fusion pore dilatation in stages [44], relative sliding of monolayers [46], and the role of membrane tension [45, 152]. All of these models had the same problem; the energy to form a stalk, up to hundreds of k_BT, was too high due to the elastic energy of the high curvature. Newer modifications of the stalk model, which is called the stress-free stalk [115], found a solution of the energy crisis [133].

The original Stalk Model

In the model from 1983 [113] the stalk was described as an hourglass-shaped connection between two membranes. The fusion of the proximal monolayers was later called the hemifusion stage and the fusion of both bilayers a fusion pore. The stalk could form after direct contact between two bulging defects in opposing bilayers that have an initial curvature c_{init}, and a spontaneous curvature c_0. It was assumed that the stalk has a circular shape as seen in Figure 1.5A). Here r is the marginal radius of the stalk, a is the shortest distance from the shown z-axis to the neutral surface of the bent layer and b is the distance from the z-axis to the point where the branches of the stalk become horizontal. The original model says that $b = a + r$. The coordinates of the stalk are x and z, the angle between the contour and the horizontal line is Ψ. According to Helfrich [84] the density of bending energy density in the

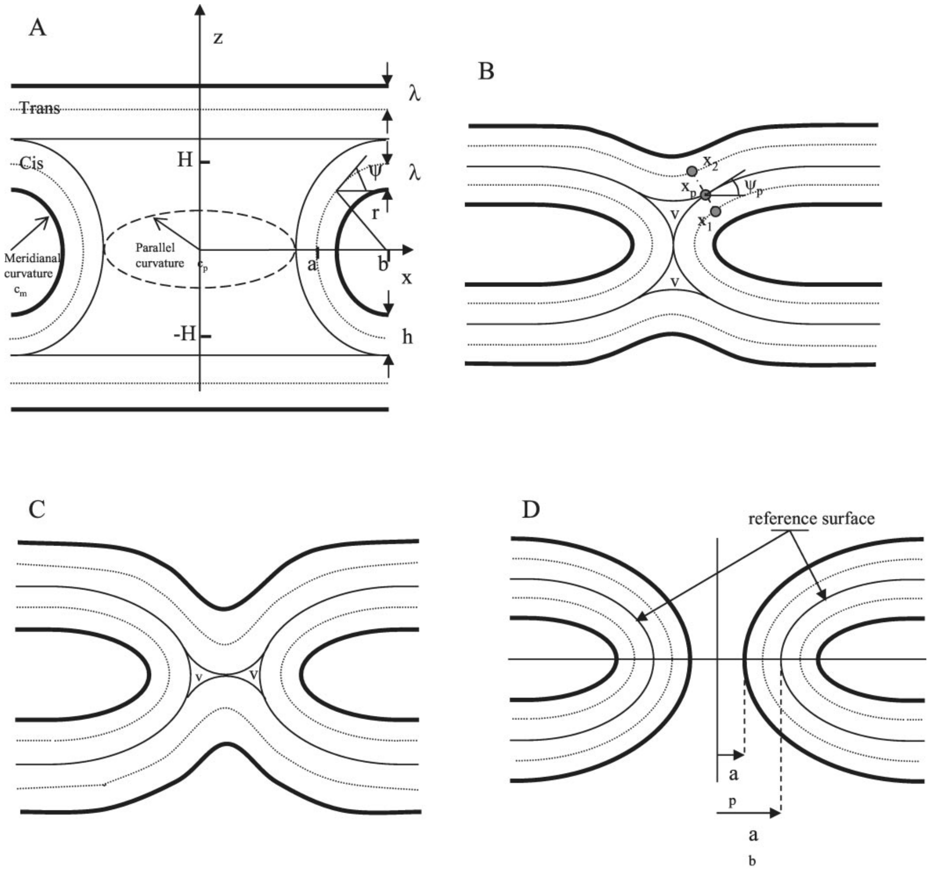

Figure 1.5: Fusion intermediates of the stalk model. Solid lines represent hydrophilic surfaces, thin lines hydrophobic ones and dotted lines neutral ones. A: Stalk. B: first hemifusion intermediate. C: Second hemifusion intermediate. D: Fusion pore. Reprinted with permission [133].

stalk is

$$w = \frac{\kappa}{2}(c_m + c_p - c_0)^2, \tag{1.5}$$

where κ is the bending rigidity, c_m and c_p are principal curvatures along the meridian and parallel to the body of revolution representing the stalk. The energy of stalk formation is given by the elastic energy of the stalk minus the initial elastic energy of the two planar layers

$$W_s = \pi\kappa \left[\int_{stalk} dA(c_m + c_p - c_0)^2 - \int_{stalk} dA(c_{init} - c_0)^2 \right]. \tag{1.6}$$

The first integral represents the bending energy of the stalk membrane and the second one the bending energy of the initial membranes. If the fusing membranes are planar, $c_{init} = 0$, which is a good approximation especially for larger vesicles. The energy of the stalk is

$$W_s = 2\pi\kappa \left[-4 - rc_0(4-\pi) + \pi a c_0 + \frac{s(r+a)^2}{r\sqrt{a(2r+a)}} \arctan\sqrt{\frac{2r}{a} + 1} \right]. \tag{1.7}$$

Without spontaneous curvature, c_0, the bending energy depends only on the ratio $\frac{r}{a}$. The energy has a minimum of $E_{min} = 3.79\kappa$, at $\frac{r}{a} = 1.671$. The minimum energy to form a monolayer stalk lies between $E_{min} = 45.5k_BT$ and $E_{min} = 37k_BT$, depending on the value of the bilayer rigidity $\kappa \approx 10^{-19}J$ [44] or $\kappa \approx 10k_BT$ [133].

The stress-free stalk

The stress-free stalk model, in contrast to the original stalk model, does not assume that the stalk has a circular shape. Instead, the shape is be calculated. It is considered to be a figure-of-revolution of some arbitrary curve. The shortest distance from the axis of revolution is a and b is the point where the stalk smoothly connects with the rest of the planar membrane. To simplify, the initial membranes are assumed to be planar. Another assumption is that the contour is smooth and has no sharp points. The curvatures of the stalk are given by [133]

$$c_p = \frac{\sin \Psi(x)}{x}, \tag{1.8}$$

$$c_m = \cos \Psi(x) \frac{d\Psi}{dx}. \tag{1.9}$$

In order for the stalk to be stress-free, the total curvature of the stalk has to be constant and is named c_{stalk}

$$c_p(x) + c_m(x) = c_{stalk}. \tag{1.10}$$

The stalk is stress free, if $c_0 = c_{stalk}$. The spontaneous curvature c_0 is depicted in Figure 1.4b). Depending on the packing parameter of a lipid, the monolayer these lipids form can either be planar or have positive or negative spontaneous curvature. The lipid DOPC for example has a slight negative spontaneous curvature of $c_0 = -0.11 nm^{-1}$, whereas DOPE has a larger negative curvature of $c_0 = -0.348 nm^{-1}$. Therefore, the exact shape of the stalk depends on the lipid composition. After some calculations the following expression for the contour of the stalk $z(x)$ is obtained

$$\frac{z}{a} = \int_1^{x/a} \left[\left[\frac{1}{2} a c_{stalk} t + \frac{1}{t} \left(1 - \frac{1}{2} a c_{stalk} \right) \right]^{-2} - 1 \right]^{-1/2} dt. \tag{1.11}$$

The parameter b can be calculated form the condition $\frac{dz}{dx} = 0$,

$$\frac{b}{a} = \sqrt{1 - \frac{2}{ac_{stalk}}}. \tag{1.12}$$

The ratio $\frac{b}{a}$ and the shape of the stalk $z(x)$ depend only on one parameter, which is the product $a \cdot c_{stalk}$. More important, the shape of the stalk is not a circular arc and its branches become horizontal towards its periphery. Furthermore $c_{stalk} = c_0$, which means that the total curvature of the stalk equals the spontaneous curvature everywhere and the stalk is stress-free. The shape of the stalk is independent of the membrane stiffness κ.

The bending energy of the stalk is $\frac{1}{2}\kappa(c_{stalk} - c_0)^2 A$, where A is the area of the stalk. If $c_{stalk} = c_0$, the stalk is stress-free and the bending energy is zero. If the spontaneous curvature of the membrane in the planar state is not zero, the initial energy has to be subtracted from the bending energy. Therefore, the energy for stalk formation is in general,

$$W_s = \frac{1}{2}\kappa A \left[(c_{stalk} - c_0)^2 - c_0^2\right]. \tag{1.13}$$

The resulting energy of a stress free stalk is $-\frac{1}{2}\kappa c_0^2 A$. To finish the calculation the area of the stalk, A, has to be calculated. Including the stalk area, the stalk energy is

$$W_s = 2\pi\kappa \cdot \int_1^{b/a} \frac{\left[(ac_{stalk} - ac_0)^2 - ac_0^2\right] t \cdot dt}{\sqrt{1 - \left[\frac{1}{2}ac_{stalk}t + \frac{1}{t}\left(1 - \frac{1}{2}c_{stalk}a\right)\right]^2}}. \tag{1.14}$$

The energies, calculated by this equation, are significantly lower than in the original stalk model as shown in reference [133]. With a spontaneous curvature of zero, the energy is $0k_BT$, but for larger curvatures a increases slightly, and the energy becomes positive, about a few k_BT. For negative spontaneous curvature, negative energies are calculated. They lie between 0 and $-10k_BT$, which is lower than the energies between $40k_BT$ and $25k_BT$ as predicted by the stalk model from 1983 [113].

Hemifusion

After stalk formation, the trans-monolayer starts peeling off of the cis-monolayer at the point x_p, which is the first step of hemifusion as shown in Figure 1.5B). The coordinates x_1 and x_2 are the projection from x_p to the middle of the trans- and cis-monolayers. The hemifusion structure can be divided into three parts: the wings, which is the part of the cis-monolayer beyond x_1; the neck, the part of the stalk for $x < x_1$ of the stalk; and the two dimples formed by trans monolayers for $x < x_2$. The total energy of the hemifusion state consists of the bending energy of these three hemifusion parts and the hydrophobic energy of the two voids, the area, enclosed by the stalk without any lipids.

The energy of the neck can be calculated by the same equation as the stalk energy using different bounds for the integration. For the energy calculation of the wings, the coordinates of the monolayer neutral surfaces are related to the reference surface. The reference surface is assumed to have a constant total curvature. The principal curvatures of the cis and trans can be calculated, and afterwards the length for the wings obtained. The energy can be calculated with the area differential. To estimate the energy of the dimple, a spherical shape is assumed. The total bending energy is the sum of the three parts and depends on the distance from the hydrophilic surface to its neutral surface, λ, the rigidity, κ, and the angle, Ψ_p. Ψ_p is the angle between a horizontal line and the line between the two monolayers at the point, where they begin to separate. If the total energy is calculated with $\lambda = 1nm$, $\kappa = 10k_BT$, and $\Psi_p = \pi/6$ [133], the total bending energy is (without spontaneous curvature) $W_h = 36.5k_BT$. The main contribution to this energy arises from the dimples, $W_d = 24.6k_BT$. With spontaneous curvature, the wing energy and the neck energy become negative, but the dimple energy is still positive and fairly large. The total energy decreases to $W_h = 24.6k_BT$. The energy of the voids W_v is calculated for different spontaneous curvatures. It depends on the angle Ψ_p and has a minimum of $50k_BT$ for $c_0 = 0$ and of $29k_BT$ for $c_0 = -0.1nm^{-1}$.

Completion of the fusion-fusion pore

After the hemifusion structure, the next step on the fusion pathway is the rupture of the trans monolayers and the completion of the fusion process by forming a fusion pore, Figure 1.5D). The simplest way to estimate the energy which is necessary to form a pore is to add the bending rigidities of the monolayers for the bilayer. This model is called a bilayer stalk and the equations from the monolayer stalk can be applied. The calculated energy is about $90k_BT$ [44], which is a gross underestimation because two monolayers are bent independently. If the elastic energy of the layers are calculated separately, the value increases to $150k_BT$.

The newer model calculates the energy with a constant total curvature. This results in a stress-free stalk for a monolayer, but in a bilayer, it is impossible to obtain a stress-free shape for both monolayers simultaneously. The bending energy of the bilayer is calculated using the equations of the hemifusion section. The interface between the two monolayers is the reference surface, which should have a constant total curvature, and the radius of the waist is a_b.

The energy depends on the constant curvature of the bilayer, the radius of the neck, the spontaneous curvature of both monolayers, and on the position of the neutral surface of each monolayer. The curvature of the reference surface is assumed to be negligibly small. If the monolayers have no spontaneous curvature, the bending energy is about $50k_BT$, much less than in the old model. If the monolayers have a negative spontaneous curvature, the energy decreases. For a curvature of $-0.05nm^{-1}$ the energy starts at about $25k_BT$ and decreases to negative values at a pore radius of $1.5nm$. When the spontaneous curvature is $-0.1nm^{-1}$, the bending energy is negative from the beginning and decreases with increasing radius.

1.3.2 Continuum Model: Self-consistent field theory

In contrast to the stalk model based on the phenomenological description relying on the macroscopic elastic moduli of the membrane, the field theoretic studies are based on the microscopic features of the lipid molecules in solution.

The system consists of an incompressible mixture of lipid molecules and solvent molecules in a volume V. Each of the n_a lipid molecules is described by a di-block polymer consisting of A hydrophilic and B hydrophobic monomers. The n_s solvent molecules are composed of hydrophilic homopolymers of A segments. f is the fraction of hydrophilic to hydrophobic monomers and the interaction strength is χ, the Flory-Huggins parameter. Since the partition function of a system of flexible chains cannot be solved analytically, the self-consistent field theory is taken as a good approximation. A description of the detailed calculations can be found in reference [105].

From hemifusion to fusion pores

Constraints in the solution of the field theory are implemented, according to the fusion pathway in Figure 1.4a), which is also used in the elastic model. Mainly, all solutions need to be axially symmetric and need to be invariant for reflection at the plane between the two opposing bilayers.

The obtained fusion pathway is defined in the following way: A first, unstable intermediate has to be overcome, to form a stalk. The energy, required to overcome this barrier, depends on the tension in the bilayers and the stalk radius, but is smaller than $13k_BT$, which is smaller than in the elastic theory. The height of the unstable barrier depends strongly on the radius and at very high tensions the energy barrier to form a stalk can vanish. The free energy of the metastable stalk depends only weakly on the radius, and the minimum in the free energy is so shallow, that these processes are easily reversible and fluctuate in size. The stalk intermediate expands into the hemifusion diaphragm. An increase in membrane tension and decrease in the head-group size favor this expansion. Before forming a fusion pore, the hemifusion area remains approximately constant. The barrier to hemifusion is considered the major limiting step in fusion, and has an energy barrier of 25 to $63k_BT$. For low tension in the membranes, the energy to expand a fusion pore increases. For small pore radii the low energy barrier can result in expansion and contraction of the pore, flickering can be observed. Usually the free energy of a fusion pore is less than the hemifusion intermediate [105].

In summary, this theory predicts the energy of stalk formation to be around $13k_BT$. The expansion to hemifusion strongly depends on f, the ratio of hydrophilic to hydrophobic monomers, which means the lipid composition. Hemifusion is stable in size before fusion. A slight negative curvature is necessary to form stalks, but if the curvature too large, the stalk becomes stable and fusion will be prohibited.

Stalk-Hole complex

An alternative fusion pathway, which breaks the axial symmetry, can also be analyzed by the self-consistent field theory. The fusion pathway has been observed in computer simulations [150], as mentioned in the following section. In brief, a stalk is built after the initial contact of the opposing bilayers. A hole which occurs in one of the membranes close to the stalk becomes surrounded by the stalk, by elongation in a wormlike manner. The hemifusion diaphragm consists of a single bilayer, not two monolayers from the different bilayers. Another hole in the hemifusion area finishes fusion. A different scenario could be a hole in each bilayer which get aligned by the stalk. Fusion is finished when the stalk has encircled the holes completely. The advantage of this fusion process is that transient leakage during fusion can be explained.

Bilayers are very stable, since one of their main functions in a cell is to keep the content of a cell confined. Therefore creating a hole in an isolated bilayer costs a lot of energy, on the order of $40k_BT$. Hole formation close to a stalk has a lower energy barrier, because the effective line tension in the part of the hole in contact with the stalk is decreased. After formation of the initially symmetric stalk, the stalk elongates in a wormlike fashion before a stalk-hole complex is formed. When the stalk-hole complex is formed, the free energy decreases, and the stalk almost completely encircles the hole. This fusion pathway also results in lower energy barriers for increasing membrane tension and increasing negative spontaneous curvature. Overall, the energy barriers obtained by this pathway are slightly smaller than the traditional ones, but just about few k_BT. With constant tension, the expansion of a fusion pore can be obtained without an additional energy barrier as already seen for the symmetric fusion intermediates [104].

To summarize, this alternative fusion pathway also exhibits two main energy barriers. The first one is due to forming the initial symmetric stalk and the second one for building the stalk-hole complex. The energy intensive step in symmetric fusion is the expansion to a hemifusion diaphragm. The equivalent in the asymmetric fusion pathway is the wormlike elongation of the stalk and the formation of a hole in its periphery. The energy values are comparable, but slightly lower for the stalk-hole complex.

1.3.3 Computer Simulations

An advantage of simulating membrane fusion over theoretical models is that the fusion pathway is not an input parameter but results from the simulation. In this way, unpredicted information about the fusion pathway can be revealed. The calculations require the same microscopic information about the fusion system as in self-consistent field theory. The disadvantage of simulations is that it is not certain, if the observations are representative of biological membrane fusion, because the architecture of the components in the simulated system may differ greatly from those of biological systems. Additionally, simulations are limited in size and simulated time. A comparison of the simulated results with experiment and theory can lead to clarification.

Monte Carlo simulations of fusion reveal that two different pathways of fusion can occur. The used coarse-grained lattice model has already investigated the self-assembly of lipidic structures successfully. Lipid molecules, with eleven hydrophilic and twenty-one hydrophobic segments were dispersed in solvent molecules of thirty-two hydrophilic segments. The bond-fluctuation model was used for the polymer chains. Segments from the same molecule were not allowed to interact with themselves. Like segments from different molecules felt an attractive square well potential and unlike segments a repulsive potential. Each contact changes the energy of the molecules and diffusion was allowed to take place without crossing. As a result, two asymmetric fusion pathways were observed. The mechanism of fusion, which can be seen in the simulation, begins with a stalk, as it is described in the stalk model. But what follows after is different from the stalk model, the fusion intermediates break the axial symmetry. The stalk destabilizes the bilayers by catalyzing the creation of small holes. Hole formation could be caused by a reduction of the energy per unit length of the edge of a hole, when the edge is adjacent to a stalk. For the same reason, once a hole appears, the stalk will try to surround the hole formed in one bilayer. Two different ways of building a complete fusion pore were observed. In the first one a hole appears in one bilayer and the stalk rapidly surrounds it. This seems similar to hemifusion, which consists of two trans monolayers of the fusing membrane, but in contrast, the observed diaphragm is made of one of the pre-existing bilayers of cis and trans leaves. In the second possibility, a hole appears in one bilayer and before the stalk can surround it, a second hole appears in the other bilayer. The stalk tries to surround them both and aligns them in doing so to complete fusion. Both methods differ only on whether the hole in the second bilayer appears before or after the stalk completely surrounds the first hole. Once the fusion pore has formed, it expands driven by the reduction in surface tension. The growth of the fusion pore ends as the pore reaches its optimum size. Both pathways allow transient leakage of content [150].

A simulation in atomic detail shows the fusion process of two vesicles, which are already connected with a stalk. In approximately $2ns$ the stalk expands to a hemifusion intermediate, which seems to be metastable and lasts around $11ns$. One-out-of-six fusion events also shows transient pores close to the stalk. Subsequently, lipid mixing occurs and the formation of a fusion pore can be initialized by a single lipid in the interior of the hemifusion diaphragm [110]. Dissipative particle dynamics simulations also reveal asymmetric stalk expansion. Additionally, an energy barrier between the stalk and the trans-monolayer contact could be found. The effect of the curvature of the bilayers has been examined [124]. Lipid rearrangements took place within $100ps - 2ns$ after removing most of the water between the bilayers. This could initiate fusion as simulated in reference [161].

Simulations also help to analyze the fusion process while systematically changing parameters of the system, like the tension in the membranes [67, 74, 193]. Tension in the bilayers can induce fusion, as shown for $28nm$ vesicles in a mesoscopic simulation [193]. Fusion was finished for all of almost one hundred fusion events in less than $350ns$.

1.3.4 Protein induced membrane fusion

In the continuum stalk model, the lipid membrane is treated as a homogenous elastic sheet. This was successful in estimating the energy landscape for fusion, but the predicted activation energies were too high, especially in the original stalk model. In biological fusion, proteins like SNAREs help to bring two membranes in close contact and can apply force and thereby lowering the energy barrier for fusion. But as seen in Figure 1.6, the application of force is not the only possibility for how proteins can induce fusion.

Figure 1.6a) demonstrates that fusion could be realized by proteinaceous fusion pores. They supposedly have a gap junction-like structure and consist of oligomeric trans-membrane proteins with a hydrophilic channel in the center that opens at the onset of fusion. The subunits assemble into ring-like oligomers and open upon membrane contact. Trans complexes form and open a central aqueous fusion pore via homophilic or heterophilic interactions, involving the cytoplasmic faces of the proteins. The subunits need to dissociate radially for pore enlargement, with phospholipids invading the space between them. Finally, the trans connection between the protein subunits breaks up to allow fusion to be completed. In fence models, Figure 1.6b), the formation of a oligomeric ring of transmembrane proteins is also required, but in comparison to the proteinaceous pore model, a patch of lipids remains in the center of the ring. The fusion process is essentially lipid-based, and the fence posts restrict

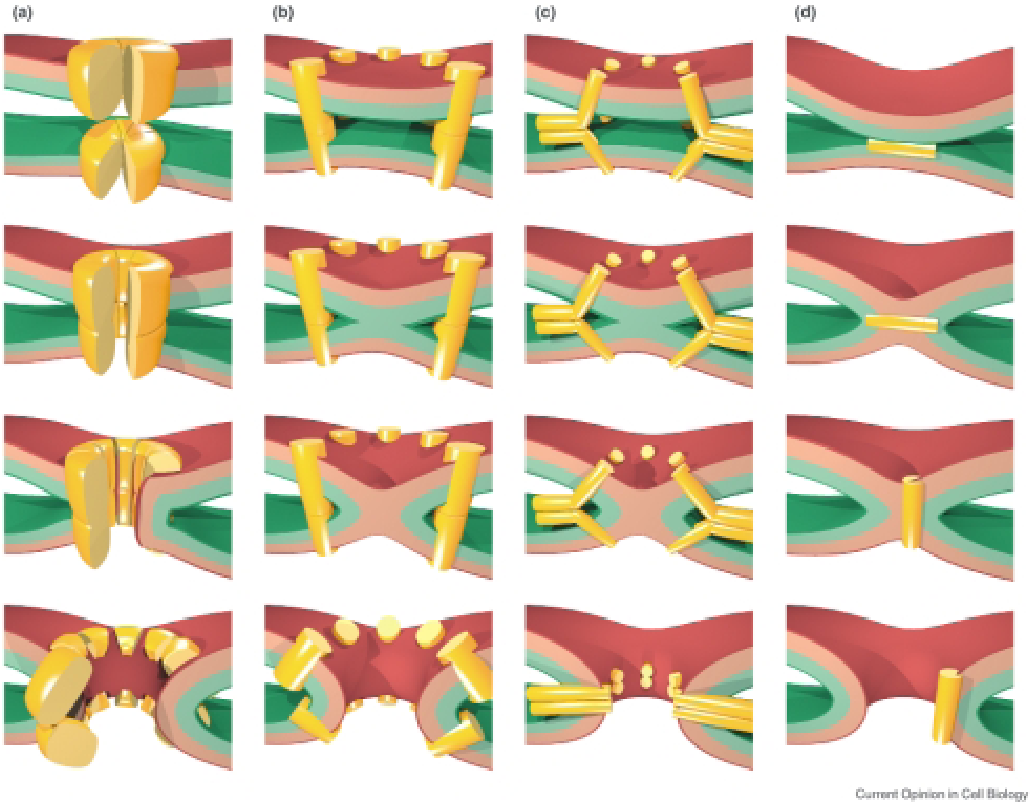

Figure 1.6: Schematic overview of four models for protein-mediated membrane fusion: a) Proteinaceous fusion prores. b) Fence model. c) Scaffold model. d) Peptide-induced fusion. Reprinted with permission [98].

the lipid flow and the composition. This fusion model has been considered for some viral fusion proteins. In the scaffold model [146], Figure 1.6c), the proteins bring the membranes into close apposition to overcome the activation energy barrier, possibly by applying mechanical forces. The model does not require, but also not preclude, that the scaffold proteins span the membrane. The SNARE protein is an example for the scaffold model. SNAREs are found in eukaryotic cells and exist of 60 to 70 amino acids. Fusion requires complementary sets of SNARE proteins to be present in both membranes. The assembly into trans-complexes ties the membranes closely together and induces fusion. Another model is the local perturbation model (Figure 1.6d)). Fusion is facilitated by perturbations in the membrane, since it more easily leads to a possible rearrangement into a fusion intermediate. Spontaneous fusion can be caused by different amphiphilic peptides, which have found to be part of many viral fusion proteins, since they induce disorder in the membranes [98].

1.4 Outline and research objectives

The first part of this dissertation presents a novel assay for the observation and characterization of single fusion events including their intermediates with high temporal and nanometer spatial resolution using a photonic force microscope [62]. To induce fusion, a membrane coated silica particle is trapped and brought to the membrane covered glass surface. Once sufficiently close, the particle randomly collides with the surface and initiates a fusion event. The laser beam of the trap is also used to measure the position of the trapped particle in three dimensions with nanometer-precision and 10 microseconds temporal resolution. We analyze fusion events by calculating three-dimensional position histograms and the viscous drag on the particle. The probability distributions experience a characteristic reduction in volume as fusion progresses, while the viscous drag increases with increasing contract area between the two membranes. This allows us, for the first time, to describe the timescales of the fusion process at an unprecedented temporal resolution while simultaneously characterizing the fusion intermediates at the nanometer scale. Additionally, we can give an estimate for the stalk radius and the energy barrier for hemifusion for single vesicle fusion events. The assay can further be used to systematically analyze the changes in the fusion behavior due to lipid composition, stress, curvature, fusion proteins and peptides.

The last chapter describes the attempt of combining the PFM fusion assay with a fluorescence lipid mixing assay. Monitoring lipid mixing allows for an additional parameter, the fluorescent signal of the bead, to distinguish fusion intermediates. Additionally, this could lead to insight about the timing of establishing a connection and lipid mixing.

Chapter 2

Background and Theory

2.1 Theory of Brownian motion

Brown first systematically studied the motion of small particles under the microscope in 1827 [27]. In acknowledgment of his work, the diffusion of small particles is called Brownian motion. In one of his famous essays of 1905, Einstein gave a mathematical and physical description of the motion of colloidal particles in solution [57].

Since the work described in this dissertation is fundamentally based on diffusion, the next chapter gives an overview over Brownian motion, the different modes of motion and how particles diffuse when they are embedded in a free or supported membrane.

2.1.1 Simple Brownian Motion

In 1905 Einstein was the first to explain the diffusion of small particles in a suspension, with a molecular-kinetic theory of heat [57]. He described the motion of the particles with fundamental equations of thermodynamics.

The assumptions are that the particles are suspended irregularly- dispersed in a fluid, that they are in dynamic equilibrium, and that the force,

K, which acts on the particles, depends on the position but not on time. For simplicity, the force should only act in one dimension. According to thermodynamics, the condition of equilibrium implies that the variation of the free energy δF goes to zero for a small displacement

$$\delta F = \delta E - T\delta S = 0. \tag{2.1}$$

With the introduction of boundary conditions, the condition for equilibrium can be rewritten as

$$-K\nu + \frac{RT}{N_A}\frac{\partial \nu}{\partial x} = 0, \tag{2.2}$$

where ν is the number of suspended particles, R the gas constant, N_A is Avogadro's number and T is the absolute temperature. According to equation (2.2), the equilibrium condition is a superposition of two opposite processes: the motion of the particles by the force K and the random movement caused by thermal molecular motion. Assuming that the particles are spherical with a radius a, the average velocity $\bar{v}$ caused by the force is

$$\bar{v} = \frac{K}{6\pi\mu a}, \tag{2.3}$$

with μ being the viscosity of the surrounding medium and D the diffusion constant. $-D\frac{\partial \nu}{\partial x}$ particles are passing through a unit area per unit of time. For dynamic equilibrium, the following condition must be fulfilled:

$$\frac{\nu K}{6\pi\mu a} = D\frac{\partial \nu}{\partial x} \tag{2.4}$$

From equations (2.2) and (2.4) the diffusion equates to

$$D = \frac{RT}{N} \cdot \frac{1}{6\pi\mu a} = \frac{k_B T}{6\pi\mu a}. \tag{2.5}$$

Looking closer at the random motion, we consider at a time interval, τ, which is chosen to be very small compared to the time of observation, but large enough for the motion between two time steps to be uncorrelated. In a suspension of n particles, in the time interval τ, the coordinates of the individual particles change by Δ, whereupon Δ has a different negative or positive value for each particle. Supposedly, the number of particles dn, which are displaced in the time interval τ between and $\Delta + d\Delta$, can be expressed as

$$dn = n\varphi(\Delta)d\Delta, \tag{2.6}$$

with the following conditions

$$\int_{-\infty}^{\infty} \varphi(\Delta)d\Delta = 1 \tag{2.7}$$

$$\varphi(\Delta) = \varphi(-\Delta). \tag{2.8}$$

To examine how the diffusion constant depends on φ, we analyze how $v = f(x,t)$ the number of particles per volume changes at time $t = \tau$. With the properties of equation (2.6), the number of particles between x and $x + dx$ is

$$f(x, t+\tau)dx = dx \cdot \int_{-\infty}^{\infty} f(x+\Delta)\varphi(\Delta)d\Delta. \tag{2.9}$$

Since τ and Δ are small, $f(x, t + \tau)$ and $f(x + \Delta, t)$ can be expanded with respect to τ and Δ up to first and second order.

$$f+\frac{\partial f}{\partial t}\tau = f\int_{-\infty}^{\infty}\varphi(\Delta)d\Delta+\frac{\partial f}{\partial x}\int_{-\infty}^{\infty}\Delta\varphi(\Delta)d\Delta+\frac{\partial^2 f}{\partial x^2}\int_{-\infty}^{\infty}\frac{\Delta^2}{2}\varphi(\Delta)d\Delta. \quad (2.10)$$

The second integral on the right hand side vanishes, since $\varphi(\Delta) = \varphi(-\Delta)$. Together with equation (2.8) this can be simplified to

$$\tau\frac{\partial f}{\partial t} = \frac{1}{2}\frac{\partial^2 f}{\partial x^2}\int_{-\infty}^{\infty}\Delta^2\varphi(\Delta)d\Delta. \quad (2.11)$$

With the diffusion coefficient

$$D = \frac{1}{\tau}\int_{-\infty}^{\infty}\frac{\Delta^2}{2}\varphi(\Delta)d\Delta \quad (2.12)$$

we get the differential equation for diffusion

$$\frac{\partial f}{\partial t} = D\frac{\partial^2 f}{\partial x^2}. \quad (2.13)$$

Making further assumptions about the probability distribution of the displacements of the particle within a unit of time, the function of the particle, which can be found on a place x for a certain time t, can be written as

$$f(x,t) = \frac{n}{\sqrt{4\pi Dt}}\cdot e^{-\frac{x^2}{4Dt}} \quad (2.14)$$

With that equation, the mean square displacement, $MSD = \langle(x(t') - x(t' - t))^2\rangle$, of a particle in one dimension can be written as

$$MSD = \overline{x^2} = 2Dt \quad (2.15)$$

If the calculations are made in two dimensions the mean square displacement increases by a factor of 2, $MSD_2 = 4Dt$, and in three dimensions, a factor of 3, $MSD_3 = 6Dt$.

2.1.2 Modes of motion

So far we have only discussed normal diffusion, however in nature different modes of motion besides normal diffusion can be observed, namely directed motion, anomalous diffusion and confined motion. For example, directed motion is observed for transport with molecular motors [31] and anomalous diffusion in yeast cells as shown in the second part of this dissertation. Confined motion is discussed in more detail in the next section, since it applies to diffusion within the harmonic trapping potential. The MSD in two-dimensions can be derived for the different modes of motion as reviewed in [183].

$$MSD = 4Dt \qquad \text{normal diffusion} \tag{2.16}$$

$$MSD = 4Dt^{\alpha} \qquad \text{anomalous diffusion} \tag{2.17}$$

$$MSD = 4Dt + (vt)^2 \qquad \text{directed motion + diffusion} \tag{2.18}$$

$$MSD \simeq \langle r_C^2 \rangle \left[1 - A_1 \exp\left(\frac{-4A_2Dt}{\langle r_C^2 \rangle} \right) \right] \qquad \text{confined motion} \tag{2.19}$$

Here, α is the anomalous diffusion exponent, v is the velocity, $\langle r_C^2 \rangle$ the corral size, A_1 and A_2 are constants determined by the corral geometry. Note that the diffusion constant in equation (2.18) is not the standard diffusion constant as defined in equation (2.15), as it has different dimensions.

$$MSD = 4Dt \qquad [D] = L^2 \cdot T^{-1} \tag{2.20}$$

$$MSD = 4Dt^{\alpha} \qquad [D] = L^2 \cdot T^{-\alpha} \tag{2.21}$$

The time-dependent diffusion constant in equation (2.18) is named the generalized diffusion coefficient [141].

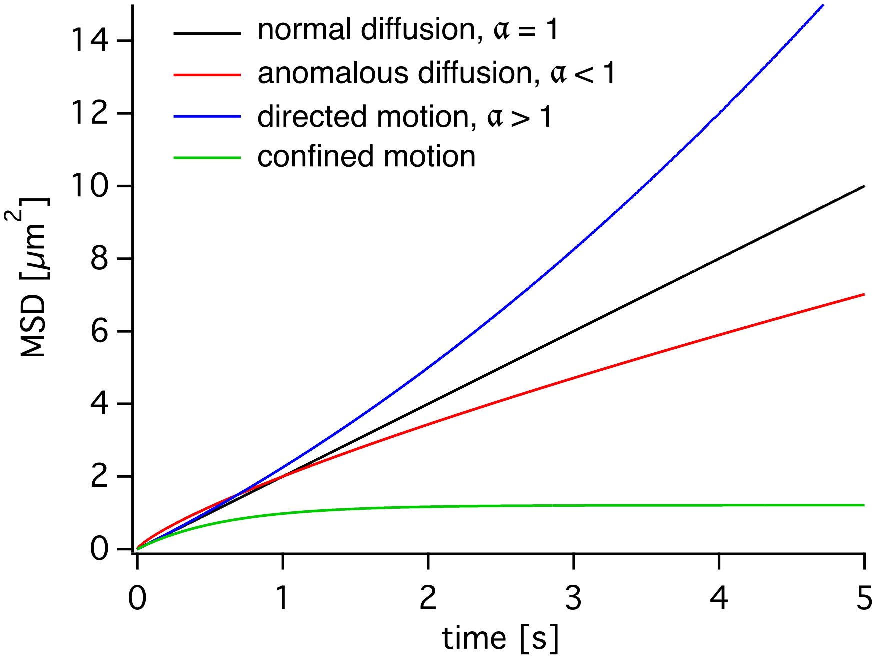

Figure 2.1: Modes of motion. If the MSD is plotted against time, normal diffusion is described by a straight line with a slope of $4D$ in two dimensions. Alpha equals one. For values of alpha less than one, the resulting motion is called anomalous diffusion. For longer times, the particle has a smaller average displacement than normal diffusion. For directed motion alpha is larger than one and on large time scales the MSD is significantly larger than the one for Brownian motion. In the case of confined motion, normal diffusion is observed on short time scales. The confinement of the particle sets a limit for the range of diffusion on longer time scales. Therefore the MSD for confined motion will plateau for long times. Parameters used to create this graph: $D = 0.5\mu m^2/s$, $\alpha = 0.78$, $v = 0.5\mu m/s$, $\langle r_c^2\rangle = (1.1\mu m)^2$, $A_1 = 1$, and $A_2 = 1$.

Figure 7.3 pictures the MSD over time for the different modes of motion. If the MSD is plotted against time, normal diffusion is described by a straight line with a slope of $4D$; alpha equals one. If alpha is less than one, the resulting motion is called anomalous subdiffusion, which is slower than normal diffusion. For longer times, the particle has a smaller average displacement than normal diffusion. For directed motion alpha is larger than one and on large time scales the MSD is significantly larger than the one for Brownian motion. In the case of confined or corralled motion, normal diffusion is observed on short time scales, but on longer time scales the confinement of the particle sets a limit for the range of diffusion. Therefore the MSD for confined motion will plateau for long times.

2.1.3 Brownian Motion in a harmonic potential

The diffusive motion as observed within optical tweezers is confined by the harmonic potential of the optical trap. The potential appears as an additional term in the equation of motion of the trapped particle. The forces acting on the trapped particle in solution are an inertial force, which depends on the mass of the particle and the acceleration, a viscous force which is proportional to the velocity of the particle and the viscous drag γ, and a force which is linear with the displacement of the particle, caused by the harmonic potential of the trap with the stiffness κ. The random motion due to thermal forces is described by a function ζ, which has a zero mean and no memory;

therefore it is random.

$$\langle \zeta(t) \rangle = 0 \tag{2.22}$$

$$\langle \zeta(t)\zeta(t') \rangle = \delta(t - t') \tag{2.23}$$

The equation of motion of the particle is

$$m\ddot{x}(t) + \gamma\dot{x}(t) + \kappa x(t) = \zeta(t)\sqrt{2k_B T\gamma}. \tag{2.24}$$

According to equation (2.15), the mean square displacement of a diffusing particle in solution rises linearly with time. This can be observed on short timescales for small displacements of the trapped particle. As soon as the particle's displacement from the trap center is noticeable, it can feel the restoring force of the trap and gets pulled back to the center. Initially, the mean square displacement rises linearly and eventually plateaus to a maximum value of displacement as shown in Figure 7.3. The black line shows the expected motion of a particle diffusing freely in solution and the green line shows the mean square displacement of a particle in an optical trap. For small time intervals, which also means small displacements, both curves overlap. For larger times the particle is limited by the trap and the MSD starts deviating from a straight line. Eventually, the particle explores the whole trapping volume and its motion cannot exceed the boundaries of the trap.

The maximum value of the mean square displacement can be used to relate the stiffness of the trap to the MSD, according to the equipartition theorem [63]

$$\tfrac{1}{2}\kappa\langle\Delta x^2\rangle = \tfrac{1}{2}k_BT. \tag{2.25}$$

2.1.4 Diffusion in proximity to surfaces

If a particle diffuses in proximity to a surface, closer than ten times the particle radius, the viscous drag on the particle increases and the equation for the Stokes' drag needs to be modified. For a particle with radius a whose center is a distance h away from the surface, the Stokes' drag γ gets a correction factor ϵ

$$\gamma = 6\pi\mu a\epsilon. \tag{2.26}$$

The correction factor ϵ is a function of a/h. The exact derivation, expression and discussion can be found in [79]. The correction is different depending on the direction of motion with respect to the surface. For motion perpendicular to the surface $\epsilon_\perp$ up to the third order, the correction is

$$\epsilon_\perp = \frac{1}{1 - \frac{9}{8}\left(\frac{a}{h}\right) + \frac{1}{2}\left(\frac{a}{h}\right)^3}. \tag{2.27}$$

For the motion of the particle parallel to the surface, the factor $\epsilon_\parallel$ is given by the following expression up to the order $(r/h)^5$

$$\epsilon_\parallel = \frac{1}{1 - \frac{9}{16}\left(\frac{a}{h}\right) + \frac{1}{8}\left(\frac{a}{h}\right)^3 - \frac{45}{256}\left(\frac{a}{h}\right)^4 - \frac{1}{16}\left(\frac{a}{h}\right)^5}. \tag{2.28}$$

The change of the drag on the particle needs to be considered for the calibration of the optical trap. Either these equations need to be incorporated into the calibration routine, or the calibration has to be done at least ten times the particle radius away from the coverslip, so that the particle can diffuse without feeling the effects of the surface boundaries. Additionally, this effect can be measured experimentally when the particle approaches the surface. It appears as a reduction of the diffusion constant of the particle in the membrane fusion experiments during the approach to the coverslip.

2.1.5 Diffusion in free-standing membranes

Saffman and Delbrueck have analyzed the Brownian motion of cylindrical particles embedded in a membrane bilayer [180], comparable to proteins and lipids diffusing within a membrane.

The membrane is assumed to be an infinite plane sheet of viscous fluid with a viscosity μ_m, according to the fluidity of the lipid bilayer. The bilayer is surrounded by a less viscous fluid, water or an aqueous solution with viscosity μ_w. Assuming the diffusing particle is a cylinder with a radius a and height h_m, equal to the thickness of the membrane, the translational mobility b_T of the diffusing particle free in solution is

$$b_T = \frac{1}{6\pi\mu_w a}. \tag{2.29}$$

There are different possibilities to calculate the mobility of a cylinder diffusing within the membrane. The viscosity of the surrounding solution could be neglected or the inertia of the viscous fluid could be taken into account, but this results in contradictions or unsatisfactory estimations. The following three alternatives result in a reasonable solution. The first restricts the membrane sheet to a finite size, with a radius much larger than the radius of the particle, which is placed in the center of the sheet. With no-slip boundary conditions on the particle's surface, the resulting mobility is

$$b_T = \frac{1}{6\pi\mu_m h_m}\left(\log\frac{R}{a} - \frac{1}{2}\right). \tag{2.30}$$

The second approach is to consider the viscosity of the solution. The amphiphilic structure of the molecules prohibits shear across the membrane, which implies that the velocity field inside the layer is two-dimensional, which is taken into account. Besides that, no-slip boundary conditions at the surfaces between the fluids ensure that the flow of the different fluids are coupled. A flow in one induces a flow in the other. That results in a translational mobility of

$$b_T = \frac{1}{4\pi\mu_m h_m}\left(\log\frac{\mu_m h_m}{\mu_w a} - \gamma\right), \tag{2.31}$$

with $\gamma = 0.5772$ being the Euler constant.

The third possibility uses irreversible thermodynamics to calculate the MSD from the Langevin equation, with the drag given by the slow viscous equations of unsteady flow. Standard methods of irreversible thermodynamics obtain a translational mobility of

$$b_T = \frac{1}{4\pi\mu_m h_m}\left(\log\frac{4\mu_m t}{\rho a^2} - \gamma - 1\right). \tag{2.32}$$

A logarithmic dependency can be observed on the radius of the particle. The work of Peters and Cherry on bacteriorhodopsin in lipid bilayers [164] confirms this theory experimentally.

2.1.6 Diffusion in supported membranes

All three approaches of the Saffman-Delbrueck theory to calculate the diffusion constant assume that the lipid layer is surrounded on both sides by a medium with lower viscosity. In many applications like the one presented in this thesis, the bilayer is supported by a solid surface like silica or glass only separated by a thin lubricating layer of the surrounding media of about $0.4-3nm$ thick [144, 102, 158, 18]. The membrane is no longer free in solution but strongly coupled to the solid support, which changes the properties of diffusion. Sackmann and Evans introduced in 1988 a phenomenological drag relation to characterize the coupling of the bilayer to a rigid substrate. With a linear velocity dependence relation of the drag, the inertialess equations of motion for flow in the membrane can be solved for steady translation and rotation of a cylindrical particle [59].

The transport of momentum from the two-dimensional membrane into the third dimension, which is dominated by the presence of the substrate, can be modeled by an interfacial drag b_s, which is proportional to the velocity of the membrane

$$b_s = \frac{\mu_w}{h}. \tag{2.33}$$

The thickness of the lubricating layer between the membrane and the rigid substrate is h. b_s is also called a surface frictional coefficient. Since the membrane has a small area compressibility, the divergence in the velocity field in the two-dimensional plane is zero. For a steady inertialess flow the Stokes approximation to the momentum equation is valid. Since the membrane is not strongly bound to the substrate, one can assume that the interfacial drag is proportional to the local velocity of the membrane relative to the substrate. A dimensionless parameter ϵ is introduced, which depends on the radius, a, of the diffusing particle, the interfacial drag b_s and the two dimensional viscosity of the membrane η_m

$$\epsilon = a\sqrt{\frac{b_s}{\eta_m}}. \tag{2.34}$$

The necessary coefficients are determined by no-slip boundary conditions around the diffusing disc. For uniform translational motion with a velocity v_0, the membrane stress resultants can be calculated, and by integrating around its perimeter the drag force F_D can be determined

$$F_D = \pi\eta_m\epsilon v_0\left[\epsilon + \frac{4K_1(\epsilon)}{K_0(\epsilon)}\right]. \tag{2.35}$$

$K_0(\epsilon)$ and $K_1(\epsilon)$ are modified Bessel functions of the second kind of order zero and one respectively. With that, the resulting drag coefficient λ_T for translation is

$$\lambda_T = 4\pi\eta_m\left[\tfrac{1}{4}\epsilon^2 + \frac{\epsilon K_1(\epsilon)}{K_0(\epsilon)}\right]. \tag{2.36}$$

For the intrinsic drag of the disc to the substrate, the drag coefficient can be rewritten as

$$\lambda_T = 4\pi\eta_m \left[\tfrac{1}{4}\epsilon^2 \left(1 + \frac{b_p}{b_s}\right) + \frac{\epsilon K_1(\epsilon)}{K_0(\epsilon)}\right]. \tag{2.37}$$

The calculation for the rotational drag coefficient is analogous to the translational drag coefficient. Since it is smaller than the translational drag coefficient, it will be neglected. The derivaion can be found in [59].

For a thin lubricating layer of bulk liquid between the membrane and the substrate, ϵ needs to be modified. The dependence of the velocity field is dominated by the membrane flow field, which decreases linearly across the liquid layer. The frictional coefficient b_s is expressed as

$$b_s = \frac{\mu_w}{h}. \tag{2.38}$$

With this frictional coefficient and the relation between the 3D viscosity and the 2D viscosity, $\eta_m = h_m \mu_m$, the dimensionless parameter ϵ can be rewritten as

$$\epsilon = a\sqrt{\frac{\mu_w}{h\eta_m}}. \tag{2.39}$$

As demonstrated the coupling to the substrate depends on two additional forces: the friction force between the membrane and the solid support induced by the velocity field of the membrane and a friction force between the diffusing particle and the support. The logarithmic dependency of the Saffman-Delbrueck equation is valid as long as the membrane is not coupled to a substrate. The logarithmic dependency implies that the diffusion constant of larger particles like proteins is similar to the one of smaller lipids. For membranes which couple to a substrate or are immobilized, the diffusion of large molecules is orders of magnitude faster than expected by the theory of Saffman-Delbrueck. This shows that the proportionality of the diffusion constant to a^{-2} for coupled membranes is reasonable [179].

2.2 Optical Traps

The radiation pressure of light was initially thought only to be important in astronomy, where high intensities and huge distances magnify the relatively small effect. After the invention of the laser, Ashkin first showed in 1970 that the light from continuous coherent light beams with high intensity and high gradients are theoretically able to create a force, around $10^{-8}N$ on a micron-sized bead [9]. This appears to be relatively small, but since the mass of the particle was very little, the acceleration on the particle was about $10^5 g$, which was large enough to accelerate, deflect, guide and trap small particles [10]. Since this first proof-of-principle and the steady improvement of lasers, trapping efficiency was improved and various types and shapes of traps were created, as reviewed in [155].

Optical traps are an essential tool in physics and biology. Since the first trapping of small dielectric spheres, many applications have been explored. In physics, optical traps are used to trap and cool atoms to a temperature of around a milli-Kelvin. Theoretical concepts in physics, like Bose-Einstein condensation, could finally be observed [10]. Optical tweezers have a great impact on biology and biophysics, because forces in the range of a pico Newton can be applied to particles on the scale of a micrometer, and their position can be detected with nanometer-to-angstrom resolution [155], a scale on which many processes in the cell occur. Various properties of biological material can be measured such as the force exceeded by molecular motors [50, 75], mechanical properties of microtubuli [106] and actin filaments or DNA [20]. Whole viruses, bacteria [11]or cell organelles can be trapped, and since the cells still continued to multiply when using an infrared laser, it could be shown that the method causes little damage to a cells. Ashkin reviews applications and experiments with optical traps in reference [10].

The following chapter focuses on the single-beam gradient force optical trap, and how it is used in the experimental setup. A single laser beam with a Gaussian profile (TEM_{00} mode) is tightly focused by an objective lens with high numerical aperture, to create an intensity gradient and a trapping potential in all three dimensions. The size of the trapped particle can be much larger, much smaller or on the order of the laser wavelength. Depending on the size of the particle different theories can be applied to explain the trapping force.

2.2.1 The Mie-Scattering regime

The Mie solution to Maxwell's equation can be used to describe the scattering of electromagnetic radiation by a sphere such as a particle in an optical trap. For particles which are much larger than the wavelength of the laser ray optics can be applied. Figure 2.2 shows the scheme of the forces acting on a dielectric particle which is trapped in a medium with a lower index of refraction than the sphere. The incident light gets scattered by the particle and therefore changes its momentum. According to Newton's third law, that interaction transfers momentum of the same amount with opposite sign to the bead. Since the intensity of the light in the center of the trap is higher than on the edges, the net force always pushes the particle back toward the center of the trap. As a result of the scattering force the trapping point lies slightly beyond the focal point on the optical axis [155].

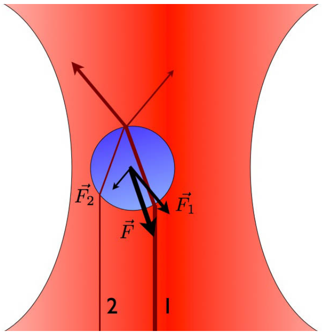

Figure 2.2: Ray optics description of trapping a dielectric particle. The sum of the forces always restores the center of the bead towards the center of the trap.

2.2.2 The Rayleigh-Scattering regime

If the size of the particle is much smaller than the wavelength, the Rayleigh scattering condition is satisfied. In this regime the particle acts like a point dipole. The scattering force is due to absorption and re-radiation of light by the dipole, and the scattering and gradient force components are readily separated.

The scattering force points in the direction of propagation of the incident light and is proportional to the light intensity. The scattering force for a bead of radius a is

$$F_{scatt} = \frac{I_0 \sigma n_m}{c} \tag{2.40}$$

$$\sigma = \frac{128\pi^5 a^6}{3\lambda^4} \cdot \left(\frac{m^2-1}{m^2+2}\right)^2, \tag{2.41}$$

where I_0 is the intensity of the incoming light, σ is the scattering cross section of the sphere, n_m the index of refraction of the surrounding medium, c the speed of light in vaccum, $m = \frac{n_p}{n_m}$ the ratio of the index of refraction of the particle to the medium, and λ is the wavelength of the laser.

The time-averaged gradient force arises from the interaction of the induced dipole with the inhomogeneous field and points up to the gradient when $m > 1$ and is given by

$$F_{grad} = \frac{2\pi\alpha}{cn_m^2} \cdot \nabla I_0 \tag{2.42}$$

$$\alpha = n_m^2 a^3 \left(\frac{m^2-1}{m^2+2}\right), \tag{2.43}$$

where α is the polarizability of the bead [155].

2.2.3 The intermediate regime

Unfortunately for beads with a size on the order of the laser wavelength, which are most commonly used, none of those approximations are valid. A more complete electromagnetic theory description is needed, which can be found in [15].

Chapter 3

Experimental Procedures

3.1 Setup

A photonic force microscope (Figure 3.1) was used to manipulate and measure the position of the membrane coated bead. The optical trap was formed by focusing an expanded 1064 nm laser beam (IRCL-850-1064-S CrystaLaser, NV, USA) on the sample through a water immersion objective lens (UPlanSApo 60x, Olympus, PA, USA) or an oil immersion lens (EC Plan-NEOFLUAR, 100x, Zeiss, Germany). A xyz-nano-positioning stage (P-561, Physik Instrumente, Germany) was used to move the sample chamber relative to the stationary trap. To measure the position of the trapped particle, the interference pattern of the transmitted light from the trapping laser and the forward-scattered light from the particle were collected by a condenser lens and focused on the quadrant photo diode (QPD). The particle's x-, y- and z-position can be related to the output voltage of the QPD [169]. The electronic bandwidth of the detection system was about 40kHz, and the position signals were sampled at a frequency of 100kHz (NI PXI 5922, National Instruments, TX, USA). The uncertainty of the position measurements was mainly caused by the position noise of the nano-positioning stage which has a standard deviation of 1nm along the axial and 1.5nm in the lateral direction

[16].

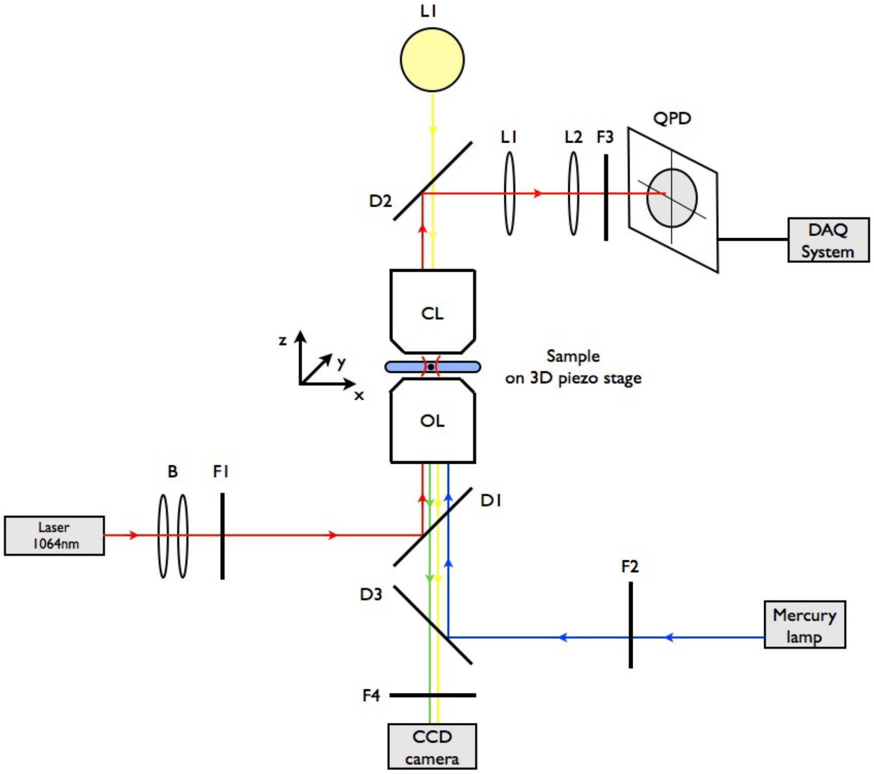

Figure 3.1: Sketch of the photonic force microscope. B: Beam expander, F1 and F3: neutral density filters, F2: fluorescence excitation filter, F4: fluorescence emission filter, L: lenses, OL: objective lens, CL: condenser lens, TL: tube lens, D: dichroic mirror, LS: light source (Bright-field), QPD: quadrant photo diode.

In addition to the laser beam path, the setup was equipped with a bright-field and a fluorescent illumination path. The bright field illumination source was an orange collimated LED light source (Thorlabs, NJ, USA) to avoid photo-bleaching of the fluorophores in the preparation stage of the membrane experiments, when the sample was viewed in bright field. For the fluorescence path, the light of a fluorescence excitation source X-Cite 120 (LDGI, ON, Canada) was focused into the back focal plane of the objective lens, to achieve homogeneous illumination of the sample. An exchangeable filter set (Chroma, VT, USA) consisting of an excitation filter, an emission filter, and a dichroic mirror was used to couple the excitation light into the beam path and to filter out stray light from the emitted light. The emitted light was then focused by the tube lens onto a CCD camera. The transmitted light in bright-field microscopy and the emitted light in fluorescence was collected on an EMCCD camera (iXon, Andor Technology, Ireland).

3.2 Sample preparation

3.2.1 Coating the silica beads with a lipid bilayer

Preparation of the small unilamellar vesicle (SUV) solution: 1,2-dioleoyl-sn-glycero-3-phosphocholine (DOPC), 1,2-dimyristoyl-sn-glycero-3- phosphocholine (DMPC), 1,2-dioleoyl-sn-glycero-3-phosphoethanolamine-N- (carboxyfluorescein), 1-oleoyl-2-6-[(7-nitro-2-1,- benzoxadiazol -4-yl)amino]hexanoyl- sn-glycero-3-phosphocholine (18:1-06:0 NBD PC) and 1-Oleoyl-2-[12-[(7-nitro-2-1,3- benzoxadiazol -4-yl)amino]dodecanoyl]-sn-Glycero-3-Phosphocholine (18:1-12:0 NBD PC) were purchased, solved in chloroform from Avanti Polar Lipids (Alabaster, AL) and used without further purification. The detergent depletion method was used with slight modifications [99, 212, 206]. An appropriate amount of DOPC or DMPC solution was added together with 1-2% fluorescein or NBD labeled lipids to a cleaned, round-bottom glass vial. The solvent was evaporated under a gentle stream of nitrogen and further treated under vacuum for a couple of hours. Dried lipids were hydrated in phosphate-buffered saline (PBS) while vortexing to achieve a final lipid concentration of 1.25mM. SUVs were prepared by sonicating the lipid solution in an ice water bath for about a minute using a tip sonicator until the solution reached translucency. Residual titanium was removed from the vesicle solution by centrifugation of 5 min at 2700g.

Coating of the beads [18]: Silica beads, with a diameter of $0.97\mu m$ or $2.5\mu m$ from Bangs Laboratories (IN, USA), were washed six times in PBS. For each washing step, the sample was centrifuged until the beads were sedimented and the supernatant was exchanged. After the sixth wash, the supernatant was discarded and replaced by the vesicle solution under rigorous vortexing. The SUVs were allowed to absorb and fuse to the beads for about one hour. Then the beads were washed with PBS at least six more times to remove the remaining vesicles, which were not fused to the beads.

Verifying the presence and fluidity of the bilayer on the beads

To verify the presence of the membrane bilayer around the silica beads, the beads were imaged by confocal microscopy. The fluidity of the membrane was examined with FRAP (Fluorescence Recovery After Photobleaching) experiments. All confocal images were taken either at the ICBM Core Microscopy facility on a Leica SP2 AOBS confocal microscope or at the Patterson Micro-

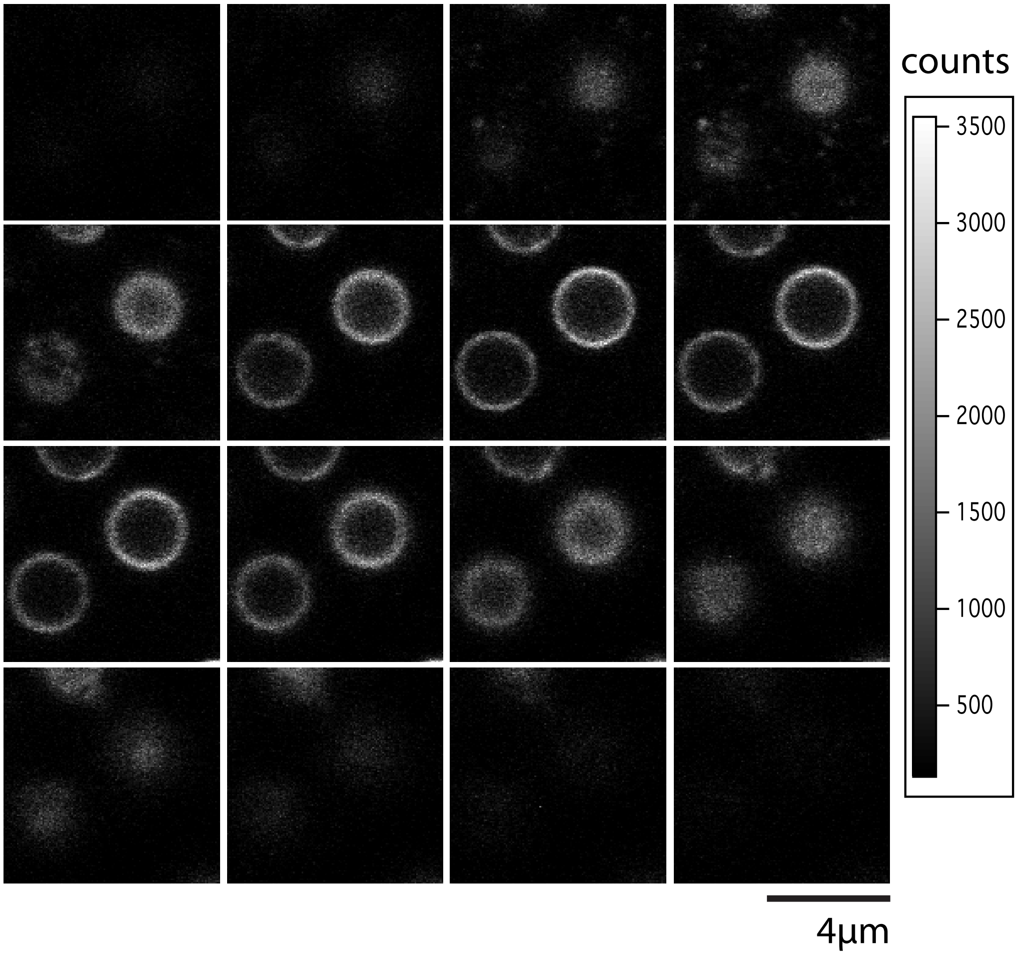

Figure 3.2: Z-stack of $2.5\mu m$ membrane coated beads imaged by confocal microscopy. The individual images are taken separated in the z-direction by 370nm. The beads are uniformly coated.

scope Center on a Leica TCS SP5 with a 63x oil immersion objective.

The presence and uniformity of a lipid bilayer around the silica beads was tested by recording z-stacks of the coated beads with a confocal microscope. The lipid bilayer on the bead contained 2mol% fluorescein labeled lipids. Figure 3.2 shows a z-stack of coated $2.5\mu m$ beads. The individual images are separated in the z-direction by $370nm$. The beads in this image show a very uniform coating with no additional unfused SUVs and no uncoated parts. In very rare cases, an adhered but unfused SUV can be seen on the bead's surface. However, most beads seemed uniformly covered by the lipid membrane.

In order to verify the fluidity of the membrane coating the beads, FRAP experiments were conducted on the beads. Since the beads have a small diameter of $2.5\mu m$, half of the fluorophores were bleached on the bead's surface in order to observe the recovery process. For a fluid membrane, the bleached fluorophores are able to diffuse within the membrane and exchange positions with the unbleached fluorophores. The mixing of bleached and unbleached fluorophores results in an uniform fluorescent signal over time on the surface of the bead. When the bilayer is not in a fluid state, there should be an observable intensity difference between the bleached and the unbleached area. The results of this experiment are shown in Figure 3.3. Figure 3.3a) shows the time sequence of the FRAP experiment, with the time between two frames being $0.703s$. The first two frames show membrane coated beads before bleaching. The lower half of the membrane on the beads was bleached between the second and third frame. The third frame clearly shows a difference in the fluorescence

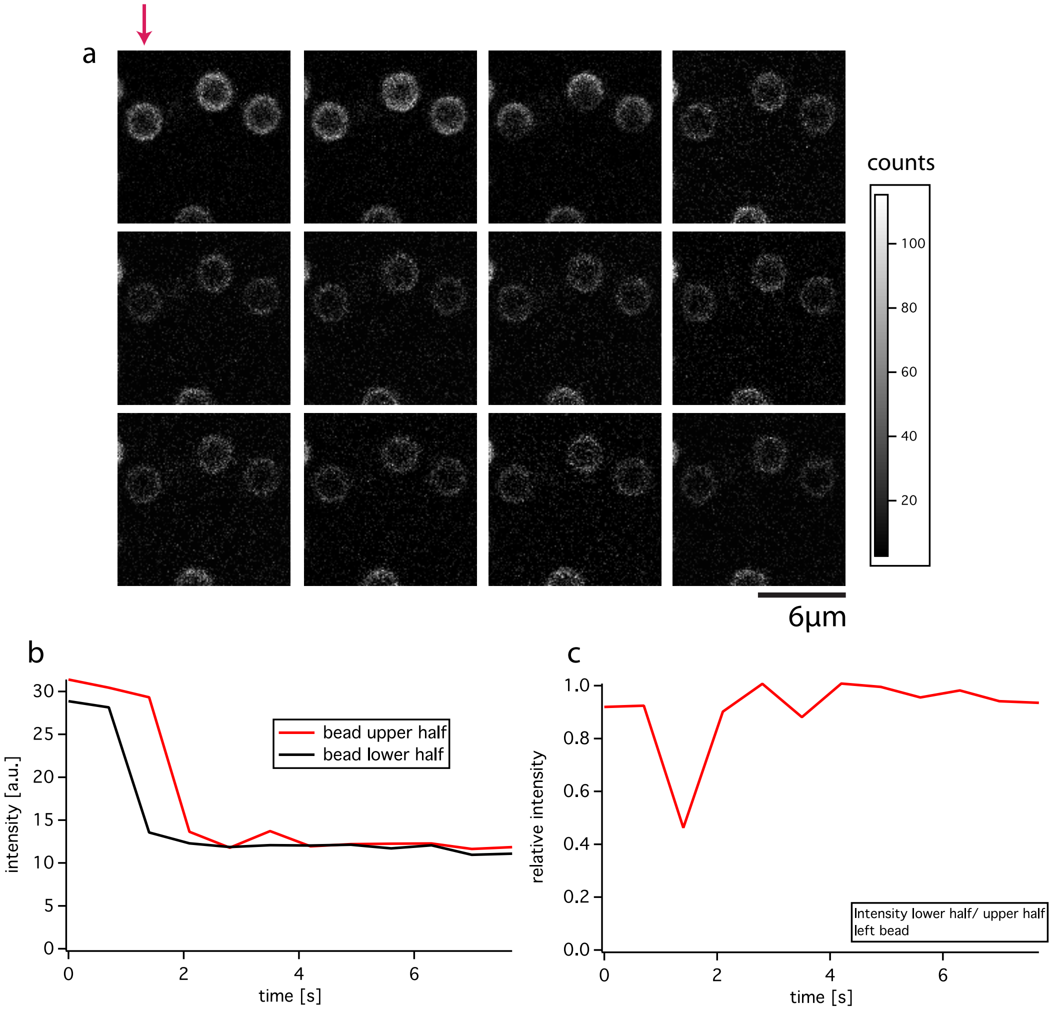

Figure 3.3: FRAP on the lipid coated silica beads. a) Time sequence of the FRAP experiment, where the lower half of three membrane coated silica beads is bleached. The individual images are separated in time by 0.703s. The first two images are taken pre-bleaching and the third image is the first one post-bleaching. b) Fluorescent intensity of the upper half and the lower half of the bleached bead, which is marked by the red arrow. The bleached half of the bead looses a half its fluorescence in the third frame, whereas the upper half follows one frame later. c) The plot of the relative intensity shows that both halves have an equal distribution of fluorophores at all times, with the exception of the first frame post-bleaching.

intensity between the lower and the upper half of the beads. Although the total intensity of the bead decreased, the difference between the upper and lower half of the beads disappeared in the subsequent frames, which can be seen in Figure 3.3b) and c). Figure 3.3b) shows the absolute intensity of the upper half versus the lower half of the left bead marked by the red arrow. Before bleaching, the intensity of the upper and the lower half are approximately the same, $\approx 30[a.u.]$, with an intensity ratio of 0.94. Directly after bleaching, the intensity of the lower half decreased to $14[a.u.]$, 50% of its pre-bleach value, whereas the intensity of the upper half remains at $\approx 30[a.u.]$. At $0.703s$ after bleaching, the fluorescently labeled lipids have redistributed and the intensity values of both halves of the beads are equal. Due to the limited reservoir of fluorophores on the bead and the weak photo-stability of the used fluorescent marker, the intensity does not recover to an average value but remains on the intensity level of the bleached half. In Figure 3.3 c), the relative intensity of the lower half versus the upper half of the beads is plotted. It shows that the intensity distribution on the surface of the bead is approximately equal at all times, with the exception of the first frame post-bleaching. Therefore, the FRAP experiments show that the beads are not only uniformly coated but that the lipid bilayer is in a fluid state.

3.2.2 Coating the glass coverslip with a lipid bilayer

Formation of a supported bilayers on the coverslip: 15mm diameter glass coverslips (Menzel-Glaeser, Germany) were immersed in a 2% Hellmanex

II solution (Hellma GmbH Co. KG, Germany) in deionized water (Milli-Q Advantage A10, EMD Millipore, MA, USA) and sonicated in a bath sonicator for 15 min. The solution was replaced by deionized water and sonicated again for 15 min. This procedure was repeated two more times. Subsequently, they were rinsed extensively with deionized water and blow-dried with nitrogen gas. SUV solution was filled in the preassembled sample chamber and absorption was allowed to take place for one hour at room temperature (for DMPC above phase transition temperature). The surplus vesicles were washed away with PBS to obtain a bilayer on the substrate without vesicles in solution.

Verifying the presence and fluidity of the bilayer on the coverslip

As described before, the lipid bilayer on the glass coverslip was first imaged by confocal microscopy to verify it's presence and uniformity and then tested for fluidity with FRAP measurements.

Figure 3.4 shows the confocal micrograph of a lipid bilayer, supported on a glass coverslip, containing 2mol% fluorescein labeled lipids. The intensity distribution on the surface is homogeneous and does not show any unfused SUVs, patches of multiple bilayers or holes in the bilayer. In some areas unfused SUVs can be found on the surface.

FRAP measurements are conducted to confirm the fluidity of the lipid bilayer. Figure 3.5a) shows the individual images in the time sequence of the FRAP experiment, which were recorded every 0.39s. The first two frames show the lipid bilayer before the bleaching event. The third frame shows the

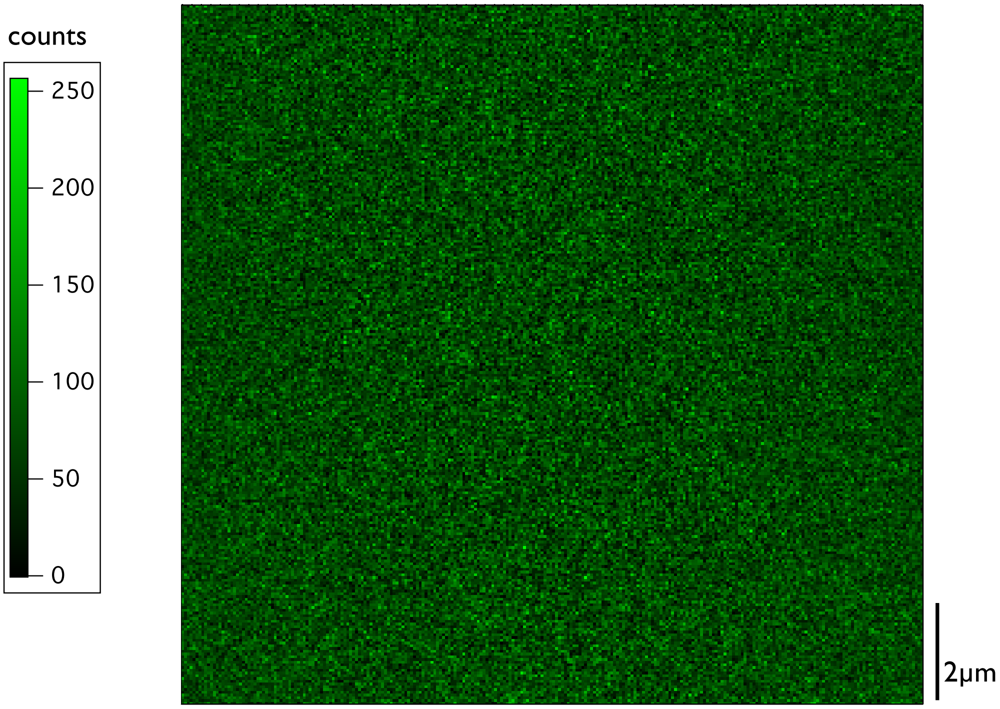

Figure 3.4: Confocal image of the lipid bilayer supported on a glass coverslip.

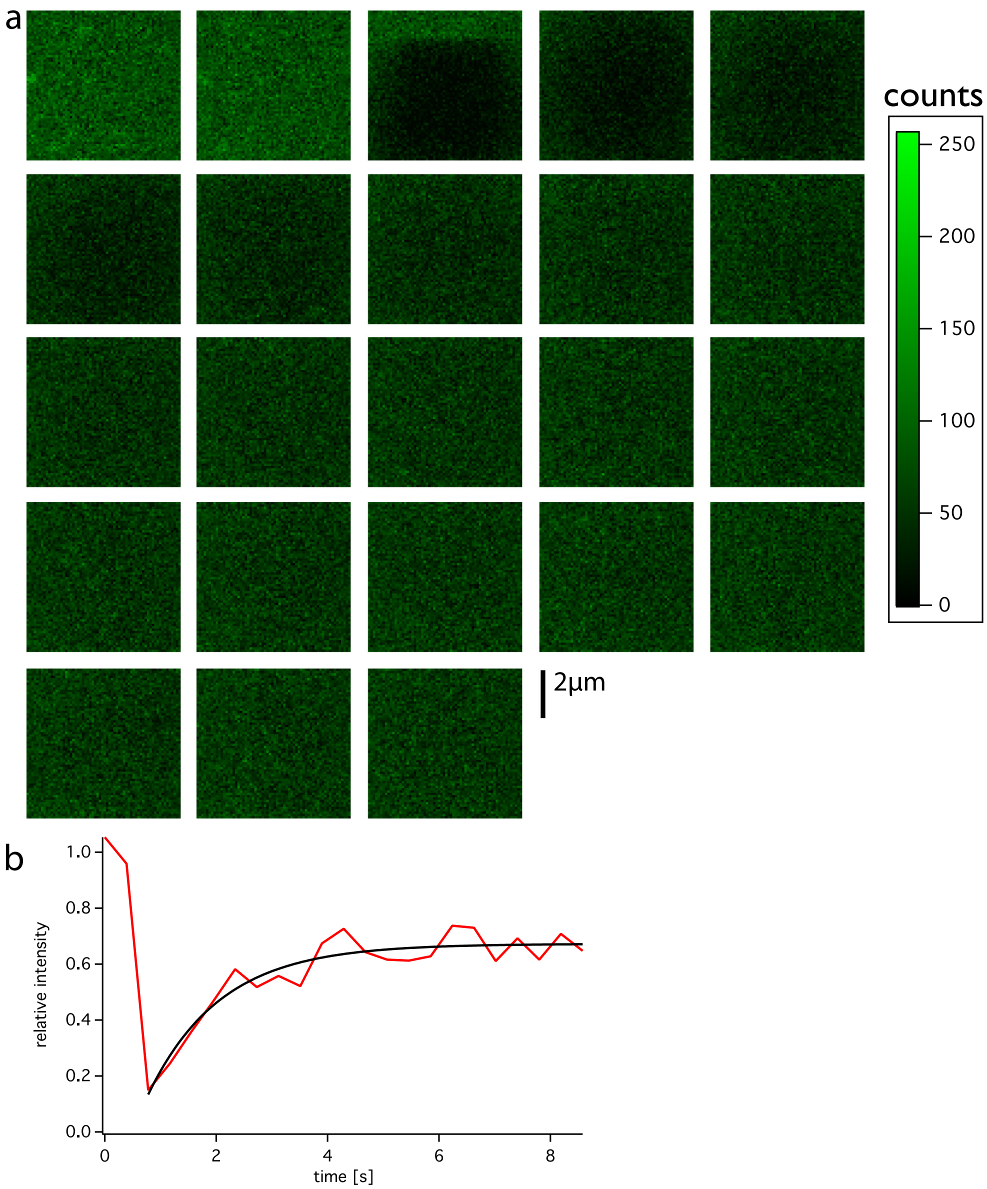

Figure 3.5: FRAP on a supported lipid bilayer. a) The first two images are pre-bleaching, the following frames post bleach. Between the second and third frame a square with a side length of $4.25\mu m$ was bleached. Frames were recorded every 0.39s. b) The relative intensity of the center over time. The pre-bleached images show maximum intensity. Post-bleach the intensity recovers exponentially over time.

membrane right after bleaching of a square with a side length of $4.25\mu m$ in its center. In the subsequent frames the intensity inside the bleached square slowly recovers, due to the rearrangement of the bleached and unbleached fluorescently labeled lipids. Figure 3.5b) shows the relative intensity of a 4 pixel wide square in the center of the field of view. The intensity in the center region is normalized to be one pre-bleach. After bleaching, the intensity in the center drops to 15% and slowly recovers exponentially over time with a time constant of $\tau = 1.3s$ to 70% of the pre-bleach intensity. Stuck SUVs, the relatively unstable fluorophore and the coupling of the membrane to the coverslip might be contributing to the incomplete recovery. In conclusion, the confocal images and the FRAP experiment show that the lipid bilayer on the glass coverslip is homogeneous, complete, and in a fluid state.

3.2.3 Imaging impurities present in the bilayers by thermal noise imaging

As shown in the prior sections, the coating of the beads and the coverslips with a lipid bilayer is reliable. Occasionally, unfused SUVs remain on the surfaces. During fusion experiments, these cases can be distinguished from the ideal fusion experiments, without excess vesicles, by their specific signature in the thermal noise data.

By evaluating the tracer particle's position data during the fusion of the bilayers, one can not only gain valuable insight into the fusion process (see chapter 4) but also probe the local properties of the membranes on the surfaces.

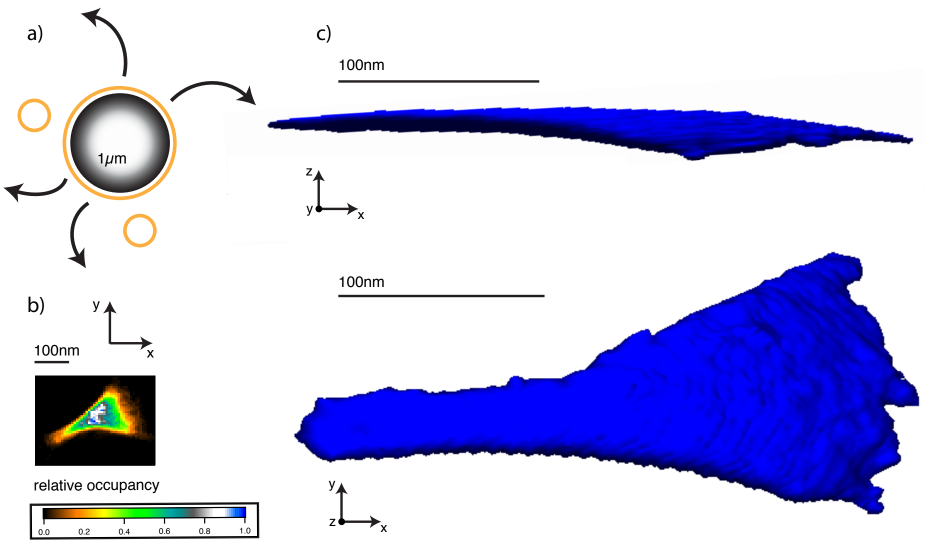

Figure 3.6: Imaging of defects in the target membrane. If there are defects in the target membrane, the data will show excluded areas in the 2D and 3D position histograms. a) Schematic of the membrane-coated $1\mu m$ bead and the two obstacles (SUVs), around which the bead has to diffuse. b) 2D histogram of the bead's position. Instead of a circular symmetric 2D histogram, the histogram has excluded areas on two edges. The obstacles restrict the bead form exploring the whole trapping volume and spare out an area in the position histogram. c) 3D histogram of the bead's position. The bead is confined in the z-direction, and can explore laterally the areas in between the two obstacles.

The 2D and 3D position histograms can reveal impurities in the surface in the area of contact between the bead and the coverslip. Figure 3.6a) shows a schematic of two unfused SUVs adhered to the membrane on the coverslip. In the hemifused state, the bead is axially confined and laterally can explore the whole trapping volume as show in Figure 4.5. If there are obstacles, the bead can not access the whole trapping volume but spares out the area around the SUVs, which can be seen as excluded area or volume in the 2D and 3D position histograms. Figure 3.6 shows the 2D position histogram of the tracer particle, which equals the negative image of the surface impurities. The same excluded volume can be seen in the 3D position histogram, Figure 3.6c).

Figure 3.7 shows the thermal noise image of an unfused SUV, which was either sitting in the center of the trapping volume or was attached to the bead. The obstacle acts as an anchor around which the particle can roll around.

Since the membrane coating is not always perfect, thermal noise imaging has the advantage, that the membranes in the contact area were imaged in each individual data set. This allows distinguishing cases where the adjacent membranes were with or without impurities. The experiments with problems in the coating, can be sorted out and excluded from further analysis.

3.3 Sample assembly

For the fusion experiments a flow chamber was used, which was built around a round magnetic metal disc. Figure 3.8a) shows a sketch of the disc.

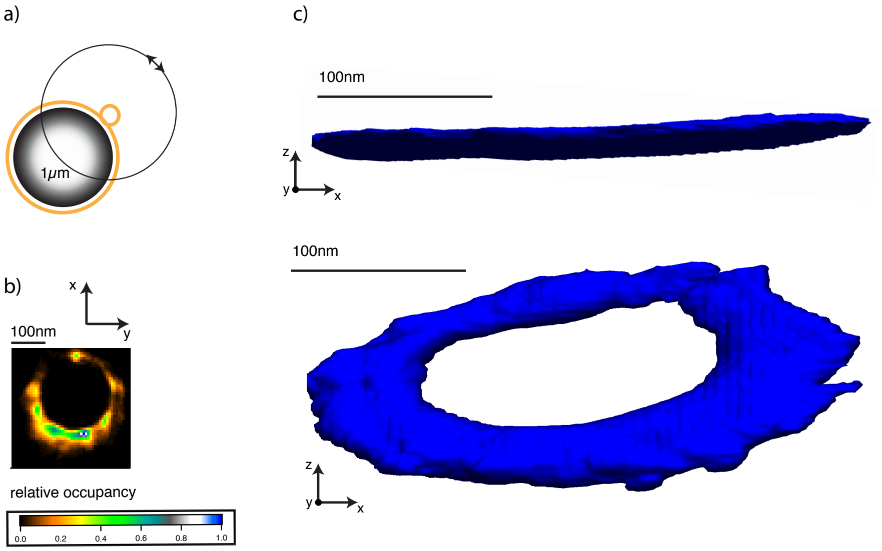

Figure 3.7: Imaging of defects in the target or vesicle membrane. If there are defects in the target or on the bead membrane, the data will show excluded areas in the 2D and 3D position histograms. a) Schematic of the membrane-coated $1\mu m$ bead and the obstacle, around which the bead has to diffuse. This can either be a SUV sitting in the center of the trapping volume on the target membrane or is a SUV, which is adhered to the bead. b) 2D histogram of the bead's position. The SUV acts as an anchor around which the bead has to diffuse. The area in the center of the trap is not accessible for the bead, therefore it is spared out in the histograms. c) 3D histogram of the bead's position. The bead is confined in the z-direction, and laterally moves around the anchor point. The 3D histogram shows the axial confinement of the tracer particle and has the shape of the 2D histogram.

The four black lines indicate tubes, used for fluid exchange. Four tubes are advantageous over two, since this configuration minimizes the dead volume within the sample. Clean coverslips were attached to both sides of the disc with vacuum crease. As shown in Figure 3.8b), $60\mu L$ SUV solution was introduced into the sample chamber with glass syringes (Hamilton, NV, USA). After an hour of absorption, a bilayer had formed on the bottom coverslip (Figure 3.8 c)). The excess SUVs were washed away with $60mL$ of PBS to gain a clean sample chamber, Figure 3.8d). This is especially important, since SUVs remaining in solution can diffuse into the trapping volume and worsen the position signal. After excessive washing, the sample was placed onto the positioning stage and the membrane coated beads were loaded in another glass syringe, so that the coated beads could be flushed into the sample chamber, Figure 3.8e). A single bead was trapped in solution and brought into contact with the bilayer on the coverslip to introduce fusion.

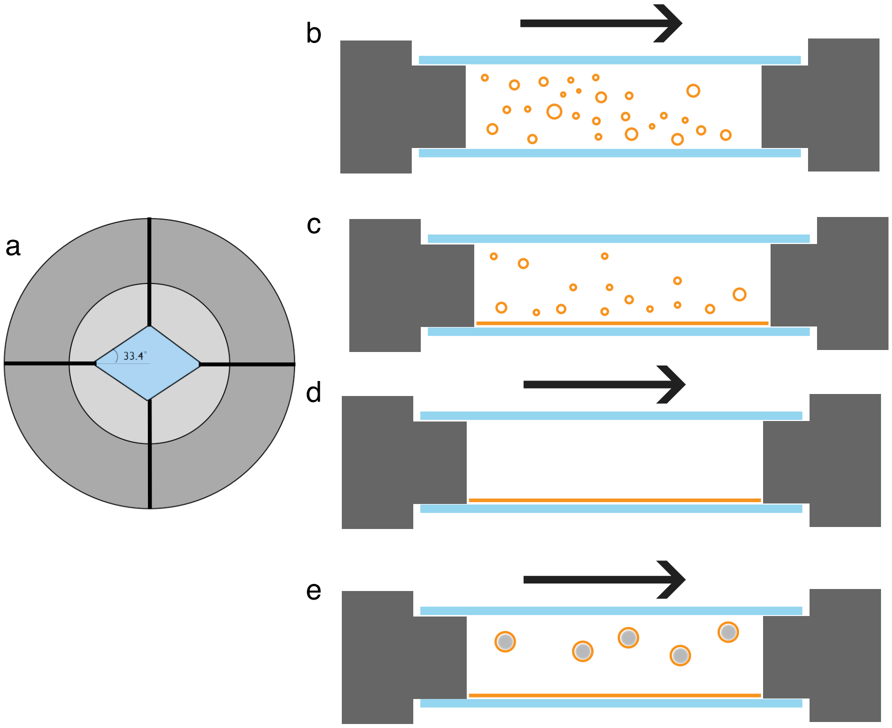

Figure 3.8: Schematic of the flow chamber used in fusion experiments and the sample preparation. a) Drawing of the metal disk used as a base for the flow chamber. The black lines indicate tubes, through which fluid can be exchanged. b) SUV solution is introduced to the sample chamber (cross-sectional view). b) Vesicles are allowed to absorb for one hour. d) Removal of the excess vesicles. e) Introduction of the membrane coated silica beads. (Arrow indicating flow)

Chapter 4

Characterization of membrane fusion intermediates with the PFM

4.1 Description of the fusion assay

The energy barrier for spontaneous membrane fusion is too large to occur on a reasonable laboratory timescale. Therefore, most fusion assays introduce fusogenic molecules into the membranes or increase the membrane's tension [193]. Here, we vary the tension of the membrane around the bead by using the area mismatch between the bilayer on the bead and the available surface area of the bead. This is achieved by preparing the membrane-coated beads above the temperature of the fusion experiment. A change in temperature of $10°C$ will result in an area mismatch of about 5% [154] and can either lead to lower or higher membrane tension depending on the sign of the temperature difference. Thus, by controlling the temperature difference between preparation and experiment, we can adjust the membrane tension, which in turn alters the energy barriers along the fusion pathway and consequently the fusion probability. In this way, we can control the fusion probability of pure lipid bilayers that would normally not fuse on a reasonable timescale without applying an external force.

To initiate membrane fusion, a DOPC membrane-coated bead ($0.97\mu m$ diameter) is trapped at low laser power (typically a few mW in the sample chamber) and brought into contact with the DOPC bilayer adsorbed on the surface of the coverslip. Silica beads are used, because lipid vesicles containing fluid are relatively soft an easily deformable. Deformations of the vesicle upon contact with surfaces make it challenging to track its center precisely and to apply force. The strong coupling of the membranes to their support suppresses membrane undulations and allows for precise position measurements. DOPC was chosen for all experiments unless otherwise noted, because it is in the fluid phase at room temperature. If the tension in the membrane is high enough, fusion intermediates can be observed by tracking the position of the trapped bead.

4.2 Initiation of membrane fusion

The magnitude of the energy barrier for the fusion of two pure lipid bilayers depends on their tension and determines the timescale on which spontaneous fusion occurs [67]. Therefore, we can verify the validity of our fusion assay by fusing two DOPC bilayers with low, intermediate and high tensions each. For low tension the sample was prepared at lower temperatures than the temperature at which the fusion experiment was performed. Figure 4.1 shows the position fluctuations of the tracer particle in all three dimensions over time. Initially, the bead is able to explore the whole trapping volume. The position fluctuations show their maximal values of $21nm$, $20nm$ and $47nm$

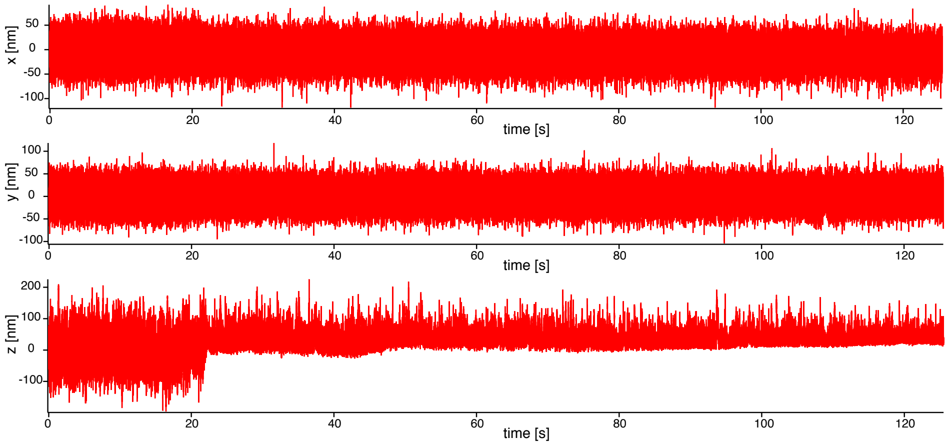

Figure 4.1: Fusion attempt of a coated bead with low tension in its membrane. The x-, y- and z-position traces show that no fusion occurs upon contact. The bead was trapped and approached the membrane on the glass coverslip at 21.7s. Although the membranes were constantly making contact, they did not fuse over more than 100s after contact.

for the standard deviation in the x-, y- and z-direction. At time $t = 21.4s$ the bead is brought into contact with the coverslip and position fluctuations in the z-direction reduce to about half of their initial value. The standard deviation reduces to $23nm$ in z-direction, whereas the values in x- and y-direction remain unchanged. This is due to the coverslip being in the center of the trap, making the lower half of the trapping volume inaccessible to the bead. For the rest of the time series, which is longer than $100s$, no change in the position signal occurs. This indicates that the bilayers do not fuse even if they are forced together, since fusion would result in a tight confinement of the axial motion. In contrast, if this experiment is repeated with a plain silica bead and a glass coverslip with no membranes, the position fluctuations reduce to their minimal value right upon contact (Figure 4.2). Multiple fusion attempts with different beads show that the fusion probability is low, as expected.

To lower the initial energy barrier in the fusion pathway, the membrane around the tracer particle was put under tension. To initiate fusion we brought beads coated with membranes of different tensions into contact with the target membrane. If the tension was intermediate, i.e. preparation of the sample and the performance of the fusion experiment at the same temperature, it can take up to tens of seconds after the initial contact before a change in the position fluctuations occurs as seen in Figure 4.3. The reduction of the position fluctuations along the z-direction but not in the lateral directions indicates a strong axial confinement without any lateral confinement. This observation is compatible with the hemifusion stage in which the particle and

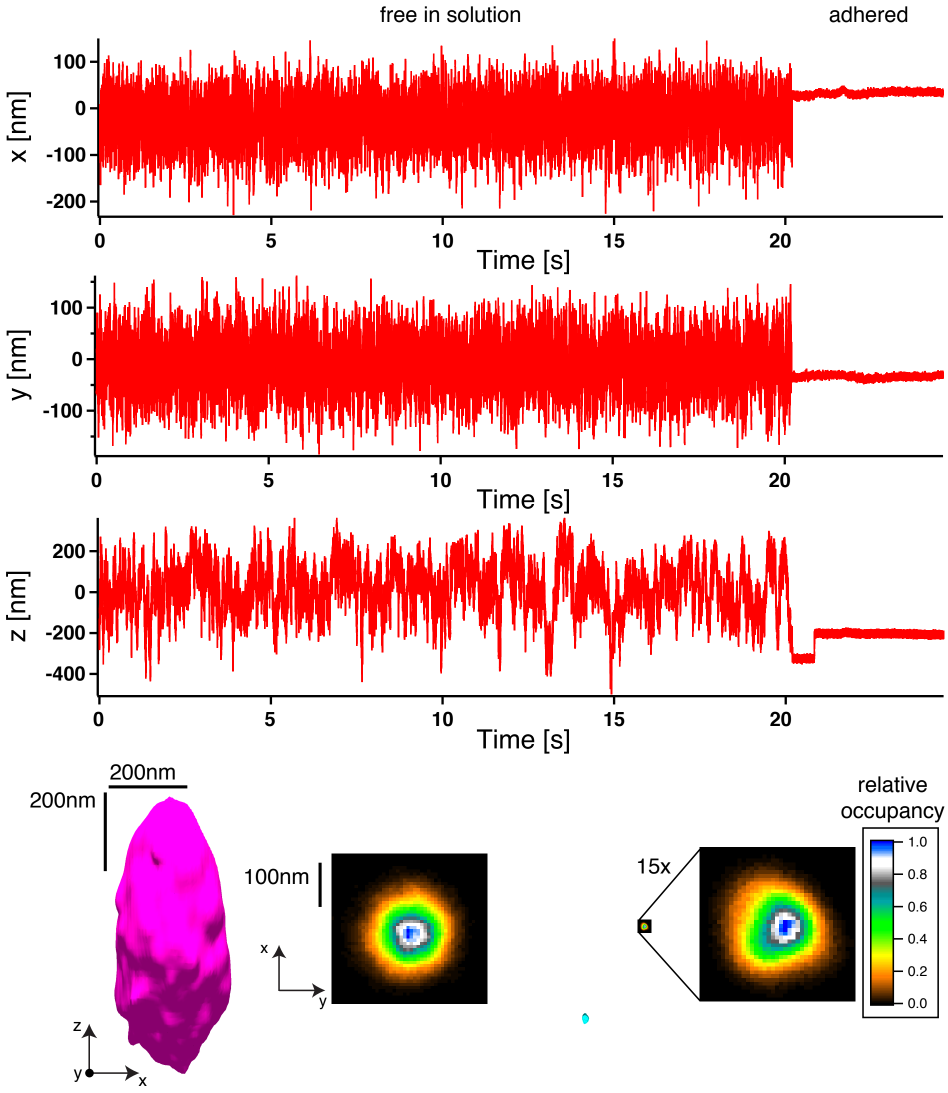

Figure 4.2: Adhesion of a silica bead to a plain glass coverslip. As soon as the trapped bead is brought into contact with the cover slide (shortly after 20s), the bead becomes immobilized and a reduction in the thermal position fluctuations is observed in the x-, y- and z-position traces, the 2D position histograms and the 3D isosurface plots. The position fluctuations in solution are maximal in all three dimensions while the bead can explore the whole trapping volume. Upon contact with the surface the position fluctuations reduce to a few nm and the bead is immobilized.

the stalk-like connection can diffuse freely in the x- and y-directions, because both membranes are in the fluid phase. For membranes with high tension, i.e. preparation of the sample at higher temperatures than the performance of the fusion experiment, the same reduction in the position fluctuations is observed instantaneous with the contact of the membranes. This first reduction of the position fluctuations is described in the following paragraph in more detail and will be interpreted as hemifusion. We show experimentally, that increasing the temperature at which the beads are prepared, equivalent to increasing tension, changes the fusion probabilities as reported in literature [193].

4.3 Characterization of fusion intermediates in DOPC bilayers

As seen in Figure 4.3, membrane fusion leads to a successive suppression of the thermal position fluctuations of the tracer particle. Here, we further characterize the fusion intermediates according to the reduction in the position fluctuations. Figure 4.3 shows time-traces of the thermal position fluctuations in x-, y- and z-directions for a particle that was either only optically trapped or in the different stages of confinement. Free in solution (Figure 4.3a), the bead can explore the whole trapping volume driven by thermal fluctuations; the standard deviation of the z-fluctuations has its maximum values of $81nm$. As the particle reaches the surface (Figure 4.3b), it still moves freely in the lateral directions, but its fluctuations are limited in axial direction by the coverslip. This confinement reduces the standard deviation along the z-axis to

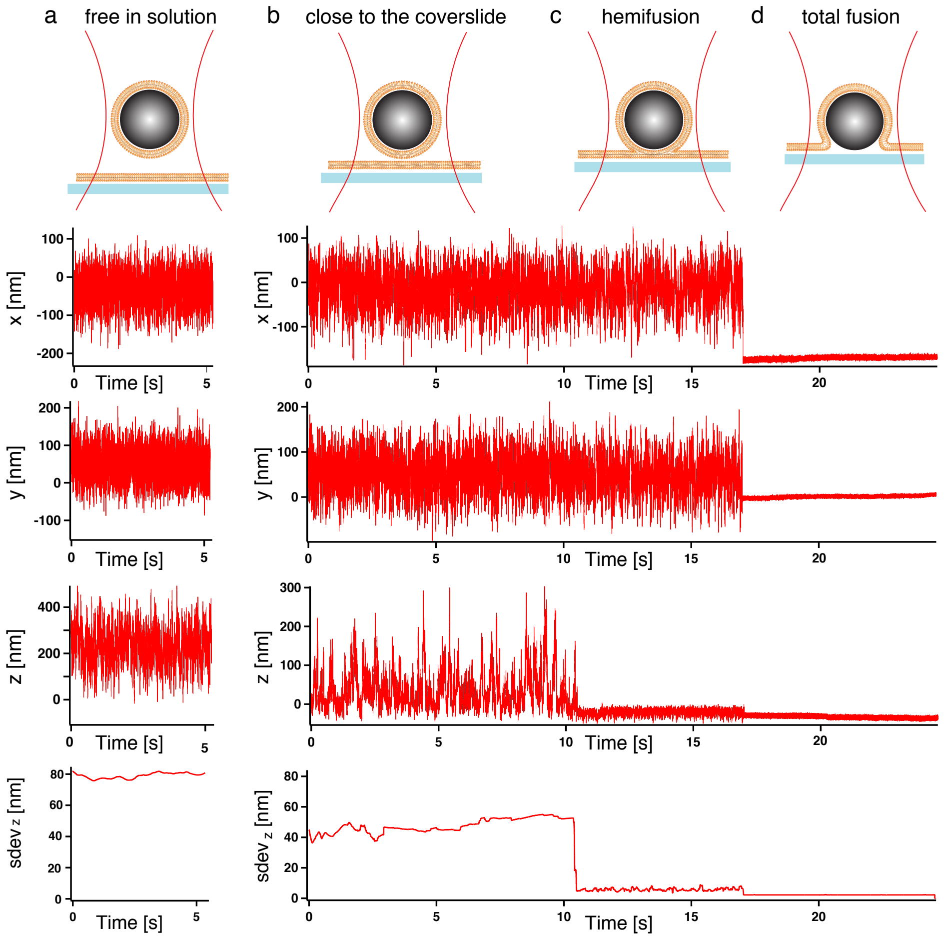

Figure 4.3: Measuring single fusion events. A $970nm$ bead coated with a lipid bilayer is trapped with weak optical tweezers and brought into contact with the supported bilayer on the glass coverslip. The x-, y- and z-position traces and standard deviation for the z component are shown below the sketch of the fusion intermediates. a) The particle diffuses freely in solution. The position fluctuations in all directions are maximal and their standard deviation along the z-axis is $81nm$. b) As the particle approaches the surface, the fluctuations in x- and y-directions remain the same, but they are restricted in the z-directions by the coverslip and the standard deviation reduces to $48m$. c) In this event, shortly after $10s$ the particle hemifuses. The particle is restricted in z direction and the standard deviation drops to 6nm. In x- and y-direction the particle is still able to diffuse with the same amplitude. d) About $6.6s$ later total fusion occurs and the particle is immobilized on the glass coverslip. The position fluctuations decrease to a minimum, and the standard deviation axially is $2nm$.

$48nm$ while the standard deviations in x and y remain the same at a values of $41nm$ and $40nm$ respectively. A dramatic further reduction to $\approx 6nm$ in the z-direction occurs at time $t = 11.9s$ (Figure 4.3c), about $25s$ after the last transient binding. Again, there are no restrictions in the lateral fluctuations, which indicates that the particle diffuses rapidly along the surface while it is strongly confined along the z-axis. This observation is compatible with the hemifusion stage. The particle and the stalk-like connection can diffuse freely in the x- and y-directions, because both membranes are in the fluid phase. After another 6.6 seconds, at $t = 18.5s$, a second drastic reduction in the thermal fluctuation takes place (Figure 4.3d); this time along all axes simultaneously. The standard deviations in all three dimensions reduce to values of $1 - 2nm$, a magnitude similar to a plain silica particle strongly adsorbed to a plain glass surface (Figure 4.2). We interpret this state as total fusion of both membranes. The particle is now in direct contact with the glass surface and no further confinement is observed.

Besides hemifusion events as shown in Figure 4.3c, transient binding events were observed occasionally. Figure 4.4 shows a transient fusion event, where the stalk-connection detached five times in approximately $20s$. The first contact occurred at $t = 5.1s$. The following step in the z-direction is due to a step of the stage to move the bead in the center of the trap. This results in an average applied force of zero and avoids inducing detachment by pulling on the stalk. In this transient fusion events, the initial connection to the membrane as indicated by the reduction of z-fluctuations, lasted only $2.8s$

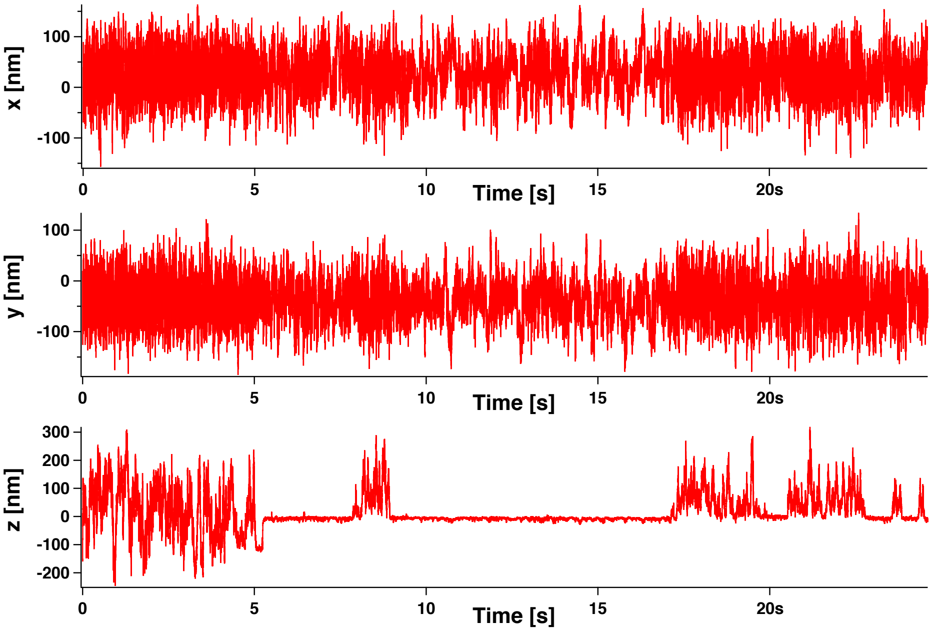

Figure 4.4: Measuring transient fusion events. The first connection is made at $t = 5.1s$. After that the bead detaches from the surface 5 more times. The detachment lasts from $2.3s$ to $0.2s$. After the first connection, the trap is moved, so that the bead is in the center of the trap and no force is applied to pull on the stalk.

until the bead detached again. The period of the detachment lasted between $0.2s$ up to $2.7s$. Such transient events can occur either not at all, once, or multiple times before the system remained in hemifusion or continued to full fusion. This state is interpreted as transient fusion. Fusion intermediates as transient fusion, hemifusion and full fusion can be clearly distinguished and fully characterized by their specific signature in the position fluctuations of the tracer particle.

In addition to the information obtained from the analysis of the one-dimensional position-time traces, insight can be gained by looking at the position data in two- and three dimensions. The position data corresponding to a particular fusion intermediate can be summarized in two- and three-dimensional position histograms (Figure 4.5). Two-dimensional histograms for the x-y plane are easier to visualize than three-dimensional histograms. However, three-dimensional histograms are more informative about the particle's binding condition. As long as the particle is only confined by the optical trap, the two-dimensional histogram is radial symmetric and a three-dimensional position isosurface has the typical cigar shape that corresponds to a three-dimensional harmonic potential with a weaker force constant along the optical axis (Figure 4.5a). When the particle is moved close to the surface, the lateral position histogram remains the same but the presence of the surface reduces the accessible volume along the optical axis (Figure 4.5b). The following reduction in position fluctuations shows no change in the two-dimensional histogram, while the three-dimensional histogram shows now a strong confinement along

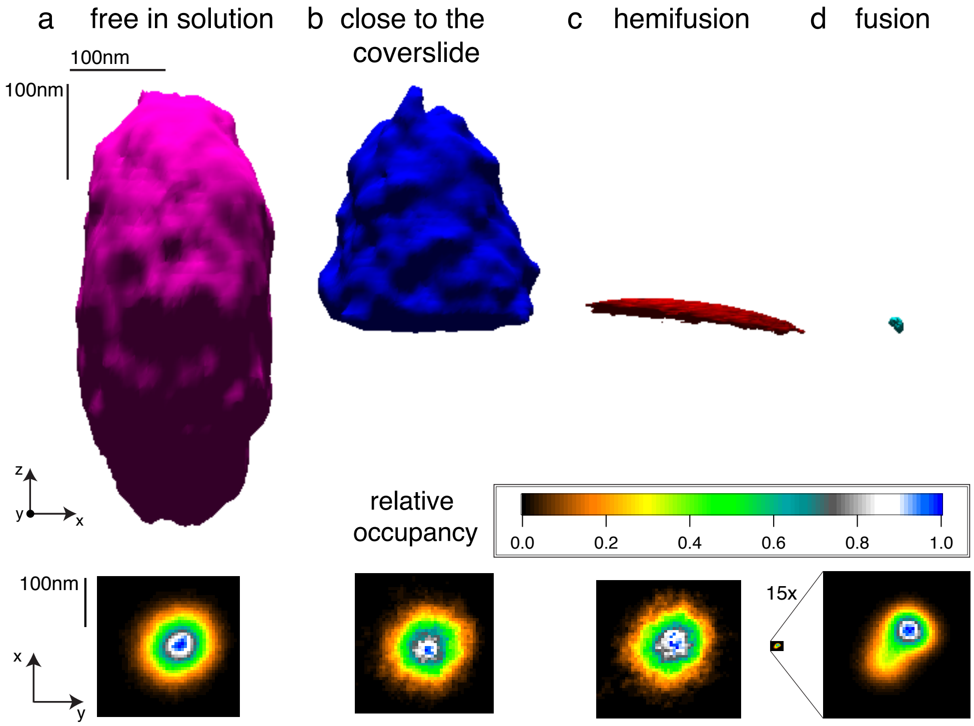

Figure 4.5: Two- and three-dimensional histograms of fusion intermediates. a) Deep in solution the particle can explore the whole trapping volume. The 2D histogram shows a radial symmetry, with the highest probability in the center. b) Approaching the surface, the trapping volume becomes restricted by the coverslip. c) As the particle hemifuses, it is confined in the axial dimension and its movement is limited to the xy-plane. The radial symmetry of the 2D histogram remains. d) At total fusion, the particle becomes immobilized at one point, which is orders of magnitude smaller than the trapping volume.

the z-axis. The two-dimensional histogram looks a little grainier which indicates a low number of independent data points for the histogram as a result of an increase viscous drag after the two membranes fuse. This corresponds to hemifusion, which is characterized by stalk formation and immobilization of the particle along the z-axis while the particle is still free to diffuse in the x-y plane. In the last step of the process the two- and three-dimensional histogram collapse to a tiny area or a small sphere, respectively (Figure 4.5d) similar to histograms for not-coated silica beads that adhered to the glass surface on first contact (see Figure 4.2). This represents the completion of the fusion process (total fusion), the particle is forced into strong contact with the surface resulting in immobilization.

In summary, we found that all intermediates are characterized by stable states of the particle and can be identified by the tracer particle's position fluctuations. Those can be visualized with the help of two- and three-dimensional histograms. The observed intermediates are compatible with the fusion intermediates described in the literature.

4.4 Fusion below the phase transition temperature

The fusion behavior of lipid membranes strongly depends on various parameters like stress [193], curvature or on lipid composition [40, 3, 109, 17]. Before, we have examined the dependence of the fusion behavior with membranes under various amounts of tension. To further demonstrate the specificity and sensitivity of our fusion assay, we use a different lipid, DMPC. The phase

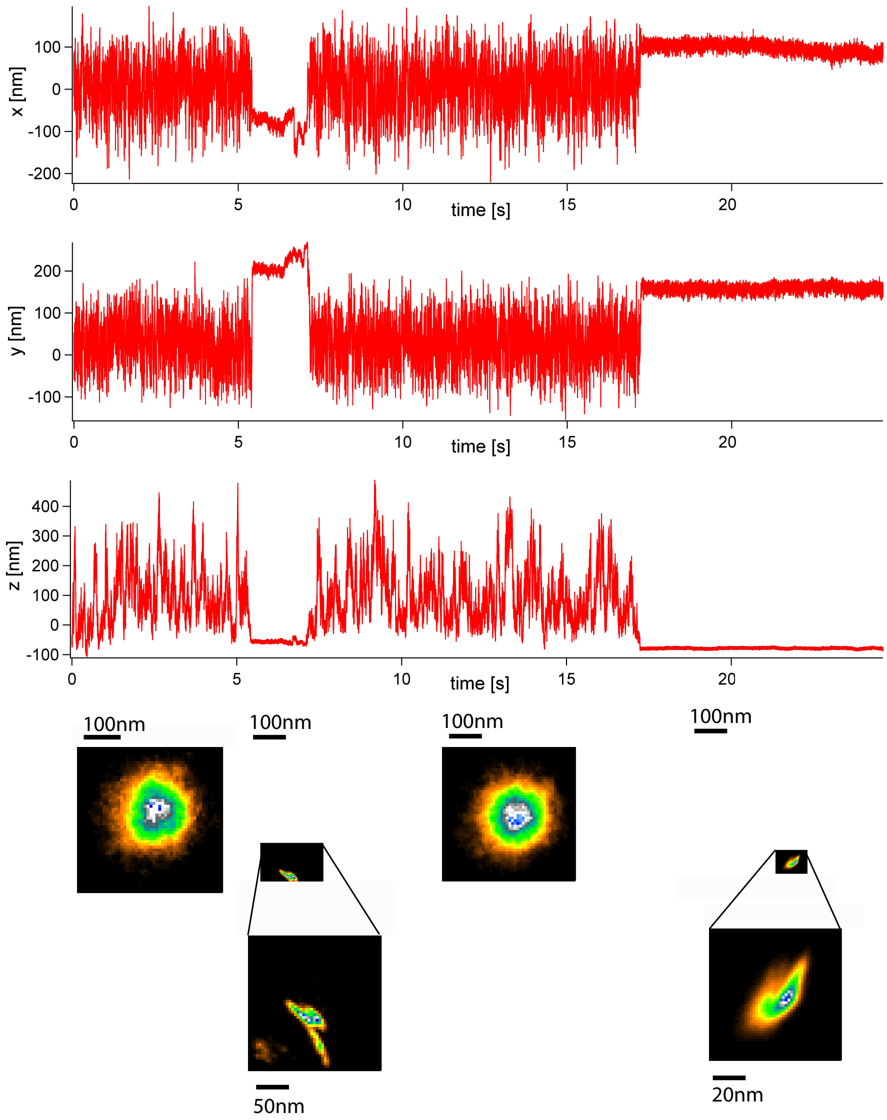

Figure 4.6: Measuring of single fusion events in DMPC bilayers around the phase transition temperature. Under the previously described experimental conditions, two DMPC bilayers will not fuse, if both of the membranes are in a gel phase. If the membranes are transitioning from a fluid to a gel phase, fusion can occur in the areas where the membranes are in a fluid phase in between the areas of gel phase. Therefore the position fluctuations in the hemifused state in x- and y-direction are significantly reduced, compared to hemifusion in fluid membranes. Although the initial hemifusion event is transient, the bead can laterally only explore little space due to the surrounding gel phase.

transition temperature of DMPC is $23°C$, which makes it an excellent choice for studying fusion behavior in the liquid and the crystalline phase. Above the phase transition temperature, we observe transient fusion, hemifusion and full fusion as observed for DOPC bilayers, with the same characteristics in the position fluctuations. However, below the phase transition temperature, two main parameters change dramatically. First, the probability for fusion drops dramatically. If the temperature is significantly below the transition temperature, when both bilayers should be completely in the crystalline phase, no fusion occurs. However, during the transition from the fluid to the crystalline phase, fusion can occur in the areas of fluid membrane patches (Figure 4.6). Second, even for transient fusion, thermal fluctuations decrease not only in the axial direction but also in the lateral direction. The standard deviations in x and y decrease about 50-90% compared with the values above the transition temperature, due to the confinement of the surrounding crystalline phase. Observing changes in the fusion behavior of DMPC above and below the phase transition temperature demonstrates that our fusion assay can detect specific properties of the lipid system.

4.5 Estimate of transition times

To address the question on which timescales the transitions between the fusion intermediates occur, we looked at the transition regions in the position time traces for DOPC (Figure 4.7). When the tracer particle transitions from diffusing in the entire trapping volume to diffusing in a more confined space due

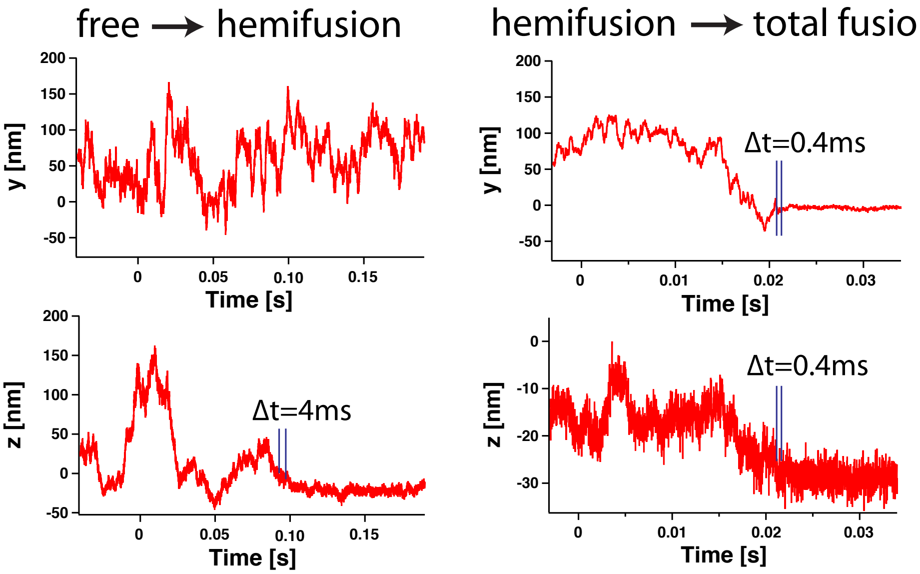

Figure 4.7: Zoom into the transition regions of Figure 4.3 The position fluctuations laterally remain unchanged in the transition from free to hemifusion. Axially, the fluctuations reduce dramatically as described before. Considering the time it takes the particle to explore the width of the fluctuations, it takes $3.8ms$ before the transition can be confirmed. b) In the transition from hemifusion to full fusion the transition can be detected faster, because the peak-to-peak fluctuations in the fully fused state are smaller. Therefore it takes about $0.4ms$ to detect full fusion.

to binding, the magnitude of the bead's thermal position fluctuations reduces. However, since the particle is still undergoing thermal motion, an apparent transient confinement on short timescales can be due to the stochastic nature of Brownian motion. This prevents instantaneous detection of transitions between fusion intermediates. In order to detect a transition with certainty, a characteristic time has to pass so that confined motion can be distinguished from free diffusion of the particle. This time depends on the magnitude of the position fluctuations in the more confined state. An upper boundary for the transition time can be estimated from the time it take the particle to diffuse further that the peak-to-peak fluctuations of the confined state. The standard deviation of the fluctuations in the z-direction in the hemifused state is $6nm$, which results in peak-to-peak fluctuations of $36nm$ (6σ). Under our experimental conditions the average time it would take a $1\mu m$ bead to diffuse further than $36nm$ is approximately $3.8ms$ assuming an increase of viscous drag by a factor of three due to hydrodynamics coupling to the target membrane. Therefore, the free to hemifusion transition can be detected with certainty after $3.8ms$. The transition from the hemifused state to complete fusion can be detected faster, because the standard deviation of the fluctuations in the fused state is smaller, $2nm$. The peak-to-peak fluctuations can be explored by a $1\mu m$ particle in proximity of the coverslip in approximately $0.4ms$. Thus this transition has to take place in less than $0.4ms$.

4.6 Estimate of energy barriers

All observed fusion events showed long stretches of stable intermediate states with fast transitions, which indicates significant energy barriers between the states. Here, we use Boltzmann statistics to transform the bead's position probability distribution into an energy landscape. Given enough time, a trapped bead driven by thermal forces will in principle explore its entire spatial energy landscape. It will remain within a given local potential minimum of the energy landscape until on an attempt to leave the potential its instantaneous thermal energy is larger than the energy barrier . The probability $p(x)d\vec{x}$ to find a small particle, exploring a potential $E(\vec{x})$, in a volume $d(\vec{x})$ in thermal equilibrium equates to

$$p(\vec{x})d\vec{x} = Ce^{-\frac{E(\vec{x})}{k_B T}} \tag{4.1}$$

according to Boltzmann statistics. C is a normalization constant, so that $\int p(\vec{x})d\vec{x} = 1$. From the bead's measured position data in the hemifused state, a position histogram can be computed which approximates its spatial probability distribution, Figure 4.8a). This probability distribution can be converted into an energy landscape using the following equation [63],

$$E(\vec{x}) = -k_B T \ln p(\vec{x}) + k_B T \ln C. \tag{4.2}$$

From the extracted energy landscapes, Figure 4.8, we estimate a minimum value for the height of the energy barrier for transitioning into hemifusion of $10 k_B T$.

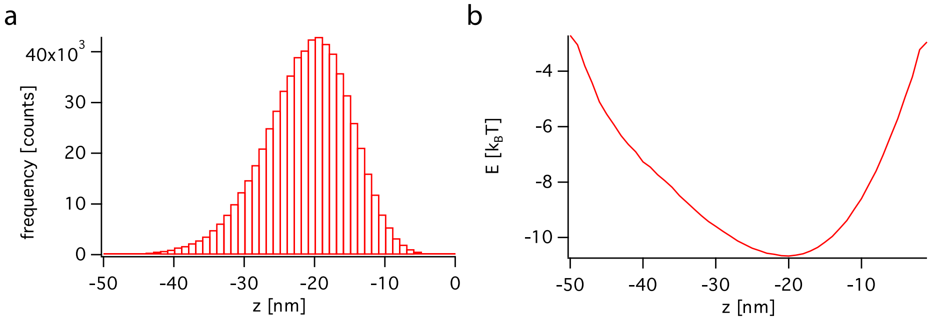

Figure 4.8: Measuring the energy landscape of the hemifusion intermediate. a) The position histogram of the z-fluctuations in the hemifused state. b) Energy landscape of the hemifusion intermediate calculated from the position histogram with Boltzmann statistics.

The position time traces allowed us to estimate the energy barrier for the transition to hemifusion. Since the intermediates are stable over long periods of time, the tracer particle had enough time to explore its entire accessible energy landscape. The depth of this landscape served as an estimate for the minimum energy barrier of $10k_BT$. The energy barriers along the fusion pathway depend strongly on a variety of parameters. These parameters include the tension in the bilayers, the membrane bending rigidity, the temperature, the size of the vesicles, the actual fusion pathway and the spontaneous curvature of the lipid monolayers, which is mostly determined by the lipid composition. DOPC has a slightly negative curvature of $c_0 = 0.11nm^{-1}$ [78]. For the spontaneous curvature of DOPC the energy barriers for stalk expansion have been calculated to be between approximately $10k_BT$ to $25k_BT$ [105] with strong dependence on membrane tension. Besides the variables mentioned before, which generally alter the energy barriers in the fusion process, the energies are influenced by additional factors in our assay. Due to the tight coupling of the membranes to their respective surfaces, the surface chemistry and the suppression of membrane undulations might alter the energy landscape. Our assay gives high control over some of these parameters: size and geometry of the system can be adjusted by varying the tracer particle diameter, the spontaneous curvature can be controlled by the lipid composition, and the membrane tension is a function of the area-mismatch between the membrane and the substrate. By choosing a certain set of parameters, the energy landscape can be altered in a way, which selects for and allows the study of specific fusion intermediates. Additionally, one can systematically study the height of the fusion barriers depending on parameters like tension, spontaneous curvature and lipid composition.

4.7 Diffusion constant distinguishes fusion intermediates

To characterize intermediate fusion states in more detail, we analyze the particle's dynamics, i.e. the viscous drag that acts on the particle and the resulting diffusion constant. A change in the viscous drag will result in a change in the diffusion constant. The diffusion constants are shown, because their values are extracted from the data. We calculate the diffusion constant from the mean square displacement of (MSD) of the thermal position fluctuations in one dimension, $\bar{x}^2 = 2D\Delta t$ at short time scales ($<< 20ms$). Far away from the surface ($> 10\mu m$), the diffusion constant of the bead has a constant value D_∞ according to the Stokes-Einstein equation for a sphere in solution

$$D = \frac{k_B T}{\gamma}, \tag{4.3}$$

$$\gamma = 6\pi\eta r. \tag{4.4}$$

Here, γ is the viscous drag, η is the viscosity of surrounding fluid, r the radius of the trapped particle and T the temperature. As the particle approaches the surface, the diffusion constant decreases due to hydrodynamic coupling. At the surface, the diffusion constant, D_0, is reduced to about a third of the diffusion constant in solution [167]. When the particle hemifuses, a sudden drop (ΔD) in the diffusion constant from D_0 to D_{hf} occurs (Figure 4.9). Total fusion leads then to the final drop in the diffusion constant from D_{hf} to almost zero. The drop in the diffusion constant (ΔD) arises from additional drag due to the stalk and the suppression of the rotational motion of the tracer particle. When a membrane connection, like a stalk or a hemifusion diaphragm, is formed, the drag on the tracer particle increases, because now the part that connects the two membranes needs to laterally move in the supported membrane, increasing the viscous drag on the particle. Here, we assume that the complete drag on the particle in the hemifused state, γ_{tot} , can be approximated by the sum of both components,

$$\gamma_{tot} = \gamma_0 + \gamma_m, \tag{4.5}$$

with γ_0 being the lateral drag on the particle by the surrounding fluid $4nm$ above the surface and γ_m the drag due to the stalk.

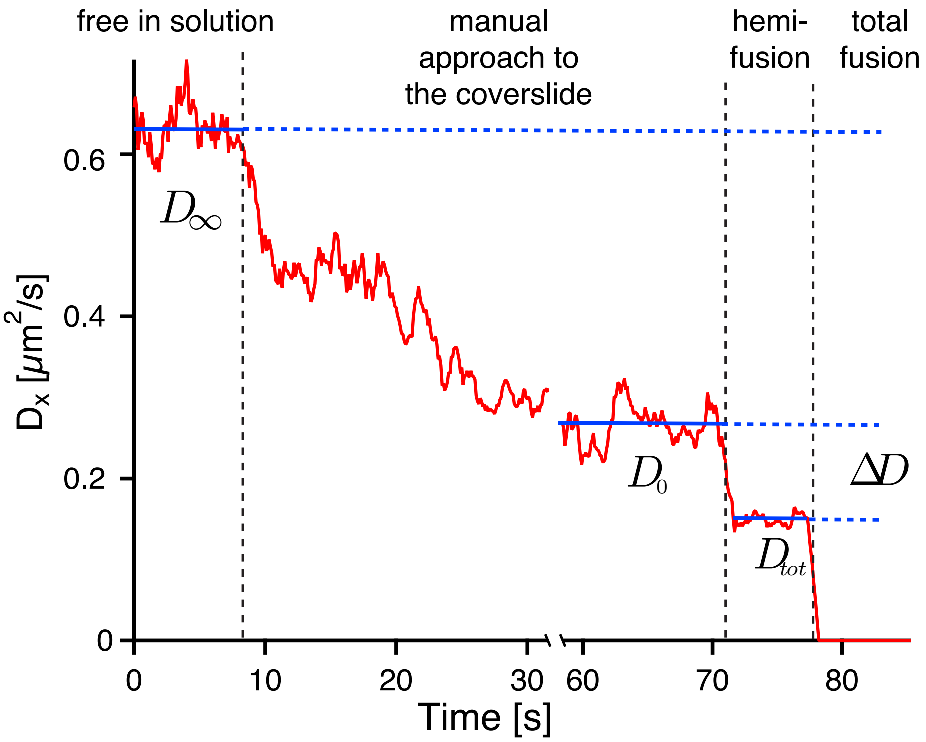

Figure 4.9: Calculated trace of the diffusion constant in the x-direction over time: At more than $10\mu m$ away from the coverslip, the particle is able to diffuse freely in solution. As the particle approaches the surface, the lateral diffusion constant decreases to about 1/3 of the diffusion constant in solution D_0. As the particle connects with the bilayer on the coverslip, the lateral diffusion constant drops suddenly by ΔD to the value D_{tot}. At total fusion, the particle becomes immobilized and the diffusion constant drops to zero..

One can expect that γ_m increases with its diameter and therefore, can serve as an independent measure for the characterization of the hemifusion state. For instance, intermediate fusion states with the same position histogram can be distinguished by a their difference in the drag γ_m. As discussed above, each time fusion between two membranes is initiated, there are two possible scenarios. First, the formed connection between the membranes can be transient (transient fusion), where the membranes remain connected only for a period of time, which we interpreted as a transient stalk formation. In the second possibility, the system can either remain in the bound state for the time of observation or transition through the bound state into the fully fused state. We interpreted this bound state as hemifusion, since the connection appears stronger. In the following we show that by evaluating the lateral diffusion constant of the tracer particle after fusion has been initiated, we can distinguish two states, which correlate well with our interpretation of a hemifused state and a state of a transiently formed stalk. Thus, although hemifusion and transient stalk formation show the same characteristic features in the position histograms, they can be distinguished by their average change in the diffusion constant upon contact. When we initiated fusion of DOPC coated beads with a supported DOPC bilayer we observed a distribution of changes in the diffusion constant ΔD upon initiation of fusion with two distinct peaks, indicating two different fusion intermediates (Figure 4.10). The peak at $D_m = 0.24 \pm 0.02 \mu m^2/s$ (±standard error of the mean) with a width of distribution of $0.17 \mu m^2/s$ belongs mainly to transient fusion and the one at $D_m = 0.044 \pm 0.006 \mu m^2/s$ with a width of $0.045 \mu m^2/s$ to hemifusion. D_m is calculated according to equation (4.5) with the relation of equation (4.4), where $D_0 = \frac{k_B T}{\gamma_0} = \frac{k_B T}{3\gamma_\infty}$ is the diffusion constant at the surface, $D_m = \frac{k_B T}{\gamma_m}$ the diffusion constant, which is due to the drag of the membrane connection and $D_{tot} = \frac{k_B T}{\gamma_{tot}}$ is the measured diffusion constant, which contains the total drag from the solution and the membrane. As shown above, the individual fusion events can be classified as hemifusion and transient fusion intermediates by evaluation of the position time traces. Such an analysis for the events contained in the histogram of ΔD reveals that the histogram's first peak is due to hemifusion and the second peak due to transient fusion.

4.8 Estimate of the contact area

Looking at the diffusion constant of the tracer particle during fusion reveals valuable insight into the fusion process as shown before. If the cause of the change in the diffusion constant due to the membrane connection is known, this allows to gain additional information about the stalk. Since the drag on the bead due to the membrane connection depends on the area of its intersection, it can be used to estimate the cross-sectional area. The theory of a diffusing cylinder in a two-dimensional fluid by Saffman and Delbrck [180] overestimates the area of connection because the target membrane is not surrounded by solution on both sides, but lies on a glass coverslip separated from it by only about $0.4 - 3nm$ of solution [18, 102, 144, 158]. The consequences of the changed boundary condition have been discussed by Sackmann and Evans

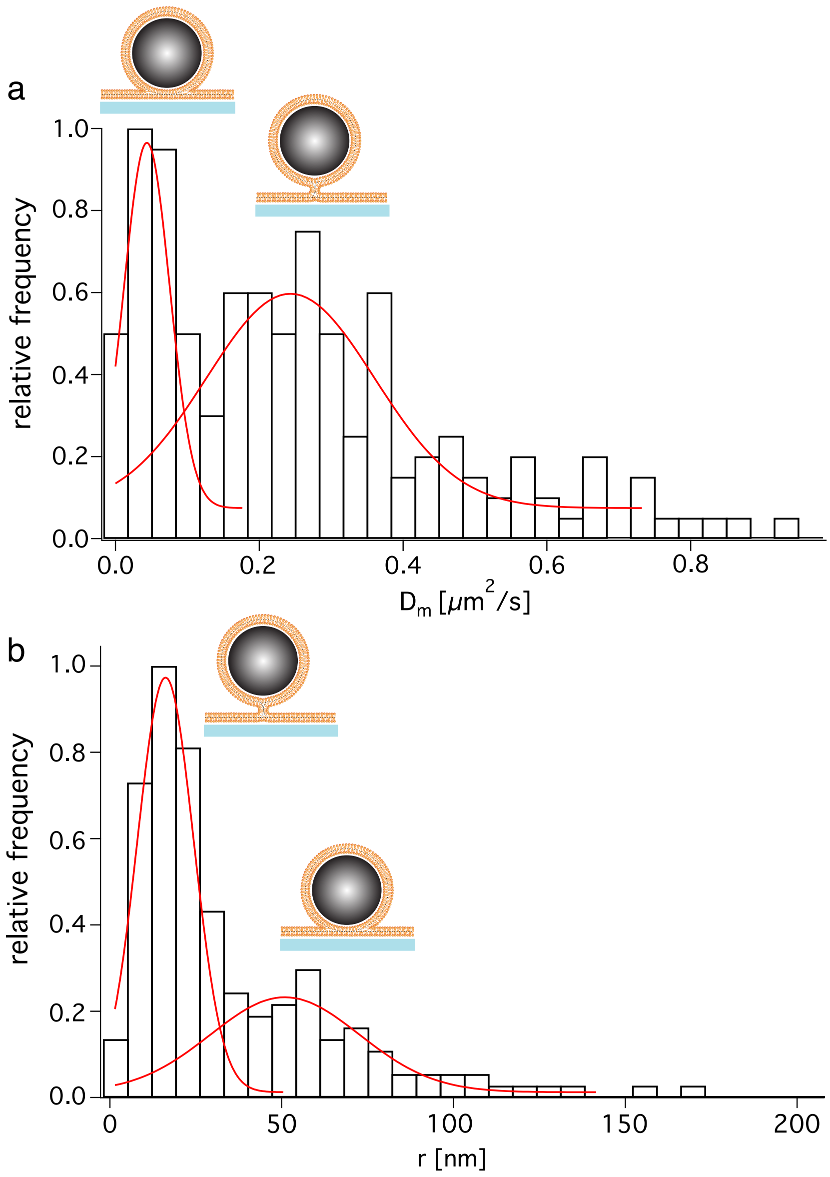

Figure 4.10: Histograms of DOPC fusion events. a) Histogram of the diffusion constant, which is caused by the additional drag of the membrane. Two peaks are noticeable. The peak at a smaller value of the diffusion constant is due to hemifusion and the one at a larger value to transient fusion. b) Histogram of the calculated radius of the connection. The two peaks of different fusion intermediates appear again. Transient fusion results in a smaller area of connection with a radius of $13nm$ than hemifusion with a radius of $47nm$.

[140, 59], whose theory takes the coupling of the membrane to the substrate into account. Due to the lack of a more appropriate theory, we will use the following equations to obtain a first approximation for the radius r of the connection:

$$D = \frac{k_B T}{4\pi\eta_m} \cdot \frac{1}{\frac{1}{4}\epsilon^2 + \epsilon\frac{K_1(\epsilon)}{K_0(\epsilon)}} \tag{4.6}$$

$$\epsilon = r \cdot \left(\frac{\mu_w}{h_g \eta_m}\right)^{1/2} \tag{4.7}$$

with and K_0 and K_1 being modified Bessel functions of zero and first order. The water gap between the membrane and the coverslip is h_g, the two-dimensional viscosity of the lipid membrane is η_m and μ_w the three-dimensional viscosity of the surrounding water. If we assume $\eta_m = h_m \mu_m$ [59], $h_m = 4.5nm$ [66], $\mu_m = 0.11 Pa \cdot s$ [164], $h_g = 0.4nm$, as measured for DOPC on glass [144, 158], and $\mu_w = 10^{-3} Pa \cdot s$, we can convert the D_m into the radius of the contact area. Figure 4.10b shows the relative frequency of radii calculated from the values in histogram Figure 4.10a. This histogram shows again the two pronounce peaks. The first peak at $13nm$ with a width of the distribution of $12nm$ is mainly due to transient fusion and the second peak at $47nm$ with a width of $31nm$ is due to hemifusion. The detailed analysis of the tracer particle's diffusion constant in the different fusion intermediates, shows two populations of radii of the contact area. The intermediate, which seems to be transient could be interpreted as a stalk and the other one as the size of the hemifusion diaphragm.

The changes in the diffusion constant of the tracer particle in different intermediate states were used to estimate the area of connection between the two bilayers in the fusion intermediates. For the stalk we got a radius of connection of $r_s = 13nm$, , which is larger than the previously observed values from x-ray diffraction of the stalk diameter in the rhombohedral phospholipid phase of approximately $4nm$ to $5nm$ [3, 231]. Although the radius of the stalk base is thought to be only a few nanometers, the curvature of the distal monolayers goes to zero at potentially much larger values [114]. This leads to measuring an effective stalk radius larger than the stalk base. The size of hemifusion diaphragms strongly depends on the geometry of the fusing membranes and can be estimated for specific cases [211]. It can range from a couple of nanometers in synaptic vesicles [234] to tens of micrometers in model systems [116]. Our calculations resulted in a value for the area of connection for the hemifusion intermediate of $r_{Hf} = 47nm$. Since in the case of hemifusion the size depends on the geometry of the system, a comparison to reported values is difficult. Nevertheless, a simple geometrical model should give an estimate of the approximate size of the hemifusion diaphragm for our fusion assay. If the micron-sized bead is submerged in a medium by $4.5nm$, which is the height of two membrane monolayers, the cross-sectional area of the bead at the interface has a radius of $66nm$. This estimate is a little smaller but comparable to our measured value. In general the size of the fusion intermediates depends on the lipid composition of the membranes and the shape of the stalk. In our model system it also depends on the strength of the coupling of the membranes to their respective substrates, the silica bead and the glass coverslip. This interaction is only represented in our calculations by the value of the gap height between the membranes and the surfaces. Additionally, one of the assumptions going into our calculation is that the drag components on the bead add up linearly, which might only be a valid first order approximation. The overestimation of the radii might arise from the fact that the estimate is not representative of the narrowest part of the intermediates. More likely, the neighboring lipids at the base of the intermediate need to be moved through the membrane as well, increasing the measured drag due to the membrane connection. This implies that the measured radii represent an effective radius, a sum of the intermediate radius and a surrounding area strongly interacting with the intermediate.

Chapter 5

Membrane fusion characterization: Combining the PFM with a fluorescent lipid mixing assay

To have an additional indicator for the different fusion intermediates, besides the position measurements with the PFM, we incorporated a fluorescent lipid mixing assay. This allows for the instantaneous measurement of the fusion intermediate due to a change in the fluorescent intensity as well as in a reduction of the position fluctuations. This assay works by having a fluorescently labeled lipid in a membrane formed around a tracer particle, Figure 5.1, but not in a target membrane on the coverslip. When the membranes hemifuse, the fluorophores in the outer layer of the bead diffuse off the bead into the target membrane, Figure 5.1b). This leads to a reduction of fluorescent intensity - ideally to half of its original value. Both membrane leaflets are connected when fusion completes, Figure 5.1c, and all the remaining fluorescently labeled lipids in the inner monolayer are able to diffuse off the bead. The fluorescence on the bead should decrease to a minimum value near zero. Therefore, monitoring the fluorescence signal of the bead will give an independent measure of membrane fusion, in addition to the PFM measurements. The present chapter integrates the fluorescent lipid mixing assay with the existing PFM assay.

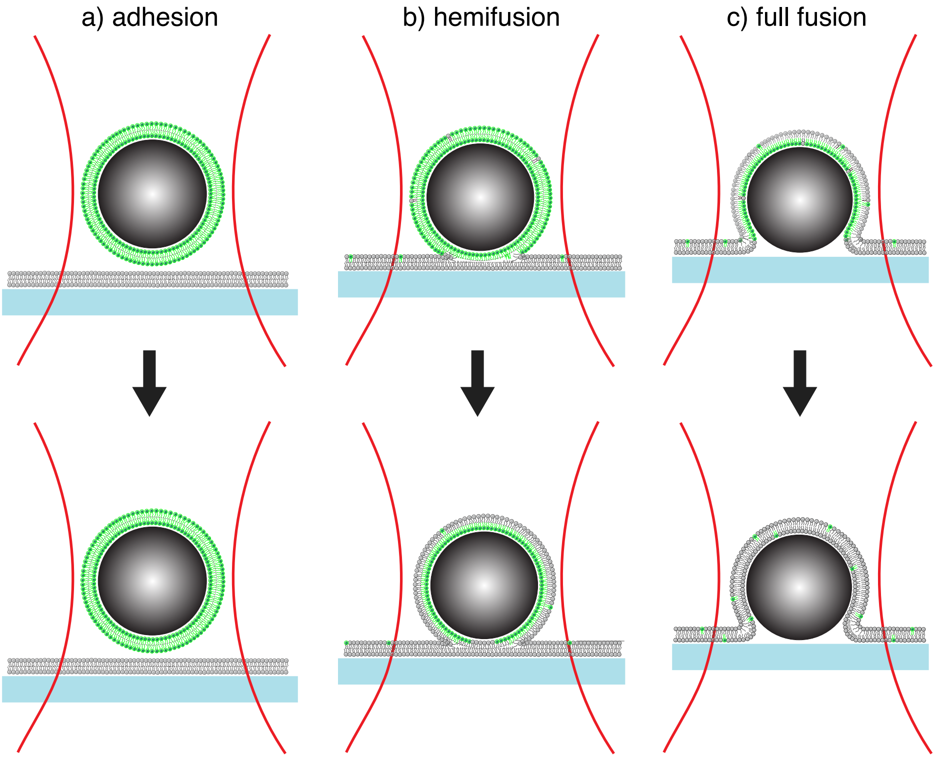

Figure 5.1: Sketch of a lipid mixing assay of a bead coated with fluorescently labeled lipids and a plain DOPC bilayer on the coverslip, in combination with the PFM. The top row of the sketch shows the lipid distribution right at contact and the lower row after getting close to equilibrium a) If the membranes only adhere and not fuse the fluorescently labeled lipids are confined to the sphere. b) Hemifusion is defined by connecting the outer monolayers, which allows the lipids on the outer layer of the bead to be exchanged with lipids from the coverslip bilayer. This will lead over time to a reduction in fluorescence intensity to half its initial value. c) When the bilayers fully fuse both monolayers connect and can exchange lipids. Due to the larger reservoir of plain lipids, the fluorescence intensity will decrease to zero.

5.1 Bulk fluorescence measurements

The fluorescence assay was tested in bulk fluorescence measurements, as a first step to combine fluorescence and position measurements,. A set of membrane coated beads containing fluorescent lipids was allowed to settle onto the supported membrane on the coverslip. There, the membranes can either hemifuse and stop, or continue to full fusion, or remain unfused. This allows to test the fluorescent mixing assay on many beads in the same sample at the same time.

5.1.1 Background calibration

In order to take quantitative fluorescence measurements in a large field of view, the measured intensities need to be corrected with respect to a potentially uneven illumination of the sample. To characterize the illumination, a $1\mu m$ commercial, fluorescent bead was scanned across the field of view. Figure 5.2 shows a long exposure ($140s$) image of a scanned bead. The bead was moved in discrete steps of $3\mu m$ and at each position the bead was kept in place for $200ms$. The Igor Pro particle finder was utilized to identify the location of a bead using a two-dimensional Gauss fit. Since the sample is a the same axial position, either the amplitude of the Gaussian or the volume integral can be used to determine the brightness of the bead at each location.

A calibration map, as shown in Figure 5.3, was made by centering a three by three micron area around the bead location and filling it with the value of the Gauss fit amplitude normalized to the maximum value in the field

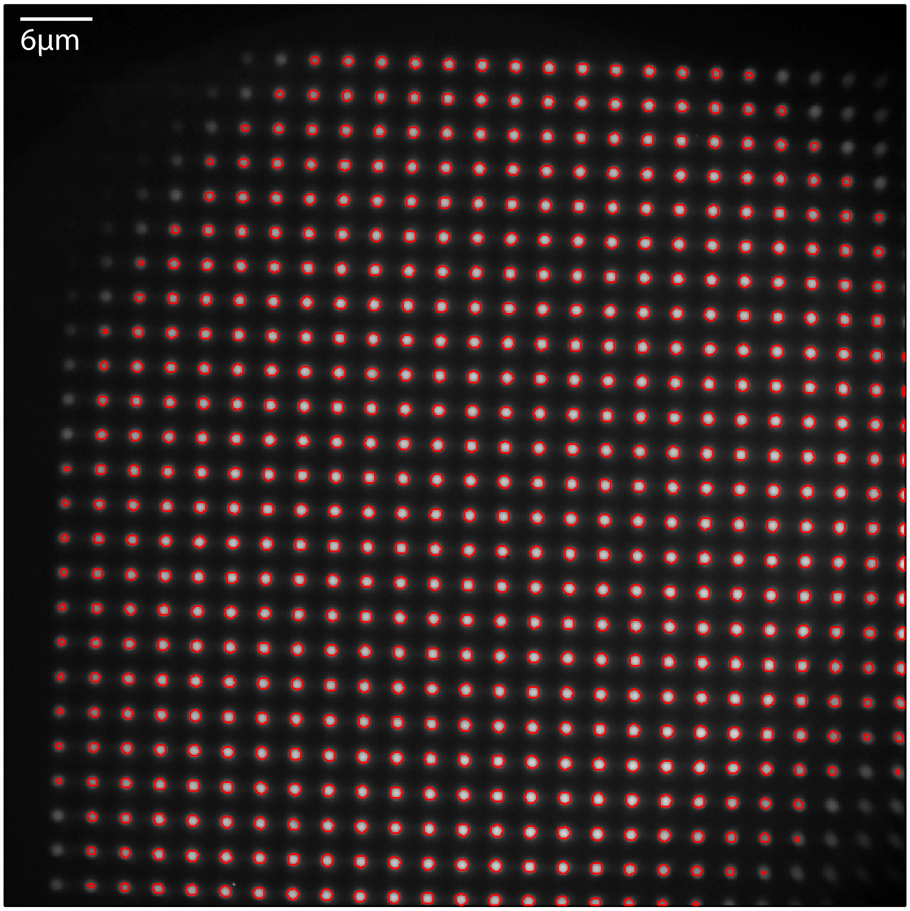

Figure 5.2: Image of a $1\mu m$ fluorescent silica bead, moved in discrete steps of $3\mu m$ across the field of view to quantify the inhomogeneous illumination of the field of view. The red rings mark the beads identified by the particle finder.

of view. This calibration matrix was used to normalize the fluorescence data within the field of view.

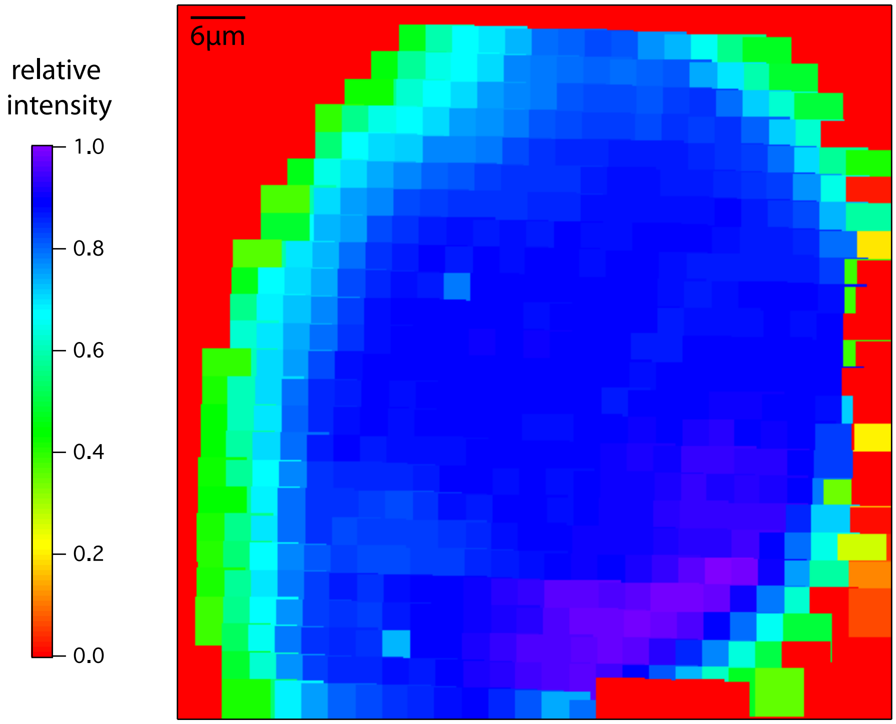

Figure 5.3: Graphical illustration of the calibration matrix for the inhomogeneous illumination of the field of view.

5.1.2 Fluorescence intensity distribution of the coated beads

In order to quantify how the fluorescence intensity of the coated beads changed due to hemifusion of fusion, the beads' initial intensity distribution and the reproducibility needs to be known. Therefore, multiple fields of view of lipid coated beads (1mol% fluorescein) adhered to a plain coverslip were imaged. All beads which were not clustered and were within the area where the illumination is at least 80% of its maximum, were fitted with a 2-dimensional Gaussian. The obtained intensity values - the volume integral over Gaussian fit - are corrected for stray light by subtracting the average background value measured around the each bead. Subsequently, the intensities are normalized with the measured calibration matrix according to their position on the CCD chip.

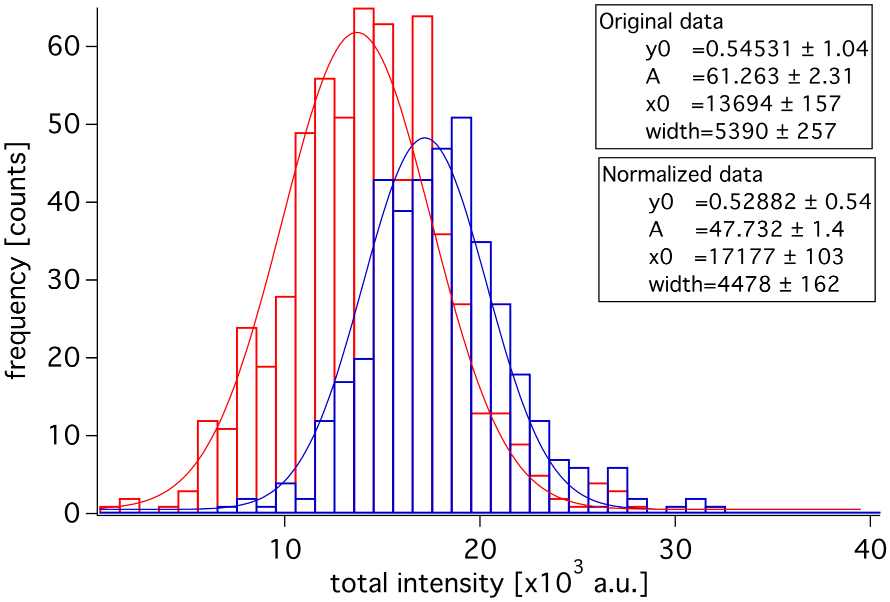

Figure 5.4: Distribution of the fluorescence intensity of the bilayer coated beads before and after calibration due to the inhomogeneous illumination. The original data is shown in red and the normalized data in blue.

Figure 5.4 shows the distribution of the fluorescence intensity of the bilayer coated beads before and after calibration of nine different fields of view.

A total of 607 beads were identified originally and 400 of those were normalized, because they were within the region where the illumination is at least 80% of its maximum value. The variation of the average intensity within different fields of view is less than 10%. The Gaussian fit of the intensity distribution of the original data has a peak at $13,694 a.u.$ and a width of $5,390 a.u.$. After normalization, the peak has shifted to a slightly higher value of $17,177 a.u$ with a narrower width of $4,478 a.u.$, indicating that the inhomogeneous illumination widens the originally present intensity distribution. The measured average value of intensity for the unfused bead yields a reference point for the bulk fluorescence measurements.

5.1.3 Fluorescent intensity distribution of the bulk fusion measurement

After measuring the average fluorescent intensity of a membrane coated bead, the change in the fluorescence intensity during the course of fusion can be measured. Theoretically, beads which are stuck in the hemifusion state should loose half of their fluorescence, since all fluorophores in the outer bilayer are able to diffuse off the bead into the surrounding membrane. The reservoir of lipids on the coverslip is large compared to the fluorescent lipids on the bead. Therefore, one can approximate that the fluorescent intensity of the bead disappears into the background. If the bilayer around the bead fuses completely with the bilayer on the coverslip, both membranes are connected to the bilayer on the coverslip allowing all fluorescently labeled lipids to diffuse off the bead.

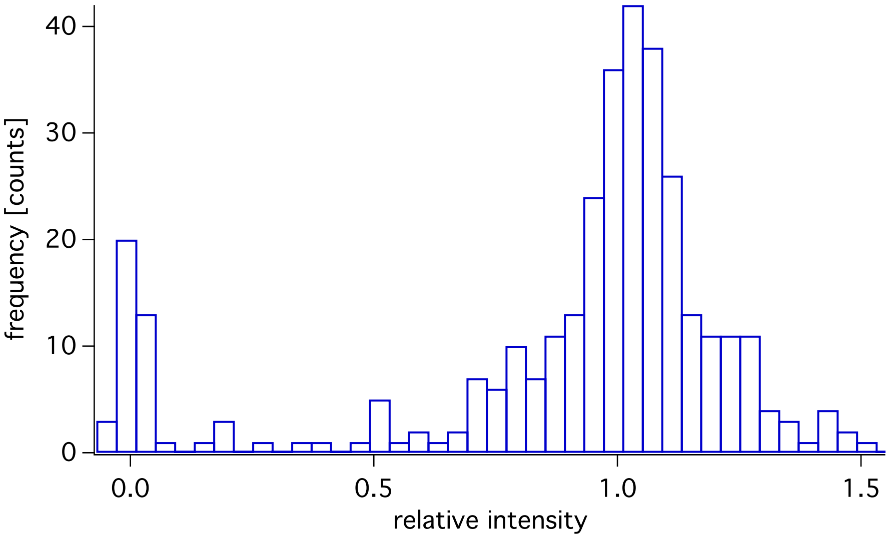

Figure 5.5: Distribution of the fluorescence intensity of the bilayer coated beads in different fusion intermediates. Most beads seem to not loose any fluorescence. There is a small peak around half of the maximum intensity, possibly corresponding to the hemifused state and another peak at zero intensity, which would be complete fusion.

The same beads that were used to determine the average fluorescence intensity, were filled into a sample chamber with a membrane bilayer coated coverslip. A bright-field image and a fluorescence image each were taken for ten different fields of view after approximately one hour after introduction of the beads into the sample. Additionally, a bright-field video was taken to quantify the mobility of the beads. The IgorPro particle finder was used on the fluorescent image to determine the position of each individual bead, which had some remaining fluorescence intensity. The beads which had lost all of their original fluorescence could not be identified in the fluorescence image alone. A comparison between the bright-field and the fluorescence image was used to determine the beads, which were immobilized and had lost their fluorescent signal completely. Their coordinates were added to a list to calculate the intensity at the area of those beads. The intensity of all found beads were calculated and calibrated if they were in the area of the image, with at least 80% illumination. In order to better compare the data of different fields of view, the calibrated intensities of the beads were normalized so that the average value of the unfused beads corresponds to one. In this normalization, the intensity of an unfused bead is approximately 1, of a hemifused bead 0.5 and of a fully fused bead 0. The histogram in Figure 5.5 shows the distribution of the normalized intensity of originally 644 beads. The histogram clearly shows the largest peak around 1, indicating a majority of unfused beads. A small peak can be seen at a value of 0.5, in agreement with a couple of beads remaining in the hemifused state. There is another significant peak around 0 which can be interpreted as beads whose membranes were fully fused. None of the beads identified as fully fused moved laterally which agrees with the idea that full fusion leads to immobilization as seen in the previous chapter. Also, nearly all of the unfused beads showed axial confinement. Axial confinement without fluorescent depletion is thought to be caused by hemifusion. The idea is that many beads are hemifused but retain their initial fluorescent intensity, because there is an energy barrier for the fluorescently labeled lipids to leave the surface of the bead.

5.1.4 Observation of the fluorescence intensity distribution over time

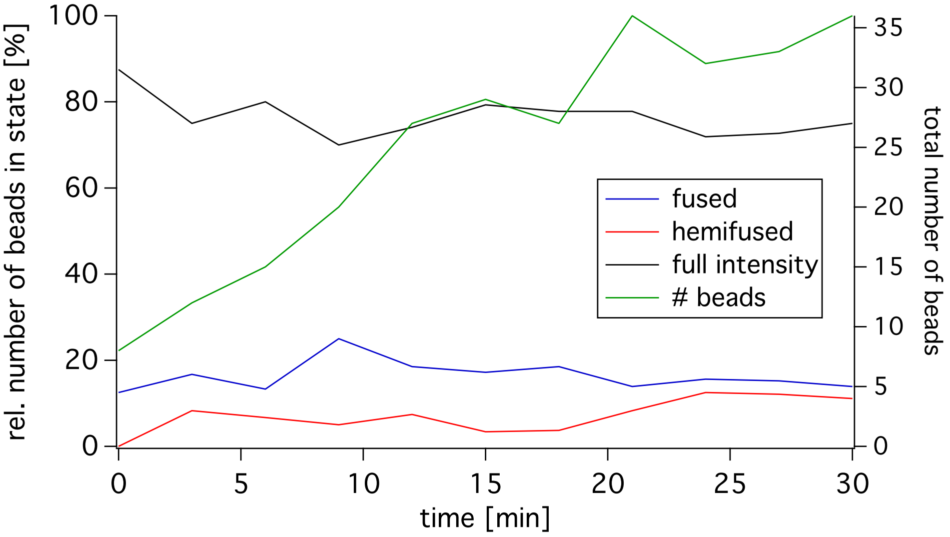

Figure 5.6: Time evolution of the fraction of fused, hemifused and unfused beads in bulk fluorescence experiments and the total number of beads.

To observe, how the distribution of fused, hemifused, and fully fused beads changed over time, a bulk fluorescent experiment was done at which fluorescent images were taken immediately after the introduction of the beads into the sample chamber and then in intervals of three minutes over the time period of 30 minutes. The procedure and analysis of the data was completed as described in the previous section. Beads coated with fluorescently labeled lipids were flowed into a sample chamber with a bilayer on the coverslip. Immediately after the first beads were sedimented onto the bilayer the first fluorescent image was taken. Bright-field videos were taken after nine minutes and and at 29 minutes in order to identify beads which were immobilized and had lost their fluorescence due to fusion. A histogram of the measured intensities, similar to Figure 5.5 was made for each image. From this histogram the number of beads which were fused, hemifused, or unfused was determined. The fully fused beads were identified by inspecting the bright-field movie and also by looking which beads had lost their intensity between consecutive frames. In order to capture the initial fusion events, the first fluorescent image was taken right after adding the beads. Since beads reach the surface by sedimentation, more beads will diffuse into the field of view over time increasing the number of beads which can be identified in each frame. Figure 5.6 shows the time evolution of the fraction of beads which are in the different fusion intermediates. As mentioned before, the total number of beads shown in green, on the right axis, increases over time. The fraction of beads which retain their fluorescence (left axis) only slightly decreased over the course of 30 minutes, from 88% to 75%. The relative number of fused beads remained practically the same at 13%. The percentage of hemifused beads increased from none to approximately 11%. This implies that the probability for full fusion under these conditions was low, 13%. Also, more than 80% of the beads retained their initial fluorescence intensity even though they showed axial confinement, again implying that there is some energy barrier for the fluorescently labeled lipids to diffuse off the sphere.

5.2 Correlation of fluorescence and position (PFM) measurements for individual fusion events

As shown in the bulk measurements, the fluorescent signal of the lipid coated beads should correlate to the fusion state they are in, and therefore also to their position fluctuations. A fully fused bead shows the strongest confinement and should show no fluorescent signal. In the hemifusion stage, a bead shows axial confinement without lateral confinement and has half of its initial fluorescence. Unfused beads should show no confinement and maximum intensity. To measure the correlation of fluorescent signal and position fluctuations on single beads fusion was initiated with an optical trap, as previously described, and the fluorescent intensity of the bead was measured simultaneously.

5.2.1 Photo-bleaching by the trapping laser

In order to measure the fluorescence intensity of the trapped bead correctly caution needs to be taken that the bead is not photo-bleached by two-

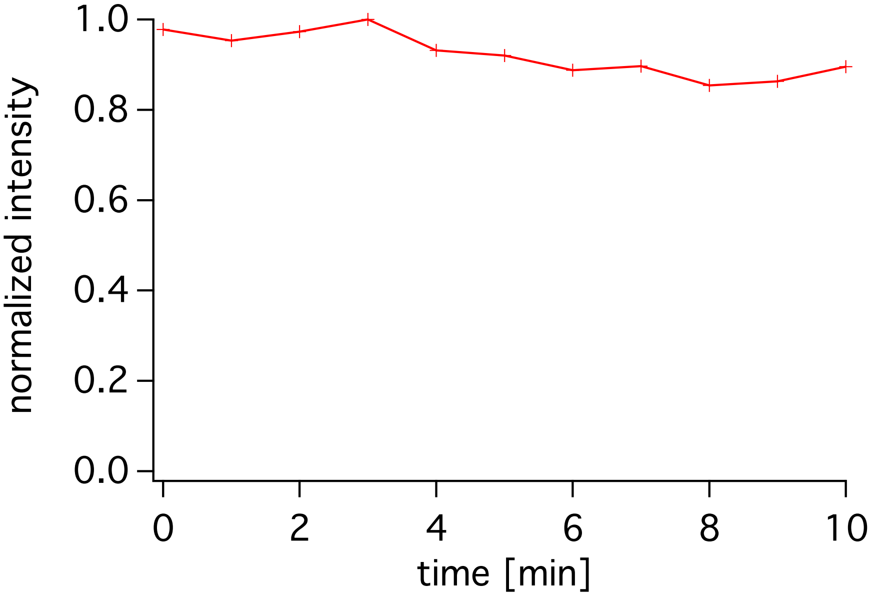

Figure 5.7: Photo-bleaching of a trapped, membrane coated bead. Over the course of 10 minutes the intensity has decreased less than 8%.

photon excitation due to the $1064nm$ trapping laser. Figure 5.7 shows the fluorescence intensity of a membrane coated, optically trapped bead over 10 minutes, during which the measured intensity decreased about 8%. This indicates, that the bleaching due to two-photon excitation of the trapping laser is low, since some loss of the intensity is due to photo-bleaching caused by the fluorescence excitation. An additional experiment to support this conclusion was made: the intensity of the trapped bead was measured over 30 minutes, by recording only a few images to minimize bleaching caused by the fluorescence excitation. After 30 minutes, the intensity of the trapped bead did not decrease. Therefore, any loss of fluorescent signal during fusion experiments can be assumed to be caused either by bleaching due to the fluorescence excitation or by fluorescently labeled lipids diffusing off the sphere across the connection between the membranes formed in the fusion intermediates.

5.2.2 Individual fluorescence intensity and instantaneous PFM measurements

To combine the PFM and the lipid mixing assay fusion experiments, a membrane coated (1mol% fluorescein) bead was trapped and brought in contact with a plain lipid bilayer on the coverslip. For the duration of the individual fusion experiments, the position of the bead was measured on the QPD to identify the fusion intermediates and the fluorescence signal was monitored with the CCD camera to observe lipid mixing.

The fluorescent intensity of a trapped, coated bead was measured, while

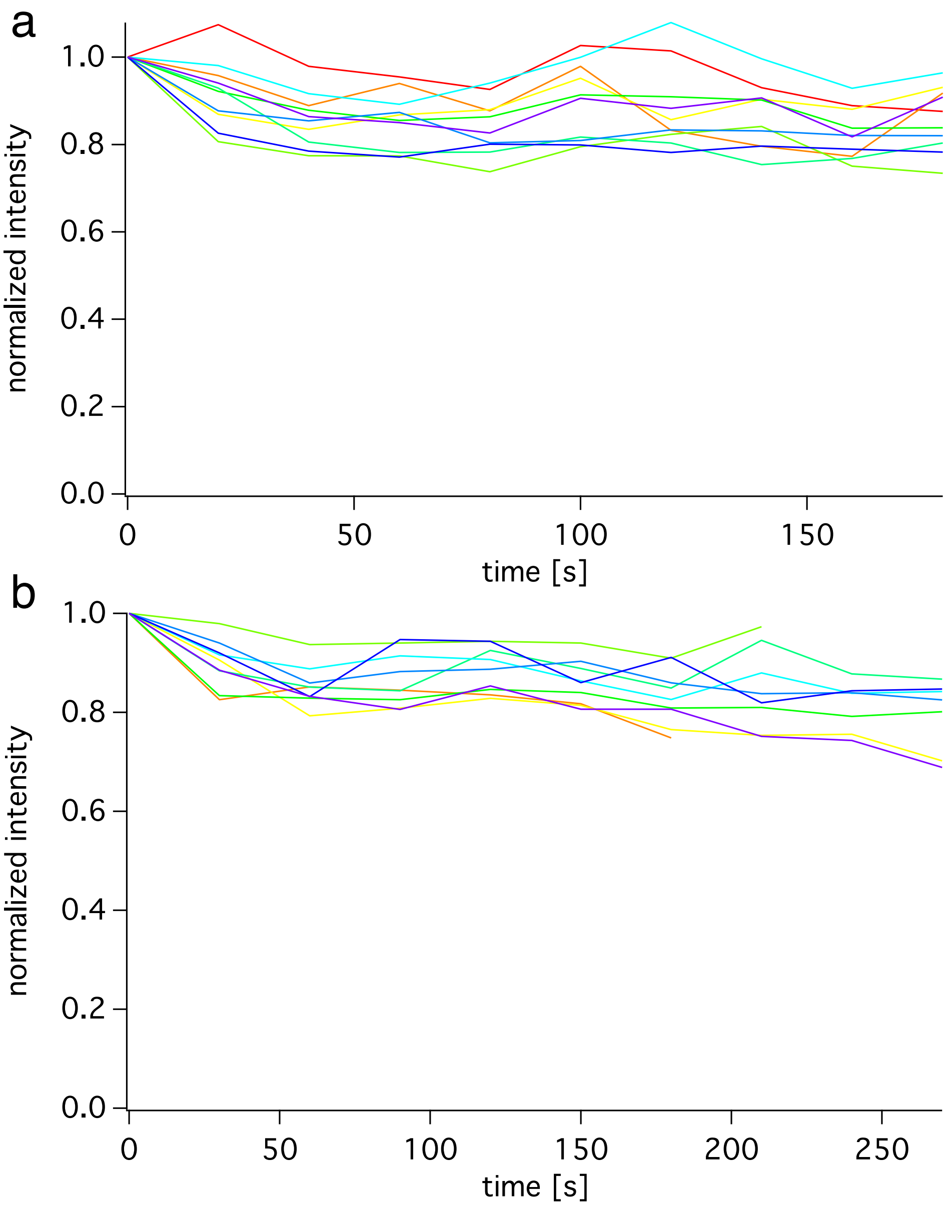

Figure 5.8: a) Fluorescence intensity of a coated, trapped bead during the approach to the surface. The intensity of the trapped bead has some fluctuations and shows an average signal reduction due to photo-bleaching. b) Fluorescence intensity of a coated, trapped bead during hemifusion. The signal does not show any additional reduction caused by hemifusion.

the bead was trapped in solution, approached and brought into contact with a plain coverslip to verify that there is no unknown change in the fluorescence signal. Figure 5.8a) shows the normalized fluorescence intensity of ten different beads over time. Images were taken every $20s$. In the first frame the bead is trapped in solution. During the second frame the trap approaches the surface and initial contact was made in the third frame. For the remainder of the time, the bead stayed in contact with the surface. The intensity of fluorescence shows a fairly constant signal over time, as seen in Figure 5.8a). Although there is some variation in the data and some loss of fluorescence due to bleaching. Overall, the majority of intensity remains above 80% of its initial value, indicating that the loss of 50% of the fluorescence signal due to hemifusion should be clearly measurable.

Fusion experiments with the same lipid-coated beads were conducted similarly to those just described. The coated bead is trapped in solution and the first fluorescence image is taken. In the second frame the bead approaches the membrane coated coverslip and a connection with the membrane was made from the third frame onward. All ten fusion attempts showed the characteristics of hemifusion in their position signal, sometimes also a transition to full fusion. Figure 5.8b) shows the normalized fluorescent intensity of the trapped beads over time. Notably, almost 200s after the membranes formed a stalk or fused, the fluorescent signal of the beads show no significant change. The graph in Figure 5.8b) is essentially identical to the one in Figure 5.8a), indicating the fluorescently labeled lipids are hindered from diffusing off the sphere

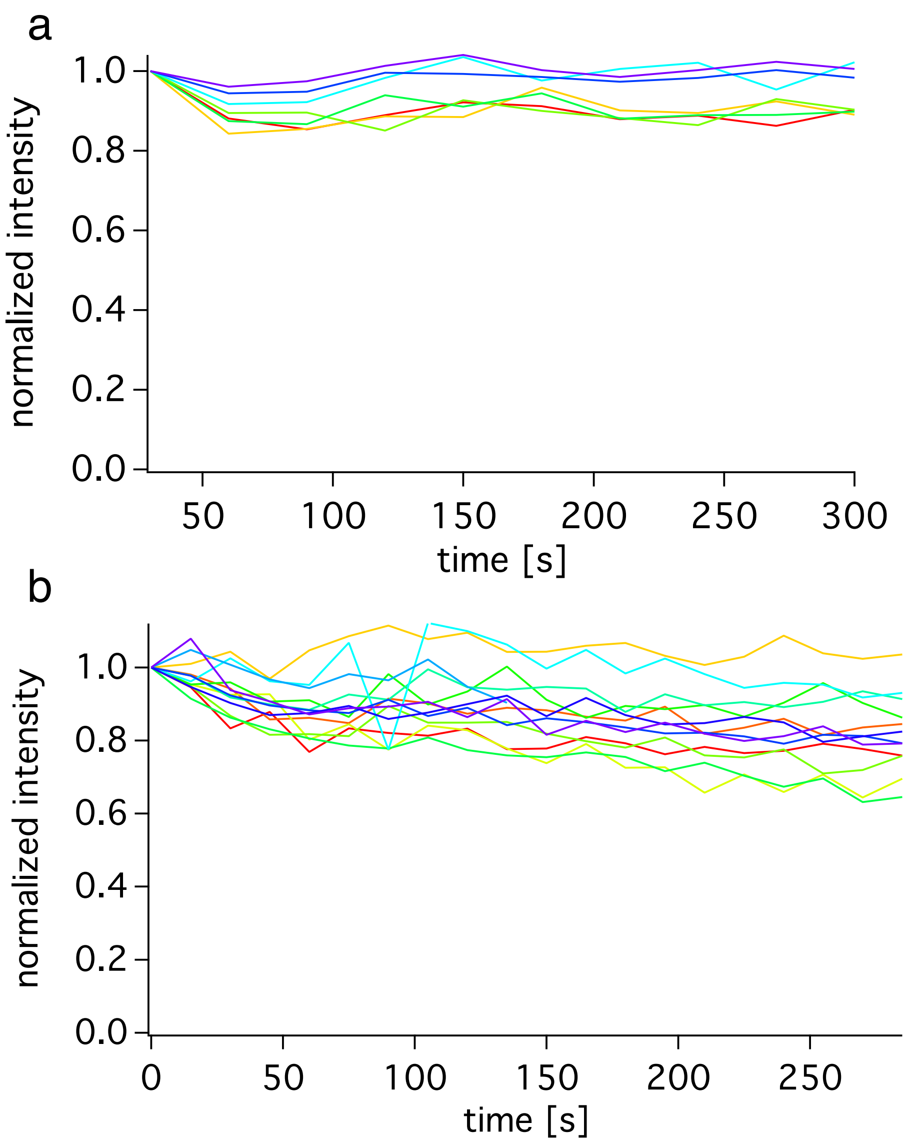

Figure 5.9: Fluorescence intensity of a coated (a) NBD 12-chain, b) NBD 6-chain), trapped bead during hemifusion. The intensity of the trapped beads have some fluctuations and shows an average signal reduction due to photobleaching, but no additional loss in intensity due to hemifusion.

into the membrane on the coverslip. One reason the lipids do not diffuse could be that the fluorophore attached to the lipid head group is too large to diffuse through the stalk, due to the high local curvature.

If this is true that high curvature prevents lipid diffusion, a lipid which has the smaller fluorophore NBD attached to the fatty acid chain instead of the head group should be able to diffuse through the stalk more easily. To test this hypothesis the fusion experiments combined with the lipid mixing assay were repeated for coated beads, which included a lipid that had NBD attached to one of the fatty acid chains after 12 carbon bonds and also one after 6 carbon bonds. Figure 5.9a) shows the fluorescent intensity of the trapped bead, coated with DOPC and 1mol% NBD labeled lipids with a 12-bond chain. In all fusion attempts, a hemifusion diaphragm was formed either between 0s and 30s or between 30s and 60s. The fluorescent intensity shows less variance and less bleaching as in the case of fluorescein labeled lipids, but no drop in intensity due to hemifusion. The same experiment was repeated with a bead coated with DOPC and 1mol% NBD labeled lipids with a 6-bond chain. The results are shown in Figure 5.9b). For those fluorescently labeled lipids, the variance in the fluorescent intensity as well as the bleaching is comparable to the fluorescein tagged lipids. The quality of the signal is sufficient to detect a reduction of the fluorescence to half its original value.

All these experiments indicate that an energy barrier existed for the tagged lipids to diffuse through the stalk into the surrounding membrane.

5.2.3 The rare case

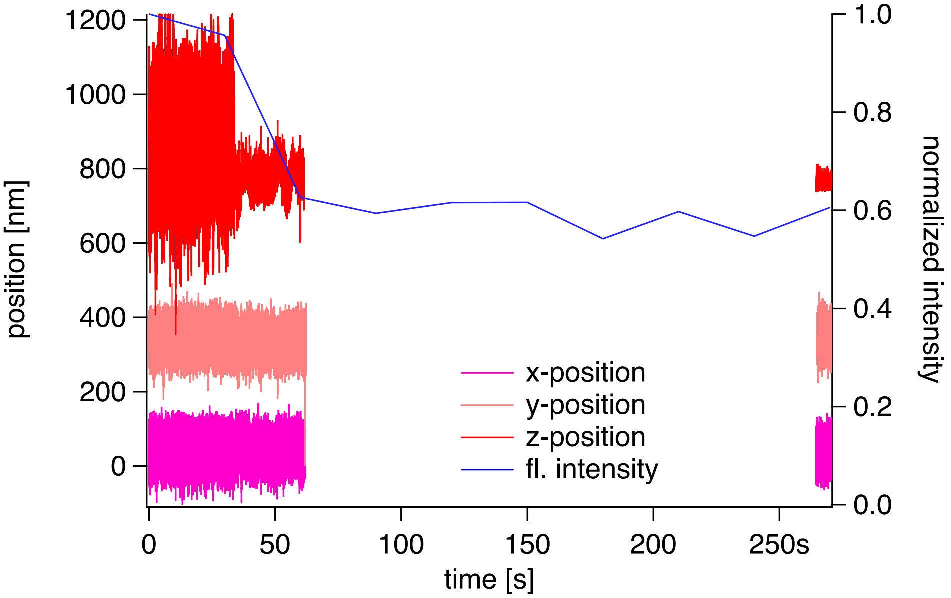

Figure 5.10: Fluorescence intensity loss of a coated, trapped bead during hemifusion. The intensity of the fluorescence signal has its maximal value in the first two frames (up to $t = 30s$). As seen in the position fluctuations, the transition into hemifusion occurs at $t = 33.8s$. The fluorescence intensity decreases at the following measurement at $t = 60s$, to approximately 60%. As the position data shows, the bead remains in the hemifused state for the remaining $240s$. The fluorescence intensity remains between 50 and 60%.

In the majority of fusion experiments, the fluorescent intensity remains constant regardless of hemifusion, Figure 5.9 and 5.8. As seen in the fluorescence bulk experiments, fluorescently tagged lipids are able to diffuse off the sphere in less than 10% of all hemifused beads, over long periods of time. This also implies that there should be the rare case in which hemifusion will lead to a loss of fluorescence. This case is shown in Figure 5.10. The fluorescent intensity of the trapped bead decreased from its maximal value to approximately 60% between $t = 30s$ and $t = 60s$. This coincided with the detection of hemifusion from the reduction of the z-position fluctuations at $t = 33.8s$. In this case the measured transition into hemifusion led to a reduction in the fluorescent signal. Unfortunately, this was observed too rarely to obtain reasonable statistics.

5.3 Simulations of the fluorescent signal

Both the fluorescent bulk measurements as well as the individual fluorescence measurements on trapped coated beads, indicate that an energy barrier exists, which prevents the exchange of fluorescently labeled lipids on the bead with their environment. In order to obtain an estimate of how the diffusion behavior is influenced by an energy barrier and the diameter of the stalk, a Brownian dynamics simulation was conducted.

Model parameters and assumptions

1. The simulation is performed on a square with an area of $2.96\mu m^2$ equal to the surface area of a sphere with a radius of $R = 0.485\mu m$, with periodic boundary conditions.
2. The fluorescently labeled lipids are free to diffuse with a diffusion constant of $D = 5\mu m^2/s$ [203, 191, 140].
3. The lipids are treated as point-like objects and are randomly distributed across the surface.

4. The time steps are chosen to be smaller than $2.5 \cdot 10^{-6}s$, the time during which the lipid would make an average step of $5nm$, the estimated size of the stalk.

5.3.1 Brownian dynamics simulation of the fluorescence signal

To find a description of the dynamics we start from the equation of motion, the Langevin equation [58].

$$m\dot{v} = -\gamma\dot{x} + F(t) \tag{5.1}$$

$F(t)$ is a random force and $-\gamma\dot{x}$ a friction term with γ being the Stokes drag. When inertia is neglected, the equation reduces to

$$\gamma\dot{x} = F(t) \tag{5.2}$$

and can be rewritten in terms of the displacement of the particle:

$$dx = \frac{dtF(t)}{\gamma} \tag{5.3}$$

The random force $F(t)$ can be written as

$$F(t) = C\zeta(t) \tag{5.4}$$

where $\zeta(t)$ is described by the normal distribution and has the following properties:

$$\langle\zeta_i\rangle = 0 \tag{5.5}$$

$$\langle\zeta_i^2\rangle = 1 \tag{5.6}$$

$$\langle\zeta(t_1)\zeta(t_2)\rangle = \delta(t_1 - t_2) \tag{5.7}$$

Looking at a spatial displacement Δx within the time interval $\tau = Ndt$, the displacement can be written as

$$\Delta x = \frac{dt}{\gamma} \sum_{i}^{N} F(t_i). \tag{5.8}$$

Calculating the MSD results in

$$\begin{aligned} \langle \Delta x(\tau)^2 \rangle &= \left(\frac{dt}{\gamma} \right)^2 \langle (\sum_{i}^{N} F(t_i))^2 \rangle & (5.9) \\ &= \left(\frac{dt}{\gamma} \right)^2 \sum_{i}^{N} \langle F(t_i)^2 \rangle, & (5.10) \end{aligned}$$

where the properties of the covariance was applied (Eq. 5.7). $\langle F(t_i)^2 \rangle$ is the definition of the variance and can be expressed with Eq. 5.4 and the properties of the variance as

$$\langle F(t_i)^2 \rangle = C^2. \tag{5.11}$$

Substituting the MSD in one dimension $MSD = 2D\Delta T$ and equation 5.11 into equation 5.10 results in

$$C = \sqrt{\frac{2D\gamma^2}{dt}}. \tag{5.12}$$

Equations 5.4, 5.3 and 5.12 combined will give the equation for the one-dimensional displacement of a Brownian particle

$$dx = \sqrt{2Ddt} \cdot \zeta(t). \tag{5.13}$$

The Brownian dynamics simulations were tested by simulating a two-dimensional random walk within the square area with periodic boundary conditions. A random walk with ten million steps was simulated for time steps from $\Delta t = 10^{-10}s$ to $\Delta t = 1s$. The MSD was calculated from the position time traces and used to determine the diffusion constant. For multiple runs, the resulting diffusion constants deviated from the diffusion constant fed to the simulation by less than 0.3%.

5.3.2 Test of the simulation: Simulating FRAP experiments

FRAP experiments were simulated and compared to the known diffusive behavior of the molecules. Lipids were randomly distributed over the square surface of $2.96\mu m^2$. The density of lipids in a circular area of interest with radius $r_{ROI} = 0.3\mu m$ was measured. Subsequently, the region was deprived of the lipids, the "bleaching" process. In each time step the position of the remaining lipids was updated according to equation 5.13 and the number of molecules present in the bleached region was recorded. A recovery curve was generated by plotting the amount of lipids present in the area of interest versus time. Fitting the recovery curve with an exponential function, the diffusion constant of the molecules could by calculated using the following equation [197].

$$D = 0.224 \cdot \frac{r_{ROI}^2}{t_{1/2}} = 0.224 \cdot \frac{r_{ROI}^2}{\tau \ln 2} \tag{5.14}$$

r_{ROI} represents the radius of the bleached circle, $t_{1/2}$ the time for half recovery and τ is the time constant from the exponential fit of the recovery curve.

To calculate the diffusion constant from the simulated recovery curve, the simulation was repeated nine times with the following parameters: the

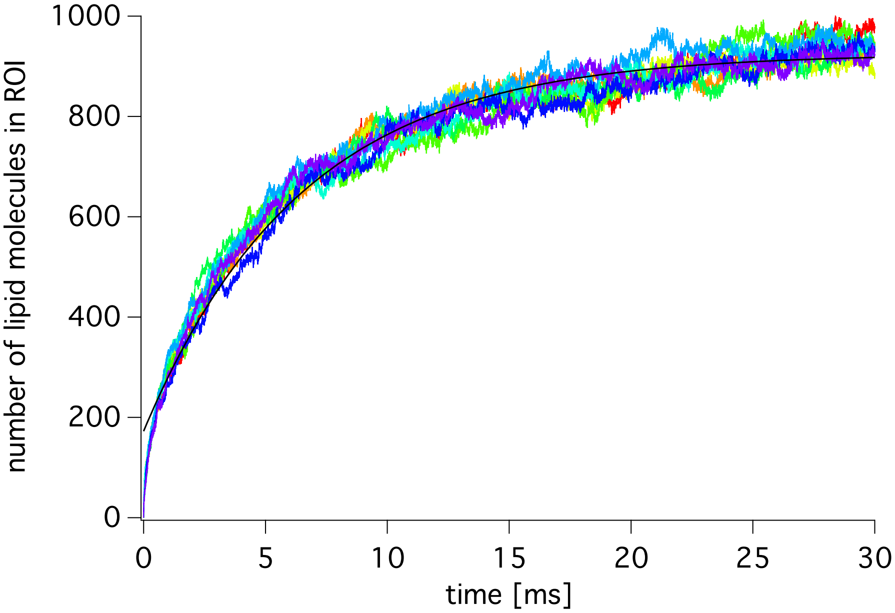

Figure 5.11: The simulated recovery curves of nine FRAP experiments with the same simulation parameters are plotted including the average exponential fit. The calculated diffusion constants of the lipids resulted in $D_{calc} = (4.6 \pm 0.5)\mu m^2/s$, which is within error of the input parameter of $D = 5\mu m^2/s$.

diffusion constant of the lipids was $D = 5\mu m^2/s$; the radius of the area of interest was $r_{ROI} = 0.3\mu m$; and 10,000 lipids were simulated over 30,000 time steps with $\Delta t = 10^{-6}s$. All individual recovery curves were fitted and the diffusion constants were extracted. The average diffusion constant was $D_{calc} = (4.6 \pm 0.5)\mu m^2/s$, which is within error of the input parameter.

These simulations show that this method is well suited to analyze the diffusive behavior of lipids leaving or entering a reservoir.

5.3.3 Simulation results and implications for the interpretation of the experimental observations

First, to get an idea of the timescale expected in the fluorescent lipid mixing experiments, fluorescent lipids diffusing on the surface, which were allowed to escape through a small opening were simulated. This mimics the diffusion of lipid molecules in the membrane bilayer on the silica bead. If the membranes hemifuse, a small connection is formed, the stalk, through which the fluorescently labeled lipids can diffuse off the sphere into the membrane on the coverslip.

1,000 lipids were randomly distributed across the square with a length of $1.7\mu m$, except in the region of interest. At each time step, $\Delta t = 10^{-7}s$, the position of the particles was updated according to equation 5.13 with a diffusion constant of $D = 5\mu m^2/s$. If the newly calculated position of the particle fell within the previously defined ROI, then it was deleted from the simulation. The number of particles in the simulation was recorded at each time step. Figure 5.12 shows a typical curve of the number of particles, equivalent to the measured fluorescent intensity, versus time with a radius of the ROI, $r = 30nm$. $30nm$ is the approximate radius which was calculated from the measured diffusion constants in the PFM experiments. The intensity dropped to 10% of its initial value in $0.64s$.

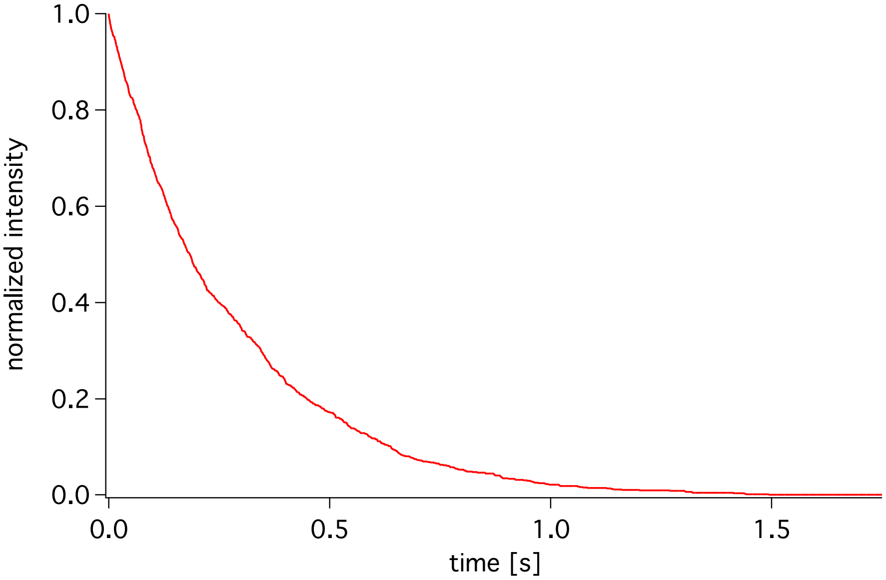

Figure 5.12: Simulation of lipid mixing. The intensity of the coated bead is shown versus time. The radius of the region of interest is 30nm.

Figure 5.13a) shows the time necessary for 90% of the lipids to diffuse off the sphere strongly depends on the radius of the opening. The times ranges from $0.05s$ for a radius of $500nm$, to $1.1s$ for a radius of $2nm$. Even for the opening of $2nm$, which is the smallest size a stalk can have, the time of fluorescence loss is still significantly smaller than the time between frames in the lipid mixing measurements, $30s$. This implies, that for regular lipid mixing the loss of fluorescent intensity should occur between two frames. The diffusion constant of the lipids, also influences the expected time scale. Figure 5.13b) shows the time it takes to lose 90% intensity depends on the diffusion constant for a constant radius of $r = 5nm$. Although, the time increases five-fold when the diffusion constant decreases to $D = 1\mu m^2/s$, similar to the diffusion constant of a supported membrane on a bead [129], the time of $5.1s$ is still shorter than the time between frames. Therefore, without any additional energy barrier, all the lipids should be able to diffuse off the sphere within a time shorter than the time between frames.

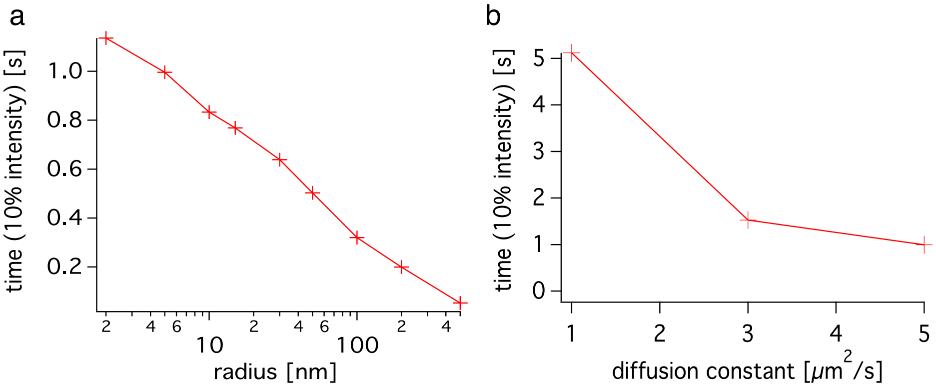

Figure 5.13: Simulation of lipid mixing, dependence on diffusion constant and radius. The time necessary for 90% of the lipids to diffuse off the sphere is dependent on a) the radius of the opening and b) the diffusion constant of the lipids.

In the experiments, no loss of fluorescence is observed within minutes, and the results of the simulation show lipid mixing, i.e., the loss of 90% of the signal, within seconds do not agree. Therefore, an energy barrier was introduced into the simulation. The simulation was repeated as described above, with the exception that every time a particle crossed into the region of interest - and would thus formerly be taken out of the simulation - a barrier was present which the particle could cross only with a probability of $p = e^{-\frac{\Delta E}{k_B T}}$. If the particle's new coordinates were in the ROI, but due to the calculated probability was not allowed to exit through the ROI, the particle remained at its current position. In the next time step new coordinates were calculated which could either be somewhere else on the surface, or in the ROI where it got another chance at crossing the barrier. Figure 5.14 shows the dependence of the time to loose 90% of the intensity on the energy barrier for a ROI of $r = 15nm$ and a diffusion constant $D = 5\mu m^2/s$. If there was no energy barrier, the time to decrease the signal to 10% was $0.8s$. An energy barrier of $5k_BT$ increased the time to $3.3s$. And an energy barrier of $E_B = 10k_BT$ increased the time to $415s = 6.9min$. If the energy barrier in our experiment was on the order of $10k_BT$, it would have been hard to measure a distinct loss of fluorescence over time due to noise and photo-bleaching.

5.4 Summary and Outlook

In the first part of this dissertation, I presented a novel assay to study fusion events with high temporal and spatial resolution which was used to characterize fusion intermediates by two-and-three-dimensional position histograms. In our experiment it is possible to observe the individual fusion

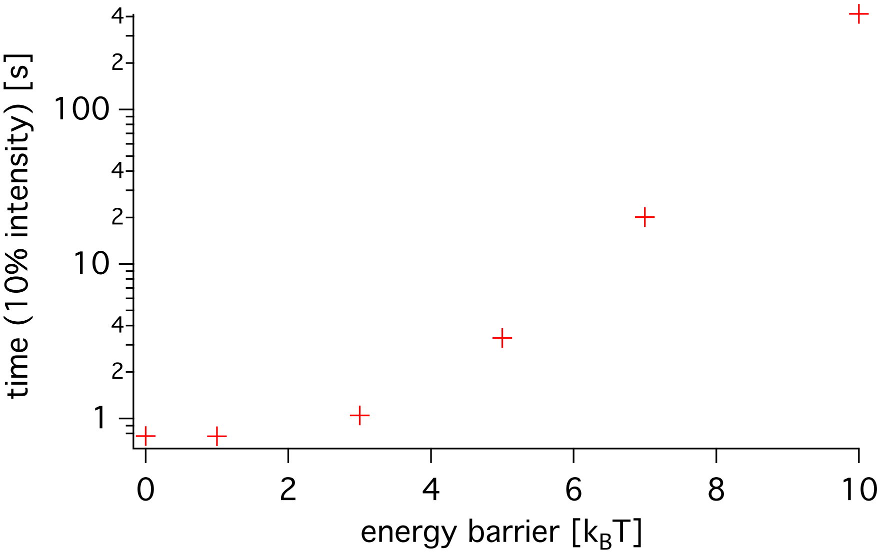

Figure 5.14: Simulation of lipid mixing, dependence on energy barrier. The time necessary for 90% of the lipids to diffuse of the sphere is plotted for different energy barriers with a ROI of $r = 15nm$.

intermediates for long periods of time, which is necessary for their detailed characterization and the calculation of their energy barriers. The energy barrier for the formation of a hemifusion diaphragm is found to be larger than $10k_BT$. The fusion intermediates are stable over long periods of time and have transitions faster than $3.8ms$ or $0.4ms$ respectively. From the position data, the stalk and hemifusion diaphragm radii were calculated to be $r_{stalk} = 13nm$ and $r_{hf} = 47nm$ respectively. This assay combined with a lipid mixing assay, was introduced and tested.

The assay could be further altered to more closely mimic biological membranes by reducing the strong coupling of the membranes to the substrates. A reduction of the coupling to the substrate can be achieved by supporting the bottom membrane on spacer molecules like polyethylene oxide polymers [153, 179], DNA [47] or a porous silicon substrate [87, 142]. This reduces the strong coupling to the glass and thus increases the mobility of the bottom monolayer and might help with the lipid mixing. Additionally, lifting the bottom membrane away from the substrate might enable the observation of the fusion pore formation because the tracer particle will no longer be immobilized when the fusion pore opens. Incorporation of a fluorescent lipid mixing assay [134] could result in additional insight into the time evolution of lipid exchange and the transition between fusion intermediates. This assay can be further used to study the influence of fusion proteins on the fusion pathway. The fusion pathway and position fluctuations in different intermediate states of protein-free bilayer fusion and fusion induced by fusion proteins, can be compared side by side and insight might be gained on the mechanisms of various fusion proteins.

Part II

Glucose starvation in fission yeast

Chapter 6

Introduction to Cell Freezing

6.1 Introduction to starvation in yeast cells

Similar to the animal's "fight-or-flight response" to stress, which is controlled by hormones at the level of the organism, cells also have a stress response. Stresses on cells can be oxidative, osmotic, anaerobic, genotoxic, and temperature related and often result in deformation or damage to proteins, DNA or macromolecules. The cellular stress response assesses and counteracts the damage, and can induce apoptosis, cell death, if the tolerated limits are exceeded [117]. Cellular stress responses to molecular damage often share common elements. Strains which result in a change in the cell's environment, homeostatic stresses, are often stressor specific [117].

A very common stress in nature is nutrient deprivation. If fission yeast cells experience a lack of nutrients they enter a quiescent, non-proliferative state until they receive fresh nutrients [229]. Growth medium contains two nutrient sources for yeast cells, glucose and nitrogen. Nitrogen starvation is well researched [159, 201, 148, 108]. Upon nitrogen starvation *S. pombe* goes through two more cell cycles. Since the cell limits its growth immediately upon nutrient deprivation, the resulting cells are short and round. This state, since it varies from all previously known phases in the life cycle, is often referred to as G0 [229]. Glucose starvation in fission yeast is less studied. Short term glucose starvation leads to the formation of cytoplasmic RNA granules, which also occurs when cells are exposed to heat stress, oxidative stress, and osmotic stress, but not during nitrogen starvation [157].

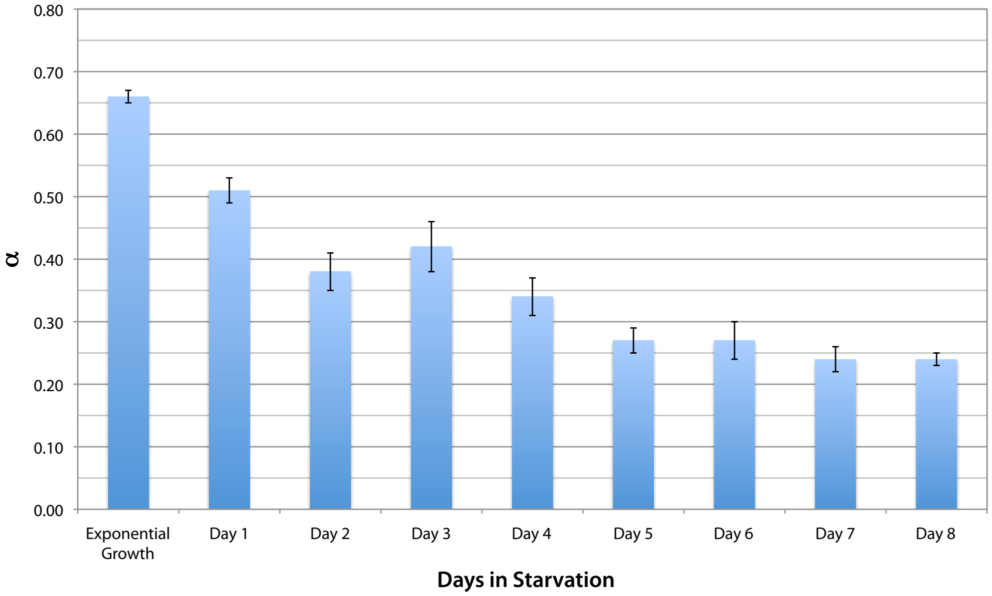

Figure 6.1: Alpha value of exponentially growing fission yeast cells and yeast cells on continuous days of starvation. Reprinted from [94].

The study of the effects of long-term glucose starvation is pioneered by Dr. Chieze Ibeneche. In her dissertational work [94] she described a previously unknown state in which fission yeast cells transition after 5 days of glucose starvation. Since the cytoplasm changes its viscoelastic properties from fluid-like in exponentially growing cells to solid-like in starved cells, this phenomenon was named cell freezing. The progression of the alpha values of lipid granules on the different days of starvation is shown in Figure 6.1. For an alpha value below 0.25, the granules show no visible motion. The effect is thought to be due to a filamentous septin network of septin 1 to 3. A possibly similar stiffening in the cytoplasm has recently been observed in the dormant state of bacterial *C. crescentus* and *E. coli* cells in response to carbon starvation among others [162]. In budding yeast cells, a slowdown of intracellular signaling was observed due to osmotic stress, which is thought to be due to molecular crowding [143].

6.2 *Schizosaccharomyces Pombe*: fission yeast

The fission yeast *Schizosaccharomyces Pombe* was discovered by Lindner in 1893, who isolated it from East African millet beer (pombe is the word for beer in Swahili) [101]. *S. Pombe* is a linear, rod-shaped, single cell eukaryote, which divides by medial fission.

First genetic studies on *S. Pombe* were conducted in the late 1940s. In the 1960s fission yeast was used as a model system for growth control due to its simple geometry and tip growth [145]. In the 1980s Nurse and others started to examine the cell cycle genes, which are highly conserved throughout metazoa, indicating that they share fundamental pathways common to all eukaryotes [65]. In 2002 its whole genome was sequenced and annotated [226]. *S. Pombe* has 4,824 protein coding genes, which is the smallest number found in eukaryotes so far. Of those, 50 genes have significant similarity with human disease genes, half of them related to cancer. It also showed highly conserved

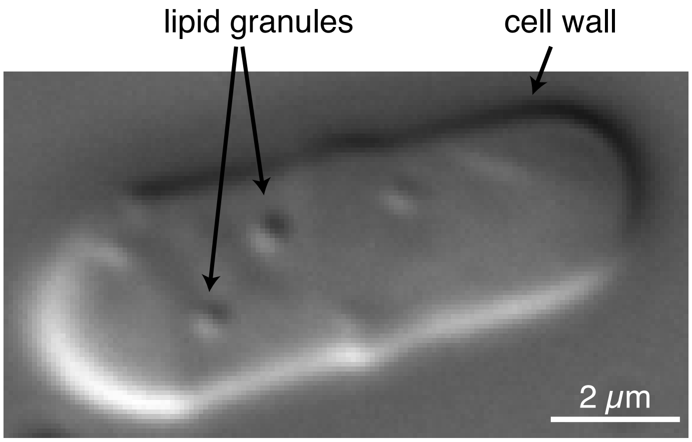

Figure 6.2: DIC image of an exponentially growing fission yeast cell.

genes for cell organization, like genes for the cytoskeleton, for cell cycle control, protein phosphorylation, and RNA splicing [226]. *S. Pombe* is also a good model system to study chromosome dynamics and damage responses [65].

The genetic information makes *S. Pombe* an outstanding model system and a good choice for this work, since it allows us to obtain mutants. Additionally helpful is the natural presence of lipid granules. Lipid granules occur most commonly toward the periphery of the cells, but can be found throughout the whole cytoplasm [101]. They are highly refractive, mostly spherical organelles, which have an average diameter of $300nm$ [207], Figure 6.2. Their position can be tracked with DIC microscopy, and they act as an indicator of the viscoelastic properties of the cell's cytoplasm. Furthermore, the cell has a well defined cell wall, resulting in a controlled environment. This is advantageous, since the motion of the granules is not influenced by shape changes or edge effects.

6.2.1 Cell cycle and cell growth

At the growing conditions used in this work, $T = 25°C$ in EMM2, *S. pombe* completes a vegetative cell cycle in four hours. In rich media, and at higher temperatures, the time can be as short as two hours. Starting the life cycle with the newborn cell, the cell first enters a phase of growth (G1), while simultaneously synthesizing DNA (S phase). Subsequently, the cells remain in the G2 phase, the second period of growth, for three quarters of the cell cycle. At the end of G2 the cell starts the regulation process to enter mitosis. Nuclear division takes place in the mitotic phase (M phase). The cell cycle is finished with cytokinesis and the birth of two new daughter cells.

Exponentially growing cells are born at a similar cell size, approximately $7.3\mu m$ long, and almost double their mass and length before cytokinesis, at which cells have a typical length of $13\mu m$. For size control of fission yeast cells, cell growth is coupled to the cell cycle. *S. pombe* cells are cylindrical with a highly controlled width, and grow by tip elongation, therefore their length is a measure for the stage in the cell cycle. The cells grow only in the first three-quarters of the cell cycle with no additional growth during septum formation, which is visible at 85% of the cycle. Septated cells towards the end of the cycle show wall growth at the septum [101]. Once a cell is separated the new daughter cells have a “new end”, formed from the splitting septum and an “old end”, which was formerly present in the mother cell. In the new daughter

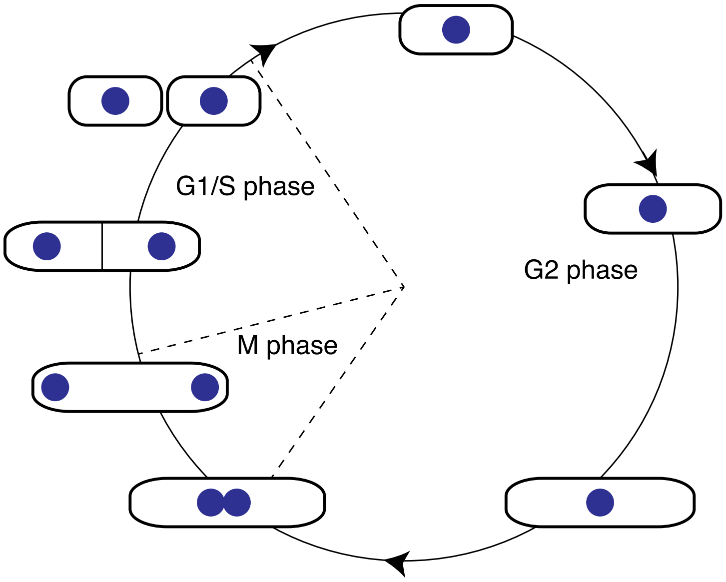

Figure 6.3: Fission yeast vegetative life cycle.

cells, the growth point moves from the new end to the old end, according to "Mitchison's rule" [29]. Tip growth at the old end is observed for the first part of the cell cycle. Later in the cycle, cell growth begins at the new end in addition to the old end, at a time called NETO (New End Take-Off). In order for NETO to occur, the cell must have completed 30% to 35% of the cell cycle, corresponding to early G2, and have a length of $9\mu m$ to $9.5\mu m$ [145]. The cell growth in the first 75% of the cell cycle appears to be linear with a rate changing point (RCP), where the growth rate increases by 35%. Most commonly RCP coincides with NETO [145].

6.2.2 Cytoplasm

Everything within the cell's plasma membrane, except for the nucleus, belongs to the cytoplasm. The cytoplasm is composed of the the membrane-bound organelles and the cytosol, which is mostly water, with dissolved ions and proteins. The cytosol makes up slightly more than half of the cell volume. Its main functions are the synthesis and degradation of small molecules and proteins [5]. Examples of organelles are mitochondria, which create ATP from nutrients; the endoplasmic reticulum, which synthesize proteins and lipids; the Golgi apparatus, which stores, packages and processes proteins for secretion; lipid granules, which store lipids; and vacuoles filled with polyphosphate, which can contain waste products and small molecules [101].

Counterintuitively, the cytoplasm is not a static, homogenous environment. It consists of dynamic assemblies of proteins and macromolecules that occur due to transient molecular interactions [93]. The cytoplasm plays an active role in many cellular functions, such as cellular communication, phagocytosis, cell motion, and shape changes. Although the cell cytoplasm is crucial to the cells functionality, the understanding of the structural organization at larger length scales is fairly poor. For example, the formation and organization of non-membrane bound macromolecular assemblies is not well understood. These macromolecular assemblies such as RNA/protein bodies, nucleoli, cajal bodies, germ granules, kinetochores, centrosomes, or adhesion complexes, are found throughout the cell and either function as reaction or storage centers. Many of these complexes are highly dynamic and have short turn-over rates.

The meso-scale organization of the cytoplasm into different liquid phases might be due to weak long-range interactions like electrostatic interaction, hydrophobic attraction, hydrogen bonding, and depletion attraction due to molecular crowding. In summary, the cytoplasm is representative of a complex emulsion of dynamic liquid-phase aggregates or droplets of RNA and proteins [93].

6.2.3 Cytoskeleton

Also found within the cytoplasm is the cytoskeleton. It usually consists of three components; microtubule, actin, and intermediate filaments as shown in Figure 6.4 and is responsible for cell shape, structure, and transport within the cell. The cytoplasm of *S. pombe* only consists of microtubule and actin, not intermediate filaments. Although traditionally not a member of the cytoskeleton, septins could be considered a member due to their similar organization and formed structures [147].

Microtubule

A microtubule is a hollow, cylindrical polymer with a diameter of $25nm$. It consists of 13 parallel protofilaments, which are polymerized by α- and β-tubulin heterodimers, each of approximately 50kDa. One α- and one β-tubulin heterodimer hydrolyze into a tubulin dimer. The tubulin dimers assemble into polar microtubules from minus to plus end. Dynamic instability drives the growth process and growth at the plus end is generally faster than at the minus end. Rapid shrinking of the microtubule caused by disassembly is called

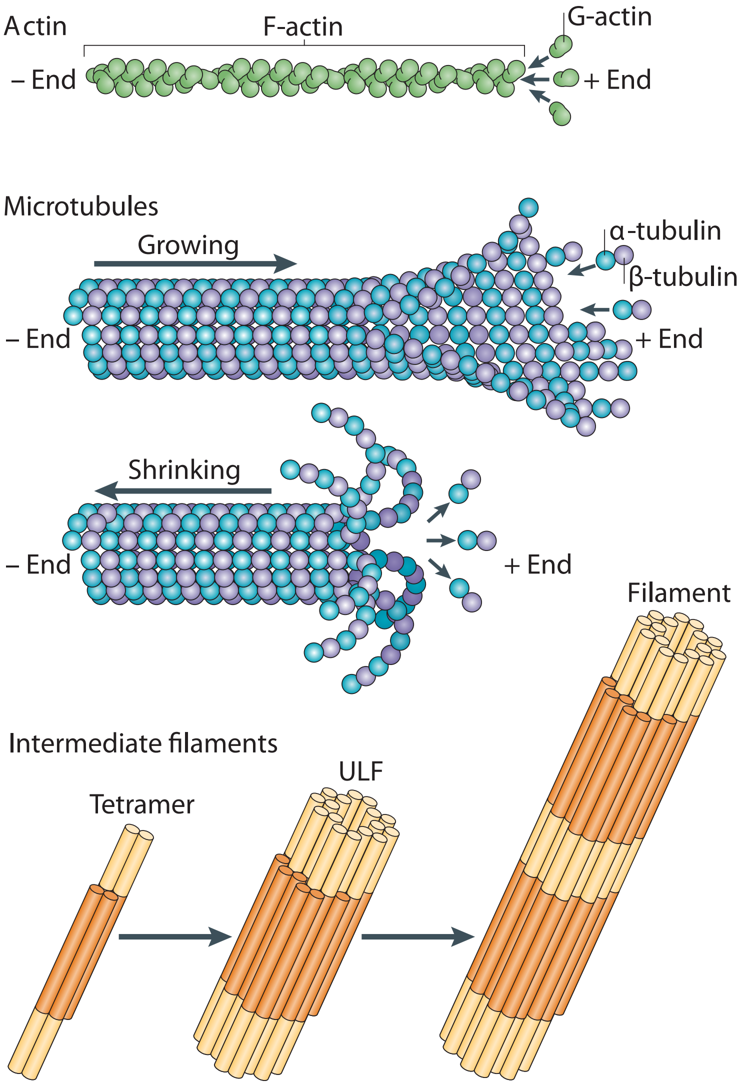

Figure 6.4: Components of the cytoskeleton, actin, microtubule, and intermediate filaments. Reprinted with permission from [147].

catastrophe and fast growth at the plus end is known as rescue [147].

Microtubules in fission yeast are involved in cell division, the correct distribution of the nuclei and mitochondria, the maintenance of cell polarity, the integrity of the golgi stack, and morphology. Mutants with defective interphase microtubules, which show no significant delay in mitosis, have three morphogenetic defects; bending, curving, and branching [77]. The microtubule occurring in the interphase are called interphase microtubules and extend along the long axis of the cell. They are arranged in four to eight microtubule bundles of two to three microtubules each. In fission yeast cells, interphase microtubules can nucleate from the spindle pole body (SPB), microtubules, additional sites on the nuclear surface, and within the cytoplasm [182]. In preparation for mitosis, microtubule activity is observed inside the nucleus where microtubules nucleate from the SPB to form the mitotic spindle. Additionally astral microtubules form and extend tangentially from the SPB into the cytoplasm, whereas the interphase microtubules disappear. At the end of mitosis equatorial microtubules appear before cytokinesis. After cytokinesis the cycle repeats and interphase microtubules reoccur [182, 77].

Actin

Filamentous actin (F-actin) is a polar, double-helical filament with a diameter of about $7nm$. It is built from monomers called globular actin (G-actin) of approximately 40kDa. Upon polymerization, ATP is hydrolyzed to ADP. Growth of actin filaments, specifically the addition of monomers, preferentially occurs at the plus end, also know as the barbed end. Depolymerization, which shortens the filament, starts mostly at the minus end, called pointed end [147].

Although fission yeast only has a single actin isoform, three different structures are built from it, namely, actin patches, cables, and the contractile ring. Actin patches assemble at sites of endocytosis and consist of approximately 150 branched filaments each 100nm to 200nm in length. About 900 fimbrin molecules cross link the approximately 7,000 actin monomers [112]. Actin patches accompany polarized cell growth at the growing tips of interphase cells and in the center of dividing cells. In newly divided cells, actin patches are located at the old end. Starting at NETO, the patches show a bipolar distribution at both growing tips [101]. As soon as the cell stops growing, the actin patches disappear from the periphery and the contractile ring appears. The contractile ring drives cytokinesis and consists of unbranched anti-parallel actin filaments. Actin cables are short bundles of unbranched parallel actin filaments, whereas the barbed end points towards the cell cortex. Cables are necessary for polarized transport by myosin V type motors of vesicles and organelles to the growing cell tips. Microtubules establish the assembly of actin cables, which is an example of collaboration between different cytoskeletal components [112].

Septins

Although traditionally not a member of the cytoskeleton, perhaps septins should be due to their organization and formed structures [147]. The septin

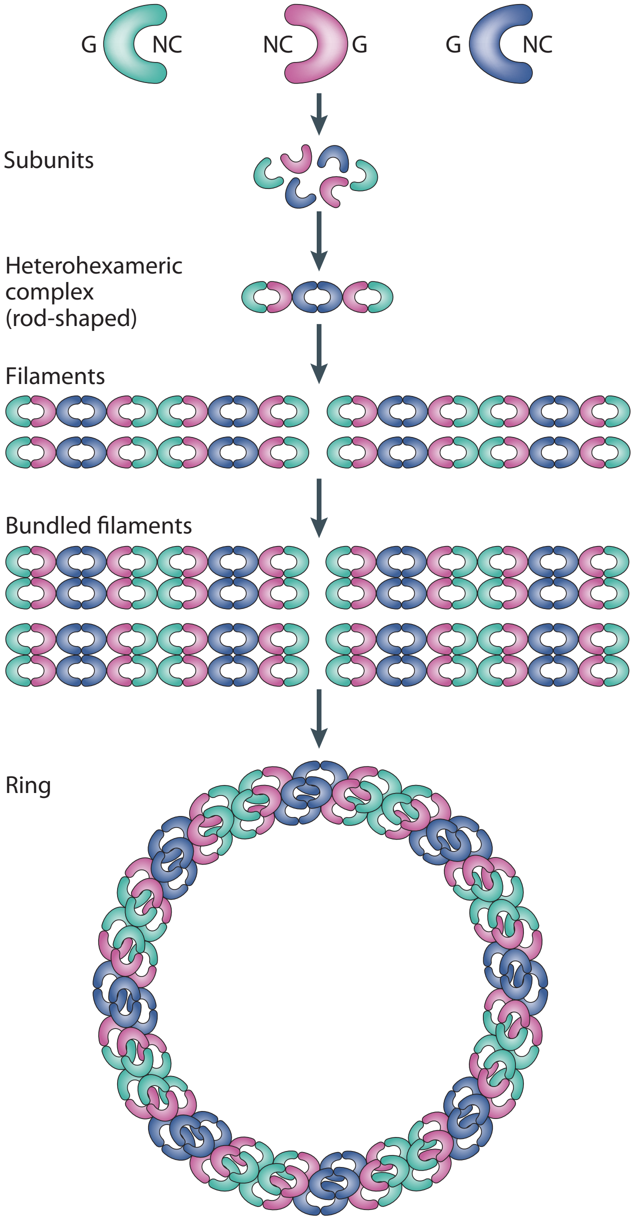

Figure 6.5: Assembly of septin constructs. Reprinted with permission from [147].

family of proteins was first discovered in the early 1970s in budding yeast [83], and were named according to their involvement in cytokinesis and septum formation [128]. Only found in fungi and animals, not in plants, septins are a conserved protein family with masses from 30kDa to 65kDa. Septin subunits have a GTP-binding domain (G-interface), through which they interact with the carboxy-terminal region (NC interface) in order to form complexes that connect end-to-end to create a filament of about 10nm [128]. In contrast to microtubule and actin, septin filaments are non-polar and have a slower turnover rate. Septin filaments can form bundles, which can associate into higher ordered complexes such as rings, cage-like structures, hourglasses, and gauzes [160]. Figure 6.5 shows the formation of heterohexameric complexes from the individual subunits, and the formation of filaments, bundles and rings. Different septins are shown in different colors. Often multiple septins, three or four, are found to form filaments and structures [147].

Generally, septins associate with actin, microtubules, and membranes [213]. They play a role in cytokinesis, host-microorganism interaction, ciliogenesis, neurogenesis, and bacterial infection. Septin filaments have a high combinatorial diversity, which might allow them to fulfill functions very specialized filaments are unable to perform. Septin's known molecular function is to build sub-cellular scaffolds to accumulate proteins, diffusion barriers in membranes, and compartmentalization [160, 147, 213].

6.3 Examining the viscoelastic properties of the cytoplasm

The first experiments to probe the cytoplasm were done as early as 1820. Researchers took cells and crushed them between two slides to observe the outcome [166]. In the early period of cytoplasmic investigation, as reviewed by Porter [166], from about 1820 to 1910, research on cells was dominated by improving light microscopes, fixation, and staining procedures. Staining and fixation techniques commonly killed the cells, and therefore could induce many artifacts.

In the middle period, from 1910 to 1940, living cells and fundamental properties of the cytoplasm could be studied, due to the invention of phase contrast microscopy. Phase contrast converts the phase difference of objects into contrast, thus transparent, living cells could be visualized [111]. Various experiments were conducted during this time, which lead to the conclusion that the cytoplasm is both fluid, but also a solid at the same time. Work by Scarth showed, that when organelles like the nucleus in cells are displaced that they tend to return to their original position, indicative to the viscoelastic properties of the cytoplasm. Ultracentrifugation of living cells at 150,000g lead to no disruption in the cell cycle. Centrifugation of ascaris eggs at 400,000g lead to a stratification of their content into three layers, which redistributed within 12h, after which the cells resumed division [19]. These experiments show that the cytoplasm has a resilient self-organization. Another attempt to investigate the viscoelastic properties of the cytoplasm was to introduce iron particles into the cell and displace them by applied magnetic fields [52]. When the magnetic field was turned off, the displaced particles experienced a recoil. They did not return to their original position, just one-third of the way. They concluded that the cytoplasm is a thixotropic gel.

In the more recent period starting from 1940, progress in the cytoplasmic research was facilitated by the invention of cell fractionation. Centrifugation led to the stratification in several layers, which are identified as various organelles [233]. A different approach to study the structure of the cytoplasm emerged with the use of electron microscopy. The development of thin sectioning in 1953 enabled the study of membrane-bound organelles and filaments [37]. Fluorescence recovery after photobleaching experiments with different sized markers in mouse 3T3 cells revealed that the cytoplasm has a viscosity four times higher than water and contains structural barriers [130, 131].

More recent approaches to describe the properties of the cytoplasm by active and passive microrheology as well as the observation of anomalous diffusion of tracer particles are described in the following sections.

6.3.1 Anomalous diffusion

For normal diffusion, the mean square displacement is proportional to time $\langle x^2(t)\rangle \sim Dt$. For more general modes of motion the MSD often shows a power law behavior, $\langle x^2(t)\rangle \sim D_\alpha t^\alpha$, where α is named the anomalous diffusion exponent. If the MSD shows a nonlinear dependency on time, $\alpha \neq 1$, the mode of motion is called anomalous diffusion. For $\alpha < 1$, the mode of motion is called anomalous subdiffusion and for $\alpha > 1$, superdiffusion. The case $\alpha = 2$ describes ballistic diffusion [141]. Determining the anomalous diffusion exponent α for tracer particles in the cytoplasm of the cell, can yield information about its viscoelastic properties and its crowdedness [214]. First, we can detect if the motion of the tracer within the cytoplasm is dominated by active transport of cargos by molecular motors or polymerization of filaments. Both can lead to superdiffusive motion or higher alpha values, even if the tracer is not actively transported by motors itself [23, 219]. Second, for subdiffusive motion the alpha value indicates, whether the cytoplasm behaves more like a liquid, corresponding to $\alpha \approx 1$, or more like a solid, $\alpha \approx 0$.

The usual laws of normal diffusion can be derived from the central limit theorem (CLT) of probability theory. Following the example described by Bouchard and Georges [21], we first look at a one-dimensional Brownian walk. At time n, a step of jump length l_n is taken according to the distribution $p(l)$. After N steps, at the time $t = N\tau$, the position is the sum of the N independent displacements

$$X_t = \sum_{n=1}^{N} l_n. \tag{6.1}$$

If the average and standard deviation of the distribution $p(l)$ are finite, the mean and variance of the position depend linearly on time,

$$\bar{X_t} = vt, \tag{6.2}$$

$$\bar{X_t^2} - \bar{X_t}^2 = 2Dt. \tag{6.3}$$

The velocity and diffusion constants can be written as

$$v = \frac{\langle l \rangle}{\tau}, \tag{6.4}$$

$$D = \frac{\langle l^2 \rangle - \langle l \rangle^2}{2\tau}. \tag{6.5}$$

These equations describe normal diffusion as discussed in Section 2.1.1. CLT provides a more precise characterization of the random walk. If $\langle l \rangle$ and $\langle l^2 \rangle$ are finite, the position, X, of the random walker at large time, t, is distributed according to a Gaussian function.

CLT applies if the random variables which are summed, the random steps, are neither too broadly distributed nor have too long-range correlations. Whenever one of the two conditions is broken, anomalous diffusion arises. One possibility which causes the break down of the CLT is the implementation of long waiting times, called the continuous time random walk (CTRW). The CTRW can be thought of as diffusion among traps, but the time a particle remains within a trap is not correlated to the lattice position, instead it is random. We consider the case where the random walker walks on a lattice, but has to wait for a time τ at each site before taking the next step. The waiting times τ are distributed according to $\psi(\tau)$. The total time after N steps can be calculated by summing the N waiting times

$$t = \sum_{n=1}^{N} \tau_n. \tag{6.6}$$

Since this represents the sum of independent, random variables, the CLT can be applied as for normal diffusion. If $\langle \tau \rangle$ is finite, t behaves as $t \sim N\langle t \rangle$ and the diffusion process is normal at long times. However, if $\psi(\tau)$ is a heavy-tailed, broad distribution in the following way,

$$\psi(\tau) \simeq \frac{\tau_0^\alpha}{\tau^{1+\alpha}},\ (\tau \to \infty), \tag{6.7}$$

then for $0 < \alpha < 1$, the average waiting time diverges, $\langle \tau \rangle = +\infty$, and t behaves like $t \sim \tau_0 N^{1/\alpha}$. This results in subdiffusion, and the MSD has a nonlinear dependence on time,

$$\bar{X^2} \sim \langle l_i^2 \rangle \left(\frac{t}{\tau_0} \right)^\alpha . \tag{6.8}$$

The CTRW represents a dynamic, cage-like environment, in which the traps are not stationary. Subdiffusion is not limited to this case, but also occurs in static environments with spatial inhomogeneities. Diffusion within static obstacles, such as the filaments of the cytoskeleton, can be modeled by a random walk on a percolation cluster [49] and also leads to subdiffusion.

Besides long waiting times, long-range correlations can also lead to the break down of the CLT and therefore to anomalous diffusion. Long-range correlations do not fulfill the requirements to apply CLT, because the summed random variables are not independent. Correlations enhance diffusion and in the case of perfect correlations it leads to ballistic motion, $\alpha = 2$ [21].

Anomalous subdiffusion in biological systems has been observed in the cytoplasm of various cells and in artificial actin networks [7, 224]. In fission yeast cells the motion of the lipid granules within the cytoplasm can be tracked with single or multiple particle tracking via video microscopy or by optical trapping. Using both methods over different timescales revealed the subdiffusive motion of the granules over a wide range of frequencies [207, 100] and in different stages of the cell cycle [188]. Subdiffusive motion also occurs on short timescales in *Amoeba proteus* [177] and in PC3 tumor cells when microtubules are disrupted and active transport is prohibited [176]. Even the cytoplasm of prokaryotes such as *E. coli* contains structure which leads to subdiffusive motion of fluorescently labeled mRNA molecules, regardless of the disruption of cytoskeletal elements [72]. Although the microscopic origin of subdiffusion in cells is not quite clear [49], it is generally thought to be due to crowdedness [214, 7]. Even though subdiffusion is slower than normal diffusion, especially on longer time scales, it improves the protein's ability to form complexes and enhances signal propagation in cells [76].

6.3.2 Microrheology

Microrheology is commonly used to study the viscoelastic properties of the cell cytoplasm. Mircorheology in cells commonly examines the cytoplasm with internal probes embedded inside the cells. Passive microrheology relies on Brownian motion to drive the probe, whereas active microrheology applies force to the sample or the tracers within the sample [222, 38].

Microrheology has been used to look at a wide variety of biological samples from artificial systems like biopolymers [2], cross-linked biopolymer networks [25], and lipid vesicles [26] to a variety of living cells [230, 176, 218, 228].

Passive microrheology

Passive microrheology relies on the observation of displacements of particles driven by Brownian motion. The tracers can be micro-injected beads, fluorescently labeled molecules, or naturally occurring organelles like the lipid granules in fission yeast. The motion of the tracer particle is observed in order to calculate a time-dependent mean square displacement. By applying the fluctuation dissipation theorem, the MSD can be converted into the frequency dependent storage and loss modulus. The particle's trajectory can be measured for example by video microscopy, laser deflection tracking, optical tweezers, diffusion wave spectroscopy, dynamic light scattering, optical interferometry, or atomic force noise analysis [38].

As mentioned before, if the material is purely viscous, the MSD increases linearly with time. For elastic solids, the MSD is time independent. At long timescales the viscoelastic properties of the cytoplasm are mainly viscous and at short time scales are more solid-like [222]. The measured probe trajectories can be transformed into the frequency dependent complex modulus G^* by using the generalized Stokes-Einstein relation (GSER) and the fluctuation dissipation theorem. A detailed calculation can be found in [199]. The MSD is related to the complex modulus by

$$G^*(\omega) = \frac{2k_BT}{3\pi a i \omega F_u[\langle \Delta r^2(t) \rangle]}, \tag{6.9}$$

where $F_u[\langle \Delta r^2(t) \rangle]$ is the unilateral Fourier transform of $\langle \Delta r^2(t) \rangle$ and a is the particle radius. The Einstein component of the GSER relates the thermal motion of the particle to its mechanical response. This assumption is violated if the examined system is not in equilibrium as in active materials. The assumptions of the Stokes component, which relates the complex mobility of a tracer to the rheological properties of the substance, can also fail. The break down can occur in materials which have material heterogeneities, so that the probe size plays an important role. It can also occur in anisotropic materials, when the probe interacts with the material, or when the elastic components of the substance are compressible [199]. In any of those cases one needs to be careful that the measurements represent the actual material properties. Passive microrheology is suitable for soft materials, since the driving force is the thermal force.

Active microrheology

The idea behind active microrheology remains the same as in traditional rheology. Stress or strain is applied to a material and the resulting strain or stress is monitored. Using the standard linear solid model and a sinusoidal driving force, the storage and the loss modulus can be determined from the amplitude and the phase shift of the response. Alternatively, a step in strain or stress can be applied and the creep response is measured. Force can be applied by oscillatory optical tweezers, magnetic twisting cytrometry, atomic force microscopy, and micropipette aspiration. Active microrheology is more versatile than passive microrheology, but the implementation is more complex. It also enables the analysis of nonlinear rheological behavior and hard samples, in which Brownian motion is not sufficient to displace the particle [38, 88].

6.4 Outline and research objectives

The second part of this dissertation is based on the work of Dr. Chieze Ibeneche, who was first to investigate and describe the frozen state of fission yeast cells due to glucose starvation [94].

In order to be able to track granules in exponentially growing cells over long periods of time, the DIC tracking algorithm was expanded into three dimensions. By image integration along the shear axis, the typical black-white contrast of small, spherical objects is transformed into a single peak. This peak can be fitted by a two-dimensional Gaussian to determine the beads lateral position with sub-nanometer precision. Two parameters determine the particle's z-position. First, the peak-to-peak intensity can be used, but it is symmetric around the focus and therefore not uniquely determined and it has poor resolution in focus. Second, the offset in intensity of the integrated Gaussian can be used, which advantageously has a linear regime around the focus. Using the offset results in an axial position detection with $5nm$ precision, even in focus. The ability to determine the bead's position in three dimensions within a single image fulfills the necessary conditions to build a feedback loop, with which a particle can be followed for extended periods of time. We demonstrate the feedback *in vitro* and *in vivo* on exponentially growing cells.

Chapter 9 furthers the understanding of cell freezing. First, we finish studies about the molecular origin of cell freezing and test actin as well as the remaining septins as potentials for forming a network. Additionally, the influence of the initial glucose concentration is investigated. Originally, the idea was that there is a growth media and a starvation media, which contains 75% less glucose. Experiments as well as simulations show that the nutrients are depleted and the cells stop growing after approximately one day, regardless of the initial glucose concentration. Therefore, the starvation of cells and cell freezing is relatively independent of the initial glucose concentration. Cells recover from the frozen state after the addition of glucose. The recovery process is observed with a flow-chamber and the first critical 10 to 15 minutes are characterized in detail, where the alpha value recovers to approximately 0.45. Cells are further observed for two hours after the addition of glucose.

In Chapter 9 we tried to understand more about why and how cells go into the frozen state, whereas in Chapter 10 we characterize this state in more detail. In order to rule out active processes which could die down during starvation and artificially alter the alpha values, the measured alpha values were correlated with the mobility of the granule when displaced by optical tweezers. Granules in exponential growth can be moved around the cell freely. During the transition into freezing, the granules start to become tethered until they are completely immobilized in frozen cells. Additionally, we determine the viscoelastic properties of the cells by passive microrheology. The frequency behavior of the storage and loss modulus of granules in the different states is examined.

Chapter 7

Materials and Methods

7.1 Yeast strains

All fission yeast strains used in this dissertation were started from strains provided by Damian Brunner, Universitaet Zuerich. Table 7.1 contains a complete list.

Table 7.1: List of yeast strains used in this study

Strain	**Description**	**Genotype**
DB 558	Wildtype	h-
DB 626	Septin 1 deletion	h-spn1-Δ1::kanMX6 leu1-32 ura4$_D18his$
DB 2793	Septin 2 deletion	h-spn2::ura4+ade6-M210 leu1-32 ura4-D18
DB 2785	Septin 3 deletion	h-spn3::ura4+leu1-32 ura4-D18
DB 627	Septin 4 deletion	h-spn4-Δ1::kanMX6 ura4-D18
DB 2787	Septin 1 and 3 deletion	h-spn1::kanr spn3::ura4+ade leu1-32 ura4-D18
DB 3324	Septin 4 deletion	h- spn4-Δ1::kanMX6
DB 3451	Septin 5 deletion	h+ spn5-Δ1::ura4 ade6-210 ura4-D18 leu1-32
DB 3452	Septin 6 deletion	h+ spn6-Δ::his3 ade6-210 his3-D1
DB 629	Septin 1 GFP	h+spn1+-GFP-kanMX6 leu1-32 ura4-D18
DB 3410	Lifeact GFP	h- Lifeact-GFP::leu+

7.2 Yeast culture media

The solid media used for growing yeast cells on plates is Yeast Extract with supplements (YES) with 2% agar (YES 225 Agar, Sunrise Science Products, CA, USA). YES is used for vegetative growth and is a rich complete media containing $224mg/L$ of adenine, leucine, uracil, histidine, and lysine hydrochloride. Edinburgh Minimal Media with 2% glucose (EMM2) is used as a liquid media for vegetative growth. EMM is synthetic and highly reproducible, and its ingredients are listed in table 7.2. Since EMM does not contain any supplements, amino acids are added at a concentration of $250mg/L$ for strains that require them. All chemicals, as well as amino acids, were purchased from Sigma-Aldrich (MO, USA). For starvation experiments EMM was used with a concentration of $5g/L$ glucose instead of $20g/L$.

Table 7.2: Edinburgh Minimal Medium (EMM2)

EMM2	
DI-water	$1L$
Potassium hydrogen phthalate	$3.0g$
Na_2HPO_4	$2.2g$
NH_4CL	$5g$
Glucose	$20g$
Salts (50x stock)	$20mL$
Vitamins (1,000x stock)	$1mL$
Minerals (10,000x stock)	$0.1mL$

50x salts	
DI-water	$250mL$
$MgCl_2 \cdot 6H_2O$	$13.125g$
$CaCl_2 \cdot 2H_2O$	$0.184g$
KCl	$12.5g$
Na_2SO_4	$0.5g$

1,000x vitamins	
DI-water	$250mL$
panthothenic acid	$0.25g$
nicotinic acid	$2.5g$
inositol	$2.5g$
biotin	$2.5mg$

10,000x minerals	
DI-water	$250mL$
boric acid	$1.25g$
$MnSO_4$	$1.0g$
$ZnSO_4 \cdot 7H_2O$	$1.0g$
$FeCl_3 \cdot 6H_2O$	$0.5g$
molybdic acid	$0.1g$
KI	$0.25g$
$CuSO_4 \cdot 5H_2O$	$0.1g$
citric acid	$2.5g$

Note: After autoclaving a few drops of preservative can be added to the mineral stock (1:1:2 chlorobenzene : dichloroethane : chlorobutane)

7.3 Yeast cell preparation

Schizosaccharomyces pombe cultures were grown from frozen stock by growing the cells on YES agar plates for 24-72 hours at $32°C$. Cells could be stored on the agar plates in the fridge at $4°C$ and used for a period up to one month.

7.3.1 Exponential culture

To prepare an exponential culture, cells are first grown in a pre-culture. For the pre-culture, cells are transferred from the agar plate with a nunc loop (Thermo Scientific, PA, USA) into a $50mL$ centrifuge tube containing $10mL$ of EMM2. The concentration of the pre-culture is adjusted to achieve an optical density (OD) of approximately 0.05 at a wavelength of $595nm$. The cells are allowed to growth overnight in a shaking incubator at $25°C$. It is important for the health of the culture that the culture does not overgrow ($OD_{595} \geq 1.0$). The culture needs to be diluted if necessary. Cells are transferred from the pre-culture to a $125mL$ Erlenmeyer flask containing $10mL$ of EMM2 at a concentration to achieve an optical density of 0.05. The culture is grown for approximately 14 to 16 hours overnight at $25°C$ in the shaking incubator. At this point the culture should be in mid-exponential growth and should double every 4 hours. The final OD should be between 0.5 and 0.8.

7.3.2 Starvation culture

To prepare cells for a classical starvation culture, an exponential culture needs to be prepared first. From the exponential culture cells are transferred into a 125mL Erlenmeyer flask containing 10mL of EMM with $5g/L$ glucose to achieve a concentration of an OD of 0.05. The cells are grown in the shaking incubator at $25°C$ for up to 8 days.

7.3.3 Disrupting the actin structures with latrunculin

We prepared cells, whose actin network is disrupted, the following way. $1mg$ of latrunculin B (Calbiochem, EMD Millipore, MA, USA) was dissolved in $253\mu L$ dimethyl sulfoxide (DMSO) (Sigma-Aldrich, MO, USA), resulting in a concentration of $10mM$. The solution is separated into $10\mu L$ aliquots, which are stored in the freezer at a temperature of $-20°C$. A starvation culture is set up as previously described. On day 1 or day 2 of starvation the culture is split into three cultures of $1.5mL$ each, and these cultures are transferred into a centrifuge tube. The first culture remains unaltered as the control. $10\mu L$ of DMSO is added to the second culture as an additional control, to test weather DMSO alters the cells behavior. $10\mu L$ of latrunculin B, which will inhibit actin polymerization and therefore over time dissolves the actin network, at a concentration of $10mM$ is added to the third culture. The resulting latrunculin B concentration in the culture is $67\mu M$, which is sufficient to disrupt the actin network in yeast cells [12, 209].

7.4 Sample preparation

Coverslip Preparation

The yeast cells were observed in sample chambers, where the cells were immobilized on 14mm round cleaned coverslips (Menzel Glaeser, Germany) coated with Poly-D-lysine hydrobromide (Sigma Aldrich, MO, USA). Poly-D-lysine is a positively charged amino acid polymer, which is used to promote cell adhesion to solid substrates. It enhances the electrostatic interaction between the negatively charged ions of the cell membrane and the coverslip [97]. This is important so that the granule motion can be measured with nanometer precision without the cell motion adding to the measured data. The coverslips were cleaned using the following standard cleaning procedure. The coverslips were immersed in a 2% Hellmanex II solution (Hellma GmbH Co. KG, Germany) in deionized water (Millipore) and sonicated in a bath sonicator for 15 min. The solution was replaced by deionized water and the coverslips were sonicated again for 15 min. This procedure was repeated two more times. Subsequently, they were rinsed extensively with deionized water and dried with nitrogen gas.

The coverslips were plasma cleaned for 30 seconds, before coating them with Poly-D-lysine. Next, a few of drops of the poly-D-lysine solution at a concentration of $2mg/mL$ were placed on the coverslip to fully cover the surface. Then, the poly-D-lysine was allowed to incubate for one hour. Subsequently, the excess poly-D-lysine was removed by pipetting $200\mu L$ of DI-water onto the coverslip and pipetting the solution off afterwards. This process was repeated two more times. Finally, the coverslips were allowed to air dry before usage.

Sample chamber assembly

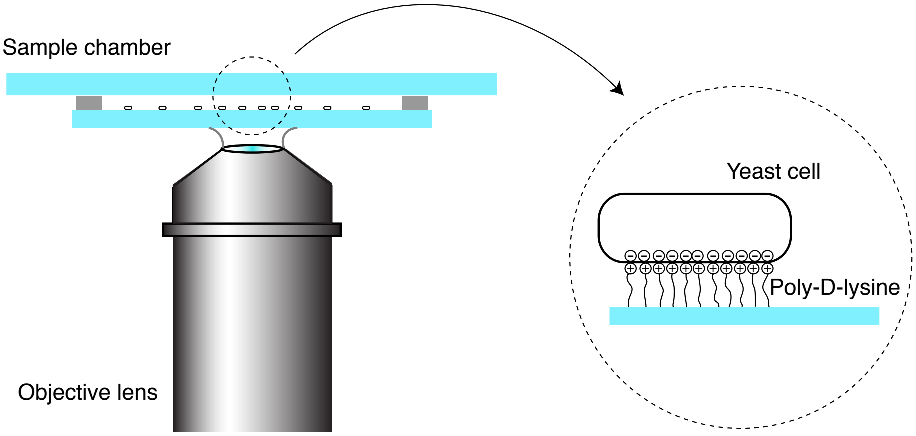

Figure 7.1: Schematic of the sample chamber, with immobilized yeast cells for single particle tracking.

To assemble the sample chamber, the poly-D-lysine coated coverslip was placed face down onto a a rectangular coverslip ($24mm \times 32mm \times 140\mu m$). Two stripes of parafilm (Pechinney Plastic Packaging, CA, USA) are used between the two coverslips as a spacer but also as an adhesive. The pre-assembled sample chamber is briefly heated on a hot plate to melt the parafilm which glues the coverslips together. $10-15\mu L$ of the cell solution is flowed in between the coverslips. The open sides of the sample chamber are sealed with vacuum grease (Dow Corning, MI, USA) to avoid the sample chamber from drying out. The sample chamber is placed onto the sample holder with the coated coverslip facing down, towards the objective.

Flow chamber assembly

In order to examine the recovery of the cells from the frozen state, fresh, nutrient-rich media needs to be added. An important part of the recovery process occurs in the first few minutes, so it is preferable that the cells can be observed under the microscope while the media is exchanged. In order to achieve stable tracking during the fluid exchange, we used a custom build flow chamber, for more details see Morgan Williamson's thesis [221]. A metal sample chamber, comparable to the one used in part one of this dissertation, was assembled by attaching a poly-D-lysine coated coverslip on one side and a cleaned one on the other side with VaLaP. VaLaP is a biological inert material for sealing coverslips. It consists of equal parts by weight of vaseline, lanolin, and paraffin wax. The sample chamber was filled with cell solution and all of the tubing in the syringe system was filled with the media the cells grew in. The media was obtained by centrifuging $3mL$ of the cell solution for $4min$ at $5000rpm$. This ensures, that the fresh media is hindered from diffusing into the sample prematurely. Syringes filled with EMM2 are attached to the filling tubes of the sample chamber with the valves closed. The computer-controlled valves can be opened and the media can be exchanged with a maximum speed of $5\mu L/s$. This system is stable enough to continuously tack individual granules during the fluid exchange.

7.5 Preparation of frozen yeast cell extract

The following protocol was used to prepare frozen yeast cell extract, in order to purify the lipid granules and to determine their index of refraction.

1. **Cell growth**: A $25 - 50mL$ pre-culture is grown. From the pre-culture a $4L$ exponential culture is started, which will be in mid-exponential growth the following morning.
2. **Cell harvesting**: Cells can be harvested, when the culture is in mid- to late-exponential growth. The cell culture is filled into appropriate centrifugation flasks so that the have the same exact weight and centrifuged for 8 minutes with $4000rpm$ at $4°C$. The supernatant is discarded and the pellets are resuspended in 15mL of PBS or water. The cells are mixed gently to wash out remaining yeast extract from the medium. The solution is centrifuged again at $2500rpm$ for 3 minutes at $4°C$. The supernatant is carefully discarded, so as to not destroy or loose the pellet.
3. **Cell freezing**: The pellet is transferred into a 20mL syringe with an 18G needle. A glass beaker is put in a larger container and both are filled with liquid nitrogen at the same time to avoid breaking. Small drops of cells are slowly squeezed out of the syringe into the beaker, which is filled with liquid nitrogen. Once the syringe is empty, the liquid nitrogen is removed from the beaker until there is almost none left. The cell pellets are poured into a 50mL tube and stored in the $-80°C$ freezer

until mortar grinding. Care needs to be taken so that the pellets do not thaw during the procedure.

4. **Mortar grinding**: The mortar grinder is placed into a cold room. The bowl and pistil are cleaned with ethanol. All parts of the grinder which come into contact with the cell pallets need to be cooled with liquid nitrogen to avoid melting. After grinding cells for 10 minutes at pressure 5 with a RM100 (Retsch, Germany) with steel pestle, or after five intervals of three minutes each at $10Hz$ (cool in liquid nitrogen in between) with a Mixer Milll MM 300 (Qiagen, Germany), the frozen cell pallet has turned into powder. The powder is collected with a pre-cooled spatula in a cooled falcon tube. The collected yeast powered can be stored for a long time at $-80°C$. $0.5mL$ yeast powder dissolved in $1mL$ of PBS results in an approximate concentration of $10mg/mL$.

7.6 Experimental Setup

All experiments were performed on a modified Zeiss Axiovert 10 inverted microscope (Zeiss, Jena, Germany) with DIC optics and a custom-built stage optimized for high mechanical stability. The objective lens used is a high numerical aperture (NA=1.3) oil lens (Zeiss, Plan-NEOFLUAR 100x, oil pol). The built-in halogen lamp was used for illumination in combination with a green band pass filter (ET525/50x, Chroma, VT, USA), a blue band pass filter (ET475/50x, Chroma, VT, USA) or on its own. Images were acquired with a Sensicam QE high sensitivity CCD camera (PCO AG, Kelheim, Germany)

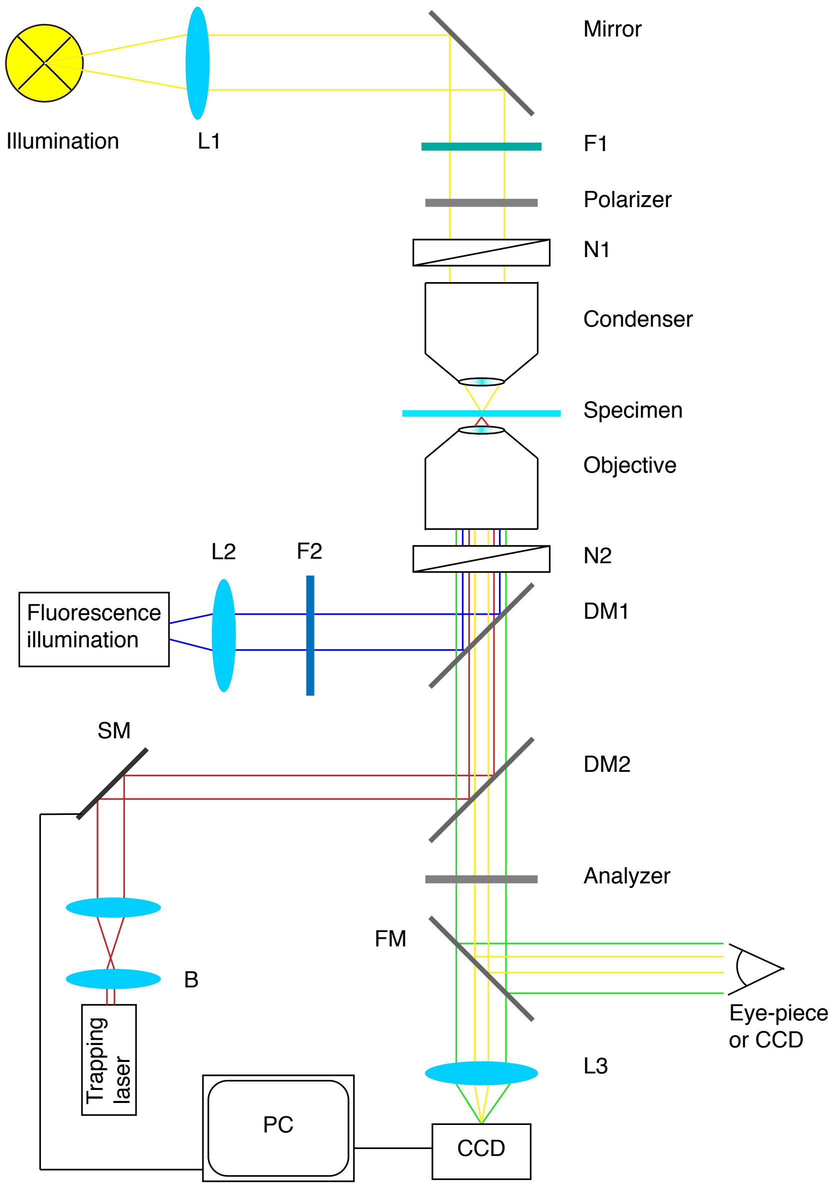

Figure 7.2: Schematic of the modified Axiovert 10 inverted microscope. L: lens, F: filter, N: Nomarski prism, B: beam expander, DM: dichroic mirror, FM: flip mirror.

attached to the top microscope port or with a 12-bit digital CCD camera (UP-600-12B, UNIQ, CA, USA) on the bottom port. The position modulation in the lateral direction was achieved with the piezo stage (NPS-XY-100A, Queensgate Instruments, Great Britain) and axially with a piezo for the objective lens (Nano-F100, Mad City Labs Inc., WI, USA). A $Nd : YVO_4$ laser with a wavelength of $1064nm$ (T20-B10-106Q, Spectra Physics, Germany) was used to form an optical trap. The positioning of the trap with respect to the sample was achieved with two scanning mirrors (Cambridge Technology, MA, USA). Figure 7.2 shows a schematic of the setup. Software for the image acquisition and the feedback loop were written in LabVIEW (National Instruments, TX, USA). Data analysis and graphs were made using custom-written software (Igor Pro, Wavemetrics, OR, USA). Fluorescent images of the cells were taken on the PFM described in Chapter 3 of this thesis.

7.7 Granule selection and the calculation of the anomalous diffusion exponent α

In exponential growth the yeast population exists of cells at different points in the cell cycle. All cells analyzed in experiments with exponential cultures were chosen to be in the interphase, and more specifically in G2. Cells are in G2 after they are born and fully separated from each other. The septum of the cells are easily visible under the DIC microscope and therefore cells in the G1/S phase can be clearly distinguished from cells in G2. Cells in the M phase are approximately $13\mu m$, whereas newly born cells are only about

$7\mu m$ long. Due to the coupling between cell cycle and cell growth, choosing granules from cells which are shorter ensures selecting cells from G2.

During starvation the cells are arrested in G2 and the culture is fairly homogenous. In this case, granules are chosen from random cells. Since granules in starved cells tend to be larger than in exponentially growing cells, an effort was made to track smaller granules. Picking granules of comparable sizes ensures that the granules probe the cytoplasm similarly, which can be important if there is a network with a mesh size on the same order of magnitude as the granules.

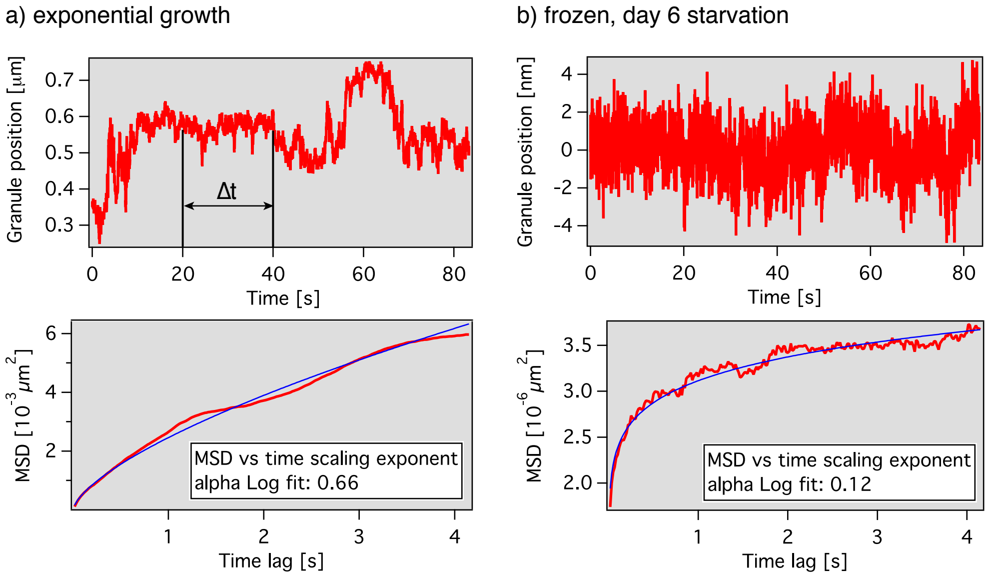

Figure 7.3: Position-time trace and MSD of a granule from a) exponentially growing cell with $\alpha = 0.66$ and b) frozen cell with $\alpha = 0.12$.

Once a granule is selected, 5000 frames are recorded at a frame rate of $60 fps$ unless otherwise noted. The large number of frames ensures that enough statistically independent data is obtained for the calculation of the MSD. The image stack of the granule is fed into the custom written tracking program further described in chapter 8, which returns the granule's x and y position-time trace. Examples for the position-time trace for a granule in an exponentially growing cell and a frozen cell on day 6 of starvation can be seen in Figure 7.3. Within $83 s$, a granule in an exponentially growing cell travels a maximum distance of $400 nm$ to $500 nm$ in one dimension, whereas the granule in the frozen cell explores less than $10 nm$. From the granule's position over time the MSD can be calculated for various time lags Δt, averaged over all data points with the same time lag. If N data points are recorded, the MSD as a function of the time lag can be calculated as

$$\langle r(\Delta t_n)^2 \rangle = \frac{1}{N-n+1} \sum_{i=0}^{N-n} (r(\tau_i + \Delta t_n) - r(\tau_i))^2. \tag{7.1}$$

Where n represents the number of frames equivalent of a time lag Δt and τ_i is the current starting time. Equation (7.1) represents the MSD in one dimension. In order to expand to two-dimensions, the MSDs can be added

$$MSD(\vec{r}) = MSD(x) + MSD(y), \tag{7.2}$$

where $\vec{r} = \binom{x}{y}$ and $\vec{r}^2 = x^2 + y^2$. In order to ensure enough data points to calculate the MSD accurately, one has to be careful to not let the time lag get too large [183]. Ibeneche had shown, that a time lag of 5%, equivalent to $4.2 s$ in this case, is a good choice [94]. The one-dimensional MSDs of the granules position-time traces are shown in Figure 7.3. To obtain the anomalous diffusion exponent α from the plot of MSD over time lag, the logarithm of the MSD is plotted against the logarithm of the time lag. The MSD for anomalous diffusion in two-dimensions is $MSD = 4Dt^{\alpha}$. Taking the logarithm on both sides of the equation results in

$$\log(MSD) = \log(4D) + \alpha \log t. \tag{7.3}$$

A linear fit in the plot of $\log(MSD)$ versus $\log t$ will reveal the anomalous diffusion exponent α as the slope of the fit and the generalized diffusion coefficient D from the y-intercept. In the example shown in Figure 7.3 the calculated alpha value for the exponentially growing cell is $\alpha = 0.66$ and for the starved, frozen cell $\alpha = 0.12$.

Often, we are not interested in the alpha values of a single cell but in the average alpha value of a whole culture. Therefore many granules are tracked for each state. Results are reported as the average alpha value ± the standard error of the mean.

Chapter 8

DIC Single particle tracking in yeast cells

8.1 Introduction to DIC microscopy and single particle tracking

Differential interference contrast (DIC) is commonly used in life sciences to observe structures and motion in unstained living cells and to perform high precision single particle tracking on small refractile objects, such as artificial tracer particles or naturally occurring organelles such as lipid granules. The high optical sectioning abilities of DIC in contrast to fluorescence make it an ideal candidate for axial position tracking. Additional benefits of using DIC are the lack of photo bleaching and the unique determination of the axial position around the focus. The optical sectioning of DIC microscopy is demonstrated in Figure 10.4. A $500nm$ polystyrene bead is imaged in steps of $1\mu m$ over the distance of $7\mu m$ for various openings of the condenser aperture. If the condenser aperture is almost closed (10% opening), the coherence of the illumination is maximal. The interference rings of the $500nm$ bead are visible over more than $\pm 4\mu m$. For an opening of 56%, the bead is only well recognizable over $\pm 2\mu m$. If the condenser aperture is maximally open, the coherence of the illumination is minimal and the bead is observable over $\pm 1\mu m$, which results in the best optical sectioning. The range marked in red in Figure

8.1c) is used for axial position detection.

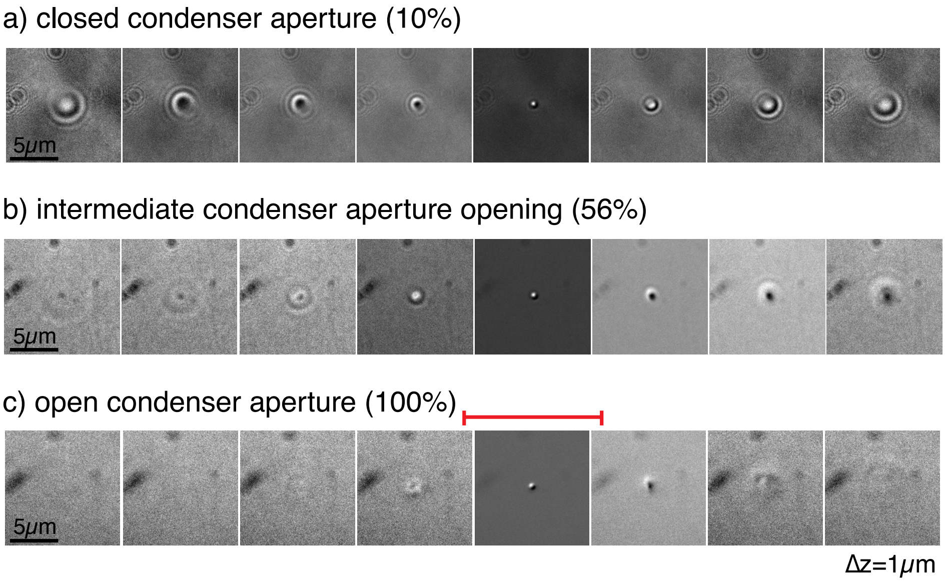

Figure 8.1: Demonstration of optical sectioning in DIC microscopy. DIC images of a $500nm$ polystyrene bead were recorded axially separated by $1\mu m$ each, covering a total of $7\mu m$ in the z-direction. For each sequence the condenser aperture opening was adjusted from a) 10% to b) 56% and to c) 100%. The optical sectioning abilities increase with the opening of the condenser aperture.

DIC microscopy is based on phase contrast microscopy, which was developed by Frits Zernike in the 1930s. For the invention of the phase contrast microscope he received the Nobel Prize in physics in 1953. Francis Smith developed a DIC technique in 1947, in which he placed one Wollaston prism between two polarizers at the front focal plane of the condenser and another in the back focal plane of the objective. However, in objective lenses with a higher numerical aperture, the back focal plane is often located inside the lens system, which restricts the placement of the prism. In 1952, Nomarski solved this problem by modifying the Wollaston prism, to achieve simultaneous spatial displacement and angular deviation [6, 165]. This Nomarski prism can be placed outside of the objective lens and enables the use of high numerical aperture objectives in DIC microscopy. In DIC contrast, the phase gradient is measured instead of the absolute phase, which leads to the characteristic three-dimensional-like contrast rich images, highly useful for position tracking of small particles.

Single particle tracking has been utilized since the beginning of the 1980s. Barack and Webb pioneered single fluorescence particle localization and tracking in the study of tagged low density lipoprotein receptors on human fibroblast cells [13, 14]. It took until 1994 to automate the tracking and localization of the fluorescently tagged receptors [70] and 1996 to image the diffusion of single fluorescence molecules in membranes [186, 187, 183]. Three-dimensional fluorescent particle tracking was first achieved by measuring the asymmetry of the fluorescent image generated by a cylindrical lens [103] in 1994 and by using the off-focus image in 2002 [198]. 1988, Gelles, et al. implemented DIC single particle tracking via cross correlation and measured kinesin driven motion with 1-2nm precision [69]. By integrating a laser interferometer [53, 202], spatial and temporal resolution were improved, so the motion of kinesin could be followed with angstrom level noise and millisecond temporal resolution. More recent ideas of single particle tracking involve the detection of the motion of heated nano-particles [173]. Boyer, et al. demonstrated the imaging of gold particles as small as $2.5nm$ with a photothermal method that combines high-frequency modulation and polarization interference contrast [22]. Common fluorescent and DIC single particle tracking methods are reviewed in [30].

Particle tracking, which relies on cross-correlation as most commonly used with DIC microscopy, can be slow and requires that the particle stays in focus. This is required, because the DIC point spread function strongly depends on the axial position which can lead to problems with the cross-correlation. The adjustment to shape and contrast changes at different axial positions can be achieved, if a mathematical function with a variable width and amplitude can be fitted to the image. An example is fitting a two-dimensional Gaussian to a particle in fluorescent microscopy. The center of the Gaussian determines the lateral position. Fitting a function to a DIC image is more complex due to the black-white transitions in the contrast. Since DIC reports on the difference in phase caused by an object, integration of the image obtains the absolute phase change of the object, at least for small particles. The absolute phase of a particle has a Gaussian shape similar to the fluorescent particle, which facilitates the use of standard single particle tracking methods. Integration of the DIC image along the shear axis converts the image from the typical black white transition to a single peak. This reduces the problem of finding the center of the particle in DIC to finding the center of a Gaussian function, an established method. Additionally, the integration of the image produces a shift in the offset of the Gaussian, which linearly depends on the axial position in the vicinity of the focal plane. Image integration can be used to determine the position of the particle laterally with sub-nanometer resolution and axially with a resolution of 5nm within a single frame. However, due to the optical sectioning of DIC, the particle can only be tracked axially within approximately 600nm. If the particle diffuses significantly in the axial direction, a feedback loop helps track the particle's center in three-dimensions over long periods of time.

8.2 DIC Microscopy

Figure 8.2 shows the schematic setup of a DIC microscope. The illumination can either be white light, or monochromatic with the addition of a band pass filter. Green light was most commonly used for imaging beads and white light for imaging cells. The light from the illumination source is polarized under $0°$ by the first polarizer. The degree of coherence of the light and the effective numerical aperture of the condenser can be adjusted by the condenser aperture. Subsequently, the light enters the compensator Nomarski prism, where it is split with respect to $-45°$ and $45°$ polarization, the ordinary and extraordinary wavefronts, and it is additionally spatially separated by a small amount. After passing through the condenser lens, the wavefronts are laterally separated by the distance s, called the shear, which is typically on the order of the resolution limit of the microscope. In the specimen, the rays pass

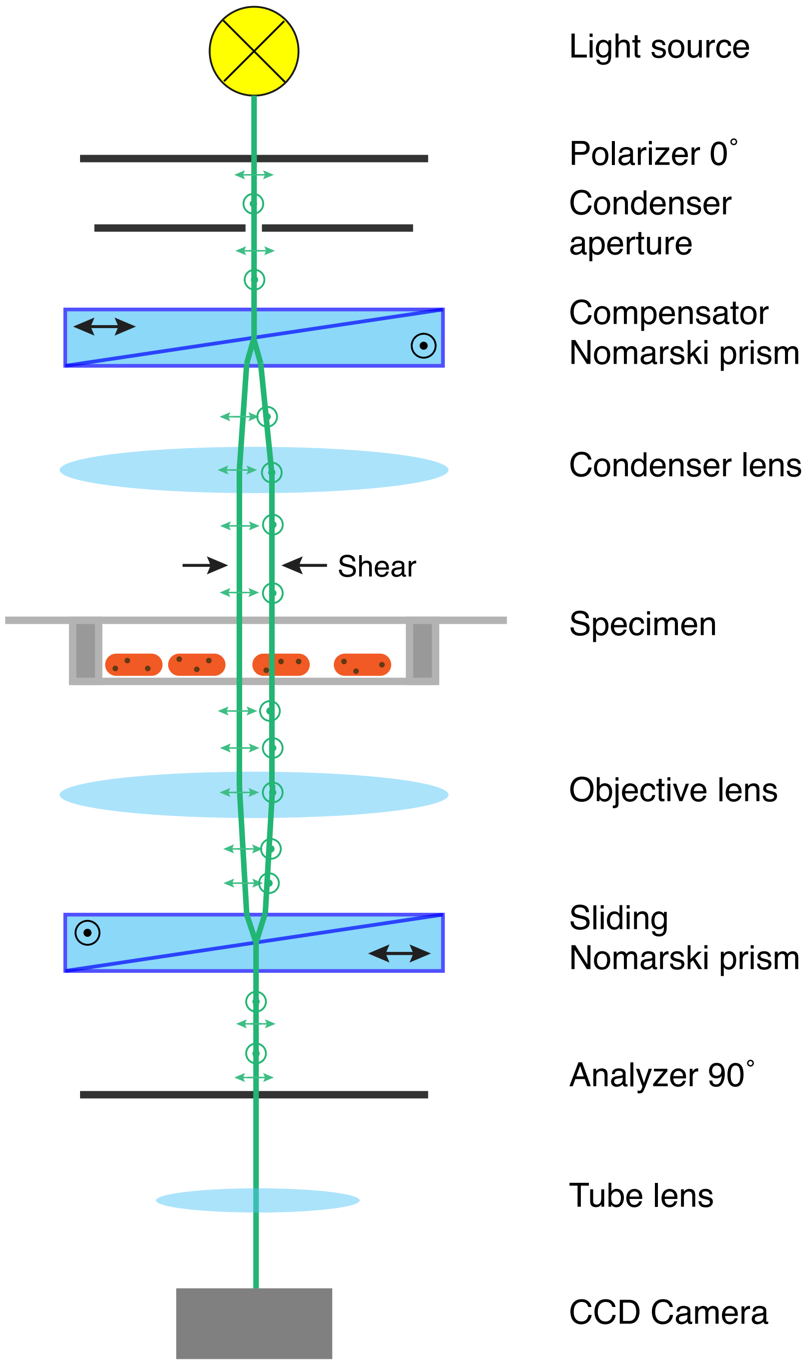

Figure 8.2: Schematic of a DIC microscope.

through different regions of the sample, where the phase of the wave is changed as it passes through a phase object. The light is collected by the objective lens and the rays are brought together to interfere by the second, sliding Nomarski prism. Depending on the path difference of the waves, the interference can be constructive or destructive. The light which had passed through empty parts of the sample is blocked by the analyzer, which is perpendicular to the polarizer. The tube lens focuses the image onto a CCD camera. Alternatively the image can be viewed through the eyepiece of the microscope. The phase gradient of the sample can be measured, by interfering rays that have been sheared by a few hundred nanometers. This leads to the characteristic shadow cast DIC images.

The position of the sliding Nomarski prism can be adjusted by a micrometer screw to change the bias retardation. The image formation process and the effect of bias retardation are shown in Figure 8.3. Figure 8.3a) shows the sheared wavefronts w_1 and w_2 for zero bias retardation, $\Delta_b = 0$, also called the extinction mode. The parts of the wavefront which were not phase shifted by an object make zero contrast, such as the background of the image. For a spherical object, the background and the center of the bead are dark, while the edges on the outside are bright, where the retardation induced by the dephasing object is Δ_{obj}. By adding a positive bias, $\Delta_b > 0$, the wavefronts are phase shifted with respect to each other. This leads to the reduction of the phase retardation of w_1, where the total phase retardation is $\Delta_{obj} - \Delta_b$. Conversely, the phase retardation of w_2 is enhanced, $\Delta_{obj} + \Delta_b$. Due to the addition of a

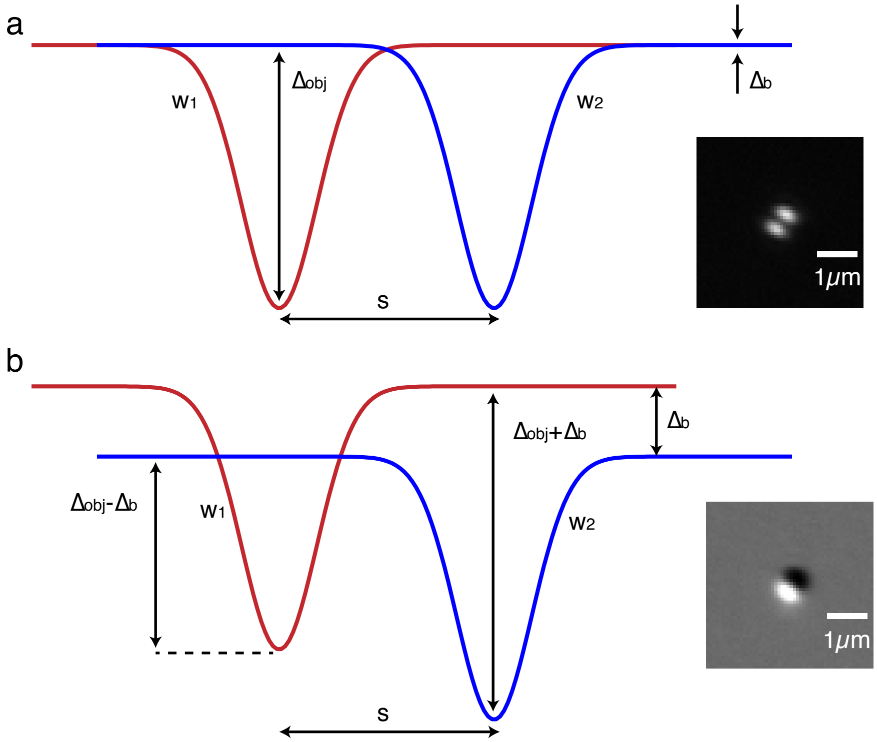

Figure 8.3: Image formation in a DIC microscope. a) Extinction mode b) positive bias retardation.

positive bias, the resulting image will have a brighter background, since the wavefronts are phase shifted by $\Delta_b > 0$ and partially pass through the analyzer. Now, one side of the spherical object has a larger phase retardation than the other, resulting in the typical DIC black-white shadow-cast contrast of the bead.

8.3 DIC single particle tracking by image integration

Although DIC single particle tracking via cross-correlation is a common method used in biology, problems can occur if the object moves in the axial direction. This is due to the DIC images having a different black and white contrast and a wider point-spread function out of focus. Figure 8.4a) shows DIC images of a baked $500nm$ polystyrene bead at different heights with respect to the focus. All images show the black-white transition along the shear axis. Already visible by eye is the effect that the amount of white versus the amount of black in each image seems to differ depending on the z-position. To quantify the apparent differences in the DIC images, we evaluate the line profile along the shear axis through the center of the bead (Figure 8.4b). The peak-to-peak intensity can be extracted from the line profile by taking the highest and lowest intensity value. The peak-to-peak intensity is highest in focus and decreases above and below the focal plane. Additionally, it is evident that the amount of white versus black changes depending on the z-position. An easy way to obtain a value for the difference of the areas of the positive peak (white) versus the negative one (black) is to integrate the line profile. To

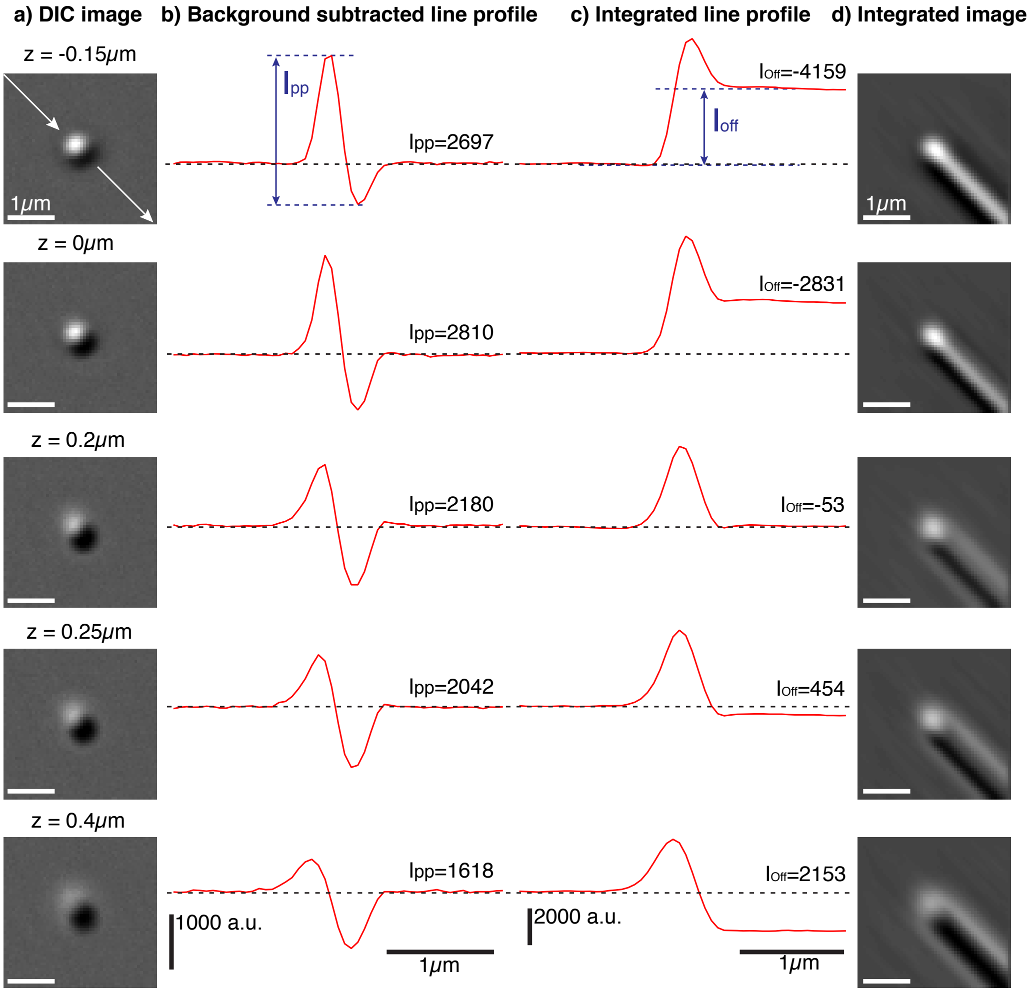

Figure 8.4: DIC images of a $500nm$ polystyrene bead at different axial positions with respect to the focal plane. The first column a) shows the DIC image, b) the background subtracted line profile along the shear axis. The line profile is typical for a DIC image with positive bias for small particles. The intensity difference between the maxima and the minima, peak-to-peak intensity I_{pp}, is dependent on the z-position and is maximal in the focus. c) The integrated line profile resembles a Gaussian function with a plateau on the right side, which is offset with respect to the origin. The magnitude and sign of the offset, I_{off}, depends on the z-position and can be used as a measure of the position of the bead with respect to the focal plane. d) Original DIC image integrated along the shear axis (45°).

avoid integrating over the constant background, which would result in a slope on top of the desired signal, the background value is subtracted from the line profile before integration. If both the positive and the negative area in the line profile are approximately equal, the result of the integration is a single Gaussian peak, as in the case of the bead at $z = 0.2\mu m$ (Figure 8.4c). If the white part dominates in the line profile, the integration still yields a Gaussian, but it is not symmetric. On the far side, the Gaussian plateaus at a positive value, which is representative of how much more white versus black contrast the DIC image contains. If black dominates the DIC image, then the value of the plateau will be negative. The difference between the plateaus on both sides of the Gaussian peak will be called the offset value and is dependent on the z-position. Figure 8.4d) shows the DIC image integrated along the shear axis.

Integration of the DIC image is an essential step for tracking the particle's position both laterally and axially. For the tracking in the x- and y-directions, the problem of finding either a black-white transition or doing cross-correlation is simplified to finding a single Gaussian peak, a standard procedure in the literature. This can easily be seen for the one-dimensional case as shown in Figure 8.4. The integration of the line profile results in a single peak, whose center can be determined with high precision by fitting it with a Gaussian. This method can be generalized to the two-dimensional case. If the whole DIC image is integrated along the shear axis, a two-dimensional peak emerges, which can be fitted with a 2D-Gaussian to identify its center position.

Integrating the DIC image and fitting it with a Gaussian is a fast and precise method to determine the center of spherical objects in DIC microscopy. Additionally, the integration of the image transforms the characteristic features of the original DIC image at different z-positions and reveals a parameter, the offset, which can be used for z-position tracking.

8.4 Axial response curves

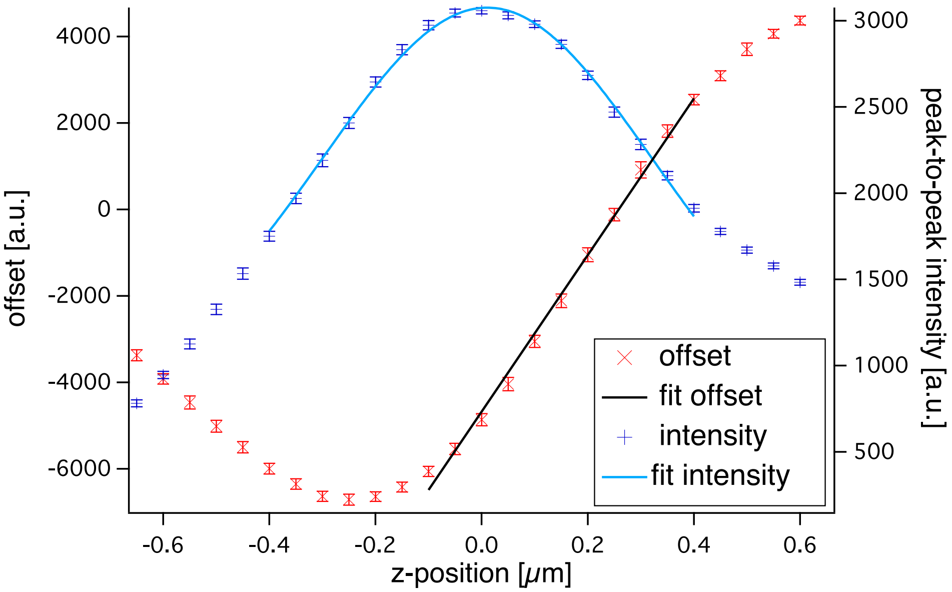

Figure 8.5: Axial response curves of the peak-to-peak intensity and the offset of the integrated intensity for a 500nm polystyrene bead. The peak-to-peak intensity has its maximum in the focus and falls off to lower values above and below it. About ±400nm around the focus the peak-to-peak intensity can be fitted by a Gaussian. The offset in intensity has a linear regime of approximately 600nm. The exact location of the center of the linear regime depends on the DIC microscope settings like bias, aperture opening and illumination light color.

a) 200nm polystyrene

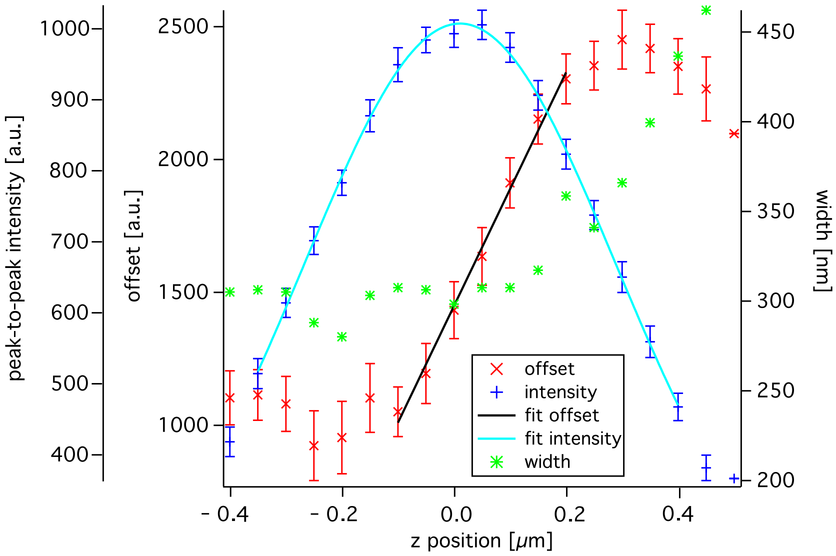

b) 800nm polystyrene

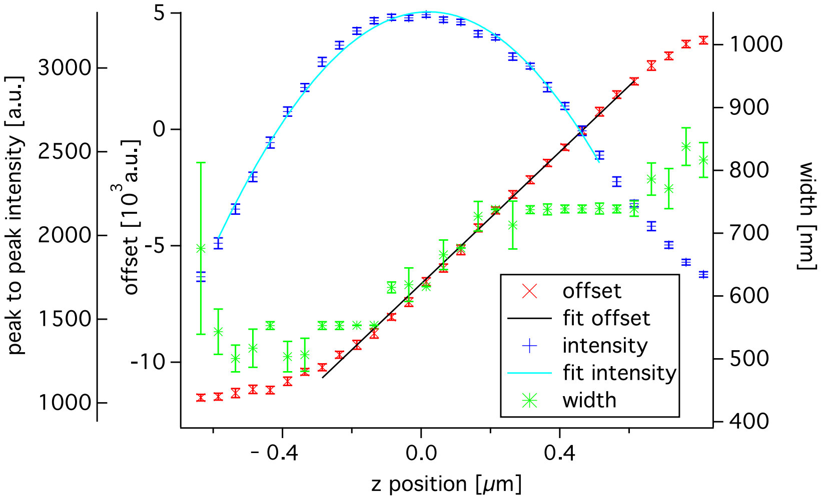

Figure 8.6: Axial response curves of the peak-to-peak intensity, the offset of the integrated intensity, and the width, the distance between maxima and minima in intensity, for a 200nm and 800nm polystyrene bead. The peak-to-peak intensity has its maximum in the focus and falls off to lower values above and below it. Around the focus the peak-to-peak intensity can be fitted by a Gaussian. The offset in intensity has a linear regime.

DIC microscopy is very well known for its outstanding optical sectioning abilities. This implies that when the image formation strongly depends on the axial position, z-position detection should be feasible. As shown in the previous paragraph, there are two possible candidates, the peak-to-peak intensity and the offset. In order to quantify how well these parameters work for axial position detection we measured the response curve for a $500nm$ bead. For this we baked a $500nm$ polystyrene bead to the coverslip and took 100 images at each position in $50nm$ steps over a range of $\pm 1\mu m$ with respect to the focal plane. The response curve for a $200nm$ and $800nm$ bead are shown in Figure 8.6. From the 100 images at each position the average peak-to-peak intensity and offset were calculated. The results are shown in Figure 8.5. As expected the peak-to-peak intensity shows a maximum at the focus and the intensity falls off to both sides symmetrically. Within a range of $\pm 400nm$ the peak-to-peak intensity can be fitted with a Gaussian. The offset behaves more complexly, but with this particular bias has a linear region from $100nm$ below the focal plane to $500nm$ above it. In principle both curves can be used for the z-position detection. The peak-to-peak intensity has the advantage of a larger usable range, but the problems with using it are that the resolution in focus is not sensitive and due to the symmetry it is impossible to decide if the object is above or below focus solely by the intensity. Using the offset for axial detection is more advantageous. Since the offset has a linear regime around the focus, z-position detection can be achieved uniquely with high resolution even in focus. In both cases the z-position can be determined by looking at a single image. The offset offers a unique solution, whereas the intensity is ambiguous.

8.5 Precision of the position tracking

Integrating the DIC images allows us to calculate the particle's position in all three dimensions with a single image. To determine how accurate this method is, we perform precision tests. For this we baked a $500nm$ bead to the coverslip and modulated the position laterally and independently in the axial direction.

The precision of the lateral position detection was tested by oscillating the Queensgate stage by $\pm 5nm$ in the x- and the y-direction. DIC images were recorded while the particle was in focus and $300nm$ above the focal plane, Figure 8.7a). Using the integrated images, the x- and y-positions were calculated. The standard deviations of the lateral position noise for each oscillation are $0.8nm$ in focus and $0.9nm$ out of focus. The precision with which the lateral position of a bead can be determined only very weakly depends on the particle size. Therefore, this method enables sub-nanometer precision single particle tracking in DIC for spherical objects of various sizes.

For the axial precision test the z-position of the objective lens was modulated by $\pm 10nm$, once with the bead in focus and once $200nm$ above the focal plane. The z-position of the bead was calculated by evaluating the offset as well as the intensity. The results are shown in Figure 8.7b). For the position detection calculated with the offset, the actual position is irrelevant

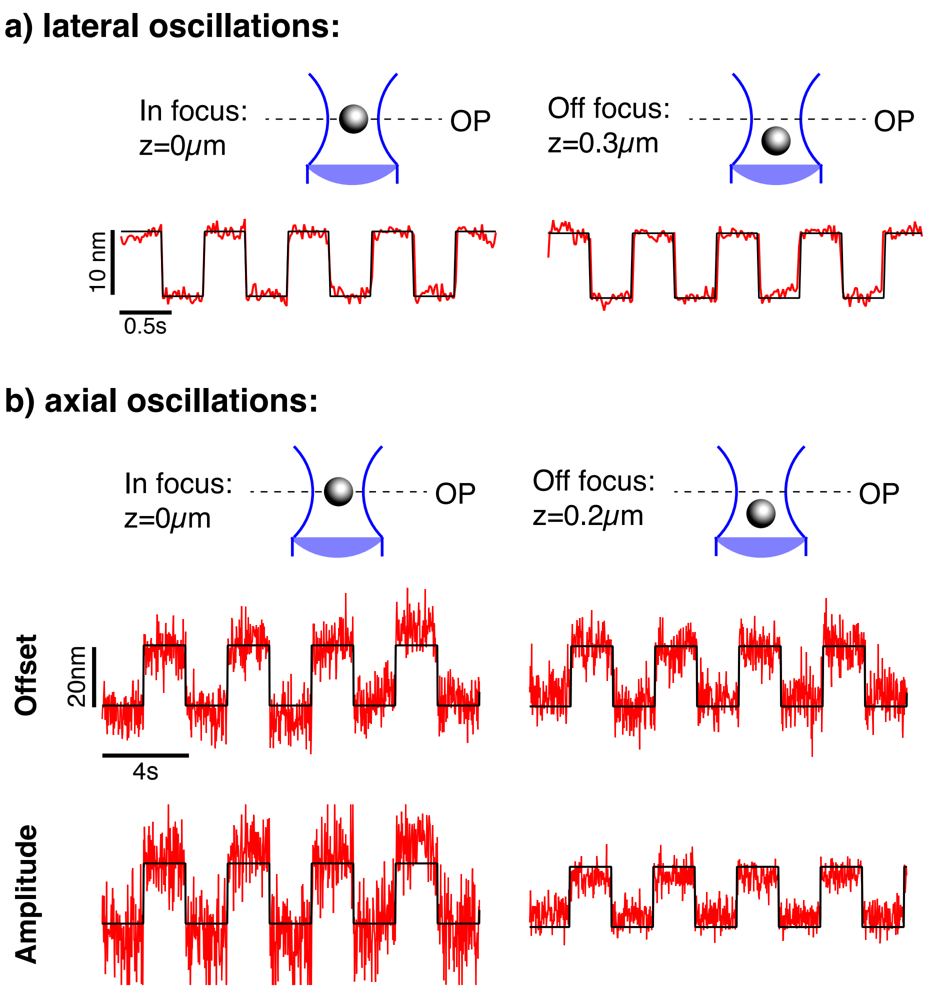

Figure 8.7: Resolution test of the lateral and axial position detection. a) Lateral oscillation of the stage of $\Delta x = \pm 5nm$ in and $300nm$ out of focus. In both cases the particle can be tracked with sub nanometer precision. b) DIC images were recorded as the axial bead position was modulated by $\pm 10nm$, once approximately in focus and once $200nm$ away from the focal plane. The z-position of the bead was calculated from the offset and the peak-to-peak intensity. When the z-position is calculated from the offset, the resolution remains the same in and out of focus, $5nm$. If the peak-to-peak amplitude is used for the position detection the resolution depends on the bead's position with respect to the focus. The closer the bead is to the focus, the worse the axial resolution gets.

for the precision, as long as it is within the linear regime. The precision achieved by evaluating the offset is $\pm 5nm$. When using the peak-to-peak intensity to calculate the z-position, the precision strongly depends on the position with respect to the focus. First, in focus the position cannot be resolved, because the slope of the response curve is zero. Second, in vicinity of the focal plane the slope of the response curve is shallow and will lead to a low resolution. Additionally, one needs to know on which side of the focus the object is to determine its absolute position. This becomes more problematic if the position changes from above to below focus randomly. Evaluating the offset can theoretically solve this problem, but the precision around the focus still remains low. Figure 8.7b) shows the position time traces extracted from the peak-to-peak intensity. Close to the focus, the measured position fluctuations are a factor of approximately 2.5x larger than $200nm$ above focus, $\pm 8nm$ versus $\pm 3nm$. The precision of the z-position measurement depends on the size of the particle. For $200nm$ beads a precision of $\pm 20nm$ was achieved with the offset and $\pm 14nm$ with the peak-to-peak intensity off focus, Figure 8.8. For the $800nm$ bead the precision was for the offset $\pm 7nm$ and for the intensity $\pm 10nm$. Utilizing the offset for axial position measurements results in a unique position calculation and has a uniform precision of $\pm 5nm$. For small position fluctuations a higher precision might be achieved by slight defocusing.

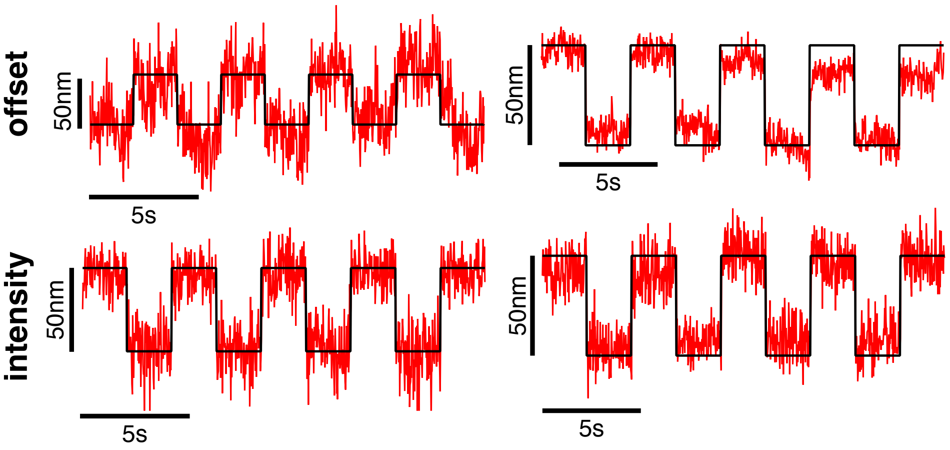

Figure 8.8: Resolution test of the axial position detection for a a) 200nm bead and b) 800nm bead. DIC images were recorded as the axial bead position was modulated by ±25nm. The z-position of the bead was calculated from the offset and the peak-to-peak intensity.

8.6 Feedback

The ability to determine a particle's position in three dimensions in a single image allows us to build a feedback loop with which we can follow a particle in a three-dimensional environment over long periods of time. To implement a feedback loop we determine a particle's relative z-position with respect to the focus and adjust the height of the objective lens, so that the particle approaches the focal plane. Since calculation of the particle's axial position depends on its size, we only determine if the particle is above or below the focus and adjust the position accordingly with a fixed step size. In order to initialize the feedback loop, a region of interest (ROI) slightly larger than the object needs to be defined around it. This marks the area of the image, which is duplicated for further image processing to determine the position of the bead. The accuracy and robustness of the feedback increases with increasing size of the ROI, because more values can be used to calculate the offset. The crowdedness of the sample sets an upper bound for the size of the ROI, since any additional structures in the ROI besides the particle can affect the correct computation of the offset.

After the first image is acquired, the area of the image marked by the ROI is copied into an array. Then the average of the array is calculated and subtracted, which helps to avoid sloping of the integrated image. Afterwards, the array is integrated along the shear axis (45°) by subsequent addition of the diagonal array elements. As seen in Figure 8.4, the integration transforms the black and white transition into a single Gaussian peak. The peak can either be fitted with a two-dimensional Gaussian function or with a one-dimensional Gaussian by using the x- and y-projection of the integrated array to obtain the current x- and y-position. The latter case is computationally faster and accurate enough to obtain the coordinates with pixel resolution. The newly calculated x- and y-position is then used as the center for the ROI position in the following acquired image. In order to obtain the particle's z-position the offset is calculated from the line profile of the integrated array. For the offset, the first few values of the line profile are subtracted from the last ones. The number of values that can be used depends on the size of the ROI with respect to the particle size and the crowdedness of the sample. The accuracy of the feedback loop increases as the number of values used to calculate the offset. The calculated value of the offset is compared to the value of the offset in focus: the set point. Depending on weather the actual value is larger or smaller than the set point, the height of the objective is adjusted accordingly by a given, fixed step size. After adjusting the z-position, a new image will be acquired and the previously calculated x- and y-coordinates are used for the center of the ROI to compute a new set of parameters. All computations used in the feedback loop are fairly simple and can be executed fast enough not to slow down the frame rate at $60fps$. The continuous adjustment of the focus and the center of the region of interest enables long-term observation of the particle since it cannot diffuse out of focus.

8.7 *In vitro* testing of the feedback

In order to test the functionality of the feedback we chose a simple model system of $500nm$ polystyrene beads dissolved in a glycerol solution. To begin with, the feedback was tested with a low concentration of beads of approximately $10^{-4} beads/\mu m^3$. The size of the square ROI was chosen to be 20 by 20 pixels. At low concentrations the particle can be observed for long periods of time, easily on the order of hours. Since cells are crowded, it is important that the feedback would work equally well in crowded environments. Therefore, the concentration of the beads was increased to a value of $0.029 beads/\mu m^3$, which is on the order of magnitude as the number of granules per cubic micrometer in a fission yeast cell. Even in this crowded environment the particle can still be followed for extended periods of time.

Here, a movie of 9000 frames, approximately $9.1min$ was recorded. Exemplary images of individual frames are shown in Figure 8.9. The bead, whose center is followed by the feedback is marked with a red square. This bead remains in focus throughout the whole movie, whereas the other beads are diffusing in and out of focus. The fact that the piezo element is constantly adjusting the height of the objective is visible when looking at the beads stuck to the surface as a reference point, marked with blue arrows in Figure 8.9. These beads can be seen in the middle parts of the movie and can be recognized by the lack of lateral diffusive motion. Additionally, this movie demonstrates very nicely that this method works even for very crowded environments. 36 seconds into the movie (panel 4 and 5 of Figure 8.9) the bead crosses paths

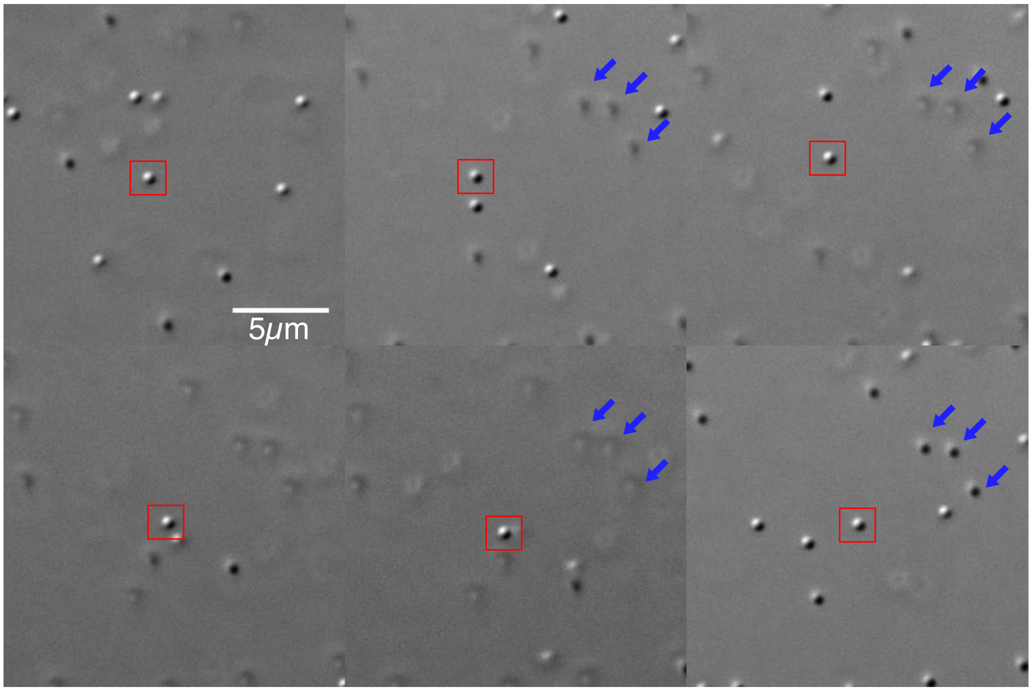

Figure 8.9: *In vitro* testing of the feedback on beads in glycerol. Beads were dispersed in glycerol at a concentration of $0.029 beads/\mu m^3$. A movie of 9000 frames, approximately $9 min$, was recorded, where the center of the bead was followed with the feedback, marked by the red square. The blue arrows mark beads attached to the coverslip, which act as an indicator for different axial positions of the images. The representative images are taken at $t = 0s$, $73.4s$, $109.6s$, $216.0s$, $227.0s$ and $293.8s$.

with another one, but the feedback remains on the original bead. Sometimes the feedback loses the bead when two or more beads collide. Generally the algorithm can be adjusted to accommodate two particle interactions. Since particles that switch positions laterally are at different heights, they should be identifiable according to their z-position. To summarize, the high optical sectioning abilities of DIC microscopy, enable the use of feedback on beads even in crowded environments.

8.8 *In vivo* testing of the feedback

After successful demonstration of the feedback in crowded environments, we have tested it by tracking lipid granules in exponentially growing fission yeast cells. The *in vivo* DIC tracking is more challenging since the cells are very crowded, they have a non-uniform background, a high contrast from the cell wall and the granules are smaller, around 300nm. Any of the aforementioned problems can lead to the loss of the lipid granule from the feedback. Nevertheless, lipid granules were successfully tracked for up to an hour in our experiments. Figure 8.10a) shows the calculated x-, y- and z-position of a lipid granule over the course of 35 minutes. Although the feedback during data acquisition calculates x- and y-positions from the Gaussian fits of the one-dimensional projection of the integrated image, the resulting image sequence is analyzed with the previously described tracking algorithm to obtain sub-pixel resolution. The z-position signal is composed from the absolute position of the nano-positioning device and the position calculated from the

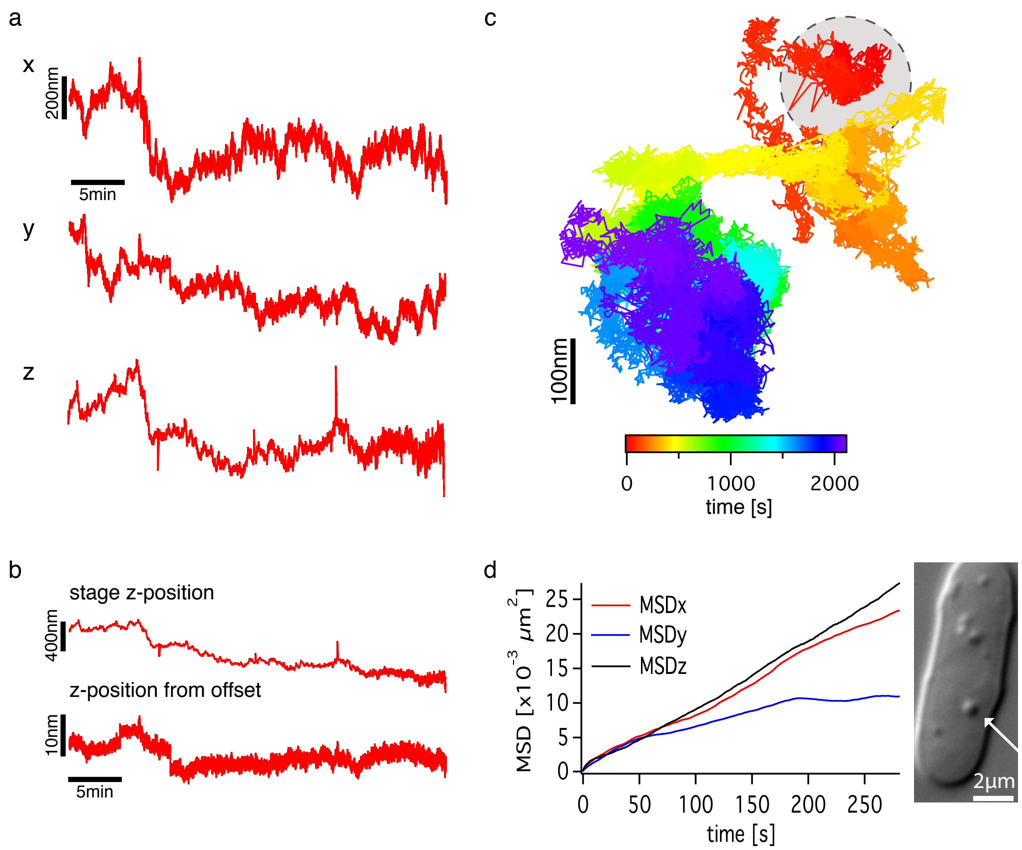

Figure 8.10: Long term tracking of fission yeast lipid granules. a) X-, y- and z-position traces of the lipid granule over time. b) The axial position signal is composed of the calculated position from the offset and the position of the piezo from the feedback. c) Plot of the position of the granule in the xy-plane. The color of the trace shows the time evolution of the granule's position. The grey circle indicates the average area the granule could have explored without the feedback. d) Plot of the MSD over time for the separate axis. For small timescales, smaller than 60s, the MSDs in all directions are comparable, due to the isomorphic structure of the cell on small length scales. For longer times, larger than 70s, the MSD in the y-direction stagnates in contrast to the MSD in the x-and z-direction. This indicates spatial confinement of the granule in the y-direction, possibly due to the nucleus above the granule.

offset (Figure 8.10b). The trace of the particle through the part of the cell is shown in a z-projection in Figure 8.10c). The position of the granule is color coded with respect to time. The particle starts its path in the middle of the grey circle and ends at the dark blue color. In exponentially growing cells, the time a granule can be observed without feedback is on the order of 1.5 minutes, before it diffuses out of focus. The grey circle indicates how much area a granule could explore in 1.5 minutes with a diffusion constant extracted from the data for this specific granule. With the feedback the granule could be observed 23 times longer and it could explore significantly more space during that time. The observation over long periods of time with a frame rate of $32 fps$ enables the accurate calculation of the mean squared displacement (MSD) for higher time lags. As shown in Figure 8.10d) on short timescales, shorter than 60 seconds, the behavior of the MSDs in all three dimensions is equal, because the explored volume is thought to be smaller than the typical length scale of confinement. All three curves for the MSD show anomalous diffusion behavior. For longer timescales, larger than 60 seconds, the MSD in the y-direction additionally shows confined motion, the MSD plateaus at a value of $11 \cdot 10^{-3} \mu m^2$, whereas, the MSD for x and z keep increasing. This indicates spatial confinement by something inside the cell. The DIC image of the cell indicates the position of the lipid granule. Just on top of the granule the nucleus is visible, which might be responsible for the confinement of the motion of the granule in the y-direction. With the help of the feedback, the position of the lipid granules can be observed for longer periods of time. During this time, it can act as a reporter of the inner cell structure and also how those structures evolve in time. Confinement of the granule's motion cannot only be observed and visualized in the two- and three-dimensional position of the granule, but also in the MSD, when measured for long enough time. Only if the particle has sufficient time to explore the boundaries of its confinement, the MSD shows a plateau on long time scales.

8.9 Discussion

We show that by image integration using DIC microscopy we can track a particle laterally with nanometer precision and axially with a precision of 5nm. The three-dimensional position detection in a single image is the base of building a feedback loop, which follows particles *in vitro* and *in vivo*.

Three-dimensional DIC single particle tracking was demonstrated for beads ranging from $200nm$ to $800nm$ diameter. Laterally, we demonstrated sub-nanometer precision on $500nm$ polystyrene beads. The precision of the lateral tracking is fairly independent of the particle radius and sub-nanometer resolution can still be achieved for the beads of different sizes. Axially, the precision of the tracking was dependent on the particle size. For $200nm$ beads the precision was three to four times lower than for the 500nm bead, which showed a tracking precision of 5nm. Also for beads larger than $500nm$ the precision decreases. A common upper boundary for precise particle tracking with this method will be the occurrence of additional interference patterns for larger beads ($> 1\mu m$ for 100x magnification). Additional interference patterns in comparison to the simple black-white transition might lead to a non-linear relationship between the offset and the z-position and changes in the Gaussian shape of the peak-to-peak intensity. A lower boundary for the single particle tracking is determined by the contrast of the bead. As long as there is visible contrast, the lateral tracking works well, the axial tracking loses some of its precision.

The exact position and the slope of the linear regime in the offset with respect to the focus depend on the bias retardation. Additionally, the slope depends on the aperture opening. Changing the bias moves the linear regime of the offset with respect to the focal plane, whereas the peak-to-peak intensity maintains its Gaussian shape. Starting with a small positive bias, very close to extinction mode, the linear regime of the offset is above the focal plane. At maximum bias retardation the linear regime is below the focal plane. At intermediate bias values, the linear regime overlaps with the maximum of the peak-to-peak intensity. The intermediate bias setting is ideal to obtain axial position detection with the offset around the focus, where the axial position detection with the peak-to-peak intensity is problematic and ambiguous. The opening of the condenser aperture influences the shape of the response curve of the peak-to-peak intensity, especially when it is open less than 20% where the response curve can have two local maxima. The further open the aperture, the narrower and more symmetric the Gaussian peak becomes. Having a narrow Gaussian peak can increase the tracking sensitivity using the intensity, especially looking at small displacements. For different aperture openings the shape of the offset response curve mostly changes outside of the linear part. The linear regime reaches its maximum slope at around 70% of the aperture opening and remains approximately constant thereafter. The noise measured at a constant offset value increases with increased aperture opening. Therefore a good setting of the aperture is 70-80% open. In summary, the best axial tracking results can be achieved by intermediate positive bias retardation and approximately 75% condenser aperture opening.

Unfortunately, the exact nature of the phenomenon we are using for the axial position detection, the varying amount of black versus white intensity depending on the height, is unknown. To ensure that the effect is not specific to our microscope and its modifications we took data at two different commercial Zeiss microscopes, a Axiovert 200 with a 40x oil lens and a Zeiss confocal microscope 710 LSM with a 63x water and a 63x oil lens. The images taken on these two microscopes show the same characteristic features as the data described in this thesis. Additionally, we could find examples in literature where the same effect can be observed. Preza et al. [170] simulated and measured the DIC image of a sphere for different heights. Although the simulated image series was symmetric above and below the focal plane, the measured image sequence showed comparable asymmetric black and white transitions. Therefore, we dismiss the assumption that the effect might be due to misalignment, but rather think that it is a so far unknown, effect.

Integrating the DIC images enables sub-nanometer lateral single particle tracking and 5nm precise axial position detection. The offset changes linearly around the focal plane, which can be used to determine the z-position with 5nm precision. Sub-nanometer precision in the lateral motion is not significantly compromised by the axial position. However, the axial position could be used to optimize the lateral resolution. Additionally, the axial signal can be used for building a feedback loop, allowing long term particle tracking in crowded environments and living cells for more than 30 minutes. The axial position of the particle can be reconstructed from the feedback position and the offset signal.

Chapter 9

Origin of cell freezing

9.1 Introduction

The frozen state, as introduced in Chapter 5, is thought to arise due a homogenous, dense, filamentous network. This idea was founded on the observation that the organelles in the cytoplasm are homogeneously immobilized and that even the application of force cannot displace the lipid granules. Candidates for the formation of this network are components of the cytoskeleton. As fission yeast does not have intermediate filaments, this leaves us with microtubule, actin, and the potential fourth member of the cytoskeleton, septins [147]. Actin as well as microtubule were discarded since fluorescent images of the labeled cytoskeletal components in starvation showed no evidence of a dense and homogenous network. Images of fixed, starved yeast cells on day 8, stained with rhodamine-phalloidin, showed the same actin structures than exponentially growing cells; patches and cables, with the exception of a ring, since starved cells are arrested in G2 and not diving. Fluorescent images of GFP-tubulin tagged cells in starvation contain at most one or two microtubule bundles, or fragments, which is also not sufficient for a homogenous network. This left septin as the last candidate, and its role in freezing was determined by single particle tracking.

9.2 Discounting actin

As described previously, actin was discounted of forming a dense, homogenous network because the fluorescent images of actin in starved cells, stained with rhodamine-phalloidin, were comparable to those in exponentially growing cells. Figure 9.1 shows fluorescent images of actin in exponentially growing cells and in deep starvation on day 8. The different actin structures in the exponentially growing cells, Figure 9.1a), are cables which are important for polarized transport, patches which play a role in endocytosis and rings which are necessary for cytokinesis [112]. The starved cells also have cables and patches, Figure 9.1b). Since the starved cells are arrested in the G2 phase of the cell cycle, the culture does not contain any dividing cells and therefore there are no actin rings visible in starved cells. The similarity of the fluorescent images in exponential growth and starvation in addition to many free spaces in the cell was used to discard actin as the protein which builds a homogenous network responsible for cell freezing.

However, the actin structures observed in starved cells seem to depend on the fluorescent marked used to stain actin. The actin stain used in the previous study could only be used on fixed cells. To ensure that the fixation process leaves the actin structures unaltered, we used Lifeact as a marker for filamentous actin which enable the live imaging of the actin structures in the cells [172]. Figure 9.2 shows exponentially growing and starved cells which express Lifeact GFP. In exponentially growing cells and in the early days of starvation the cells have actin patches and cables, as seen previously. The

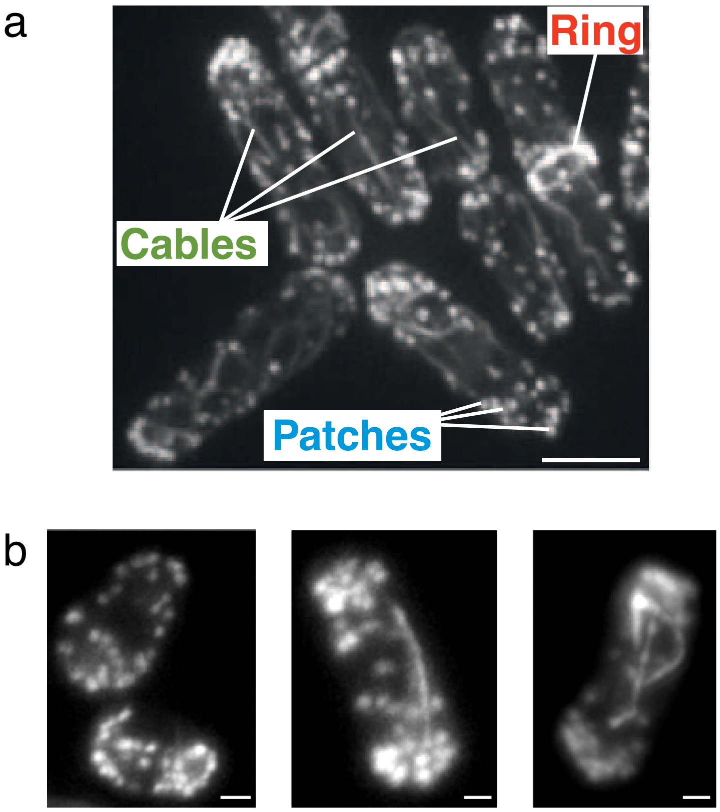

Figure 9.1: Fluorescent images of actin in exponentially growing and starved cells. a) Exponentially growing yeast cells expressing the general F-actin marker GFP-CHD. Formed structures by actin are patches, cables and rings. Image reprinted with permission [112]. b) Fluorescent image of fixed day 8 starved cells, stained with rhodamine-phalloidin. Cells in starvation still show actin patches as well as cables. Scale bars: $1\mu m$. Image reprinted from [94].

alpha value demonstrates if the cell is frozen or not on the respective day of starvation. On day 6 and especially on day 7 when the cells are transitioning in the frozen state, a new actin structure appears, which we call shoelaces. Although some of the cells still have enough empty space around the shoelaces to be the cause of a homogeneous network, other cells show a fairly dense shoelace construct. The newfound actin structure in starved cells reduces the former confidence in discarding actin as playing a role in cell freezing.

In order to ensure that actin is not responsible for cell freezing, we prevented the polymerization of actin filaments with Latrunculin B, effectively depolymerize actin. Since actin is essential for cells and their growth, Latrunculin B (Lat B) was added on day 1 of starvation in order to have a sufficiently grown cell culture. The result of the disruption of the actin filaments on different days of starvation is summarized in Figure 9.3. Exponentially growing cells and cells on day 1 of starvation expressing Lifeact GFP show actin cables and patches as in Figure 9.2, since latrunculin is only added on day 1 starvation. Starting on day 2 of starvation, the cells show a higher homogeneous background signal due to the free actin monomers, and only a few patches. On the later days of starvation most of the actin is dissolved and only very few patches remain, no actin shoelaces occur. The fluorescent images demonstrate that the actin structures were successfully depolymerized.

The depolymerization of actin allows to examine the role actin plays in cell freezing by measuring alpha values in cells with a disrupted actin network and comparing them to cells with an intact actin cytoskeleton. The average

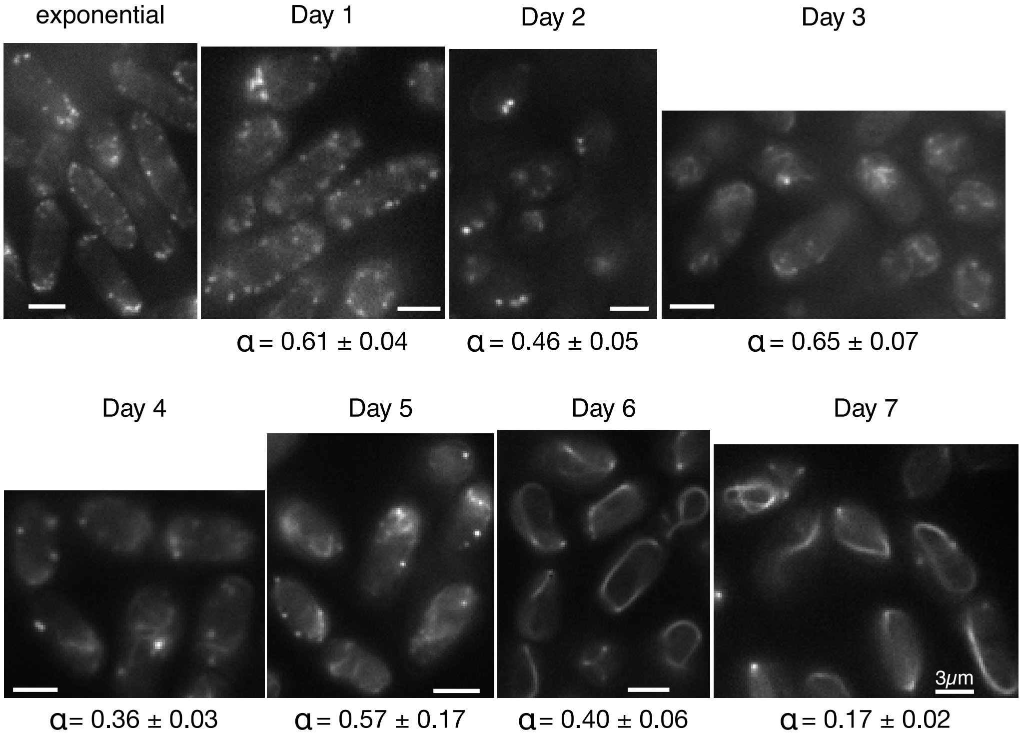

Figure 9.2: Starvation of cells expressing Lifeact GFP. Cells in exponential growth show mostly actin patches and some filaments. When cells start to freeze, actin patches disappear and fibers appear. If the cells are not frozen, these filaments fluctuate, if the cells are frozen, the filaments are immobilized as well.

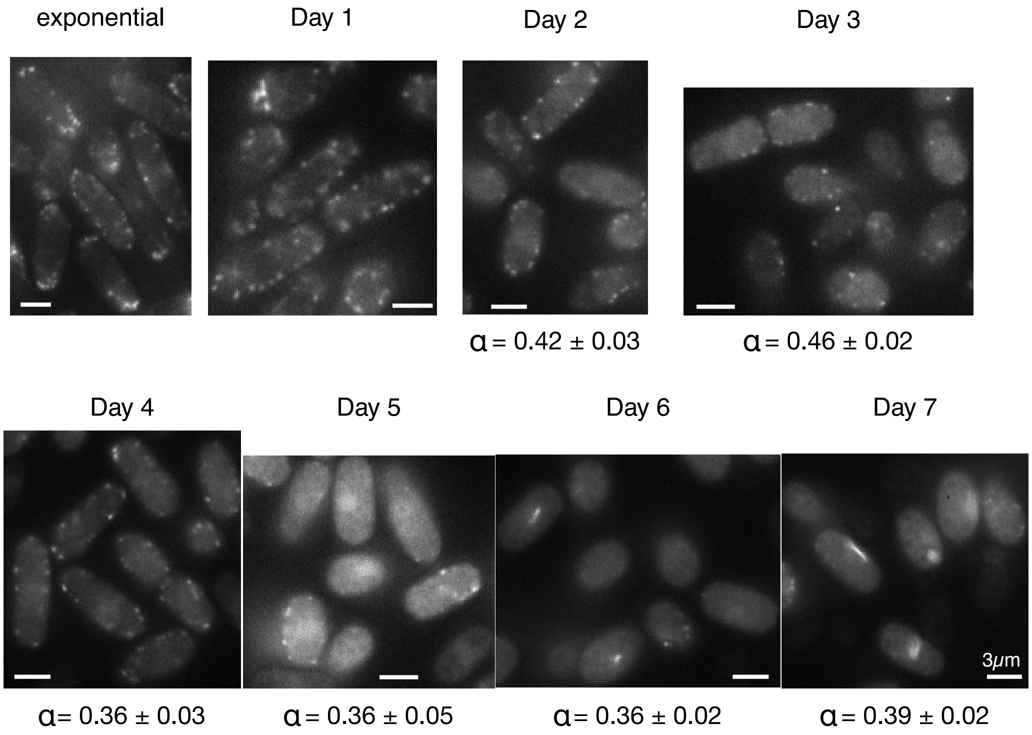

Figure 9.3: Starvation of cells marked with LifeAct, whose actin polymerization is hindered by the addition of latrunculin.

alpha value from single particle tracking of the lipid granules and its standard error for yeast cells marked with Lifeact GFP with and without the addition of latrunculin are shown in Figure 9.2 and Figure 9.3. Figure 9.2 shows that the Liefact cells seem to transition into the freezing state with a delay of two days. The Lifeact cells treated with latrunculin show no freezing up to seven days of starvation, Figure 9.3. Keeping in mind that Lifeact cells only froze on day 7 additional factors like a smaller culture size could be responsible in a further delay of cell freezing.

Figure 9.4 shows a summary of the systematic experiments to discard actin by effective depolymerization of the actin structures. Parallel cultures of Lifeact and wild type cells were used to have a handle on the potential delay in freezing for the Lifeact cells. Additionally, cultures were grown in 10mL cultures in Erlenmeyer flasks and in 1.5mL cultures in culture tubes. since the volume of the culture and the container can affect the timeline of freezing. Both wild type and Lifeact cells had not frozen on day 5 if they were grown in a 1.5mL culture in culture tubes, having an alpha value of $\alpha_{WT} = 0.56$ and $\alpha_{LA} = 0.6$. Only on day 7 they do have lower alpha values, $\alpha_{WT} = 0.21$ and $\alpha_{LA} = 0.16$, which is below $\alpha = 0.27$, indicating freezing. This result was not affected by the addition of DMSO, the solvent for latrunculin, to the 1.5mL cultures on day 1 of starvation. The average alpha value of wild type cells with the addition of DMSO was $\alpha_{WT} = 0.33$ on day 5 and $\alpha_{WT} = 0.21$ on day 7, for Lifeact cells $\alpha_{LA} = 0.41$ on day 5 and $\alpha_{LA} = 0.19$ on day 7. The same was observed when Latrunculin was added to the 1.5mL culture, only for wild

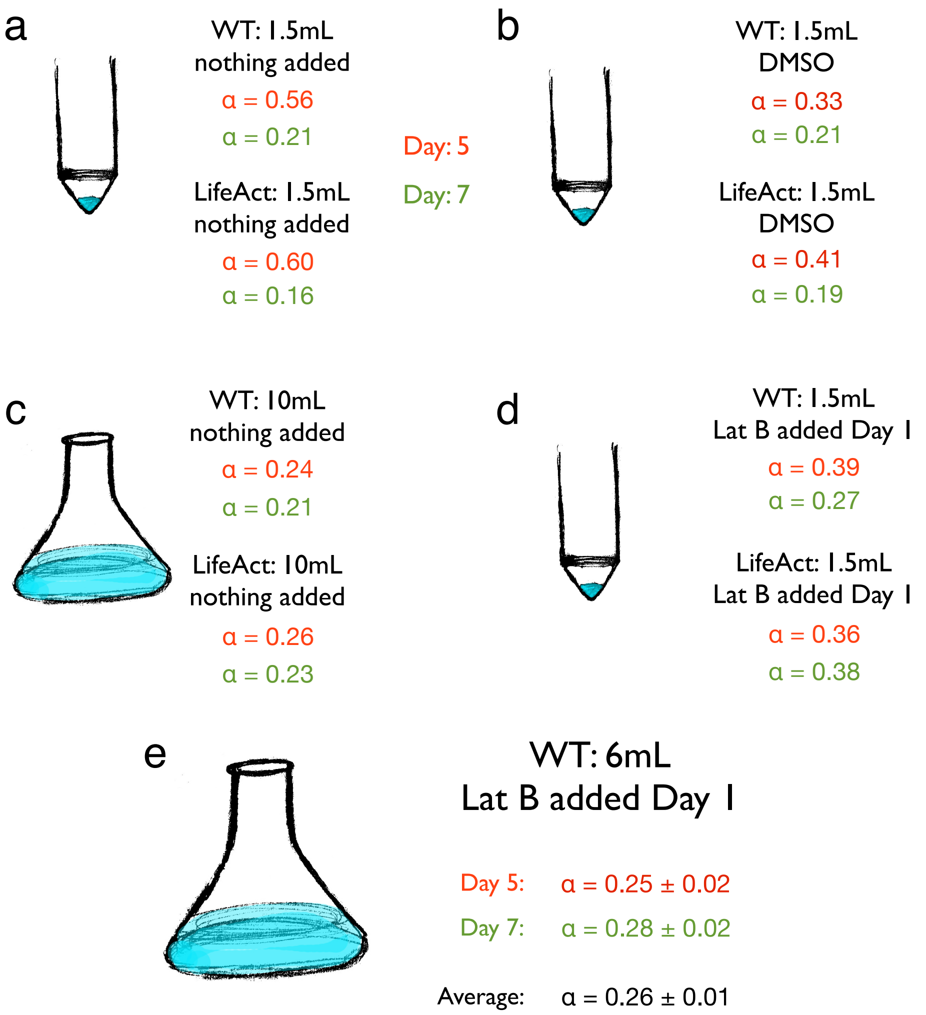

Figure 9.4: Summary of starvation experiments with wild type and LifeAct cells, with the addition of latrunculin. a) Control experiment, starvation of a 1.5mL culture in a culture tube. b) Control experiment with the addition of DMSO, also of a 1.5mL culture in a tube. c) Control experiment with a 10mL culture in a 125mL Erlenmeyer flask. d) Starvation experiment with a 1.5mL culture in a culture tube with the addition of latrunculin. e) Starvation experiment with wild type cells, whose actin polymerization is hindered by latrunculin, a 6mL culture in an Erlenmeyer flask.

type cells, where alpha dropped from $\alpha_{WT} = 0.39$ to $\alpha_{WT} = 0.27$ between days 5 and 7 of starvation. Lifeact cells still had $\alpha = 0.38$ on day 7. For the smaller culture in the culture tubes, all samples show a delay in freezing. To determine that the delay in freezing is due to the smaller culture or the different container a control experiment was conducted with both cell types grown in the regular 10mL cultures in an Erlenmeyer flask. Lifeact and wild type cells have alpha values below $\alpha = 0.27$ on day 5 and day 7 of starvation. This result indicates that indeed the previous culture conditions are responsible for the delay in freezing and do not indicate an involvement of the actin filaments in cell freezing. To demonstrate that cells treated with latrunculin can freeze a 6mL wild type culture was grown in an Erlenmeyer flask and latrunculin was added on day 1 of starvation. The measured alpha values for this culture on day 5 was $\alpha_{WT} = 0.25 \pm 0.02$ and on day 7, $\alpha_{WT} = 0.28 \pm 0.02$, resulting in an average value for both days of $\alpha_{WT} = 0.26 \pm 0.01$. With this experiment we can finally discard actin as the filament responsible for cell freezing. This result is in agreement with the observation, e.g. that the actin shoelaces can diffuse if the cell is close to but not quite frozen and are immobilized when the cell transitions into freezing.

9.3 Septin results

Septins, a protein family which is known to have the capability to form filaments, are another possible candidate for building the homogeneous network. Seven proteins belong to the septin family, septin 1-7. Single particle tracking was done on almost all of the septin deletion mutants to determine their role in cell freezing. As demonstrated with actin, if we delete the septins, and the cells still freeze, then septins are not the cause of cell freezing. If the cells are not frozen, septins do seem to play a role in freezing.

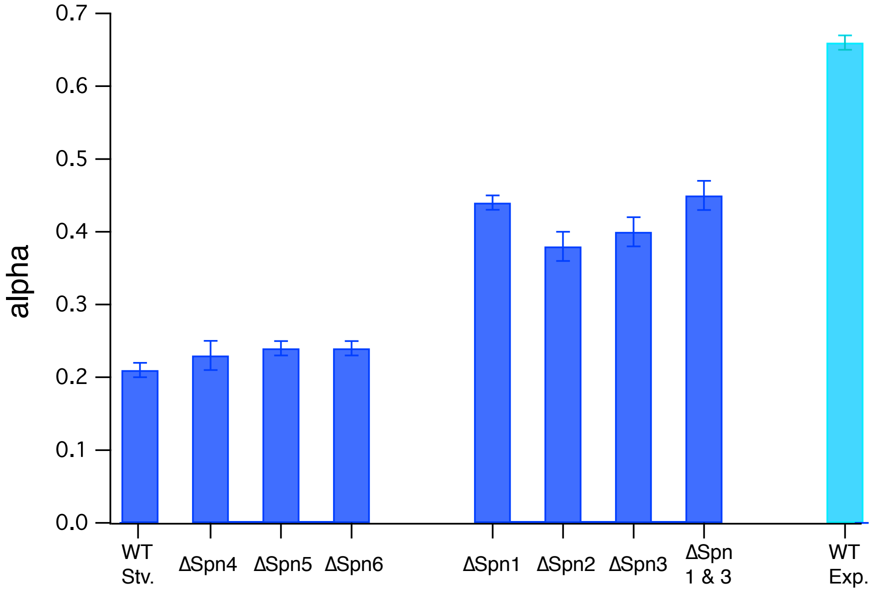

Figure 9.5: Septin deletion tracking results. Septin 4, 5 and 6 deletion show the same alpha value as wild type cells within error. The alpha value of septin 1, 2 and 3 deletion as well as a 1 and 3 double deletion is significantly higher than wild type. WT in exponential growth is shown for comparison. Graph adapted from [94].

Figure 9.5 shows the summary of the calculated average alpha values for septin deletion mutants and wild type for day 5-8 of starvation. Some of the data are taken from Ibeneche's dissertation and shown for comparison and completion. Unfortunately, septin 7 deletion grew at a significantly slower rate than the other cells, therefore a comparison for day 5-8 was questionable and no tracking data was obtained. The starved wild type cells show an average alpha value of $\alpha = 0.21 \pm 0.01$. Comparable alpha values are found for septin 4-6 deletion mutants; septin 4: $\alpha = 0.23 \pm 0.02$, septin 5: $\alpha = 0.24 \pm 0.01$ and septin 6: $\alpha = 0.24 \pm 0.01$. The alpha values for septin 1, 2, 3, and 1 and 3 double deletion mutants are significantly higher; septin 1: $\alpha = 0.44 \pm 0.01$, septin 2: $\alpha = 0.38 \pm 0.02$, septin 3: $\alpha = 0.40 \pm 0.02$, and the septin 1 and 3 double deletion: $\alpha = 0.45 \pm 0.02$. Although, the alpha values for the septin 1-3, and 1 and 3 mutants are higher, around 0.4, comparable to WT and Septin 4-6 around 0.22, their alpha values only recovers partially, not completely to the alpha value of exponential growing cells of $\alpha = 0.66 \pm 0.01$. This indicates that septin 1-3 seem to be involved in cell freezing, but not septin 4-6. These single particle tracking results lead to the proposed septin vacuole model as described by Ibeneche [94].

Table 9.1: Summary SPT results of septin deletion mutants. The table summarizes the alpha values for each of the mutants including the number of granules tracked and the percentage of granules which had an alpha below 0.25.

cell type	**alpha**	**granules**	**% frozen**
WT Stv	0.21 ± 0.01	138	78%
$\Delta Spn4$	0.23 ± 0.02	73	58%
$\Delta Spn5$	0.24 ± 0.01	48	58%
$\Delta Spn6$	0.24 ± 0.01	44	57%
$\Delta Spn1$	0.44 ± 0.01	91	2%
$\Delta Spn2$	0.38 ± 0.02	46	20%
$\Delta Spn3$	0.40 ± 0.02	68	13%

A different way to analyze the septin results is to look at the percentage of frozen cells in each sample, as summarized in table 9.1. If a culture like wild type cells shows an average alpha value, $\alpha = 0.21 \pm 0.01$, there is a possibility that there are individual cells, which have an alpha value higher than than the cut-off for frozen cells. We pick a fairly conservative cut-off of $\alpha = 0.25$ for cell freezing, according to which each measured cell in the culture can be labeled as frozen or not. If the cell's alpha value is smaller than 0.25 it is frozen and if it is equal or higher than 0.25 we count this cell as not frozen. In a frozen wild type culture of $\alpha = 0.21 \pm 0.01$, 78% of the cells are by definition frozen. Looking at the septin 1-3 deletion mutants shows that the percentage of frozen cells is lower than in wild type, between 57% and 58%. Although their alpha values partially agree within error, there appears to be a larger variety in the culture. This might indicate that either septins 4-6 have a small influence on cell freezing or the overall larger number of vacuoles in the mutants might be the cause of this difference. Looking at the septin 1-3 deletion mutants show that they also have frozen cells occasionally, but only 2% for septin 1 deletion, 20% for septin 2 deletion, and 13% for septin 3 deletion. These are significantly smaller amounts of frozen cells as in wild type or septin 4-6 deletion mutants, further indicating a possible involvement of septin 1-3 in cell freezing. Although these results seem to indicate that septins 1-3 are involved in cell freezing, current experiments test this hypothesis. Other factors such as the genetic background might influence cell freezing in the case of the septin mutants.

9.4 Dependence of freezing on glucose concentration

Preliminary experiments by Ibeneche showed that cells will go into the frozen state in starvation on day 5 regardless if the EMM contains $5g/L$ glucose, the traditional starvation media, or $4 - 1g/L$ glucose. These results imply that the time to build a filamentous network which restricts the granule motion is significantly longer than the time in which the cells run out of glucose. Since at low glucose levels the time to obtain freezing is dominated by the time to build the network, we examined how cell freezing changes at higher glucose concentrations and if cells can go into the freezing state with the traditional growth media, containing $20g/L$ glucose.

9.4.1 SPT of starved cells in various media

In order to examine the freezing behavior of yeast cells at different glucose concentrations, the anomalous diffusion exponent α was measured on day 4, 5 and 6 of starvation for different media. Cells were taken from an exponential culture and grown in EMM with $5g/L, 10g/L, 15g/L$ and $20g/L$ glucose respectively. Single particle tracking data was taken on day 4, 5 and 6 of starvation for three different cultures. For EMM with $5g/L$ glucose between 50 and 60 granules were tracked each day and for the higher glucose concentrations between 60 and 70 granules each. The alpha values presented in Figure 9.6 shows the mean ± the standard error of the mean.

Surprisingly, the cells grown in different media show a very similar freezing behavior. The alpha values of cells grown in EMM with $10, 15$ and

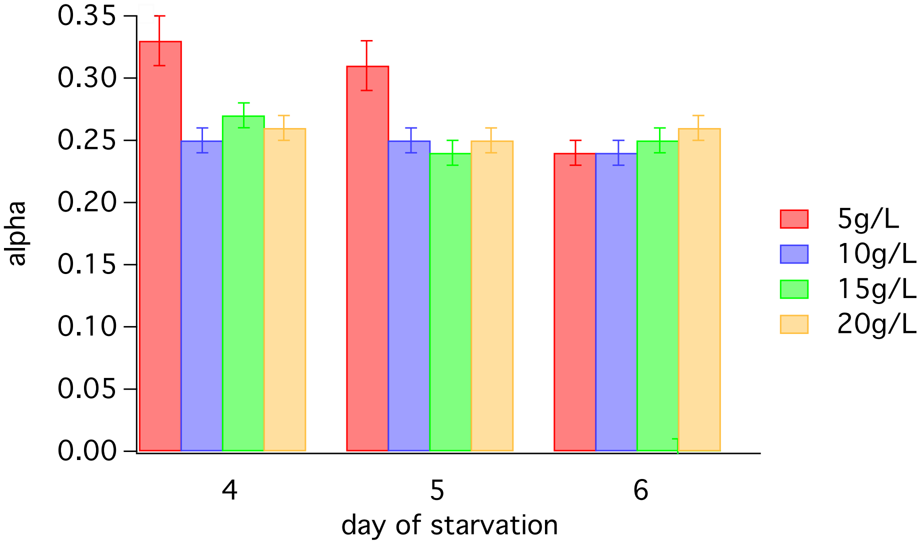

Figure 9.6: Cells transition into the freezing state independently of the glucose concentration of the media.

$20g/L$ glucose on day 4, 5 and 6 are equal within error and centered around 0.25. This means that the cells are frozen one day earlier than the cells grown in $5g/L$ EMM. Only the cells grown in $5g/L$ are not yet frozen on day 4 and are still a little faster on day 5 than the cells in the higher glucose media.

9.4.2 Simulation and measurement of cell growth in media with different glucose concentrations

The surprising observation, that cell freezing is not delayed in cells growing in media containing higher concentrations of glucose but rather occurs at the same time as cells grown in low glucose media, lead to a more detailed investigation of yeast growth in media with different glucose concentrations.

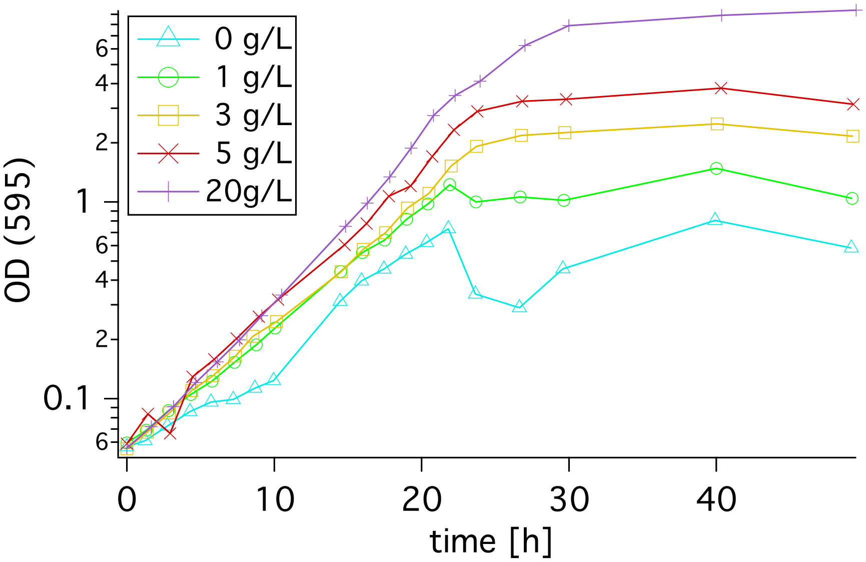

Figure 9.7: Measured growth curves for various glucose concentrations. The optical density (OD) represents the biomass of the culture; $OD_{595} = 0.1$ equals to $2 \cdot 10^6 cells/mL$. The growth curve is composed of two different cultures, which were started half a day apart. At low glucose concentrations, the transferred glucose has a dramatic influence on the maximal cell growth, which leads to inconsistencies at $0g/L$ glucose.

In order to simulate cell growth and glucose consumption of a cell culture over time, first the growth curves were measured. Cells were transferred from an exponentially growing culture in EMM2 to new media containing between 0 and $20g/L$ glucose. During the transfer of cells, approximately $8.4mg$ of glucose is added from the old media to the new one. This increases the amount of glucose of the new media by $0.79g/L$. This explains, how cell growth could be observed for EMM without glucose. Figure 9.7 shows the measured growth curves. The optical density is proportional to the number of cells in the culture and $OD_{595} = 0.1$ represents $2 \cdot 10^6 cells/mL$. The growth curves are measured over a time span of 50h. In order to do so, two independent cultures were measured, which were started half a day apart. Especially for media with very little to no glucose, the measurement of two cultures can lead to anomalies in the data, due to slightly different starting conditions. The growth curves display two important features. First, the cell growth seems to stagnate and plateau for all glucose concentrations at a similar time, between 25 to 30h. Second, the initial growth rate of the cells is fairly independent from the glucose concentration.

For the simulation of the culture growth, two variables were extracted from the growth curves, the growth rate with respect to glucose concentration and the glucose consumption per cell per growth cycle. The measured growth rates are shown in Figure 9.8. The data is fit with an exponential function to calculate the value K_s, the glucose concentration at which the growth rate is half of its maximum value. The calculated value from the fit is $K_s =$

$0.44g/L$. The consumption of glucose per cell varies slightly with the glucose concentration. Values range from $1.1 \cdot 10^{-10} g/cell$ for cells grown in $20g/L$ glucose to $7.1 \cdot 10^{-11} g/cell$ for $1g/L$ of glucose in the media.

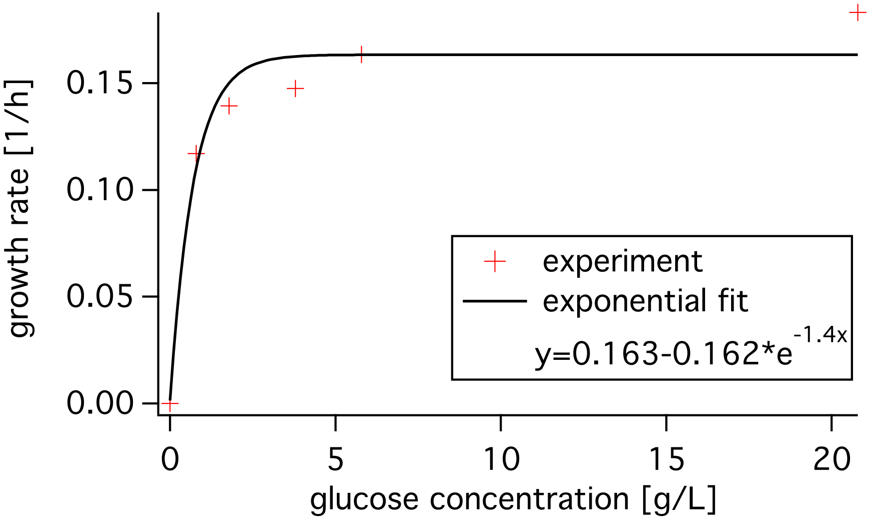

Figure 9.8: Measured growth rate with respect to glucose concentration. Growth rates are extracted from the linear regime of the growth curves in the log-log plots for different glucose concentrations.

The Monod equation [127] was used to simulate cell growth

$$\frac{dx(t)}{dt} = x(t)\mu_m \frac{S(t)}{K_s + S(t)}, \tag{9.1}$$

where $x(t)$ is the biomass concentration at time t, μ_m is the maximum specific growth rate, $S(t)$ is the substrate concentration at time t, and K_s is the substrate concentration at half the maximum growth rate. For the substrate consumption [232] we assumed

$$\frac{dS(t)}{dt} \propto -k_G \frac{dx(t)}{dt} = -k_G x(t)\mu_m \frac{S(t)}{K_s + S(t)}, \tag{9.2}$$

where k_G is a substrate consumption rate, in our case the glucose consumption rate. The following parameters were used for the simulation:

$x_0 = 0.05$	initial cell density (OD)
$S_0 = 0.79g/L, \ldots, 20.79g/L$	initial glucose concentration
$K_G = 1.15 \cdot 10^{-10} \frac{g}{cell \cdot 4h}$	glucose consumption rate
$\mu_m = 0.19 \frac{1}{h}$	maximal growth rate
$K_s = 0.44g/L$	glucose concentration at half growth rate

Figure 9.9a) shows the simulated and the measured growth curves for an initial glucose concentration of $20.79g/L$ as well as the glucose concentration. The measured and the simulated growth curves match very well and are comparable to the ones found in literature [220, 178]. In Figure 9.9b) the measured and simulated growth curves are shown for all used glucose concentrations. Overall, the highest glucose concentration shows the best agreement with the simulation. The measured rate of glucose consumption, as extracted form the measured growth curves, showed a dependency on the initial glucose concentration. Since in this simulation the glucose consumption rate was assumed to be constant and equal for all initial glucose concentrations, a discrepancy between the data and the simulation is to be expected. Also, the model used is fairly simple and the addition of a second growth limiting substrate or the addition of growth limiting factors due to waste products like ethanol could improve the agreement of the simulation with the data. Nevertheless, the discrepancy is sufficiently small so that glucose consumption curves

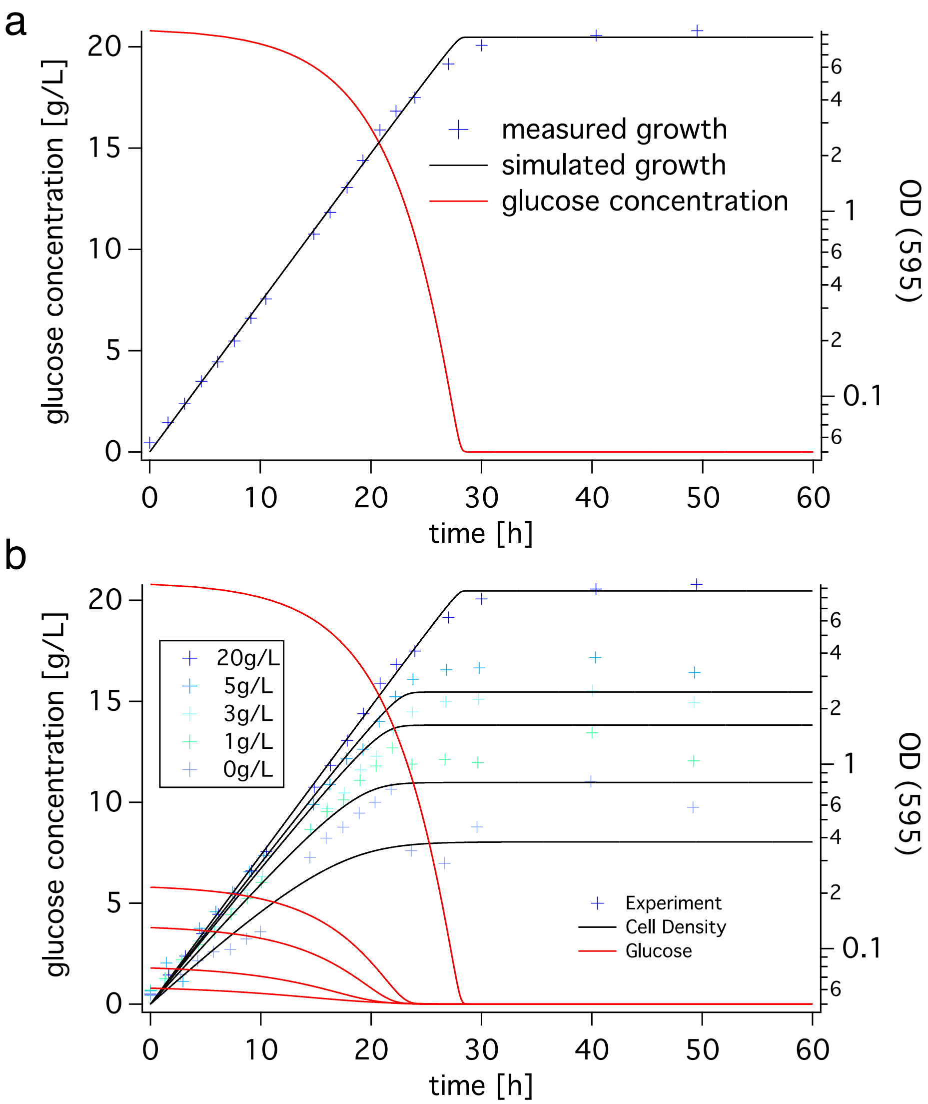

Figure 9.9: Simulated growth curves for various glucose concentrations. a) Measured and simulated growth curves are plotted as well as the glucose concentration over time for a media with $20g/L$ glucose. b) Measured and simulated growth curves are plotted as well as the glucose concentration over time for media with various initial glucose concentrations.

are representative of the experimental conditions as seen in the supplemental material of reference [178]. Most interestingly, the simulations show that the glucose in the growth media is consumed within approximately one day for all initial glucose concentrations. The difference in depletion the initial glucose between $5g/L$ and $20g/L$ of initial glucose concentration is $4.5h$. Since this time gap is only 4.5h, it is not surprising that cells transition into the freezing state on the same day regardless of the initial glucose concentration.

Simulations and experiment show that cells transition into the freezing state on day 5 of starvation regardless of the initial glucose concentration of the media. Additionally, these experiments indicate that after depleting the glucose reservoir, cells need four more days to achieve cell freezing. This might be the time it takes the cell to build the proposed network.

9.5 Recovery of the frozen state by the addition of glucose

Cells are able to recover from the frozen state, if glucose-rich media is added to the culture. In the first 8 hours after the addition of glucose the mobility of the granules increases, but the density of the culture remains approximately equal. After an additional eight hours the culture has doubled in density and eight hours later the culture has grown from $OD_{595} = 0.95$ to $OD_{595} = 2.91$ [94]. In 24 hours the cells have gone through slightly more than 3 cell cycles. For exponentially growing cells at $T = 25°C$ in EMM2, cells double every four hours, which results in six doublings during 24h. This indicates that the previously starved cells take some time to start growing and continue to grow at a slower rate for an extended period of time.

Regardless of the delay in growth for the first eight hours, the motion of the granules has changed drastically already after a few minutes. In order to study the change in alpha values of the lipid granules in the first few minutes and hours after the addition of glucose, we examine the recovery of the cells in a flow chamber. All the tubes leading to the flow chamber are filled with the media extracted from the starved cell culture. A syringe filled with EMM2 is initially separated from the system by a closed valve. This allows to observe the cells before and during the addition of glucose.

Figure 9.10 shows the lateral position fluctuations and their standard deviation of an individual granule during the recovery process. Videos were recorded for $29min$ at $6fps$. The pump with the fresh media was started at $t_1 = 60s$. At $t_2 = 120s$, the glucose-rich media arrived in the observed ROI. The two jumps in the position data, at the start of the pump and at $t = 150s$, were caused by the valve opening and closing. Before the addition of glucose, the standard deviation in x and y were $\sigma_x = 3.4nm$ and $\sigma_y = 4.9nm$ respectively. Up to $200s$, approximately $80s$ after the arrival of glucose, the standard deviations remained comparable. After $200s$, the position fluctuations, and therefore their standard deviations, increased. For the remainder of the time the standard deviation of the position fluctuations increased to $\sigma_x = 12nm$ and $\sigma_y = 23nm$. This experiment shows that the first phase of the recovery takes place in the first few minutes after the addition of glucose.

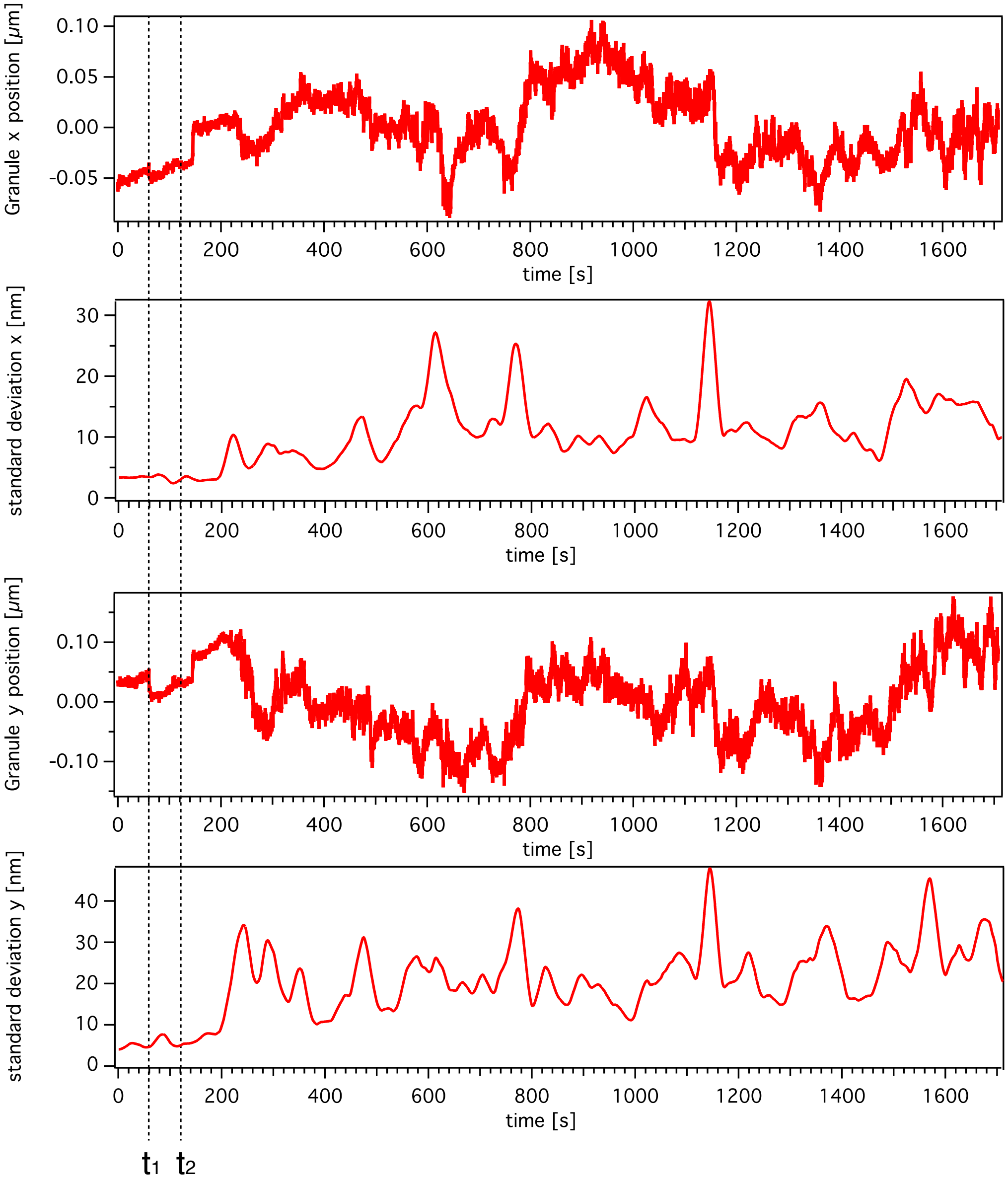

Figure 9.10: Position fluctuations and their standard deviation during the recovery process. The pump, which introduces fresh glucose-rich media into the sample chamber, is started at $t_1 = 60s$. At $t_2 = 120s$, the new media arrived in the center of the sample chamber. Position fluctuations increase at approximately $t = 200s$.

In order to observe the initial recovery process with better time resolution, we recoded videos with a frame rate of $60fps$ for approximately 10 minutes after introducing fresh media. Figure 9.11 shows the two parameters which can be used to characterize the recovery process, the standard deviation of the position fluctuations and the anomalous diffusion exponent alpha. The standard deviation of the position fluctuations was calculated using a sliding window of 600 data points, equal to $10s$. The alpha value was calculated with a window size of 3600 data points, equal to $1min$. The initial point of the window to calculate alpha was shifted by 900 data points, $0.25min$, to examine the evolution of alpha with higher temporal resolution than one minute. More data points are necessary to obtain a reliable value for alpha than for the standard deviation. Therefore, the transition out of freezing can be detected faster by evaluating the standard deviation. The granule, whose motion is shown in Figure 9.11, was taken from a frozen cell with an initial alpha value $\alpha = 0.22$. Fresh media arrived in the sample chamber at $t_1 = 80s$. The standard deviation of the position fluctuations in x and y, Figure 9.11a) and b), was on average $2nm$, and remained constant up to $t_x = 3.6min$ in the x-direction and $t_y = 4.4min$ in the y-direction. The average standard deviation, for the remainder of the time shown, were $\sigma_x = 11nm$ and $\sigma_y = 10nm$. This corresponds to a lag time between the arrival of glucose and the initial steps of recovery of $2.3min$ in the x-direction and $3.1min$ in the y-direction. Figure 9.11c) and d) show the alpha values for the x- and the y-component. The time of initial recovery, equivalent to the time at which alpha increased from below

0.25 to values larger than 0.3, is consistent with the time observed from the change in the standard deviation. The slightly more confined motion in the y-direction resulted in overall smaller alpha values during the recovery process. The resulting, average alpha was $\alpha_x = 0.46$ and $\alpha_y = 0.36$. About $3.5min$ after the start of the fluid exchange, the alpha value of the two-dimensional motion started to rise first to $\alpha = 0.29$ and at $3.75min$ to $\alpha = 0.41$, Figure 9.11e). Subsequently, alpha fluctuates within the next five minutes probably due to structural rearrangements, and has an average value of $\alpha = 0.42$. As seen in the example before, the initial recovery of the frozen state occurs on the order of minutes. Alpha changed from $\alpha = 0.22$ at $t = t_1$ to $\alpha = 0.41$ in approximately $180s$. After the initial quick recovery from a frozen, immobile state to the tethered state, a significantly slower recovery process on the order of hours occurs to raise alpha to the value of exponentially growing cells, $\alpha_{exp} = 0.66$.

The recovery experiments showed that the initial transition from the frozen cell to a cell, which shows motion, occurred within a few minutes. In this first phase of recovery, alpha did not increase to the value of exponentially growing cells, but remained at an intermediate value of approximately 0.4. Additionally, the onset of motion can be different for the x- and y-component. One possible scenario is that the initial step is to dissolve the cross links of the network. If the immobilization is caused by larger-scale structures, disassembly can lead to spatial inhomogeneities, which result in variations of the mobility of the granule in the x- and y-direction. Even after the disassembly

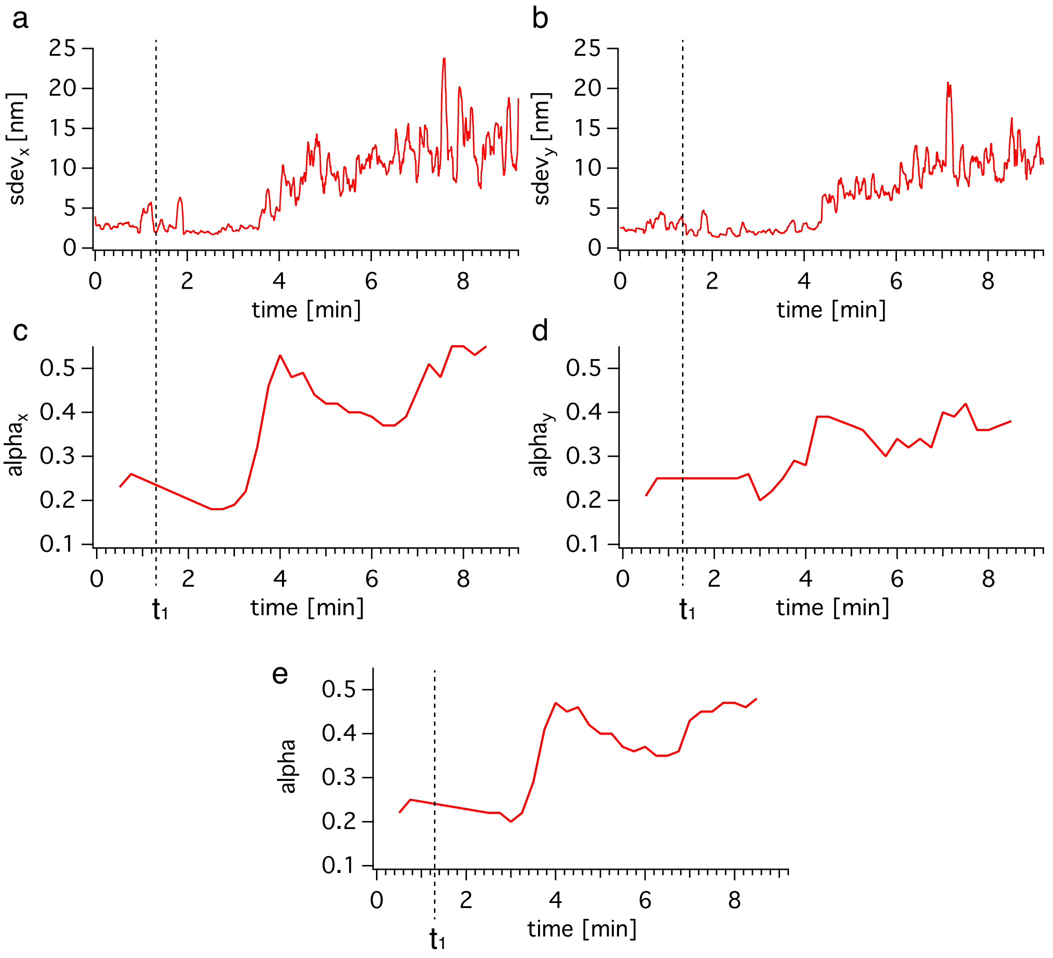

Figure 9.11: Standard deviation of the position fluctuations during the recovery process in a) x- and b) y-direction. The anomalous diffusion exponent during the recovery process is shown independently for the c) x- and d) y-component and also e) the combined alpha value. Media exchange is initiated at time $t_0 = 0s$ and glucose arrived in the ROI at $t_1 = 80s$.

of the network, the previously starved cell is more crowded than exponentially growing cells, due to increased amounts of vacuoles, which were found in electron microscopy images [94]. The increased crowdedness leads to lower alpha values as seen in the initial phase of recovery. The second phase of recovery, to achieve the state of exponentially growing cells, occurred on the order of multiple hours. Cell growth could be observed after 10 to 12 hours.

Chapter 10

Further characterization of the frozen state

The yeast cell's frozen state was further characterized by using tools of microrheology. We probed the confinement of the lipid granules in different stages of starvation by actively applying force with optical tweezers. We determine the size of the granules to obtain qualitative data for passive microrheology. Therefore, the index of refraction of the granules was determined, which enables us to calculate the size of each granule form its DIC image. With that information we can determine the storage and loss moduli of exponentially growing and starved yeast cells.

10.1 Index of refraction measurement of fission yeast lipid granules

The contrast mechanism in DIC microscopy relies on differences in the index of refraction of an object with respect to its surrounding media. Therefore, the apparent size of an object depends, in addition to its size, on the difference between the index of refraction of the object itself and its environment. A demonstration of this principle is shown in Figure 10.1. The same silica bead with an index of refraction of $n_{bead} = 1.45$ is imaged once in DI-water, $n_{DI} = 1.33$ and once in immersion fluid $n_{If} = 1.55$. Since in one case the index of refraction of the bead is higher than the one of the water and in the other it is lower, the resulting contrast changes direction. The white-black transition in DI-water goes from northwest to southeast. In the immersion fluid it is reversed and goes from southeast to northwest. We use this feature of DIC microscopy to determine the index of refraction of the lipid granules in fission yeast. By placing the granules in media with increasing index of refraction, the contrast changes orientation once the index of the fluid is higher than the one of the granules.

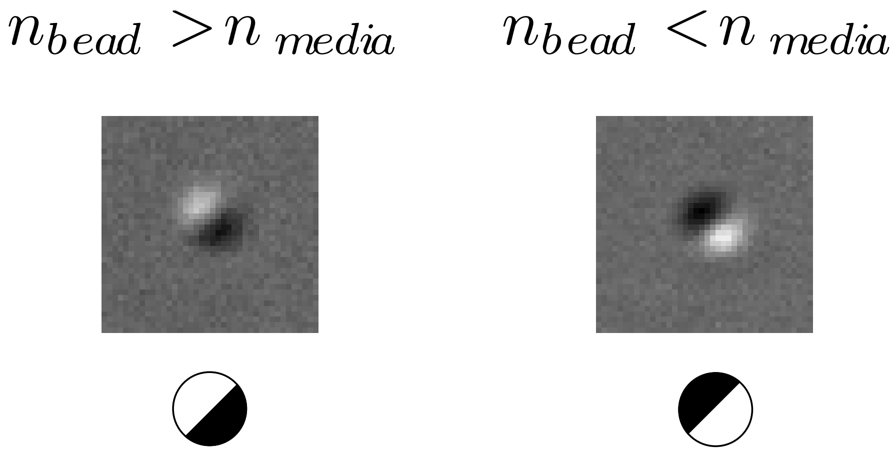

Figure 10.1: DIC contrast for beads in media with different index of refraction. If the index of refraction of the bead is larger than the one of the surrounding media, like silica beads in DI-water, the north-west corner is brighter and the south-east corner darker than the background. If the same bead is imaged in a media with a higher index of refraction than the bead, the orientation of the contrast reverses.

1x PBS was mixed with increasing amounts of immersion fluid, to obtain fluids with increasing index of refraction. The immersion fluid (Cargille

Immersion liquid, Cargille Laboratories, NJ, USA) has an index of refraction of $n = 1.5560 \pm 0.0005$, measured at $\lambda = 589.3nm$ at $25°C$. The index of refraction of the mixture was measured using a digital hand-held refractometer (AR 200, Reichert, NY, USA). The yeast extract was dissolved in PBS and centrifuged for 15min at 14,000rpm. Since the density of the lipid granules is smaller then the density of PBS, the granules sediment at the top. The upper layer of the centrifuged yeast extract is pipetted off and added to the right amount of immersion fluid to obtain the desired index difference. The contrast of the granules was observed with a DIC microscope for increasing values n of the liquid.

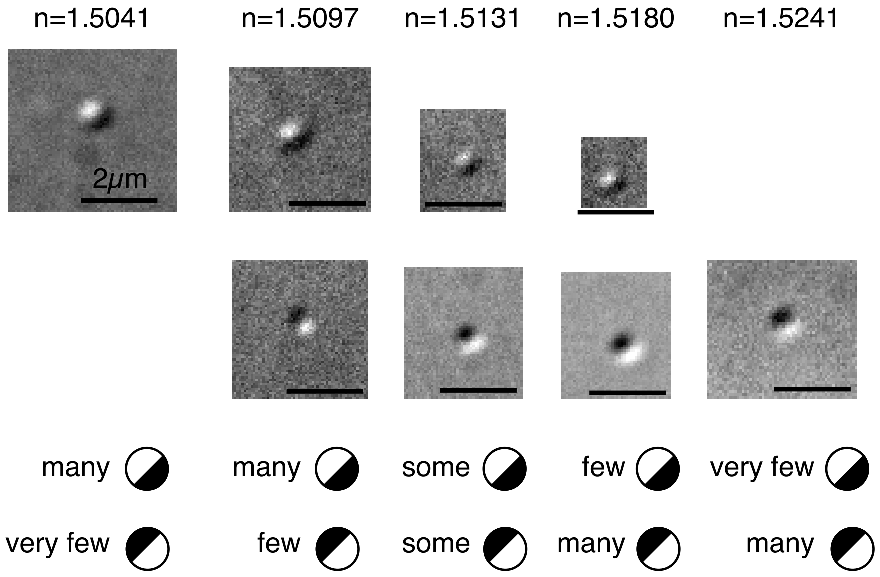

Figure 10.2: Index matching to determine refractive index of the lipid granules. The distribution of granules with a certain contrast changed with increasing index of the media.

Figure 10.2 summarizes the the changing contrast of the granules for increasing index of refraction of the surrounding fluid. At an index of refraction of the fluid of $n = 1.5041$, almost all of the granules have the contrast, where the north-west corner is white. This indicates that the index of the granules is higher than the index of the fluid. Only very rarely granules with the opposite contrast could be found. Many granules with the north-west white corner were found at $n = 1.5097$, and only few with the opposite contrast. A fairly even mixture was observed at $n = 1.5131$. At $n = 1.5180$, there were few granules with the white north-west corner and many with the opposite contrast, implying the the index of the granules is lower than the one of the liquid. At an even higher index of $n = 1.5241$, almost all granules had a south-east white corner and only very few the opposite. In addition to finding the average index of the granules, these experiments also reveal a good estimate of the uncertainty of the measured index. From these observations we conclude that the index of refraction of fission yeast's lipid granules is

$$n_{LG} = 1.51 \pm 0.01.$$

Knowing the index of refraction of the lipid granules allows us to create a calibration curve from apparent size of the granule in the DIC image to actual size in nanometer.

10.2 Determining the size of the lipid granules

The difference in index of refraction between the lipid granules and the cytosol is the base for a conversion chart from the appearance of the lipid granules in a DIC image of the cell to the size of the granule in nanometer. Assuming that the index of refraction of the cytosol is approximately the same as water, the difference between the indices of cytosol and granules is $\Delta n = 0.18$. Beads of known size (200nm, 300nm, 400nm, and 500nm) are immersed in a liquid with an index of refraction such that the index difference is equal to 0.18. The distance between the points of maximum and minimum intensity in the DIC image of a particle is used to represent its size. Plotting the measured distance over the bead's nominal size results in a calibration curve, which can be used to determine the size of the lipid granules in yeast cells.

Figure 10.3 shows the calibration curves: the measured width of the beads versus the nominal size for beads in PBS and in the higher index fluid. Both Figure 10.3 a) and b) contain the same data points. In Figure 10.3a) the dotted lines represent the enveloping functions, parabolas, to obtain error estimates for the size conversion, extracted from the beads in higher index liquid. An enveloping function for the beads in PBS is pictured in Figure 10.3b). For each bead size, the data points for beads in PBS and in index matched fluid overlap within error. Better statistics for the beads in PBS and the selection of beads in the center region of the images lead to smaller error bars. The expected average granule size in exponentially growing cells is approximately $300nm$ [207]. Especially for smaller sizes around $300nm$, there is no measurable difference in size between the beads in PBS and in the higher index fluid. For future calculations the sizes of the granules are extracted from

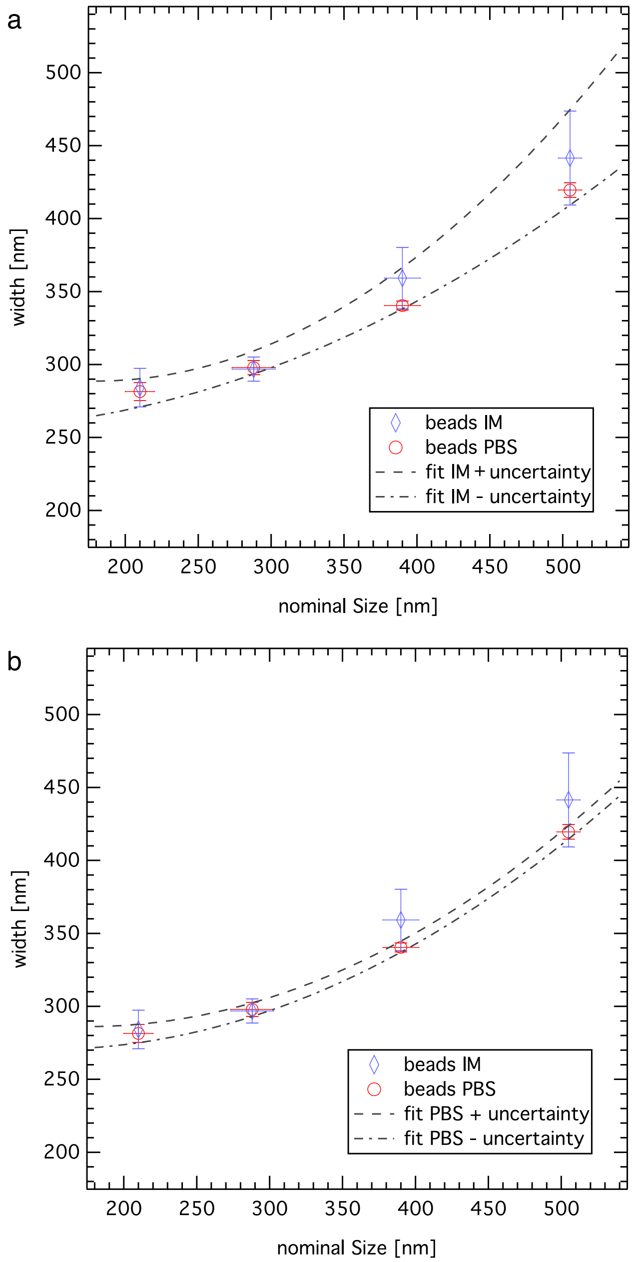

Figure 10.3: Measured versus actual bead size in DIC microscopy. a) Using the beads in a higher index fluid to obtain the particle size. b) Using the beads dispersed in PBS to determine the particle size. In both cases the fit function is a parabola, once to the measured values plus the error to obtain an upper bound and once to the value minus the error for the lower bound.

Figure 10.3a). The peak-to-peak distance for the granule is first extracted from the original DIC image. Then, the intercept of the measured distance with the fit function is obtained for the upper bound and the lower bound. The particle size is calculated as the average of both intercepts and the uncertainty as half of the difference of the two values.

10.3 Correlation of SPT tracking results with mobility of granules measured with optical tweezers

The motion of the granules in the cell could be due to two processes. The first possibility is purely Brownian motion. A second possibility is the combination of Brownian motion and movements which can look diffusive, but are due to active forces like polymerization of actin filaments and microtubule, or arise from collisions with actively transported cargoes. If a cell is lacking nutrients and needs to conserve energy, active transport and polymerization might be minimized and therefore the observed motion could decrease. In order to ensure that the reduction in alpha as well as the diffusion constant is due to a change in the viscoelastic properties of the cell cytoplasm and not the lack of active processes, we conducted active microrheology experiments. The goal of these experiments is to inspect the correspondence between the anomalous diffusion exponent α and the ability of the granule to be actively displaced within the cytoplasm.

In order to minimally disturb the state of the cell, an image sequence to determine α was taken before force was applied to the granule. The response

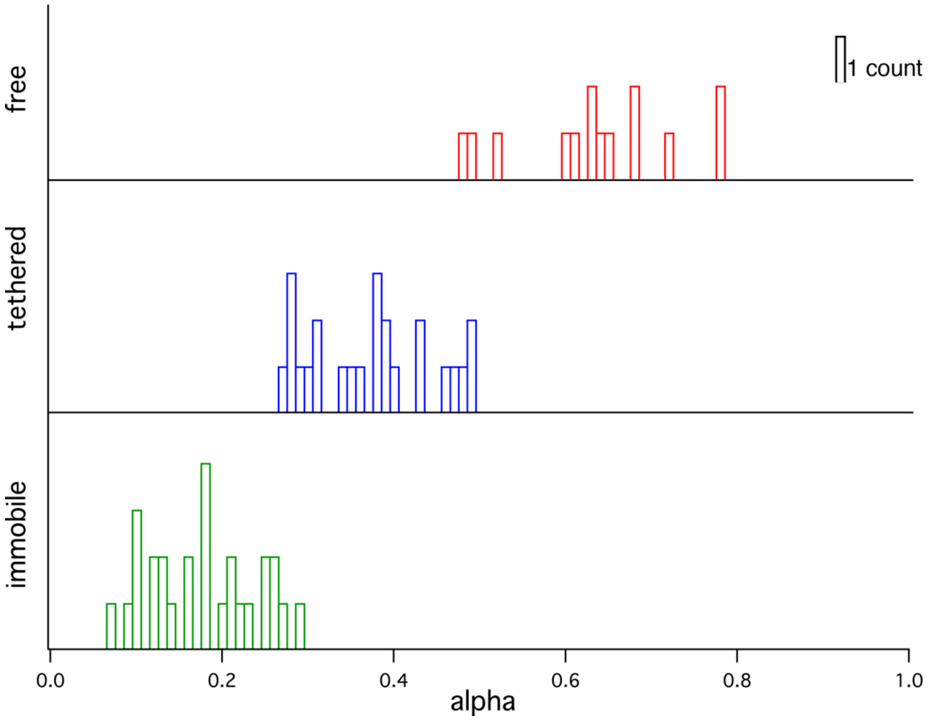

Figure 10.4: Correlation of SPT tracking with mobility of granules tested with optical tweezers. When a force was applied to the individual granules with optical tweezers, the displacement of the granules can be divided into three groups. If the cells have a high value of alpha, between 0.5 and 0.8, the granules can be easily displaced from their origin, over a range of microns. In the range of alpha values of 0.27 to 0.5, granules can only be displaced by a small amount, and often the granule is pulled back to its original position. This state is called tethered. For the low alpha values below 0.26, the granules cannot be visibly displaced.

of the granule to the applied force was divided into three categories. First, in exponentially growing cells, if the granule can be displaced easily over a distance of microns, we call the granule “free”. In the early days of starvation, the granule generally follows the motion of the trap, but the displacement is limited to a few 100nm. Spring like behavior is observed, the granule tends to return to its initial position. This state is called “tethered”. If the cell is frozen, the granule shows no visible displacement when force is applied, the particle is “immobile”. Figure 10.4 shows a summary of the experiments. Granules with alpha values $0.5 < \alpha < 0.8$ are easily displaced by an applied force; they are free. Cells in the category free consist of exponentially growing cells and some cells on day 1 and 3 of starvation. For $0.27 < \alpha < 0.5$, cells are in the tethered state; they are commonly between day 1 and day 4 of starvation. Frozen cells with immobile granules occur on day 4 to 7 of starvation, and the range for alpha is $\alpha < 0.26$.

Measuring the correlation between the anomalous diffusion exponent α and the ability to displace a granule when applying force shows that the viscoelastic properties of the cell cytoplasm are changing in starvation. Additionally, this experiment shows that α is a parameter that represents the viscoelastic properties very well, and that calculating α is sufficient to report on the status of the cell.

10.4 Passive microrheology

In passive microrheology, thermal forces drive the motion of tracer particles. From the particles trajectory, the MSD can be calculated, which can be used to determine the complex modulus G^* according to equation (6.9). The complex modulus can be expressed as the sum of the storage and the loss modulus

$$G^* = G' + iG''. \tag{10.1}$$

The storage modulus, the real part of the complex modulus, represents the elastic portion, and the loss modulus, the imaginary part, represents the viscous portion. The frequency dependence of the elastic and the storage modulus follows a power law

$$G'(\omega) = G'_0\omega^{\beta}, \tag{10.2}$$

$$G''(\omega) = G''_0\omega^{\beta}, \tag{10.3}$$

with $\omega = 2\pi f$ being the angular frequency. In the literature the exponent is often referred to as α, but to avoid confusion with the anomalous diffusion exponent, it is named β here. If $\beta = 1$ the system shows fluid like behavior, and if $\beta = 0$ the material behaves like a solid. In a plot of the logarithm of the modulus versus the logarithm of the frequency β and G_0 can be calculated from the slope and the intercept.

Figure 10.5 shows the frequency dependent storage and loss modulus for a free granule from an exponentially growing cell, a tethered granule from

a) free: alpha=0.63

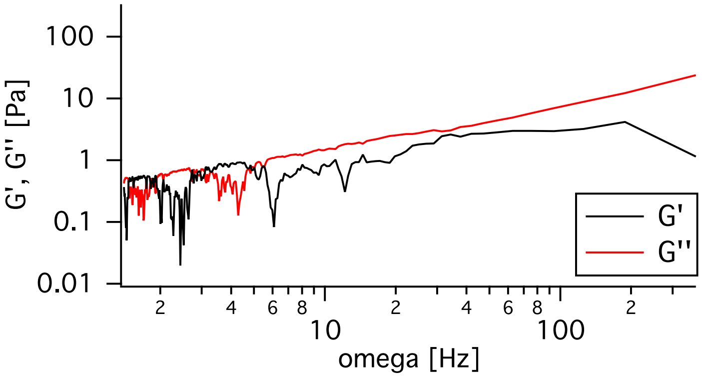

b) tethered: alpha=0.42

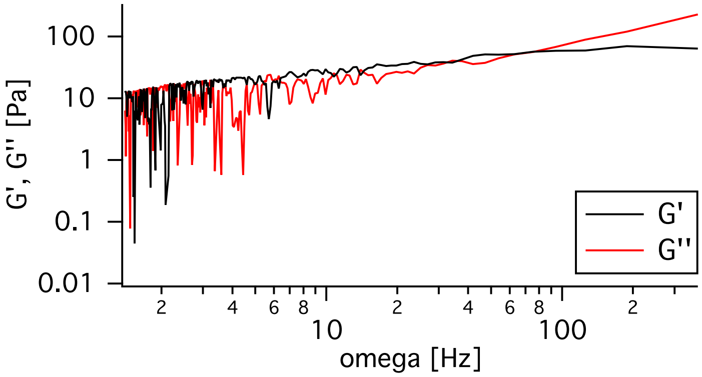

c) immobile: alpha=0.16

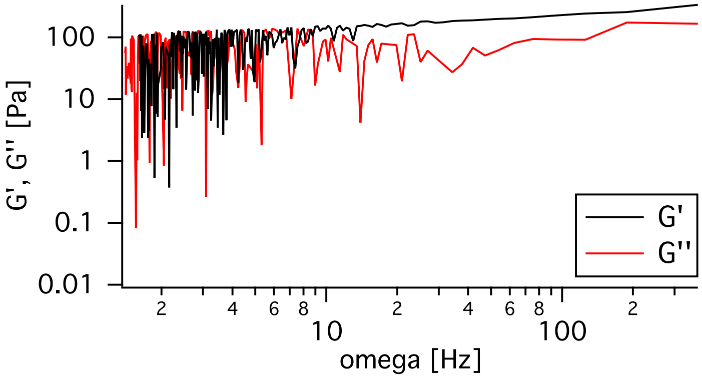

Figure 10.5: Storage and loss modulus of a) free, b) tethered, and c) immobile granules.

a cell on day 1 of starvation, and an immobile granule from a frozen cell on day 8 of starvation. In all three cases the storage and the loss modulus are very similar in the frequency behavior as well as in the absolute values of the moduli. Looking at the different granules, the slope decreases for decreasing alpha value, and the values of the moduli increase with decreasing alpha. The free granule has $\beta_{free} = 0.61$, when averaged over the storage and the loss modulus. The tethered granule has a shallower slope of $\beta_{teth} = 0.43$ and the immobile one the shallowest one of $\beta_{im} = 0.13$. The decreasing values for increasingly starved cells indicate that the cytoplasm is transitioning from a more fluid-like state to a more solid-like state. The value of the storage modulus of the free granule is $G'_0 = 0.26Pa$, for the tethered one $G'_0 = 8.9Pa$, and for the frozen one $G' = 89Pa$. The values of the loss modulus are on the same order of magnitude as the ones for the storage modulus; for the free granule it is $G''_0 = 0.25Pa$, for the tethered one $G''_0 = 7.1Pa$, and for the frozen one $G''_0 = 71Pa$. Between each of these three stages the moduli increase by at least one order of magnitude.

The passive microrheology experiments demonstrate that the yeast's cytoplasm transitions from $\beta_{free} = 0.61$, a more fluid-like behavior, in exponentially growing cells to $\beta_{im} = 0.13$, a more solid-like behavior, in frozen cells. Additionally the storage and the loss modulus increase from $G_0 = 0.26Pa$ each in exponential cells by more than two orders in magnitude to $G'_0 = 89Pa$ and $G''_0 = 71Pa$ in frozen cells. The large increase of the moduli, together with the decrease in β, emphasize the dramatic structural changes of the cytoplasm in response to glucose starvation. The viscoelastic properties of the exponentially growing cells match very nicely with the ones of *Dictyostelium* cells [218]. For a $300nm$ probe the modulus is $G_0 = 0.27Pa$ and the exponent is $\beta = 0.59$. Comparing our results to the viscoelastic properties of biological polymer networks [200] shows that tethered cells have a similar storage modulus to fibrin and collagen networks and frozen cells are comparable to cross-linked actin networks, measured at $10Hz$. However, depending on the preparation, actin, in the absence of cross-links, can have an elastic modulus of only $G_0 \approx 0.5Pa$ at a frequency of $0.1Hz$ [25].

10.5 Summary and outlook

In the second part of this dissertation we used the thermal motion of endogenous lipid granules in fission yeast to characterize the cytoplasmic response to glucose starvation.

The granule's trajectory was recorded with a DIC microscope. In order to track the granule's position in three dimensions a novel axial tracking algorithm was developed. It uses image integration to determine the particle's coordinates axially with $5nm$ and laterally with sub-nanometer precision. The ability to obtain the particle's three-dimensional position within a single frame provides the basis for building a feedback which allows to track granules in exponentially growing cells for more than 30 minutes. In the future the axial tracking possibilities can lead to automated three-dimensional multi-particle tracking, which is necessary to increase the number of tracked granules in individual experiments for better statistics.

We furthered the understanding of cell freezing. First, we finished studies about the molecular origin of cell freezing and examined actin as well as the remaining septins as candidates for forming a network. Additionally, the influence of the initial glucose concentration was investigated. Experiments as well as simulations showed that the nutrients were depleted, and the cells stopped growing, after approximately one day regardless of the initial glucose concentration. Therefore, the phenomenon of cell freezing and the time it takes to transition into the frozen state is independent of the initial glucose concentration in the range of $20g/L$ to $1g/L$ glucose. Cells recovered from the frozen state after the addition of glucose. The alpha value increased, $1-2$ minutes after the addition of glucose, from a value corresponding to a frozen, immobile granule, $\alpha \approx 0.2$, to a tethered granule, $\alpha \approx 0.45$. The remaining recovery from the tethered state to the free state of exponentially growing cells occurs on the order of hours.

In order to further characterize the frozen state, the measured alpha values were correlated with the mobility of the granule, when displaced by optical tweezers. Granules in exponential growth could be moved around the cell freely over a distance of microns. During the transition into freezing, the granules were in a tethered state, with a limited ability to be displaced. The granules of frozen cells were completely immobilized. Additionally, we determine the viscoelastic properties of the cell's cytoplasm by passive microrheology. The frequency behavior of the storage and loss moduli of granules in the three different states, free, tethered, and immobile were examined. The moduli in each of these three stages increased by approximately an order of magnitude with decreasing alpha. The storage modulus increased by a factor of 340 from exponential growth to the frozen state and the loss modulus by a factor of 280. The exponent of the power law behavior decreases with decreasing alpha, indicating a transition from a more fluid-like cytoplasm to a more solid-like one during starvation.

To further our understanding of cell freezing in fission yeast, we will need to image the network in order to confirm its presence for example by super resolution imaging techniques or electron microscopy. Determining the mesh size of the network would help identifying the size distribution of affected particles in the cytoplasm and which processes it might influence. Active microrheology is necessary to examine a potential nonlinear response of the cell cytoplasm in its different phases, since a larger force needs to be applied to drive the displacement of the granules.

Furthermore, it would be interesting to study if cell freezing is only triggered by glucose starvation or also by other stresses. Similarly, there might also be additional factors like gas exchange, the pH, or waste products, which can have an effect on cell freezing. Longer observations during cell recovery can lead to insight into the transition from the tethered state to cell growth. A more in depth knowledge of the frozen state will hopefully also lead to the discovery of its evolutionary advantage.

Bibliography

[1] M H Abdulreda and V T Moy. Atomic Force Microscope Studies of the Fusion of Floating Lipid Bilayers. *Biophysical Journal*, 92(12):4369–4378, March 2007.

[2] Karim Addas, Christoph Schmidt, and Jay Tang. Microrheology of solutions of semiflexible biopolymer filaments using laser tweezers interferometry. *Physical Review E*, 70(2):021503, August 2004.

[3] Sebastian Aeffner, Tobias Reusch, Britta Weinhausen, and Tim Salditt. Energetics of stalk intermediates in membrane fusion are controlled by lipid composition. *Proceedings of the National Academy of Sciences*, 109(25):E1609–E1618, 2012.

[4] Audrey Agopian and Sabine Castano. Biochimica et Biophysica Acta. *Biochimica Et Biophysica Acta-Biomembranes*, 1838(PB):117–126, January 2014.

[5] Bruce Alberts, Alexander Johnson, Julian Lewis, Martin Raff, Keith Roberts, and Peter Walter. *Molecular Biology of the Cell.* Reference edition. Garland Science, fifth edition edition, 2008.

[6] R D Allen, G B David, and Gf Nomarski. The zeiss-Nomarski differential interference equipment for transmitted-light microscopy. *Zeitschrift fur*

wissenschaftliche Mikroskopie und mikroskopische Technik, 69(4):193, 1969.

[7] F Amblard, A C Maggs, B Yurke, A N Pargellis, and S Leibler. Subdiffusion and anomalous local viscoelasticity in actin networks. *PRL*, 77(21):4470–4473, 1996.

[8] R T Armstrong, A S Kushnir, and J M White. The transmembrane domain of influenza hemagglutinin exhibits a stringent length requirement to support the hemifusion to fusion transition. *Journal Of Cell Biology*, 151(2):425–438, 2000.

[9] A ASHKIN. Acceleration and Trapping of Particles by Radiation Pressure. *PRL*, 24(4):156–&, 1970.

[10] A ASHKIN. Optical trapping and manipulation of neutral particles using lasers. *Proceedings Of The National Academy Of Sciences Of The United States Of America*, 94(10):4853–4860, 1997.

[11] A ASHKIN and JM DZIEDZIC. Optical Trapping And Manipulation Of Viruses And Bacteria. *Science*, 235(4795):1517–1520, 1987.

[12] Kathryn R Ayscough, Joel Stryker, Navin Pokala, Miranda Sanders, Phil Crews, and David G Drubin. High rates of actin filament turnover in budding yeast and roles for actin in establishment and maintenance of cell polarity revealed using the actin inhibitor latrunculin-A. *Journal Of Cell Biology*, 137(2):399–416, 1997.

[13] L S BARAK and W W Webb. Fluorescent Low-Density Lipoprotein for Observation of Dynamics of Individual Receptor Complexes on Cultured Human-Fibroblasts. *Journal Of Cell Biology*, 90(3):595–604, 1981.

[14] L S BARAK and W W Webb. Diffusion of Low-Density Lipoprotein-Receptor Complex on Human-Fibroblasts. *Journal Of Cell Biology*, 95(3):846–852, 1982.

[15] JP BARTON, DR ALEXANDER, and SA SCHAUB. Theoretical Determination Of Net-Radiation Force And Torque For A Spherical-Particle Illuminated By A Focused Laser-Beam. *Journal Of Applied Physics*, 66(10):4594–4602, 1989.

[16] Tobias F Bartsch, Samo Fišinger, Martin D Kochanczyk, Rongxin Huang, Alexandr Jonáš, and Ernst-Ludwig Florin. Detecting Sequential Bond Formation Using Three-Dimensional Thermal Fluctuation Analysis . *ChemPhysChem*, 10(9-10):1541–1547, July 2009.

[17] G Basanez, FM Goni, and A Alonso. Effect of single chain lipids on phospholipase C-promoted vesicle fusion. A test for the stalk hypothesis of membrane fusion. *Biochemistry*, 37(11):3901–3908, 1998.

[18] TM Bayerl and M Bloom. Physical properties of single phospholipid bilayers adsorbed to micro glass beads - A new vesicular model system studied by h-2-nuclear magnetic resonance. *Biophysical Journal*, 58(2):357–362, 1990.

[19] H W Beams and R L King. Survival of Ascaris Eggs after Centrifuging. *Science*, 84(2171), August 1936.

[20] U Bockelmann, P Thomen, B Essevaz-Roulet, V Viasnoff, and F Heslot. Unzipping DNA with optical tweezers: high sequence sensitivity and force flips. *Biophysical Journal*, 82(3):1537–1553, 2002.

[21] J P BOUCHAUD and A GEORGES. Anomalous Diffusion in Disordered Media - Statistical Mechanisms, Models and Physical Applications. *Physics reports*, 195(4-5):127–293, November 1990.

[22] D Boyer. Photothermal Imaging of Nanometer-Sized Metal Particles Among Scatterers. *Science*, 297(5584):1160–1163, August 2002.

[23] C P Brangwynne, G H Koenderink, F C Mackintosh, and D A Weitz. Cytoplasmic diffusion: molecular motors mix it up. *The Journal of Cell Biology*, 183(4):583–587, November 2008.

[24] C P Broedersz and F C Mackintosh. Molecular motors stiffen non-affine semiflexible polymer networks. *Soft Matter*, pages 1–6, 2011.

[25] Chase P Broedersz, Karen E Kasza, Louise M Jawerth, Stefan Münster, David A Weitz, and Frederick C MacKintosh. Measurement of nonlinear rheology of cross-linked biopolymer gels. *Soft Matter*, 6(17):4120, 2010.

[26] Aidan T Brown, Jurij Kotar, and Pietro Cicuta. Active rheology of phospholipid vesicles. *Physical Review E*, 84(2):021930, August 2011.

[27] Robert Brown. A brief account of microscopial observations made in the months of June, July and August, 1827, on the particles contained in the pollen of plants; and on the general existence of active molecules in organic and inorganic boides. *unpublished*, page 24, 1827.

[28] KNJ Burger. Greasing membrane fusion and fission machineries. *Traffic*, 1(8):605–613, 2000.

[29] G B CALLEJA, B Y YOO, and B F JOHNSON. Fusion and Erosion of Cell-Walls During Conjugation in Fission Yeast (Schizosaccharomyces-Pombe). *Journal of Cell Science*, 25(JUN):139–155, 1977.

[30] Brian C Carter, George T Shubeita, and Steven P Gross. Tracking single particles: a user-friendly quantitative evaluation. *Physical Biology*, 2(1):60–72, March 2005.

[31] Avi Caspi, Rony Granek, and Michael Elbaum. Diffusion and directed motion in cellular transport. *Physical Review E*, 66(1):011916, July 2002.

[32] Hirak Chakraborty, Pradip K Tarafdar, Michael J Bruno, Tanusree Sengupta, and Barry R Lentz. Activation Thermodynamics of Poly(Ethylene Glycol)-Mediated Model Membrane Fusion Support Mechanistic Models of Stalk and Pore Formation. *Biophysj*, 102(12):2751–2760, June 2012.

[33] Y Chan and S Boxer. Model membrane systems and their applications. *Current Opinion in Chemical Biology*, 11(6):581–587, December 2007.

[34] Yee-Hung M Chan, Bettina van Lengerich, and Steven G Boxer. Effects of linker sequences on vesicle fusion mediated by lipid-anchored DNA oligonucleotides. *Proceedings Of The National Academy Of Sciences Of The United States Of America*, 106(4):979–984, January 2009.

[35] Jinyoung Chang, Sun-Ae Kim, Xiaobing Lu, Zengliu Su, Seong Keun Kim, and Yeon-Kyun Shin. Fusion Step-Specific Influence of Cholesterol on SNARE-Mediated Membrane Fusion. *Biophysj*, 96(5):1839–1846, April 2009.

[36] A Chanturiya, L V Chernomordik, and J Zimmerberg. Flickering fusion pores comparable with initial exocytotic pores occur in protein-free phospholipid bilayers. *Proceedings of the National Academy of Sciences*, 94(26):14423–14428, 1997.

[37] G B CHAPMAN and J HILLIER. Electron Microscopy of Ultra-Thin Sections of Bacteria .1. Cellular Division in Bacillus-Cereus. *Journal Of Bacteriology*, 66(3):362–373, 1953.

[38] Daniel T N Chen, Qi Wen, Paul A Janmey, John C Crocker, and Arjun G Yodh. Rheology of Soft Materials. *Annual Review of Condensed Matter Physics*, 1(1):301–322, August 2010.

[39] Elizabeth H Chen, Eric Grote, William Mohler, and Agnes Vignery. Cell-cell fusion. *FEBS LETTERS*, 581(11):2181–2193, 2007.

[40] L Chernomordik, A Chanturiya, J Green, and J Zimmerberg. The Hemifusion Intermediate and its Conversion to Complete Fusion: Regulation by Membrane Composition. *Biophysical Journal*, 69(3):922–929, 1995.

[41] Leonid V Chernomordik and Michael M Kozlov. Mechanics of membrane fusion. *Nature Structural & Molecular Biology*, 15(7):675–683, July 2008.

[42] LV Chernomordik, VA Frolov, E Leikina, P Bronk, and J Zimmerberg. The pathway of membrane fusion catalyzed by influenza hemagglutinin: Restriction of lipids, hemifusion, and lipidic fusion pore formation. *Journal Of Cell Biology*, 140(6):1369–1382, 1998.

[43] LV Chernomordik and MM Kozlov. Membrane hemifusion: Crossing a chasm in two leaps. *Cell*, 123(3):375–382, 2005.

[44] Y A Chizmadzhev, F S Cohen, A Shcherbakov, and J Zimmerberg. Membrane Mechanics Can Account for Fusion Pore Dilation in Stages. *Biophysj*, 69(6):2489–2500, December 1995.

[45] Ya Chizmadzhev, PI Kuzmin, DA Kumenko, J Zimmerberg, and FS Cohen. Dynamics of fusion pores connecting membranes of different tensions. *Biophysical Journal*, 78(5):2241–2256, 2000.

[46] Yuri A Chizmadzhev, Dimetry A Kumenko, Peter I Kuzmin, Leonid V Chernomordik, Joshua Zimmerberg, and Fredric S Cohen. Lipid Flow

through Fusion Pores Connecting Membranes of Different Tensions. *Biophysj*, 76(6):2951–2965, June 1999.

[47] Minsub Chung, Randall D Lowe, Yee-Hung M Chan, Prasad V Ganesan, and Steven G Boxer. DNA-tethered membranes formed by giant vesicle rupture . *Journal of Structural Biology*, 168(1):190–199, October 2009.

[48] Marcus D Collins and Sarah L Keller. Tuning lipid mixtures to induce or suppress domain formation across leaflets of unsupported asymmetric bilayers. *Proceedings Of The National Academy Of Sciences Of The United States Of America*, 105(1):124–128, 2008.

[49] S Condamin, V Tejedor, R Voituriez, O Benichou, and J Klafter. Probing microscopic origins of confined subdiffusion by first-passage observables. *Proceedings of the National Academy of Sciences*, 105(15):5675–5680, April 2008.

[50] C M Coppin, J T Finer, J A Spudich, and R D Vale. Detection of sub-8-nm movements of kinesin by high-resolution optical-trap microscopy. *Proceedings Of The National Academy Of Sciences Of The United States Of America*, 93(5):1913–1917, 1996.

[51] JM Crane and LK Tamm. Role of cholesterol in the formation and nature of lipid rafts in planar and spherical model membranes. *Biophysical Journal*, 86(5):2965–2979, 2004.

[52] FHC CRICK and AFW HUGHES. The Physical Properties of Cytoplasm - a Study by Means of the Magnetic Particle Method .1. Experimental. *Experimental cell research*, 1(1):37–80, 1950.

[53] W DENK and W W Webb. Optical Measurement of Picometer Displacements of Transparent Microscopic Objects. *Applied Optics*, 29(16):2382–2391, 1990.

[54] M K Domanska, V Kiessling, A Stein, D Fasshauer, and L K Tamm. Single Vesicle Millisecond Fusion Kinetics Reveals Number of SNARE Complexes Optimal for Fast SNARE-mediated Membrane Fusion. *Journal Of Biological Chemistry*, 284(46):32158–32166, November 2009.

[55] D Duelli and Y Lazebnik. Cell-to-cell fusion as a link between viruses and cancer. *Nature Reviews Cancer*, 7(12):968–976, 2007.

[56] Michael Edidin. The State Of Lipid Rafts: From Model Membranes To Cells . *Annual Review Of Biophysics And Biomolecular Structure*, 32(1):257–283, June 2003.

[57] Albert Einstein. Über die von der molekularkinetischen Theorie der Wärme geforderte Bewegung von in ruhenden Flüssigkeiten suspendierten Teilchen. *Annalen der physik*, 322(8):549–560, 1905.

[58] Donald L Ermak and J A McCammon. Brownian dynamics with hydrodynamic interactions. *The Journal of Chemical Physics*, 69(4):1352, 1978.

[59] Evan Evans and Erich Sackmann. Translational and rotational drag coefficients for a disk moving in a liquid membrane associated with a rigid substrate. *Journal Of Fluid Mechanics*, 194:553–561, April 1988.

[60] Ben Fabry, Geoffrey Maksym, James Butler, Michael Glogauer, Daniel Navajas, and Jeffrey Fredberg. Scaling the Microrheology of Living Cells. *Physical Review Letters*, 87(14):148102, September 2001.

[61] TH M FISCHER, P DHAR, and P HEINIG. The viscous drag of spheres and filaments moving in membranes or monolayers. *Journal Of Fluid Mechanics*, 558:451, July 2006.

[62] E-L Florin, A Pralle, JKH Horber, and EHK Stelzer. Photonic force microscope based on optical tweezers and two-photon excitation for biological applications. *Journal of Structural Biology*, 119(2):202–211, 1997.

[63] EL Florin, A Pralle, EHK Stelzer, and JKH Horber. Photonic force microscope calibration by thermal noise analysis. *Applied Physics A-Materials Science & Processing*, 66:S75–S78, 1998.

[64] Daniel L Floyd, Justin R Ragains, John J Skehel, Stephen C Harrison, and Antoine M van Oijen. Single-particle kinetics of influenza virus membrane fusion. *Proceedings Of The National Academy Of Sciences Of The United States Of America*, 105(40):15382–15387, 2008.

[65] Susan L Forsburg. The yeasts Saccharomyces cerevisiae and Schizosaccharomyces pombe: models for cell biology research. *Gravitational and space biology bulletin : publication of the American Society for Gravitational and Space Biology*, 18(2):3–9, June 2005.

[66] J Gallová, D Uhríková, A Islamov, A Kuklin, and P Balgavy. Effect of cholesterol on the bilayer thickness in unilamellar extruded DLPC and DOPC liposomes: SANS contrast variation study. *General physiology and biophysics*, 23:113–128, 2004.

[67] Lianghui Gao, Reinhard Lipowsky, and Julian Shillcock. Tension-induced vesicle fusion: pathways and pore dynamics. *Soft Matter*, 4(6):1208–1214, 2008.

[68] Y Gao, S Zorman, G Gundersen, Z Xi, L Ma, G Sirinakis, J E Rothman, and Y Zhang. Single Reconstituted Neuronal SNARE Complexes Zipper in Three Distinct Stages. *Science*, 337(6100):1340–1343, September 2012.

[69] J GELLES, B J SCHNAPP, and M P SHEETZ. Tracking Kinesin-Driven Movements with Nanometre-Scale Precision. *Nature*, 331(6155):450–453, 1988.

[70] R N Ghosh and W W Webb. Automated Detection and Tracking of Individual and Clustered CellSurface Low Density Lipoprotein Receptor Molecules . *Biophysj*, 66(5):1301–1318, May 1994.

[71] C G Giraudo, C Hu, D You, A M Slovic, E V Mosharov, D Sulzer, T J Melia, and J E Rothman. SNAREs can promote complete fusion and hemifusion as alternative outcomes. *Journal Of Cell Biology*, 170(2):249–260, 2005.

[72] Ido Golding and Edward Cox. Physical Nature of Bacterial Cytoplasm. *Physical Review Letters*, 96(9):098102, March 2006.

[73] Jixian Gong, Xueming Zhao, Qirong Xing, Fang Li, Huanyu Li, Yanfeng Li, Lu Chai, Qingyue Wang, and Aleksei Zheltikov. Femtosecond laser-induced cell fusion. *Applied Physics Letters*, 92(9):093901, 2008.

[74] Andrea Grafmüller, Julian Shillcock, and Reinhard Lipowsky. Dissipative particle dynamics of tension-induced membrane fusion. *Molecular Simulation*, 35(7):554–560, June 2009.

[75] Steven P Gross, Michael Vershinin, and George T Shubeita. Cargo transport: Two motors are sometimes better than one. *Current Biology*, 17(12):R478–R486, 2007.

[76] Gernot Guigas and Matthias Weiss. Sampling the Cell with Anomalous Diffusion—The Discovery of Slowness. *Biophysj*, 94(1):90–94, January 2008.

[77] I M Hagan. The fission yeast microtubule cytoskeleton. *Journal of Cell Science*, 111 (Pt 12):1603–1612, June 1998.

[78] C Hamai, T Yang, S Kataoka, P S Cremer, and S M Musser. Effect of average phospholipid curvature on supported bilayer formation on glass by vesicle fusion. *Biophysj*, 90(4):1241–1248, 2006.

[79] J Happel and H Brenner. Low Reynolds Number Hydrodynamics. *Prentice-Hall, Inc*, 1965.

[80] ME Haque and B R Lentz. Influence of gp41 fusion peptide on the kinetics of poly(ethylene glycol)- mediated model membrane fusion. *Biochem*, page 11, 2002.

[81] Gregory J Hardy, Rahul Nayak, and Stefan Zauscher. Current Opinion in Colloid & Interface Science. *Current Opinion in Colloid & Interface Science*, 18(5):448–458, October 2013.

[82] Stephen C Harrison. Viral membrane fusion. *Nature Structural & Molecular Biology*, 15(7):690–698, 2008.

[83] L H Hartwell. Genetic control of the cell division cycle in yeast. IV. Genes controlling bud emergence and cytokinesis. *Experimental cell research*, 69(2):265–276, December 1971.

[84] W Helfrich. Elastic properties of lipid bilayers: theory and possible experiments. *Zeitschrift für Naturforschung. Teil C: Biochemie, Biophysik, Biologie, Virologie*, 28(11):693–703, November 1973.

[85] Kristian Helmerson, Joseph E Reiner, Erge Edgu-Fry, Jeffrey Wells, Rani Kishore, Laurie Locascio, and Michael Gilson. Optical manipulation of

nano-containers for biotechnology. In *Proc. of SPIE*, pages 91–98. SPIE, October 2004.

[86] J M Hernandez, A Stein, E Behrmann, D Riedel, A Cypionka, Z Farsi, P J Walla, S Raunser, and R Jahn. Membrane Fusion Intermediates via Directional and Full Assembly of the SNARE Complex. *Science*, 336(6088):1581–1584, June 2012.

[87] I Höfer and C Steinem. A membrane fusion assay based on pore-spanning lipid bilayers. *Soft Matter*, 7(5):1644–1647, 2011.

[88] Brenton D Hoffman and John C Crocker. Cell Mechanics: Dissecting the Physical Responses of Cells to Force. *Annual Review Of Biomedical Engineering*, 11(1):259–288, August 2009.

[89] Mathias W Hofmann, Karolina Peplowska, Jan Rohde, Bernhard C Poschner, Christian Ungermann, and Dieter Langosch. Self-interaction of a SNARE Transmembrane Domain Promotes the Hemifusion-to-fusion Transition. *Journal Of Molecular Biology*, 364(5):1048–1060, December 2006.

[90] Aurelia R Honerkamp-Smith, Sarah L Veatch, and Sarah L Keller. An introduction to critical points for biophysicists; observations of compositional heterogeneity in lipid membranes. *Biochimica Et Biophysica Acta-Biomembranes*, 1788(1):53–63, January 2009.

[91] Suzanne Hoppins, Laura Lackner, and Jodi Nunnari. The machines that divide and fuse mitochondria. *Annual Review of Biochemistry*, 76:751–780, 2007.

[92] S W Hui, T P Stewart, L T Boni, and P L Yeagle. Membrane fusion through point defects in bilayers. *Science (New York, NY)*, 212(4497):921–923, 1981.

[93] Anthony A Hyman and Clifford P Brangwynne. Beyond Stereospecificity:Liquids and Mesoscale Organization of Cytoplasm. *Developmental Cell*, 21(1):14–16, July 2011.

[94] Chieze Ibeneche. Cell Freezing in Response to Advanced Glucose Starvation: A Novel Cytoplasmic State in Fission Yeast. *Dissertation*, pages 1–165, December 2011.

[95] Takehiko Inaba, Yoshiro Tatsu, and Kenichi Morigaki. Fusion of Lipid Vesicles with Planar Lipid Bilayers Induced by a Combination of Peptides. *Langmuir*, 27(20):12515–12520, October 2011.

[96] Jacob N Israelachvili. *Intermolecular and Surface Forces.* Third Edition. Academic Press, third edition edition, July 2011.

[97] B S JACOBSON and D BRANTON. Plasma-Membrane - Rapid Isolation and Exposure of Cytoplasmic Surface by Use of Positively Charged Beads. *Science (New York, NY)*, 195(4275):302–304, 1977.

[98] R Jahn and H Grubmuller. Membrane fusion. *Current Opinion In Cell Biology*, 14(4):488–495, 2002.

[99] J Jass, T Tjarnhage, and G Puu. From liposomes to supported, planar bilayer structures on hydrophilic and hydrophobic surfaces: An atomic force microscopy study. *Biophysical Journal*, 79(6):3153–3163, 2000.

[100] Jae-Hyung Jeon, Vincent Tejedor, Stas Burov, Eli Barkai, Christine Selhuber-Unkel, Kirstine Berg-Sørensen, Lene Oddershede, and Ralf Metzler. In Vivo Anomalous Diffusion and Weak Ergodicity Breaking of Lipid Granules. *Physical Review Letters*, 106(4):048103, January 2011.

[101] Byron F Johnson, Paul Young, and A Nasim. *Molecular biology of the fission yeast*. Cell biology. Academic Press, San Diego, 1989.

[102] S J Johnson, TM Bayerl, D C McDermott, G W Adam, A R Rennie, R K Thomas, and E Sackmann. Structure of an adsorbed dimyristoylphosphatidylcholine bilayer measured with specular reflection of neutrons. *Biophysical Journal*, 59(2):289–294, 1991.

[103] H P Kao and A S Verkman. Cylindrical Optics. *Biophysj*, 67(3):1291–1300, September 1994.

[104] K Katsov. Field Theoretic Study of Bilayer Membrane Fusion: II. Mechanism of a Stalk-Hole Complex. *Biophysical Journal*, 90(3):915–926, October 2005.

[105] K Katsov, M Muller, and M Schick. Field theoretic study of bilayer membrane fusion. I. Hemifusion mechanism. *Biophysj*, 87(5):3277–3290, 2004.

[106] JWJ Kerssemakers, M E Janson, A van der Horst, and M Dogterom. Optical trap setup for measuring microtubule pushing forces. *Applied Physics Letters*, 83(21):4441–4443, 2003.

[107] M Kielian and FA Rey. Virus membrane-fusion proteins: more than one way to make a hairpin. *Nature Reviews Microbiology*, 4(1):67–76, 2006.

[108] Lila Kim, Kwang-Lae Hoe, Yeong Man Yu, Ji-Hyun Yeon, and Pil Jae Maeng. The Fission Yeast GATA Factor, Gaf1, Modulates Sexual Development via Direct Down-Regulation of ste11+ Expression in Response to Nitrogen Starvation. *Plos One*, 7(8):e42409, August 2012.

[109] PKJ Kinnunen and J M Holopainen. Mechanisms of initiation of membrane fusion: Role of lipids. *Bioscience Reports*, 20(6):465–482, December 2000.

[110] Volker Knecht and Siewert-Jan Marrink. Molecular dynamics simulations of lipid vesicle fusion in atomic detail. *Biophysical Journal*, 92(12):4254–4261, 2007.

[111] A Köhler and W Loos. Das Phasenkontrastverfahren und seine Anwendungen in der Mikroskopie. *Die Naturwissenschaften*, pages 49–64, 1941.

[112] David R Kovar, Vladimir Sirotkin, and Matthew Lord. Three's company: the fission yeast actin cytoskeleton. *Trends In Cell Biology*, 21(3):177–187, March 2011.

[113] MM Kozlov and VS Markin. Possible Mechanism of Membrane-Fusion. *Biofizika*, 28(2):242–247, 1983.

[114] Y Kozlovsky. Stalk Phase Formation: Effects of Dehydration and Saddle Splay Modulus. *Biophysical Journal*, 87(4):2508–2521, October 2004.

[115] Y Kozlovsky and M M Kozlov. Stalk model of membrane fusion: solution of energy crisis. *Biophysj*, 82(2):882–895, 2002.

[116] T Kuhl, YQ Guo, JL Alderfer, AD Berman, D Leckband, J Israelachvili, and SW Hui. Direct measurement of polyethylene glycol induced depletion attraction between lipid bilayers. *Langmuir*, 12(12):3003–3014, 1996.

[117] Dietmar Kültz. MOLECULAR AND EVOLUTIONARY BASIS OF THE CELLULAR STRESS RESPONSE. *Annual Review of Physiology*, 67(1):225–257, March 2005.

[118] PI Kuzmin, J Zimmerberg, Ya Chizmadzhev, and FS Cohen. A quantitative model for membrane fusion based on low-energy intermediates. *Proceedings Of The National Academy Of Sciences Of The United States Of America*, 98(13):7235–7240, 2001.

[119] J Lee and BR Lentz. Evolution of lipidic structures during model membrane fusion and the relation of this process to cell membrane fusion. *Biochemistry*, 36(21):6251–6259, 1997.

[120] J Lee and BR Lentz. Secretory and viral fusion may share mechanistic events with fusion between curved lipid bilayers. *Proceedings Of The National Academy Of Sciences Of The United States Of America*, 95(16):9274–9279, 1998.

[121] J Y Lee and M Schick. Field Theoretic Study of Bilayer Membrane Fusion III: Membranes with Leaves of Different Composition. *Biophysical Journal*, 92(11):3938–3948, March 2007.

[122] GH Lei and RC MacDonald. Lipid bilayer vesicle fusion: Intermediates captured by high-speed microfluorescence spectroscopy. *Biophysical Journal*, 85(3):1585–1599, 2003.

[123] BR Lentz, V Malinin, ME Haque, and K Evans. Protein machines and lipid assemblies: current views of cell membrane fusion. *Current Opinion In Structural Biology*, 10(5):607–615, 2000.

[124] Da-Wei Li and Xiang Yang Liu. Examination of membrane fusion by dissipative particle dynamics simulation and comparison with continuum elastic models. *The Journal of Chemical Physics*, 122(17):174909, 2005.

[125] Daniel Lingwood and Kai Simons. Lipid Rafts As a Membrane-Organizing Principle. *Science*, 327(5961):46–50, 2010.

[126] T Liu, T Wang, E R Chapman, and J C Weisshaar. Productive hemifusion intermediates in fast vesicle fusion driven by neuronal SNAREs. *Biophyisical Journal*, 94(4):1303–1314, 2008.

[127] J R Lobry, J P Flandrois, G Carret, and A Pave. Monod's bacterial growth model revisited. *Bulletin of Mathematical Biology*, 54(1):117–122, 1992.

[128] M S Longtine, D J DeMarini, M L Valencik, O S Al-Awar, H Fares, C De Virgilio, and J R Pringle. The septins: roles in cytokinesis and other processes. *Current Opinion In Cell Biology*, 8(1):106–119, February 1996.

[129] Bärbel Lorenz, Rabea Keller, Eva Sunnick, Burkhard Geil, and Andreas Janshoff. Colloidal probe microscopy of membrane–membrane interactions: From ligand–receptor recognition to fusion events. *Biophysical Chemistry*, 150(1-3):54–63, June 2010.

[130] Katherine Luby-Phelps, Philip E Castle, D Lansing Taylor, and Frederick Lanni. Hindered diffusion of inert tracer particles in the cytoplasm of mouse 3T3 cells. *Proceedings Of The National Academy Of Sciences Of The United States Of America*, 84(14):4910–4913, 1987.

[131] Katherine Luby-Phelps, D Lansing Taylor, and Frederick Lanni. Probing the Structure of Cytoplasm. *Journal Of Cell Biology*, 102(6):2015–2022, June 1986.

[132] V S Markin, M M Kozlov, and V L Borovjagin. On the theory of membrane fusion. The stalk mechanism. *Gen. Physiol. Biophys*, 3(5):361–377, 1984.

[133] VS Markin and JP Albanesi. Membrane fusion: Stalk model revisited. *Biophysical Journal*, 82(2):693–712, 2002.

[134] Hana Robson Marsden, Itsuro Tomatsu, and Alexander Kros. Model systems for membrane fusion. *Chemical Society Reviews*, 40(3):1572, 2011.

[135] Sascha Martens and Harvey T McMahon. Mechanisms of membrane fusion: disparate players and common principles. *Nature Reviews Molecular Cell Biology*, 9(7):543–556, 2008.

[136] PL McNeil and RA Steinhardt. Plasma membrane disruption: Repair, prevention, adaptation. *Annual Review Of Cell And Developmental Biology*, 19:697–731, 2003.

[137] JA McNew. Regulation of SNARE-mediated membrane fusion during exocytosis. *Chemical Reviews*, 108(5):1669–1686, 2008.

[138] Thomas J Melia. Putting the clamps on membrane fusion: How complexin sets the stage for calcium-mediated exocytosis. *FEBS LETTERS*, 581(11):2131–2139, 2007.

[139] GB Melikyan, J M White, and F S Cohen. GPI-anchored Influenza Hemagglutinin Induces Hemifusion to both Red Blood Cell and Planar Bilayer Membranes. *Journal Of Cell Biology*, 131:13, 1995.

[140] R Merkel, E Sackmann, and E Evans. Molecular friction and epitactic coupling between monolayers in supported bilayers. *Journal de Physique*, 50(12):1535–1555, 1989.

[141] Ralf Metzler and Joseph Klafter. The random walk's guide to anomalous diffusion: a fractional dynamics approach. *Physics reports*, 339(1):1–77, 2000.

[142] Ingo Mey, Milena Stephan, Eva K Schmitt, Martin Michael Mueller, Martine Ben Amar, Claudia Steinem, and Andreas Janshoff. Local Membrane Mechanics of Pore-Spanning Bilayers. *Journal Of The American Chemical Society*, 131(20):7031–7039, 2009.

[143] Agnès Miermont, François Waharte, Shiqiong Hu, Megan Nicole McClean, Samuel Bottani, Sébastien Léon, and Pascal Hersen. Severe osmotic compression triggers a slowdown of intracellular signaling, which can be explained by molecular crowding. *Proceedings Of The National Academy Of Sciences Of The United States Of America*, 110(14):5725–5730, 2013.

[144] C E Miller, J Majewski, T Gog, and T L Kuhl. Characterization of biological thin films at the solid-liquid interface by X-ray reflectivity. *Physical Review Letters*, 94(23):238104, 2005.

[145] J M MITCHISON and P NURSE. Growth in Cell Length in the Fission Yeast Schizosaccharomyces-Pombe. *Journal of Cell Science*, 75(APR):357–376, 1985.

[146] J R MONCK and J M FERNANDEZ. The Exocytotic Fusion Pore and Neurotransmitter Release. *Neuron*, 12(4):707–716, April 1994.

[147] Serge Mostowy and Pascale Cossart. Septins: the fourth component of the cytoskeleton. *Nature Reviews Molecular Cell Biology*, 13(3):183–194, February 2012.

[148] Hiroyuki Mukaiyama, Mai Nakase, Taro Nakamura, Yoshimi Kakinuma, and Kaoru Takegawa. Autophagy in the fission yeast Schizosaccharomyces pombe. *FEBS LETTERS*, 584(7):1327–1334, April 2010.

[149] M Muller, K Katsov, and M Schick. New mechanism of membrane fusion. *The Journal of Chemical Physics*, 116(6):2342–2345, 2002.

[150] M Muller, K Katsov, and M Schick. A new mechanism of model membrane fusion determined from Monte Carlo simulation. *Biophysical Journal*, 85(3):1611–1623, 2003.

[151] Heidemarie Müllner and Günther Daum. Dynamics of neutral lipid storage in yeast. *Acta biochimica Polonica*, 51(2):323–347, 2004.

[152] C NANAVATI, VS Markin, AF OBERHAUSER, and JM FERNANDEZ. The Exocytotic Fusion Pore Modeled As A Lipidic Pore. *Biophysical Journal*, 63(4):1118–1132, 1992.

[153] C A Naumann, O Prucker, T Lehmann, J Rühe, W Knoll, and C W Frank. The Polymer-Supported Phospholipid Bilayer: Tethering as a New Approach to SubstrateâMembrane Stabilization. *Biomacromolecules*, 3(1):27–35, January 2002.

[154] Christoph Naumann, Thomas Brumm, and Thomas M Bayerl. Phase transition behavior of single phosphatidylcholine bilayers on a solid spherical support studied by DSC, NMR and FT-IR. *Biophysj*, 63(5):1314–1319, November 1992.

[155] KC Neuman and SM Block. Optical trapping. *Review Of Scientific Instruments*, 75(9):2787–2809, 2004.

[156] Jörg Nikolaus, Martin Stöckl, Dieter Langosch, Rudolf Volkmer, and Andreas Herrmann. Direct Visualization of Large and Protein-Free Hemifusion Diaphragms. *Biophysj*, 98(7):1192–1199, April 2010.

[157] D Nilsson and P Sunnerhagen. Cellular stress induces cytoplasmic RNA granules in fission yeast. *RNA*, 17(1):120–133, December 2011.

[158] Eva Nováková, Klaus Giewekemeyer, and Tim Salditt. Structure of two-component lipid membranes on solid support: An x-ray reflectivity study. *Physical Review E*, 74(5):9, November 2006.

[159] Paul Nurse and Yvonne Bissett. Gene required in G1 for commitment to cell cycle and in G2 for control of mitosis in fission yeast. *Nature*, 1981.

[160] Younghoon Oh and Erfei Bi. Septin structure and function in yeastand beyond. *Trends In Cell Biology*, 21(3):141–148, March 2011.

[161] S Ohta-Iino, M Pasenkiewicz-Gierula, Y Takaoka, H Miyagawa, K Kitamura, and A Kusumi. Fast lipid disorientation at the onset of membrane fusion revealed by molecular dynamics simulations. *Biophysical Journal*, 81(1):217–224, 2001.

[162] Bradley R Parry, Ivan V Surovtsev, Matthew T Cabeen, Corey S O'Hern, Eric R Dufresne, and Christine Jacobs-Wagner. The Bacterial Cytoplasm Has Glass-like Properties and Is Fluidized by Metabolic Activity. *Cell*, 156(1-2):183–194, January 2014.

[163] I Pera, R Stark, M Kappl, HJ Butt, and F Benfenati. Using the atomic force microscope to study the interaction between two solid supported lipid bilayers and the influence of synapsin I. *Biophysical Journal*, 87(4):2446–2455, 2004.

[164] R Peters and R J Cherry. Lateral and Rotational Diffusion of Bacteriorhodopsin in Lipid Bilayers: Experimental Test of the Saffman-Delbruck Equations. *Proceedings Of The National Academy Of Sciences Of The United States Of America-Biological Sciences*, 79(14):4317–4321, 1982.

[165] Maksymilian Pluta. Nomarski's DIC micmscopy: a review. *SPIE*, 1846:10–25, November 2004.

[166] Keith R Porter. The cytomatrix: a short history of its study. *Journal Of Cell Biology*, 99(1):3s–12s, 1984.

[167] A Pralle, E-L Florin, EHK Stelzer, and JKH Horber. Local viscosity probed by photonic force microscopy. *Applied Physics A-Materials Science & Processing*, 66:71–73, 1998.

[168] A Pralle, P Keller, EL Florin, K Simons, and JKH Horber. Sphingolipid-cholesterol rafts diffuse as small entities in the plasma membrane of mammalian cells. *Journal Of Cell Biology*, 148(5):997–1007, 2000.

[169] A Pralle, M Prummer, EL Florin, EHK Stelzer, and JKH Horber. Three-dimensional high-resolution particle tracking for optical tweezers by forward scattered light. *Microscopy Research And Technique*, 44(5):378–386, 1999.

[170] C Preza, D L Snyder, and J A Conchello. Theoretical development and experimental evaluation of imaging models for differential-interference-contrast microscopy. *Journal of the Optical Society of America a-Optics Image Science and Vision*, 16(9):2185–2199, September 1999.

[171] Paul Primakoff and Diana G Myles. Cell-cell membrane fusion during mammalian fertilization. *FEBS LETTERS*, 581(11):2174–2180, 2007.

[172] Julia Riedl, Alvaro H Crevenna, Kai Kessenbrock, Jerry Haochen Yu, Dorothee Neukirchen, Michal Bista, Frank Bradke, Dieter Jenne, Tad A Holak, Zena Werb, Michael Sixt, and Roland Wedlich-Söldner. Lifeact:

a versatile marker to visualize F-actin. *Nature Methods*, 5(7):605–607, June 2008.

[173] Daniel Rings, Romy Schachoff, Markus Selmke, Frank Cichos, and Klaus Kroy. Hot Brownian Motion. *Physical Review Letters*, 105(9):090604, August 2010.

[174] Josep Rizo and Christian Rosenmund. Synaptic vesicle fusion. *Nature Structural & Molecular Biology*, 15(7):665–674, 2008.

[175] Silvio O Rizzoli and Reinhard Jahn. Kiss-and-run, Collapse and 'Readily Retrievable' Vesicles. *Traffic*, 8(9):1137–1144, September 2007.

[176] Damien Robert, Thi-Hanh Nguyen, François Gallet, and Claire Wilhelm. In Vivo Determination of Fluctuating Forces during Endosome Trafficking Using a Combination of Active and Passive Microrheology. *Plos One*, 5(4):e10046, April 2010.

[177] Salman S Rogers, Thomas A Waigh, and Jian R Lu. Intracellular Microrheology of Motile Amoeba proteus. *Biophysj*, 94(8):3313–3322, April 2008.

[178] Antoine E Roux, Alexandre Leroux, Manal A Alaamery, Charles S Hoffman, Pascal Chartrand, Gerardo Ferbeyre, and Luis A Rokeach. Pro-Aging Effects of Glucose Signaling through a G Protein-Coupled Glucose Receptor in Fission Yeast. *PLoS Genetics*, 5(3):e1000408, March 2009.

[179] E Sackmann. Supported membranes: Scientific and practical applications. *Science*, 271(5245):43–48, 1996.

[180] P G Saffman and M Delbrück. Brownian motion in biological membranes. *Proceedings Of The National Academy Of Sciences Of The United States Of America*, 72(8):3111–3113, 1975.

[181] Amir Sapir, Ori Avinoam, Benjamin Podbilewicz, and Leonid V Chernomordik. Viral and developmental cell fusion mechanisms: Conservation and divergence. *Developmental Cell*, 14(1):11–21, 2008.

[182] Kenneth E Sawin and P T Tran. Cytoplasmic microtubule organization in fission yeast. *Yeast*, 23(13):1001–1014, 2006.

[183] M J Saxton and K Jacobson. Single-particle tracking: applications to membrane dynamics. *Annual Review Of Biophysics And Biomolecular Structure*, 26:373–399, 1997.

[184] M J Saxton and K Jacobson. Single-particle tracking: Applications to membrane dynamics. *Annual Review Of Biophysics And Biomolecular Structure*, 26:373–399, December 1997.

[185] M Schick. Biological physics in four lectures and three applications. *Physica A: Statistical and Theoretical Physics*, 369(1):100–121, September 2006.

[186] T Schmidt, G J Schutz, W Baumgartner, H J Gruber, and H Schindler. Imaging of single molecule diffusion. *Proceedings Of The National*

Academy Of Sciences Of The United States Of America, 93(7):2926–2929, 1996.

[187] G J Schutz, H Schindler, and T Schmidt. Single-Molecule Microscopy. *Biophysj*, 73(2):1073–1080, August 1997.

[188] Christine Selhuber-Unkel, Pernille Yde, Kirstine Berg-Sørensen, and Lene Oddershede. Variety in intracellular diffusion during the cell cycle. *Physical Biology*, 6(2):025015, June 2009.

[189] Yafell Serulle, Mutsuyuki Sugimori, and Rodolfo R Linas. Imaging synaptosomal calcium concentration microdomains and vesicle fusion by using total internal reflection fluorescent microscopy. *Proceedings Of The National Academy Of Sciences Of The United States Of America*, 104(5):1697–1702, 2007.

[190] K J Seu, A P Pandey, F Haque, E A Proctor, A E Ribbe, and J S Hovis. Effect of Surface Treatment on Diffusion and Domain Formation in Supported Lipid Bilayers. *Biophysical Journal*, 92(7):2445–2450, January 2007.

[191] Kalani J Seu, Anjan P Pandey, Farzin Haque, Elizabeth A Proctor, Alexander E Ribbe, and Jennifer S Hovis. Effect of surface treatment on diffusion and domain formation in supported lipid bilayers. *Biophysical Journal*, 92(7):2445–2450, 2007.

[192] Andrey S Shaw. Lipid rafts: now you see them, now you don't. *Nature Immunology*, 7(11):1139–1142, 2006.

[193] Julian C Shillcock and Reinhard Lipowsky. Tension-induced fusion of bilayer membranes and vesicles. *Nature Materials*, 4(3):225–228, March 2005.

[194] Dp Siegel. Energetics of Intermediates in Membrane Fusion; Comparison of Stalk and Inverted Micellar Intermediate Mechanisms. *Biophysical Journal*, 65(5):2124–2140, 1993.

[195] Kai Simons and Mathias J Gerl. Revitalizing membrane rafts: new tools and insights. *Nature Publishing Group*, 11(10):688–699, January 2010.

[196] Kai Simons and Winchil L C Vaz. Model Systems, Lipid Rafts, And Cell Membranes. *Annual Review Of Biophysics And Biomolecular Structure*, 33(1):269–295, June 2004.

[197] D M Soumpasis. Theoretical analysis of fluorescence photobleaching recovery experiments. *Biophysical Journal*, 41(1):95–97, 1983.

[198] M Speidel, A Jonas, and E-L Florin. Three-dimensional tracking of fluorescent nanoparticles with subnanometer precision by use of off-focus imaging. *Optics Letters*, 28(2):69–71, 2003.

[199] Todd M Squires and Thomas G Mason. Fluid Mechanics of Microrheology. *Annual Review of Fluid Mechanics*, 42(1):413–438, January 2010.

[200] Cornelis Storm, Jennifer J Pastore, F C Mackintosh, T C Lubensky, and Paul A Janmey. Nonlinear elasticity in biological gels. *Nature*, 435:191–194, 2005.

[201] S S Su, Y Tanaka, I Samejima, K Tanaka, and M Yanagida. A nitrogen starvation-induced dormant G0 state in fission yeast: the establishment from uncommitted G1 state and its delay for return to proliferation. *J Cell Sci*, 109 (Pt 6):1347–1357, June 1996.

[202] K SVOBODA, C F Schmidt, B J SCHNAPP, and S M BLOCK. Direct Observation of Kinesin Stepping by Optical Trapping Interferometry. *Nature*, 365(6448):721–727, 1993.

[203] L K Tamm and H M McConnell. Supported phospholipid bilayers. *Biophysj*, 47(1):105–113, January 1985.

[204] Charles Tanford. *The hydrophobic effect.* formation of micelles and biological membranes. John Wiley & Sons, January 1980.

[205] Pradip K Tarafdar, Hirak Chakraborty, S Moses Dennison, and Barry R Lentz. Phosphatidylserine Inhibits and Calcium Promotes Model MembraneFusion. *Biophysj*, 103(9):1880–1889, November 2012.

[206] Fuyuki Tokumasu, Albert J Jin, Gerald W Feigenson, and James A Dvorak. Atomic force microscopy of nanometric liposome adsorption and nanoscopic membrane domain formation. *Ultramicroscopy*, 97(1-4):217–227, October 2003.

[207] Iva Tolić-Nørrelykke, Emilia-Laura Munteanu, Genevieve Thon, Lene Oddershede, and Kirstine Berg-Sørensen. Anomalous Diffusion in Living Yeast Cells. *Physical Review Letters*, 93(7):078102, August 2004.

[208] Sofie Trier, Jonas R Henriksen, and Thomas L Andresen. Membrane fusion of pH-sensitive liposomes – a quantitative study using giant unilamellar vesicles. *Soft Matter*, pages 1–8, 2011.

[209] T Wakatsuki, B Schwab, N C Thompson, and E L Elson. Effects of cytochalasin D and latrunculin B on mechanical properties of cells. *J Cell Sci*, 114(Pt 5):1025–1036, March 2001.

[210] Xuemin Wang. Lipid signaling. *Current Opinion in Plant Biology*, 7(3):329–336, June 2004.

[211] Jason M Warner and Ben OShaughnessy. The Hemifused State on the Pathway to Membrane Fusion. *PRL*, 98(7):1192–1199, 2012.

[212] T Weber, BV Zemelman, JA McNew, B Westermann, M Gmachl, F Parlati, TH Sollner, and JE Rothman. SNAREpins: Minimal machinery for membrane fusion. *Cell*, 92(6):759–772, 1998.

[213] Christine S Weirich, Jan P Erzberger, and Yves Barral. The septin family of GTPases: architecture and dynamics. *Nature Reviews Molecular Cell Biology*, 9(6):478–489, May 2008.

[214] Matthias Weiss, Markus Elsner, Fredrik Kartberg, and Tommy Nilsson. Anomalous Subdiffusion Is a Measure for Cytoplasmic Crowding in Living Cells. *Biophysj*, 87(5):3518–3524, November 2004.

[215] Winfried Weissenhorn, Andreas Hinz, and Yves Gaudin. Virus membrane fusion. *FEBS LETTERS*, 581(11):2150–2155, 2007.

[216] Shannon D Whitman and Rebecca Ellis Dutch. Surface density of the Hendra G protein modulates Hendra F protein-promoted membrane fusion: Role for Hendra G protein trafficking and degradation. *Virology*, 363(2):419–429, 2007.

[217] William Wickner. Membrane Fusion: Five Lipids, Four SNAREs, Three Chaperones, Two Nucleotides, and a Rab, All Dancing in a Ring on Yeast Vacuoles. *Annual Review Of Cell And Developmental Biology*, 26(1):115–136, November 2010.

[218] Claire Wilhelm. Out-of-Equilibrium Microrheology inside Living Cells. *Physical Review Letters*, 101(2):028101, July 2008.

[219] Claire Wilhelm. Effective temperature inside living cells. *Mater. Res. Soc. Symp. Proc.*, 1227:1–10, February 2010.

[220] P Williams, E Keshavarz-Moore, and P Dunnill. Production of cadmium sulphide microcrystallites in batch cultivation by Schizosaccharomyces pombe. *Journal of biotechnology*, 48(3):259–267, July 1996.

[221] Morgan Williamson. High Precision Fluid Exchange System for Particle Tracking in Fission Yeast Cells. Technical report, April 2014.

[222] Denis Wirtz. Particle-Tracking Microrheology of Living Cells: Principles and Applications. *Annual Review of Biophysics*, 38(1):301–326, June 2009.

[223] J Wolfe, E Perez, M Bonanno, and J P Chapel. The interaction and fusion of bilayers formed from unsaturated lipids. *European Biophysics Journal*, 19(5):275–281, 1991.

[224] I Wong, M Gardel, D Reichman, Eric Weeks, M Valentine, A Bausch, and D Weitz. Anomalous Diffusion Probes Microstructure Dynamics of Entangled F-Actin Networks. *Physical Review Letters*, 92(17):178101, April 2004.

[225] JY Wong, CK Park, M Seitz, and J Israelachvili. Polymer-cushioned bilayers. II. An investigation of interaction forces and fusion using the surface forces apparatus. *Biophysical Journal*, 77(3):1458–1468, 1999.

[226] V Wood and et al. The genome sequence of Schizosaccharomyces pombe. *Nature*, 415(6874):871–880, 2002.

[227] Y Xu, F Zhang, Z Su, J A McNew, and Y K Shin. Hemifusion in SNARE-mediated membrane fusion. *Nature structural & molecular biology*, 12(5):417–422, 2005.

[228] Soichiro Yamada, Denis Wirtz, and Scot C Kuo. Mechanics of living cells measured by laser tracking microrheology. *Biophysj*, 78(4):1736–1747, 2000.

[229] Mitsuhiro Yanagida. Cellular quiescence: are controlling genes conserved? *Trends In Cell Biology*, 19(12):705–715, December 2009.

[230] M Yanai, James P Butler, T Suzuki, H Sasaki, and H Higuchi. Regional rheological differences in locomoting neutrophils. *AJP: Cell Physiology*, 287(3):C603–C611, September 2004.

[231] L Yang and H W Huang. Observation of a membrane fusion intermediate structure. *Science (New York, NY)*, 297(5588):1877–1879, 2002.

[232] Myrto-Panagiota Zacharof and Robert W Lovitt. Modelling and simulation of cell growth dynamics, substrate consumption, and lactic acid production kinetics of Lactococcus lactis. *Biotechnology and Bioprocess Engineering*, 18(1):52–64, March 2013.

[233] M ZALOKAR. Cytochemistry of Centrifuged Hyphae of Neurospora. *Experimental cell research*, 19(1):114–132, 1960.

[234] G A Zampighi, L M Zampighi, N Fain, S Lanzavecchia, S A Simon, and E M Wright. Conical electron tomography of a chemical synapse: Vesicles docked to the active zone are hemi-fused. *Biophysical Journal*, 91(8):2910–2918, 2006.

[235] J Zimmerberg and LV Chernomordik. Membrane fusion. *Advanced Drug Delivery Reviews*, 38(3):197–205, 1999.

Vita

Andrea Keidel was born in Wuerzburg, Germany. After graduating from the Mozart - und Schoenborn Gymnasium in Wuerzburg in 2004, she started studying physics at the Julius-Maximilians-Universitaet in Wuerzburg, Germany, where she received her Vordiplom in October 2006. After studying physics for another year in Wuerzburg, she participated in the America exchange program of the department of physics and enrolled in the graduate school at the University of Texas at Austin in August 2007. There she received her Master of Arts in December 2008. She continued her graduate studies in 2009. In May of 2014, she graduated from the program thereby earning her Ph.D. in physics.

Permanent address: andreakeidel@yahoo.com

This dissertation was typeset with LaTeX[†] by the author.

[†] LaTeX is a document preparation system developed by Leslie Lamport as a special version of Donald Knuth's TeX Program.